



UNIVERSITÀ  
DI TRENTO

Department of  
Industrial Engineering

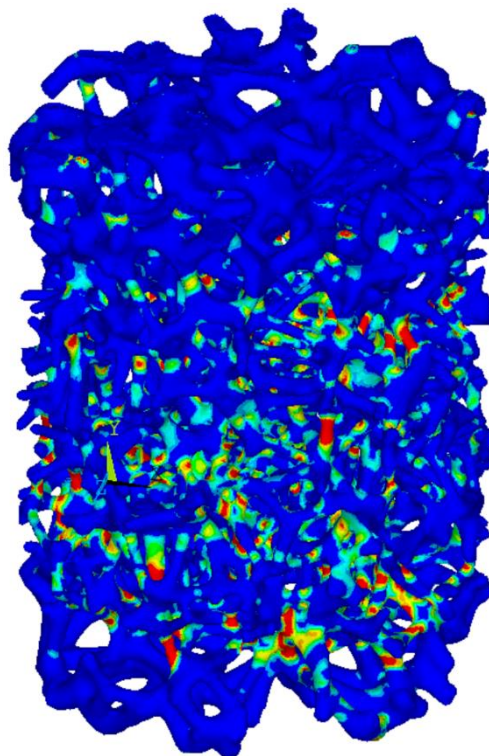
XXXIII cycle

Doctoral School in Materials, Mechatronics and System Engineering

---

# Metallurgical and Mechanical Properties of Additively Manufactured Cellular Structures

*Sunil Raghavendra*



---

March 2021



# Metallurgical and Mechanical Properties of Additively Manufactured Cellular Structures

Sunil Raghavendra

sunil.raghavendra@unitn.it

**Approved by:**

Prof. Matteo Benedetti, Supervisor  
*Dept. of Industrial Engineering*  
University of Trento, Italy.

Prof. Alberto Molinari  
*Dept. of Industrial Engineering*  
University of Trento, Italy.

**PhD Commission:**

Prof. Vigilio Fontanari  
*Dept. of Industrial Engineering*  
University of Trento, Italy.

Prof. Seyed Mohammad Javad Razavi  
*Dept. of Mechanical and Industrial  
Engineering*  
Norwegian University of Science and  
Technology, Norway.

Dr. Sara Bagherifard  
*Dept. of Mechanical Engineering*  
Politecnico di Milano, Italy.

University of Trento  
Department of Industrial Engineering

March 2021

University of Trento - Department of  
Industrial Engineering

Doctoral Thesis

Sunil Raghavendra - 2021

Published in Trento (Italy) – by University of Trento

To my parents, in-laws, and  
my beloved wife, Priya



---

## Abstract

---

Naturally occurring cellular materials are always optimized in terms of morphology, structural resistance, and functionality. The use of cellular materials is based on the application as well as the loading condition. Cellular materials are composed of an interconnected network of struts, plates, or repeating unit cells, forming edges or faces. The properties of these structures can be tailored according to the requirements by changing one or more of the parameters mentioned above. This makes cellular materials suitable for various applications ranging from aerospace to biomedical. In biomedical applications, these cellular materials can be used to manufacture porous implants to match the properties of the surrounding bone. They can also be used as coatings on solid implants to promote bone tissue ingrowth for better implant fixation. The production of these complex, porous implants using traditional manufacturing methods is a difficult task. However, the development of additive manufacturing processes such as Laser Powder Bed Fusion (LPBF) has made it possible to manufacture complex and intricate shaped cellular materials with minimum material wastage and considerable accuracy. Therefore, with the combination of the LPBF process and cellular materials design, it is possible to produce a wide range of cell topologies with customized mechanical properties depending on the implant location, material, and the needs of the patient. Titanium and its alloys such as Ti6Al4V have been used in biomedical applications due to their high strength to weight ratio, corrosion resistance, and good biocompatibility. Also, the LPBF process has been used to produce various Ti6Al4V components for various applications including cellular materials. The development of cellular materials for implants is dependent on the relative density, response of the unit cell to loading conditions, and the optimal pore size for bone ingrowth. Studies have been carried out to understand the behavior of the cellular materials under compressive loads since most of the implants experience compression loads during their operation. Nevertheless, the implants also undergo fatigue loading due to day-to-day activities and tensile loads when the implant is loose or when the host performs an extensive physical activity. Therefore, designing and studying the cellular materials for these loads is necessary to completely understand their behavior. Considering the pore size, studies have suggested that a pore size of  $\sim 800 \mu\text{m}$  is suitable to induce bone ingrowth after implantation. The cellular materials can be broadly classified into stretching and bending dominated. Stretching dominated cellular materials are characterized by high strength and stiffness while bending dominated structures are high compliant. This behavior of cellular materials is dependent solely on the unit cell topology. Therefore, the development of different types of cell topologies and their characterization is required to produce optimized fully porous implants. Also, the effect of the LPBF process on the designed parameters of the unit cell alters the obtained mechanical properties from the desired values.

The present work aims at developing different Ti6Al4V cellular materials that can be potentially used for application in implants. A combination of different cellular materials can be used to develop completely porous implants or single cellular materials can be used as coatings for solid implants to induce osseointegration. A major portion of the work is focused on the mechanical properties of LPBF manufactured cellular materials characterized using static and fatigue tests. The study also investigates the discrepancy between the as-designed and as-built geometrical parameters of these cellular structures. Finite elements analysis and the Gibson-Ashby modeling has been employed to understand the difference between the as-designed and as-built properties. Another part of the study was focused on the effect of designed geometrical parameters on the as-built geometry of cellular materials. The aim was to develop a relationship between the as-designed and the as-built parameters.

This thesis covers all the aspects mentioned in the above paragraph in detail. The research work has been provided in three different chapters (Chapter 2, 3, and 4) which are well connected to each other. Each chapter is composed of an abstract, introduction, materials and methodology, results and discussion, and conclusion. A conclusion on the complete research and the future scope is provided at

the end. The first chapter introduces all the aspects concerned with the development of cellular materials for biomedical applications. Literature review on all aspects have been provided, ranging from the properties of the bone, cellular materials, manufacturing process for cellular materials, and the properties of bulk materials suitable for biomedical applications.

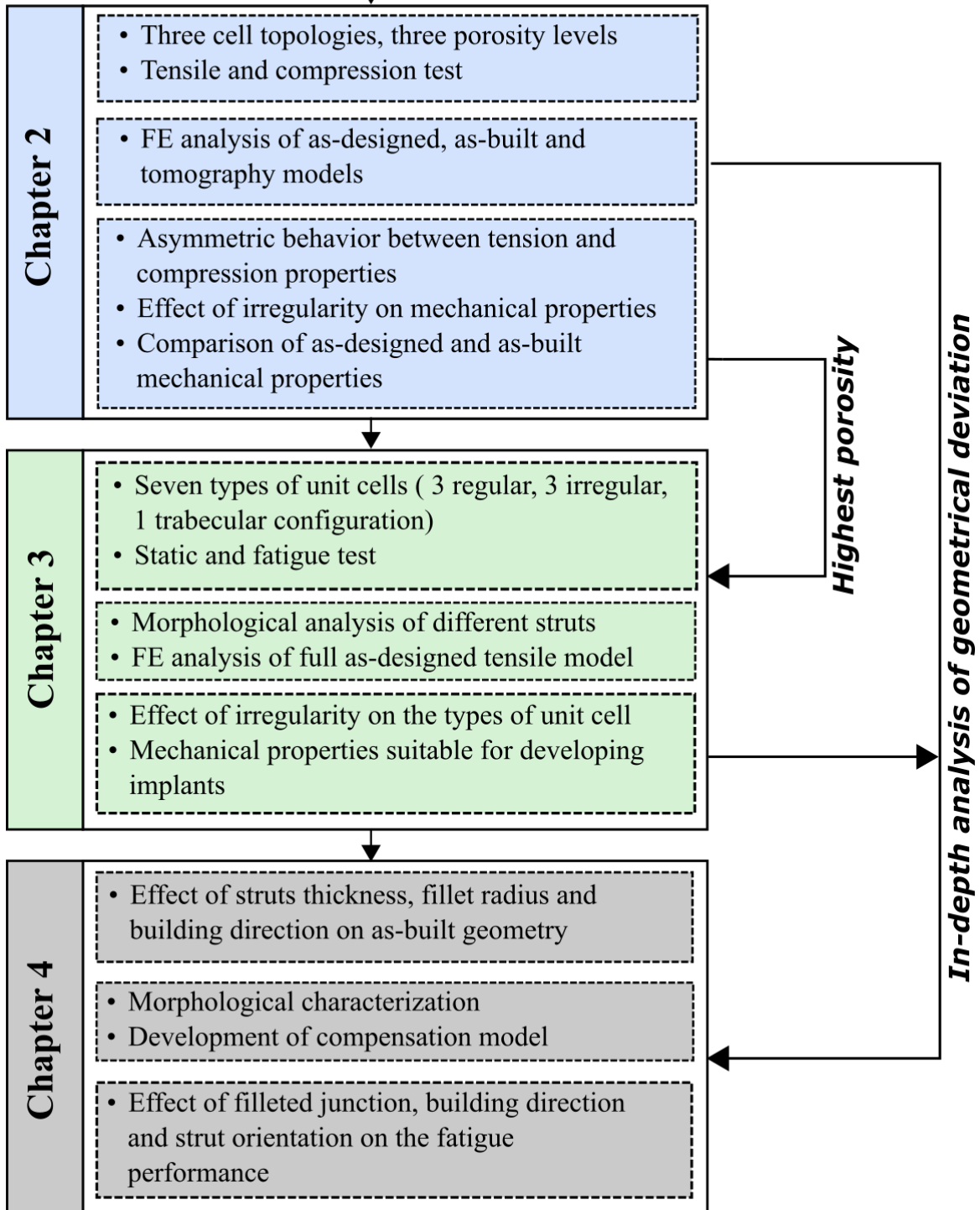
In chapter 2, Ti6Al4V cellular materials with three different cell topologies namely cubic regular, cubic irregular, and trabecular have been investigated. The irregular specimens are obtained by skewing the junctions of the cubic regular configuration. Trabecular specimens are designed by randomly joining 4-6 struts at a node to mimic human trabecular bone. The three cell topologies were manufactured at three different porosity levels by changing their strut thickness and pore size. The cubic regular cells are considered due to their stable and simple configuration, while irregular and trabecular based specimens have shown promising results in the osseointegration according to the partner company. However, the mechanical properties of irregular and trabecular specimens play an important role in implant design. Therefore, all the specimens were subjected to compression test and as well as a novel tensile test under two different types of loading conditions, monotonic and cyclic to obtain their strength and stiffness. However, a misalignment in the struts with the loading direction in compression led to an asymmetric behavior between tensile and compression. Higher strength and stiffness values were observed under tensile loading, the results of which were in conjunction with the theoretical prediction from the Gibson-Ashby model. The experimental results indicated the irregularity tends to reduce the strength, stiffness and induce bending dominate behavior. Morphological analysis was carried out to obtain the discrepancy between the as-designed and the as-built thickness values. This led to the FE analysis of as-designed models to obtain the difference in the properties of as-designed and as-built cellular materials. Furthermore, as-built FE models were generated using morphological data to study the effect of strut defects and compare them with the experimental results. The next step involved comparing the experimental results with the FE analysis carried out tomography-based FE models. The last part of the study involved obtaining a relation between the as-designed and as-built Young's modulus for cubic regular, cubic irregular, and trabecular specimens to create a reference database. The mechanical properties from the compression and tensile test of the highest porosity specimens were closer to the properties of human bone. The tensile tests were successful in predicting the mechanical properties accurately. These observations were the motivation to further study the effect of irregularity on various cell topologies, by subjecting them to static and fatigue loads.

In chapter 3, seven different types of unit cells, three regular configurations, three irregular configurations, and one trabecular based unit cell. The unit cells used in the study consisted of regular and irregular configurations of the cubic-based, star-based, and cross-based specimens. These specimens were selected to have a comparison of properties from stretching dominate cubic specimen to bending dominated cross-shaped specimens and to study the effect of irregularity. Therefore, the specimens were subjected to and mechanical characterization using compression, tension, and compression – compression fatigue tests along with porosity and morphological analysis. The tensile specimens in this chapter were designed with a thicker transition at the ends, while compression specimens had uniform configuration throughout the specimen. FE analysis was carried on the as-designed configuration of these specimens to study the effect of transition and to compare the as-designed and tensile experimental results to understand the effect of decreased porosity on the failure mechanisms. Fatigue tests were carried under compression-compression load and failure mechanisms in different unit cells were captured. The results of the study indicated that the irregularity has a greater effect on the strength and stiffness of stretching-dominated cellular material and has a negligible effect on bending-dominated cross-based specimens. The trabecular specimens display excellent mechanical properties under static load with good strength, stiffness and sustain high strain values. The normalized S-N curves indicate a clear demarcation between the bending and stretching-dominated cellular materials. The FE analysis showed a similar failure location as compared to the experimental results despite the decrease in the porosity due to manufacturing. The morphological analysis showed the effect of strut orientation of the as-built thickness. The morphological analysis and the difference between the

as-designed and as-built geometrical parameters show that an in-depth study on the geometrical deviation due to the LPBF process is necessary. The next chapter focuses on the geometrical deviation in LPBF manufactured cellular specimens and the parameters influencing this deviation.

In chapter 4, cubic regular cellular materials with filleted junctions are studied for geometrical deviation and to obtain a relationship between the as-designed and as-built geometric parameters. Initially, nine different specimens with different strut thickness, fillet radius, and unit cell size were manufactured at three different orientations with respect to the printing plane. The main aim of this study was to devise a compensation strategy to reduce the geometrical deviation due to the LPBF process. A linear relation between the as-designed and as-built geometrical values is obtained, which is used for compensation modeling. Struts perpendicular to the building plane were uniform in cross-sections while horizontal and inclined struts had an elliptical cross-section. The internal porosity analysis has been carried out which indicates that the porosity at the junctions is lesser than the porosity at the junctions. The compensation strategy worked well for the second set of specimens produced using the same parameters, thereby reducing the geometrical deviation between the as-designed and the as-built parameters. Finally, the effect of filleted junctions, building directions, and compensation modeling on fatigue properties have been studied. Specimens with load-bearing struts printed parallel to the building plane had the lowest mechanical properties, while the specimens with struts inclined to the loading direction and building plane displayed excellent static and fatigue properties. The fillets at the junctions improve the fatigue resistance of the specimen by reducing the stress concentration. The printing direction and the presence of fillets influence the fatigue failure locations as well. Therefore, filleted junctions that can be reproduced well by the LPBF process can be used to reduce the stress concentration in cellular materials. The workflow adopted in this study is provided on the next page.

## Characterization of Ti6Al4V cellular materials



---

## Table of contents

---

|   |            |
|---|------------|
| <b>ABSTRACT.....</b>  | <b>I</b>   |
| <b>TABLE OF CONTENTS .....</b>  | <b>V</b>   |
| <b>LIST OF FIGURES .....</b>  | <b>IX</b>  |
| <b>LIST OF TABLES .....</b>   | <b>XIV</b> |
| <b>CHAPTER 1: INTRODUCTION.....</b>   | <b>1</b>   |
| <b>1.1. HUMAN BONE AND IMPLANTS .....</b>                                       | <b>1</b>   |
| 1.1.1. COMPOSITION AND STRUCTURE OF HUMAN BONE .....                            | 1          |
| 1.1.2. MECHANICAL PROPERTIES OF HUMAN BONE .....                                | 2          |
| 1.1.3. BONE TISSUE REPAIR AND ROLE OF IMPLANTS.....                             | 4          |
| 1.1.4. BIOMATERIALS AND THEIR BIOCOMPATIBILITY.....                             | 5          |
| 1.1.4.1. Polymers .....   | 6          |
| 1.1.4.2. Ceramics .....   | 7          |
| 1.1.4.3. Metals.....  | 7          |
| 1.1.5. JOINT REPLACEMENT IMPLANTS AND THEIR PERFORMANCE .....                   | 8          |
| 1.1.5.1. Requirements and issues of joint replacement .....                     | 9          |
| 1.1.5.2. Cemented Implants.....   | 10         |
| 1.1.5.3. Cementless Implants .....  | 10         |
| 1.1.5.4. Total joint replacement : Hip, Knee, and Vertebral implants .....      | 11         |
| 1.1.6. STRESS SHIELDING .....   | 15         |
| 1.1.6.1. Porous orthopedic implants.....  | 16         |
| <b>1.2. INTRODUCTION TO CELLULAR MATERIALS.....</b>                             | <b>17</b>  |
| 1.2.1. STRETCHING AND BENDING DOMINATED CELLULAR MATERIAL .....                 | 19         |
| 1.2.2. RELATIVE DENSITY OF CELLULAR MATERIAL .....                              | 19         |
| 1.2.3. MECHANICAL PROPERTIES OF CELLULAR MATERIAL.....                          | 20         |
| 1.2.4. MECHANICAL MODELLING OF CELLULAR MATERIALS.....                          | 21         |
| 1.2.5. DEFECTS FOUND IN AM MANUFACTURED CELLULAR MATERIALS .....                | 23         |
| 1.2.5.1. Internal Porosity .....  | 23         |
| 1.2.5.2. Unmelted particles .....   | 24         |
| 1.2.5.3. Geometrical deviation: As-designed vs As-built .....                   | 24         |
| 1.2.6. STATIC AND FATIGUE PROPERTIES OF CELLULAR MATERIALS .....                | 26         |
| 1.2.6.1. Effect of cell type and porosity on quasi-static properties .....      | 26         |
| 1.2.6.2. Effect of cell type and porosity on fatigue properties .....           | 29         |
| 1.2.6.3. Effect of process parameters on mechanical properties .....            | 32         |
| 1.2.6.4. Effect of post manufacturing treatments on mechanical properties ..... | 33         |
| <b>1.3. ADDITIVE MANUFACTURING OF METALS.....</b>                               | <b>33</b>  |
| 1.3.1. ELECTRON BEAM – POWDER BED FUSION (EB – PBF) .....                       | 34         |
| 1.3.2. LASER POWDER BED FUSION (LPBF) .....                                     | 35         |
| 1.3.3. COMPARISON OF LPBF AND EB – PBF .....                                    | 36         |

|  |   |           |
|--|---|-----------|
| 1.3.4.   | DESIGN FOR ADDITIVE MANUFACTURING .....   | 37        |
| <b>1.4.</b>  | <b>TITANIUM AND ITS ALLOY FOR BIOMEDICAL APPLICATIONS .....</b>                     | <b>38</b> |
| 1.4.1.   | TITANIUM VS OTHER METAL ALLOYS.....   | 38        |
| 1.4.2.   | METALLURGY .....  | 39        |
| 1.4.3.   | MECHANICAL PROPERTIES OF Ti6Al4V .....  | 42        |
| 1.4.4.   | CORROSION BEHAVIOR OF TITANIUM.....   | 44        |
| 1.4.5.   | BIOCOMPATIBILITY .....  | 45        |
| 1.4.6.   | ADDITIVE MANUFACTURING OF Ti6Al4V: LASER POWDER BED FUSION.....                     | 46        |
| <b>1.5.</b>  | <b>REFERENCES.....</b>  | <b>47</b> |
| <b>CHAPTER 2: TENSILE AND COMPRESSION PROPERTIES OF CUBIC REGULAR, CUBIC IRREGULAR AND TRABECULAR CELLULAR MATERIALS .....</b> |   | <b>58</b> |
| <b>2.1.</b>  | <b>INTRODUCTION.....</b>  | <b>59</b> |
| <b>2.2.</b>  | <b>MATERIALS AND METHODS .....</b>  | <b>60</b> |
| 2.2.1.   | LPBF PROCESS AND SPECIMEN DETAILS.....  | 60        |
| 2.2.2.   | MICROSTRUCTURE .....  | 62        |
| 2.2.3.   | POROSITY MEASUREMENT.....   | 62        |
| 2.2.4.   | MORPHOLOGICAL ANALYSIS.....   | 62        |
| 2.2.5.   | X-RAY COMPUTED TOMOGRAPHY .....   | 63        |
| 2.2.6.   | COMPRESSION AND TENSILE TEST.....   | 63        |
| 2.2.7.   | FINITE ELEMENT ANALYSIS.....  | 64        |
| 2.2.7.1.   | <i>FE analysis elastic region.....</i>  | <i>65</i> |
| 2.2.7.2.   | <i>FE analysis elastic-plastic region.....</i>                                      | <i>65</i> |
| 2.2.7.3.   | <i>FE analysis with strut defects .....</i>   | <i>67</i> |
| 2.2.7.4.   | <i>Tomography FE model.....</i>   | <i>69</i> |
| <b>2.3.</b>  | <b>RESULTS AND DISCUSSION .....</b>   | <b>70</b> |
| 2.3.1.   | MICROSTRUCTURE .....  | 70        |
| 2.3.2.   | POROSITY ANALYSIS .....   | 70        |
| 2.3.3.   | MORPHOLOGICAL ANALYSIS.....   | 71        |
| 2.3.4.   | MORPHOLOGICAL ANALYSIS USING TOMOGRAPHY DATA .....                                  | 72        |
| 2.3.5.   | EXPERIMENTAL RESULTS .....  | 73        |
| 2.3.5.1.   | <i>Compression test.....</i>  | <i>73</i> |
| 2.3.5.2.   | <i>Tensile test .....</i>   | <i>75</i> |
| 2.3.5.3.   | <i>Comparison of compression and tensile test.....</i>                              | <i>76</i> |
| 2.3.6.   | FE ANALYSIS .....   | 77        |
| 2.3.6.1.   | <i>FE analysis elastic region.....</i>  | <i>77</i> |
| 2.3.6.2.   | <i>FE analysis elastic-plastic region.....</i>                                      | <i>79</i> |
| 2.3.6.3.   | <i>FE analysis with strut defects .....</i>   | <i>82</i> |
| 2.3.6.4.   | <i>FE analysis of tomography model.....</i>   | <i>83</i> |
| 2.3.7.   | FRACTOGRAPHY .....  | 85        |
| <b>2.4.</b>  | <b>EMPIRICAL RELATION BETWEEN AS-DESIGNED AND AS-BUILT CELLULAR MATERIALS .....</b> | <b>86</b> |

|   |   |            |
|---|---|------------|
| 2.4.1.  | SPECIMEN DETAILS.....   | 86         |
| 2.4.2.  | RELATION BETWEEN RELATIVE DENSITY AND RELATIVE YOUNG’S MODULUS .....      | 86         |
| <b>2.5.</b>   | <b>SECTION SUMMARY .....</b>  | <b>90</b>  |
| <b>2.6.</b>   | <b>REFERENCES.....</b>  | <b>91</b>  |
| <b>2.7.</b>   | <b>APPENDIX 2.....</b>  | <b>95</b>  |
| 2.7.1.  | AN EXAMPLE OF MESH CONVERGENCE .....                                      | 95         |
| 2.7.2.  | AN EXAMPLE OF EFFECT OF RVE SIZE ON STRESS VALUES .....                   | 95         |
| <b>CHAPTER 3: STATIC AND COMPRESSION – COMPRESSION FATIGUE PROPERTIES OF DIFFERENT CELLULAR MATERIALS.....</b>  |   | <b>96</b>  |
| <b>3.1.</b>   | <b>INTRODUCTION.....</b>  | <b>97</b>  |
| <b>3.2.</b>   | <b>MATERIALS AND METHODS .....</b>  | <b>98</b>  |
| 3.2.1.  | LPBF PROCESS .....  | 98         |
| 3.2.2.  | SPECIMEN DESIGN.....  | 98         |
| 3.2.3.  | MICROSTRUCTURE AND POROSITY.....  | 99         |
| 3.2.4.  | STRUT THICKNESS ANALYSIS .....  | 99         |
| 3.2.5.  | STATIC TENSILE AND COMPRESSION TEST.....                                  | 100        |
| 3.2.6.  | FATIGUE TEST.....   | 100        |
| 3.2.7.  | FINITE ELEMENT MODELLING.....   | 101        |
| <b>3.3.</b>   | <b>RESULTS AND DISCUSSION .....</b>                                       | <b>102</b> |
| 3.3.1.  | MICROSTRUCTURE .....  | 102        |
| 3.3.2.  | POROSITY ANALYSIS .....   | 102        |
| 3.3.3.  | STRUT THICKNESS ANALYSIS OF ALL CELL TOPOLOGIES .....                     | 103        |
| 3.3.4.  | COMPRESSION TEST.....   | 104        |
| 3.3.5.  | TENSILE TEST .....  | 106        |
| 3.3.6.  | FATIGUE TEST.....   | 109        |
| 3.3.7.  | FRACTURE PLANE AND FRACTURE SURFACE .....                                 | 112        |
| 3.3.8.  | FE ANALYSIS .....   | 116        |
| 3.3.8.1.  | <i>As-designed elastic.....</i>   | <i>116</i> |
| 3.3.8.2.  | <i>As-designed vs As-built elastic plastic .....</i>                      | <i>117</i> |
| 3.3.8.3.  | <i>Comparison of experimental and FE of tomography model .....</i>        | <i>120</i> |
| <b>3.4.</b>   | <b>SECTION SUMMARY .....</b>  | <b>120</b> |
| <b>3.5.</b>   | <b>REFERENCES.....</b>  | <b>121</b> |
| <b>3.6.</b>   | <b>APPENDIX 3.....</b>  | <b>124</b> |
| 3.6.1.  | STL FILES OF THE CELLULAR PART OF TENSILE SPECIMENS WITH TRANSITION ..... | 124        |
| 3.6.2.  | COMPARISON OF AS-BUILT YOUNG’S MODULUS IN THE ABSENCE OF TRANSITION ..... | 124        |
| 3.6.3.  | AS-DESIGNED AND AS-BUILT STRESS-STRAIN CURVES UNDER TENSILE LOADING ..... | 125        |
| <b>CHAPTER 4: EFFECT OF BUILDING ORIENTATION, STRUT THICKNESS, AND FILLET RADIUS ON MORPHOLOGY AND FATIGUE OF Ti6Al4V CUBIC CELLULAR STRUCTURE.....</b> |   | <b>126</b> |
| <b>4.1.</b>   | <b>INTRODUCTION.....</b>  | <b>127</b> |
| <b>4.2.</b>   | <b>MATERIALS AND METHODS .....</b>  | <b>128</b> |

|             |   |            |
|-------------|---|------------|
| 4.2.1.      | SPECIMEN DESIGN .....   | 128        |
| 4.2.2.      | GEOMETRICAL ANALYSIS.....                                       | 129        |
| 4.2.3.      | INTERNAL POROSITY ANALYSIS .....                                | 133        |
| 4.2.4.      | MECHANICAL TEST.....  | 133        |
| 4.2.4.1.    | <i>Specimen details</i> .....                                   | 134        |
| 4.2.4.2.    | <i>Metrological analysis</i> .....                              | 136        |
| 4.2.4.3.    | <i>Compression test</i> .....                                   | 136        |
| 4.2.4.4.    | <i>Fatigue test</i> .....                                       | 136        |
| <b>4.3.</b> | <b>RESULTS AND DISCUSSION: GEOMETRICAL ANALYSIS .....</b>       | <b>136</b> |
| 4.3.1.      | GEOMETRICAL ANALYSIS.....                                       | 136        |
| 4.3.1.1.    | <i>Strut thickness</i> .....                                    | 138        |
| 4.3.1.2.    | <i>Excess material</i> .....                                    | 141        |
| 4.3.1.3.    | <i>Fillet radius</i> .....                                      | 143        |
| 4.3.1.4.    | <i>Distortion</i> .....   | 150        |
| 4.3.1.5.    | <i>Compensation of geometrical parameters</i> .....             | 151        |
| 4.3.1.6.    | <i>Evaluation of compensation model</i> .....                   | 153        |
| 4.3.2.      | INTERNAL POROSITY ANALYSIS .....                                | 157        |
| <b>4.4.</b> | <b>MECHANICAL TEST .....</b>                                    | <b>159</b> |
| 4.4.1.      | METROLOGICAL ANALYSIS .....                                     | 159        |
| 4.4.2.      | COMPRESSION TEST.....   | 160        |
| 4.4.3.      | FATIGUE TEST.....   | 160        |
| <b>4.5.</b> | <b>SECTION SUMMARY .....</b>                                    | <b>162</b> |
| <b>4.6.</b> | <b>REFERENCES.....</b>  | <b>163</b> |
|             | <b>CONCLUSION AND FUTURE SCOPE .....</b>                        | <b>165</b> |
|             | <b>CONCLUSION .....</b>   | <b>165</b> |
|             | <b>FUTURE SCOPE.....</b>  | <b>166</b> |
|             | <b>SCIENTIFIC PUBLICATIONS.....</b>                             | <b>167</b> |
|             | <b>CONFERENCES, SUMMER SCHOOLS AND WORKSHOPS ATTENDED .....</b> | <b>168</b> |
|             | <b>APPENDIX I : ANSYS CODES .....</b>                           | <b>169</b> |
|             | ANSYS CODE FOR ELASTIC ANALYSIS .....                           | 169        |
|             | ANSYS CODE FOR ELASTIC PLASTIC ANALYSIS .....                   | 171        |
|             | <b>ACKNOWLEDGEMENT.....</b>                                     | <b>177</b> |

## List of Figures

|  |    |
|--|----|
| Figure I - 1 Hierarchical structure of bone ranging from macro to sub-nanostructure scale .....  | 1  |
| Figure I - 2 Section of proximal tibia representing the cortical and cancellous bone .....   | 2  |
| Figure I - 3 Stress-strain curve of cortical bone loaded at various strain rates.....  | 3  |
| Figure I - 4 Stress-strain curve of trabecular bone for different relative density.....  | 4  |
| Figure I - 5 Variation of Young's modulus with density of human bone.....  | 4  |
| Figure I - 6 Pull off test to obtained cohesive strength. Comparison of non-bioactive and bioactive ceramics ...   | 7  |
| Figure I - 7 Different macroscopic surface irregularities (a) Plasma spray coating (b) Sintered wire mesh coating (c) Sintered beads and (d) Porous cellular tantalum .....  | 10 |
| Figure I - 8 Fixation mechanism in cemented, cementless, and osseointegrated implants .....  | 11 |
| Figure I - 9 (a) Components of total hip arthroplasty (b) Stem inserted in intramedullary cavity of femur and acetabular component inserted in hip .....   | 12 |
| Figure I - 10 Different types of knee prostheses (a) Hinged (metal) (b) Hinged design (Plastic liner) (c) semi constrained (d) replacement for surface (e) uni-compartmental (f) bi-compartmental replacement .....  | 13 |
| Figure I - 11 (a) Representation of intervertebral disc between two vertebrae (b) Load distribution in intervertebral disc.....  | 14 |
| Figure I - 12 (a) PEEK spinal cage with Ti between bone and implant surface (b) Porous titanium spinal cage .....  | 14 |
| Figure I - 13 TDA implant: Prodisc-C with metal on polymer articulation .....  | 14 |
| Figure I - 14 Stress shielding in the proximal part of the femur due to bone-implant stiffness mismatch. Radiography compares the bone after 5 years of implantation (locations are highlighted) .....   | 16 |
| Figure I - 15 Fully porous stem developed by a tetrahedron unit cell .....   | 17 |
| Figure I - 16 Representation of various unit cells (a) Cubic (b) BCC (c) BCC-Z (d) FCC (e) FCC-Z (f) Tetrahedron (g) Octet truss (h) Honeycomb (i) Diamond (j) Truncated cuboctahedron (k) Truncated cube (l) Rhombic cuboctahedron (m) Rhombic dodecahedron (n) Skeletal gyroid (o) Sheet gyroid (p) I-WP (q) Sheet diamond (r) Primitive ..... | 18 |
| Figure I - 17 Application of cellular material with respect to porosity.....   | 18 |
| Figure I - 18 Pin jointed frame for illustrating (a) Bending dominated mechanism (b) Stretching dominated – structure(c) Loading in bending dominated unit cell (d) Loading in stretching dominated unit cell .....  | 19 |
| Figure I - 19 Planar lattice with same relative density, but different fraction of material between joints .....   | 20 |
| Figure I - 20 Illustration of compressive stress-strain curve for bending and stretching dominated cellular material.....  | 21 |
| Figure I - 21 Deformation of FCC-Z cellular material under compression load.....   | 21 |
| Figure I - 22 Design variables that influence the behavior of cellular materials.....  | 21 |
| Figure I - 23 (a) Relative density vs relative Young's modulus (b) Relative density vs relative strength for different cellular solids, indicating ideal behavior.....   | 22 |
| Figure I - 24 Internal porosity from the PBF process, spherical pores (indicated by white arrow), irregular pores (indicated by blue arrows).....  | 24 |
| Figure I - 25 Illustration of effect of building direction on surface roughness of struts.....   | 24 |
| Figure I - 26 Effect of strut orientation on strut morphology (a) heat is carried away more evenly (b) heat is conducted in other directions in inclined struts due to formation of stair-case effect and to lower layer in horizontal struts.....   | 24 |
| Figure I - 27 Deviations in struts (a) Thickness variation in strut (b) Strut waviness.....  | 25 |
| Figure I - 28 Stress-strain curves for different cell types indicating the effect in vertical struts, that introduces peaks and valleys in plateau region.....   | 27 |
| Figure I - 29 Different types of tensile cellular specimens .....  | 29 |
| Figure I - 30 Representation of three stages of fatigue failure in porous cellular material .....  | 30 |
| Figure I - 31 (a) Absolute S-N curve with varying porosity (b) Normalized S-N curve for truncated cuboctahedron .....  | 30 |
| Figure I - 32 S-N curve differentiating struts based and TPMS based cellular material .....  | 31 |
| Figure I - 33 Normalized S-N curve indicating the effect of base material on rhombic-dodecahedron cellular material.....   | 31 |

|   |    |
|---|----|
| Figure I - 34 Representation of variation in accumulated strain in graded cellular material with number of cycles .....   | 32 |
| Figure I - 35 Steps involved in AM process : CAD to Part .....  | 34 |
| Figure I - 36 Schematic representation of EB-PBF process (www.arcam.com) .....  | 35 |
| Figure I - 37 Schematic representation of L - PBF process .....   | 35 |
| Figure I - 38 Phase transformation of titanium alloy with variation in % of V.....  | 40 |
| Figure I - 39 (a - c) microstructure of $\alpha+\beta$ phase titanium alloy (d) microstructure in $\alpha'$ martensitic phase ...   | 41 |
| Figure I - 40 S-N curve for different Ti6Al4V microstructure under fully reversed condition .....   | 43 |
| Figure I - 41 Schematic representation of interaction between titanium implant and body fluid .....   | 45 |
| Figure I - 42 Microstructure of Ti6Al4V alloy (a) As-built EB-PBF (b) HIPed EB-PBF (C) As-built LPBF and (d) HIPed LPBF process .....   | 46 |
| Figure I - 43 Defects from AM process (a) Internal porosity (b) Entrapped unmelted powder particles (c) formation of internal cracks .....  | 46 |
|   |    |
| Figure II - 1 Schematic representation of (a) Pore size and strut thickness (b) compression test sample (c) tensile test sample.....  | 61 |
| Figure II - 2 Cell topologies considered in the study (a) cubic regular (b) cubic irregular (c) trabecular .....  | 61 |
| Figure II - 3 (a) Instron universal testing machine (b) tensile test of cellular specimen (c) compression test of cellular specimen.....  | 63 |
| Figure II - 4 (a) Typical compression stress-strain curve for cellular material[48] (b) Typical tensile stress-strain curve[49].....  | 64 |
| Figure II - 5 (a) RVE model of cubic irregular and description of sides (b) FE model indicating the mesh .....  | 65 |
| Figure II - 6 Tensile stress-strain curve for bulk Ti6Al4V manufactured using LPBF process used for cellular material.....  | 66 |
| Figure II - 7 Boundary conditions used for FE elastic-plastic analysis (a) tensile loading (b) compression loading with inclined load .....   | 67 |
| Figure II - 8 Defects in LPBF manufactured cubic regular cellular material.....   | 68 |
| Figure II - 9 Representation of elliptical cross-section used to study defects (a) varying cross-section used to generate struts (b) AD model with uniform thickness along strut (c) VCS model with thickness variation along a strut (d) VCS with offset considering strut waviness (e) overlap of AD and VCS with offset CAD model .....  | 69 |
| Figure II - 10 Conversion of point cloud to FE model .....  | 69 |
| Figure II - 11 RVE FE models of (a) Cubic regular (b) Cubic irregular (c) Trabecular.....   | 70 |
| Figure II - 12 Microstructure (a) horizontal plane; perpendicular to printing direction (b) lateral plane; parallel to printing direction .....   | 70 |
| Figure II - 13 (a) SEM image showing the strut thickness (b) stereomicroscope image indicating the pore outline.....  | 71 |
| Figure II - 14 Evaluation of strut thickness using tomography data (a) Representation of strut thickness variation in cubic regular (b-d) Strut thickness variation in cubic regular, cubic irregular, and trabecular structure respectively (red peaks is due to the complex topography of the strut surfaces as explained by Zanini et al.[57], hence it is not considered); (e) Difference between as-built and as-designed strut (f) Normalized center offset for different strut orientation ..... | 73 |
| Figure II - 15 (a) General stress-strain curve obtained for different batches (b) 0.2% offset yield strength in compression.....  | 74 |
| Figure II - 16 Variation of compression Young's modulus with porosity (a) monotonic Young's modulus (b) Cyclic Young's modulus.....   | 74 |
| Figure II - 17 (a) General stress-strain curve obtained for different batches (b) 0.2% offset yield strength in tensile.....  | 75 |
| Figure II - 18 Variation of tensile Young's modulus with porosity (a) monotonic Young's modulus (b) Cyclic Young's modulus.....   | 76 |
| Figure II - 19 Comparison of tensile and compression (a) monotonic Young's modulus (b) cyclic Young's modulus.....  | 76 |
| Figure II - 20 (a) Comparison of offset yield strength in tensile and compression (b) variation of cyclic Young's modulus with each cycle.....  | 77 |
| Figure II - 21 (a) Comparison of FEM and theoretical Young's modulus for designed porosity samples (b) Comparison of monotonic tensile Young's modulus with theoretical Young's modulus .....   | 78 |

|   |     |
|---|-----|
| Figure II - 22 (a) Effect of inclination on measured stiffness values (b) Comparison of cyclic compression Young's modulus in compression and tensile Young's modulus with FEM (vertical and inclined loading) .....  | 79  |
| Figure II - 23 Tensile stress-strain curves in experimental (as-built) and FEM (as-designed): (a) and (b) batch A, (c) and (d) batch B, (e) and (f) batch C.....  | 80  |
| Figure II - 24 Compression stress-strain curves in experimental (as-built) and FEM (as-designed): (a) and (b) batch A, (c) and (d) batch B, (e) and (f) batch C.....  | 81  |
| Figure II - 25 Comparison of FEM and experimental behavior of as-built regular structures (a) Tensile loading (b) Compression loading - Inclined.....   | 82  |
| Figure II - 26 Comparison of (a) Tensile Young's modulus and (b) offset yield strength in elliptical and rectangular cross-section models compared with as-designed FE and experimental values.....   | 83  |
| Figure II - 27 Comparison of stress-strain curves of different FE models with experimental curve (a) elliptical cross-section (b) rectangular cross-section.....  | 83  |
| Figure II - 28 Comparison of tensile experimental curves with tomography FE analysis (a) Cubic regular (b) Cubic irregular (c) Trabecular.....  | 84  |
| Figure II - 29 Failure location in tomography FE models obtained from the equivalent plastic strain plots (a) Cubic regular (b) Cubic irregular (c) Trabecular.....   | 85  |
| Figure II - 30 Fracture surface images of cubic regular specimen (a),(b) Tensile test fracture surface (c) compression test failure (d) compression test fracture surface .....   | 85  |
| Figure II - 31 (a) Variation of relative Young's modulus with relative density (b) log-log curve indicating the behavior of cell topology.....  | 87  |
| Figure II - 32 Power law fitting for tensile and compression Young's modulus (a) cubic regular (b) cubic irregular and (c) trabecular .....   | 87  |
| Figure II - 33 Comparison of Gibson - Ashby parameters C and n in (a) compression (b) tensile.....  | 88  |
| Figure II - 34 Relation between as-designed Young's modulus with as-built Young's modulus based on pore size and loading (a) cubic regular compression (b) cubic regular tension (c) cubic irregular compression (d) cubic irregular tension (e) trabecular tension (f) trabecular compression..... | 89  |
| Figure II - A 1 Representation of mesh convergence analysis shown for batch C cubic regular (as-designed) (a) convergence for elastic analysis (b)convergence for elastic-plastic analysis .....  | 95  |
| Figure II - A 2 Representation of effect of RVE size variation shown for tomography models for (a) cubic regular, based on number of unit cells in each direction (b) cubic irregular and trabecular based on RVE size in mm.....   | 95  |
| Figure III - 1 Schematic representation of the topology using STL files; (a) Cubic regular, (b) Cubic irregular, (c) Star regular, (d) Star irregular, (e) Cross regular, (f) Cross irregular, (g) Trabecular.....  | 98  |
| Figure III - 2 (a) Compression and fatigue test specimen (b) Tensile test specimen with transition highlighted and (c) Thickness increase in tensile specimens.....   | 99  |
| Figure III - 3 Spectro microscopy images for morphological analysis (a) Cubic irregular (b) Star regular indicating the measured strut thickness ( $\mu\text{m}$ ) .....  | 100 |
| Figure III - 4 (a) RUMUL fatigue testing machine (b) Fatigue test setup with star regular cellular material .   | 101 |
| Figure III - 5 FE model of tensile as-designed specimen (a) With transition (b) Without transition .....  | 102 |
| Figure III - 6 Microstructure of Ti6Al4V cellular material (a) XY plane (b)XZ plane.....  | 102 |
| Figure III - 7 (a) Strut thickness of struts oriented in different direction (b) Normal distribution of strut thickness .....   | 104 |
| Figure III - 8 Compression test stress-strain curves (a) Monotonic condition (b) Cyclic condition.....  | 104 |
| Figure III - 9 Fracture planes under compression loading (a) Cubic regular (b) Cubic irregular (c) Star regular (d) Star irregular (e) Cross regular (f) Cross irregular (g) Trabecular (h) SEM image of fracture surface indicating shear .....  | 105 |
| Figure III - 10 Tensile test stress-strain curves (a) Monotonic condition (b) Cyclic condition .....  | 106 |
| Figure III - 11 SEM images of tensile fracture surface (a) Cup formation in the strut (b) Peaks and valleys indicating ductile failure .....  | 107 |
| Figure III - 12 S-N curves from fatigue test of cellular material with asymptotic curve fitting and 95% confidence band (a) Cubic based (b) Star based (c) Cross based (d) Trabecular.....  | 110 |
| Figure III - 13 Frequency variation during the fatigue test (a) steady decrease in cross regular specimen (b) formation of peaks and valleys in trabecular specimen.....  | 111 |

|   |     |
|---|-----|
| Figure III - 14 (a) S-N curve normalized with yield stress (b) S-N curve normalized with cyclic Young's modulus   | 112 |
| Figure III - 15 Undeformed and deformed cellular specimens under fatigue loading (a-b) Cubic irregular (c-d) Star regular (e-f) Star irregular (g-h) Cross regular (i-j) Cross irregular (k-l) Trabecular                                       | 114 |
| Figure III - 16 SEM images of fatigue fracture surface (a) Crack propagation at junctions (b) Irregular surface near crack (c) Crack initiation at surface dimple (d) Internal porosity at the crack surface                                    | 115 |
| Figure III - 17 Effect of transition of the experimental tensile cyclic modulus using the ratio from FE analysis  | 116 |
| Figure III - 18 Comparison of failure locations in as-designed FE model and experimental specimens (a-b) Cubic regular (c-d) Cubic irregular (e-f) Star regular (g-h) Star irregular (i-j) Cross regular (k-l) Cross irregular (m-n) Trabecular | 119 |
| Figure III - 19 (a) Porosity difference between specimens from two chapters and tomography FE model (b) Stress-strain curves cubic regular (c) Stress-strain curves cubic irregular (d) Stress-strain curves cubic trabecular                   | 120 |
| Figure III - A 1 STL files for manufacturing tensile specimens indicating the transition at the top and bottom  | 124 |
| Figure III - A 2 Comparison of as-designed (FEM) and as-built (experimental) stress - strain curves for tensile loading   | 125 |
| Figure IV - 1 (a) Representation of unit cell parameters (b) Unit cell with fillet radius at junctions  | 128 |
| Figure IV - 2 (a-c) STL files of as-designed cubic cellular structure along with orientation (d-f) Manufactured specimens with three different orientation  | 129 |
| Figure IV - 3 (a) Representation of different planes of 0° specimen, printed along Z-direction (b) Optical microscope image of 0° specimen in XY plane  | 130 |
| Figure IV - 4 Unit cell image segmentation and analysis to measure different geometrical parameters   | 130 |
| Figure IV - 5 Junction center estimation (a) MATLAB® algorithm used for the analysis (b) Parameters used for the junction center estimation   | 131 |
| Figure IV - 6 Modified parameters for the junction center estimation due to material accumulation at the fillets due to LPBF process (highlighted by red circle)  | 132 |
| Figure IV - 7 (a) Procedure used to overlap the as-designed and as-built geometry (b) Indication of excess material in the strut obtained through overlapping   | 133 |
| Figure IV - 8 (a) Algorithm used in MATLAB to calculate fillet radius (b) Convergence method used to fit the fillet radius  | 133 |
| Figure IV - 9 Cellular specimen for mechanical test (a) Isometric view of full specimen (b) Cross-section indicating the cellular part diameter (c) Cross-section indicating strut transition and bell-shaped center of the flange              | 134 |
| Figure IV - 10 (a) Compensated horizontal strut cross-section (b) Compensated vertical strut cross-section (c) Compensated unit cell CAD model with printing along Z-direction  | 135 |
| Figure IV - 11 Different configurations of cellular specimens used for mechanical testing   | 135 |
| Figure IV - 12 Unit cell images indicating the accumulation of powder particles on struts (a) 0° specimen (b) 45° specimens ; arrow indicates the printing direction  | 136 |
| Figure IV - 13 Overlapping of as-designed and as-built geometry of specimen #3 printed at 0° (a) Unit cells perpendicular to printing direction (b) Unit cells parallel to printing direction   | 137 |
| Figure IV - 14 (a) Orientation of struts in the 45° specimens with respect to the printing plane (b) Skewed view of the horizontal strut when capturing images along XY and XZ planes   | 138 |
| Figure IV - 15 Comparison of as-designed and as-built thickness in for different strut orientation in 0° specimens. The dashed lines represent linear fitting   | 138 |
| Figure IV - 16 Comparison of as-designed and as-built thickness in for different strut orientation in 0° specimens. The dashed lines represent linear fitting   | 139 |
| Figure IV - 17 Comparison of as-designed thickness and as-built diameter for struts oriented at 45° - 35.26°. The dashed lines represent linear fitting   | 140 |
| Figure IV - 18 Excess material on struts in 0° specimens, categorized based on struts orientation and excess material location. Dashed lines represent linear curve fitting   | 142 |
| Figure IV - 19 Excess material on struts in 45° specimens, categorized based on struts orientation and excess material location. Dashed lines represent linear curve fitting  | 142 |

|   |     |
|---|-----|
| Figure IV - 20 Excess material on struts in 45° - 35.26° specimens, categorized based on the excess material location. Dashed lines represent linear curve fitting.....   | 143 |
| Figure IV - 21 Classification of different fillets in the specimen (a) Parallel to printing direction (b) Perpendicular to printing direction (c) Inclined .....  | 143 |
| Figure IV - 22 As-built fillet radii values for different fillets in 0° specimens.....  | 144 |
| Figure IV - 23 As-built fillet radii values for different fillets in 45° specimens.....   | 145 |
| Figure IV - 24 As-built fillet radii values for different fillets in 45° - 35.26° specimens.....  | 146 |
| Figure IV - 25 Variation of as-built fillet radii with as-designed radii and thickness for 0° specimens (a) Positive fillets (b) Negative fillets (c) Lateral fillets.....  | 147 |
| Figure IV - 26 Variation of as-built fillet radii with as-designed radii and thickness for fillets in the vertical plane of 45° specimens (a) Positive fillets (b) Negative fillets (c) Lateral fillets.....  | 148 |
| Figure IV - 27 Variation of as-built fillet radii with as-designed radii and thickness for fillets in the inclined plane of 45° specimens (a) Positive fillets (b) Negative fillets. ....   | 149 |
| Figure IV - 28 Variation of as-built fillet radii with as-designed radii and thickness for 45° - 35.26° specimens (a) Positive fillets (b) Negative fillets (c) Lateral fillets. ....   | 150 |
| Figure IV - 29 Distortion of lattice in all the specimens (a) 0° Specimens (b) 45° specimens (c) 45 - 35.26° specimens.....   | 151 |
| Figure IV - 30 Representation of compensated CAD model to obtain the nominal or desired geometry from LPBF process. ....  | 152 |
| Figure IV - 31 Illustration of compensation principle in a strut with excess material. ....   | 152 |
| Figure IV - 32 Illustration of two compensation techniques on horizontal strut (a) Standard method with compensated and desired cross-section (b) Alternative method with compensated and desired cross-section (c) CAD model with standard compensation (d) CAD model with alternative compensation. ....                        | 153 |
| Figure IV - 33 Overlapping of desired unit cell and as-built geometry obtained from compensation model (a) Standard compensation (b) Alternative compensation. ....   | 154 |
| Figure IV - 34 As-built strut thickness of struts obtained from using compensated and uncompensated CAD models (a) Vertical axis of strut parallel to printing plane (b) Horizontal axis of strut parallel to printing plane (c) Strut perpendicular to printing plane. The solid line indicates perfect as-built thickness. .... | 156 |
| Figure IV - 35 As-built strut thickness of inclined struts obtained from using compensated and uncompensated CAD models.....  | 157 |
| Figure IV - 36 Polished unit cell to reveal the internal porosity in the struts (b) classification of pores in the unit cell into junctions and struts using MATLAB code.....   | 157 |
| Figure IV - 37 Variation of (a) Porosity in specimen (b) Porosity in different struts (c) Porosity in junctions (d) Average pore diameter at different locations. ....  | 158 |
| Figure IV - 38 As-built thickness values for specimens A-E compared with the as-designed thickness value. .   | 159 |
| Figure IV - 39 As-built fillet radius for specimens A-E compared with the as-designed radius values .....   | 159 |
| Figure IV - 40 Monotonic compressive stress-strain curves for all specimens .....   | 160 |
| Figure IV - 41(a) Absolute S-N curve (b) Normalized S-N curve with 10% and 90% failure probability for all the specimens.....   | 161 |
| Figure IV - 42 Fatigue fracture surfaces of (a) Specimen A indicating failure closer to the junctions (b) Specimen B with failure at the middle of the struts .....   | 162 |

---

## List of Tables

---

|  |            |
|--|------------|
| <i>Table I - 1 Mechanical properties of cortical bone .....</i>  | <i>3</i>   |
| <i>Table I - 2 Mechanical properties of trabecular bone.....</i>   | <i>4</i>   |
| <i>Table I - 3 Load on hip and knee joint due to daily activities.....</i>   | <i>11</i>  |
| <i>Table I - 4 Comparison of process parameters between EB - PBF and LPBF.....</i>   | <i>37</i>  |
| <i>Table I - 5 Mechanical properties of most common biomedical metal alloys .....</i>  | <i>39</i>  |
| <i>Table I - 6 Characteristics of most common biomedical metal alloys .....</i>  | <i>39</i>  |
| <i>Table I - 7 Composition of Ti6Al4V (Grade 5) alloy in %wt .....</i>   | <i>40</i>  |
| <i>Table I - 8 Variation of properties in <math>\alpha</math>, <math>\alpha+\beta</math> and <math>\beta</math> Ti alloys .....</i>  | <i>41</i>  |
| <i>Table I - 9 Influence of microstructure on properties of Ti alloys.....</i>   | <i>42</i>  |
| <i>Table I - 10 Mechanical Properties of Ti6Al4V alloy for various microstructures (Note: d, is for mill annealed condition which is similar to equiaxed microstructure) .....</i> | <i>43</i>  |
| <i>Table I - 11 Rotating bending fatigue strength (<math>R = -1</math>) of Ti6Al4V - Equiaxed .....</i>  | <i>44</i>  |
| <i>Table I - 12 Breakdown potential (Hank's solution) and repassivation times (in 0.9% NaCl solution with pH=7.4) for most common biomedical alloys .....</i>                      | <i>45</i>  |
|  |            |
| <i>Table II - 1 Designed strut thickness and pore size for different batches.....</i>  | <i>61</i>  |
| <i>Table II - 2 Boundary conditions used in FE elastic analysis .....</i>  | <i>65</i>  |
| <i>Table II - 3 Measured strut thickness and center offset in all the three directions measured for struts in cubic regular cellular material .....</i>                            | <i>68</i>  |
| <i>Table II - 4 Measured and designed porosity with relative error for all batches and topology .....</i>  | <i>71</i>  |
| <i>Table II - 5 Strut thickness and feret diameter along lateral plane; parallel to printing direction .....</i>   | <i>72</i>  |
| <i>Table II - 6 Strut thickness and feret diameter along horizontal plane; perpendicular to printing direction .....</i>   | <i>72</i>  |
| <i>Table II - 7 Comparison of Young's modulus for batch C and batch Ci.....</i>  | <i>77</i>  |
| <i>Table II - 8 Comparison of properties from tensile experimental and tomography FE models .....</i>  | <i>84</i>  |
| <i>Table II - 9 Designed strut thickness and pore size .....</i>   | <i>86</i>  |
| <i>Table II - 10 Gibson - Ashby parameter for relative Young's modulus .....</i>   | <i>88</i>  |
|  |            |
| <i>Table III - 1 Comparison of designed, measured and <math>\mu</math>CT porosity for all topologies .....</i>   | <i>103</i> |
| <i>Table III - 2 Monotonic and cyclic Young's modulus under tensile and compression loading.....</i>   | <i>108</i> |
| <i>Table III - 3 Yield and maximum strength values under tensile and compression loading .....</i>   | <i>108</i> |
| <i>Table III - 4 S-N curve fitting parameters and fatigue data scatter.....</i>  | <i>110</i> |
| <i>Table III - 5 Fatigue strength for different cell topologies .....</i>  | <i>111</i> |
| <i>Table III - 6 As-designed Young's modulus with and without transition .....</i>   | <i>116</i> |
| <i>Table III - 7 Comparison of porosity and Young's modulus between as-designed and as-built configuration .....</i>   | <i>117</i> |
| <i>Table III - 8 Comparison of yield strength and maximum strength between as-designed and as-built.....</i>   | <i>117</i> |
|  |            |
| <i>Table III - A 1 Effect of transition on as-built Young's modulus .....</i>  | <i>124</i> |
|  |            |
| <i>Table IV - 1 Specimen details with combination of geometric parameters .....</i>  | <i>129</i> |
| <i>Table IV - 2 Nominal as- designed geometrical parameters .....</i>  | <i>135</i> |
| <i>Table IV - 3 Specimen dimensions.....</i>   | <i>135</i> |
| <i>Table IV - 4 As-designed and as-built thickness values for all the specimens printed at <math>0^\circ</math> .....</i>  | <i>139</i> |
| <i>Table IV - 5 As-designed and as-built thickness values for all the specimens printed at .....</i>   | <i>140</i> |
| <i>Table IV - 6 As-designed thickness and as-built diameters values for.....</i>   | <i>141</i> |
| <i>Table IV - 7 As-built fillet radii for <math>0^\circ</math> specimens with standard deviation (values in <math>\mu\text{m}</math>) .....</i>                                    | <i>144</i> |
| <i>Table IV - 8 As-built fillet radii for <math>45^\circ</math> specimens with standard deviation (values in <math>\mu\text{m}</math>) .....</i>                                   | <i>145</i> |
| <i>Table IV - 9 As-built fillet radii for <math>45^\circ - 3.5.26^\circ</math> specimens with standard deviation (values in <math>\mu\text{m}</math>) .....</i>                    | <i>146</i> |
| <i>Table IV - 10 Nominal and compensated parameters for <math>0^\circ</math> specimens .....</i>   | <i>154</i> |

|   |            |
|---|------------|
| <i>Table IV - 11 Nominal and compensated parameters for 45° - 35.26° specimens .....</i>  | <i>154</i> |
| <i>Table IV - 12 Comparison of average error from uncompensated and compensated 0° specimens .....</i>                          | <i>156</i> |
| <i>Table IV - 13 Comparison of average error from uncompensated and compensated 45° -35.26° specimens...</i>                    | <i>157</i> |
| <i>Table IV - 14 As-designed thickness of specimens used for internal porosity analysis .....</i>                               | <i>158</i> |
| <i>Table IV - 15 Mechanical properties from compression test (Young's modulus measured from loading - unloading curve).....</i> | <i>160</i> |

---

# Chapter 1

## Introduction

---

### 1.1. Human bone and implants

#### 1.1.1. Composition and Structure of Human bone

Human bone is a complex composite structure consisting of organic matrix with inorganic minerals, water, and cell. The organic component of the bone makes up for 40% dry weight of the bone, which mainly composes of Type I collagen. The inorganic composition mainly composes of hydroxylapatite(HA) which is a crystalline form of calcium phosphate. Therefore, the human bone acts as a reservoir for the release of calcium and phosphate in a controlled manner. Minerals such as carbonates, fluorides and magnesium are also present[1].

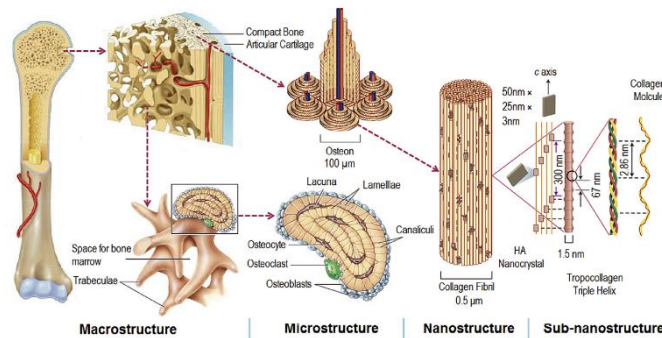


Figure I - 1 Hierarchical structure of bone ranging from macro to sub-nanostructure scale[2]

A clear representation of bone and its building blocks at various levels is as illustrated in Fig.I-1. The basic building block of the bone at the sub-nanostructure level is the tropocollagen (triple helical molecule with a length of 300nm and a diameter of ~1.5nm) which are arranged to form a collagen fibril with a diameter of 500nm. These fibrils also consist of type I collagen which is the main organic component and hydroxyapatite (HA),  $\text{Ca}_{10}(\text{PO}_4)_6(\text{OH})_2$  in the form of nanocrystals which form the main inorganic component. Along with these, other minerals are also present as mentioned above. The minerals in the bone contribute majorly to its mechanical properties such as strength and stiffness. The anisotropy in the mechanical properties is mainly due to the crystal orientation of the minerals. The collagen in the bone also contributes to the mechanical properties, but mostly towards the toughness and the post-yielding behavior. Studies have indicated that the deterioration of the collagen has minimum effect on the strength and stiffness of the bone[2, 3].

At the macroscopic level, the bone can be categorized as compact bone(cortical bone) which forms the outer thick layer and trabecular bone(cancellous bone) as shown in Fig.I-2. The bone is covered with articular cartilage near the joints which reduces friction between bone and enhances easy movement of joints. The cortical bone is dense and complex architecture with contributes to 80% of the skeletal weight. The porosity of the cortical bone is between 5-10% which is contributed by the canals and resorption cavities which contain blood vessels and nerves. Cortical bone consists mainly of osteons, which are lamellar structures composed of collagen fibrils arranged in concentric circles. The gap between the osteons consists of lacunae and interstitial tissue. Lacunae consist of osteocytes which bone cells and communicate through tiny channels called canaliculi. Cortical bone mainly acts as protective layer and its thickness is mainly dependent on the location, mechanical loading, and various factors[2, 4–6].

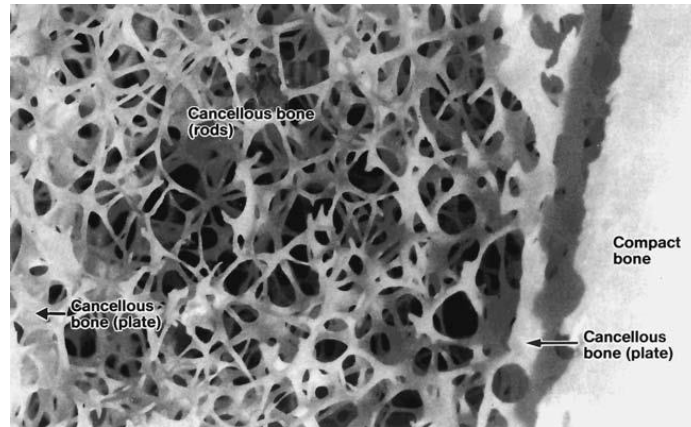


Figure 1 - 2 Section of proximal tibia representing the cortical and cancellous bone[7]

The cancellous bone (trabecular bone) has porosity in the range of 75-95% and are present inside long cortical bones. It is formed by the interconnection of rod and plates like structures known as trabeculae as shown in Figure 2. Each trabecula is composed of several lamella with the total thickness not more than 200 - 400 $\mu$ m, which enables diffusion of nutrients without the presence of Haversian system (no blood cells or osteons)[1]. The pores in the trabecular bone are filled with bone marrow[2, 3]. Cancellous bones are lighter in weight, have a higher surface area and have lesser stiffness. They act as spacing filling structures without increasing the bone-weight. The density of the cancellous bone varies according to the age, locations, and various other factors. The cancellous bone density is high in regions like knee and pelvis and have lower density in locations such as vertebrae. The study of cancellous bone is important since age related fractures initiate at the trabecular locations[6].

Bone growth and modelling are simultaneous process that are influenced by various local factors. During bone growth, the addition of outer layer of the bone (periosteal bone) is faster compared to the removal of the internal surface of the bone (endosteal bone). Modeling of the bone influences the shape, size, anatomy, formation of joints and the overall growth rate of the bone. The modelling of bone, i.e., increase in dimensions, mass and strength of the bone is initiated once a bone reaches its threshold strain [7]. Even after the complete growth of the bone, remodeling takes place with replacement of old bone tissue with new tissues, repair of injured bone with new one tissues. The remodeling is mainly dependent on two types of cells, osteoclasts which help in removal of old bone while osteoblasts which help in formation of new bones. The modelling and remodeling were influenced by the mechanical loads, exercise, lifestyle and also diet[6, 8].

### 1.1.2. Mechanical Properties of Human Bone

As mentioned earlier, bone is a complex hierarchical system which influences the mechanical properties at each hierarchy. Also, mechanical properties of the bone are highly dependent on various factors such as age, mineral composition, gender, and anatomical location [3]. The bone mineral density (BMD) of the bone which decreases with age or with the presence of diseases such as osteoporosis [3, 9]. Therefore, it is not recommended to provide a general conclusion on the mechanical properties of the bone without considering the above-mentioned factors. Some on the external factors that influence the mechanical properties are loading direction and strain rates [3, 10]. The mechanical properties of the bone are discussed at the macroscopic level as cortical and trabecular bone.

Cortical or compact bone is considered to be transversely isotropic since the osteons are oriented along the longitudinal direction of the bone [7]. Therefore, the mechanical properties of cortical bone are highly dependent on the direction of the loading direction, mineral content, mode of loading along with the anatomical site. One of the examples for variation with anatomical site is, human femoral bone has a lower Young's modulus than the human tibia. Full characterization of the bone is carried out by

considering multiple samples and testing under tension, compression, bending, and sometimes shear [3]. Some of the mechanical properties of cortical bone are as tabulated in Table I-1.

Table I - 1 Mechanical properties of cortical bone

| Property                               | Longitudinal Direction                   | Transverse Direction            | Shear | Bending |
|--|--|---------------------------------|-------|---------|
| <b>Young's Modulus (GPa)[7]</b>        | 17.4                                     | 9.6                             | 3.5   | 14.8    |
| <b>Poisson's Ratio[3]</b>              | 0.58                                     | 0.46                            | -     | -       |
| <b>Strength(MPa)[10]</b>               | 124-174(Tensile)<br>170-193(Compression) | 49(Tensile)<br>133(Compression) | 59    | 160     |
| <b>Tensile Yield Strength(MPa)[11]</b> | 148                                      | 49                              | -     | -       |

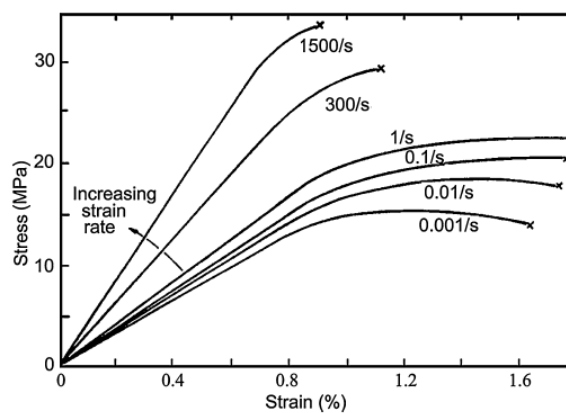


Figure I - 3 Stress-strain curve of cortical bone loaded at various strain rates[10]

The mechanical properties indicate that the cortical bone is stiffer along the longitudinal direction since the loading is parallel to the osteons while it decreases along the transverse direction. The strength value is highest along the longitudinal direction, especially under compression loading while the least strength is observed in transverse direction in tension [3]. A typical stress-strain curve of the cortical bone is as shown in Fig.I-3. The curve has a linear elastic region followed by a plateau depending on the loading rate, which clearly effects the measured properties of cortical bone. The measured strength and stiffness of the bone increases with increase in the loading rate. However, the properties such as fracture toughness and failure strain reach a maximum and then decrease. This indicates that a low strain rates, the hierarchy of the cortical bone delays the crack propagation there by increasing the toughness [10, 12].

Trabecular bone has higher porosity than cortical bone in the range of 70-90%, this leads to a reduced stiffness but has higher surface area which helps in remodelling process. The density and the distribution of trabecular bone is highly dependent on the location, age, and individuals. The density of the trabecula bone also changes along the length of a long bone [3]. The direction of growth or the mechanical anisotropy of trabecular bone is aligned with respect to the principal stress experienced by the bone [6, 13]. As explained before density of the trabecular bone changes with respect to the location. Therefore, the relative density of the bone plays a major role on its strength and stiffness, this is represented through the stress-strain curve as shown in Fig. I-4. The compressive stress-strain curve shown consists of three regions, linear elastic regions, plastic-collapse or yielding with a plateau, followed by the densification of bone which increase the stress. The mechanical properties of trabecular bone are as mentioned in Table I-2.

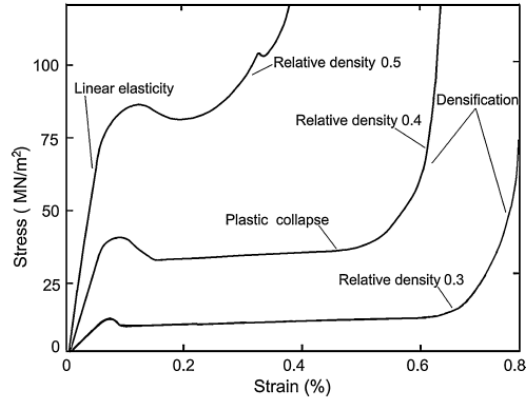


Figure I - 4 Stress-strain curve of trabecular bone for different relative density[10]

Table I - 2 Mechanical properties of trabecular bone

| Property                     | Longitudinal Direction | Transverse Direction |
|------------------------------|------------------------|----------------------|
| <b>Young's Modulus (GPa)</b> | 0.26-0.9[4];5[10]      | 0.01-0.4[4];0.1[10]  |
| <b>Strength(MPa)</b>         | 3.6-9.3[4];12[10]      | 0.6-4.9[4];2[10]     |

Similar to cortical bone, the mechanical properties of bone vary with respect to the type of load applied. Trabecular bone exhibits higher strength in compression than in tension. This is applicable for loads applied in longitudinal as well as in transverse direction. Therefore, when measuring the exact properties of the bone, parameters such as strain rate, loading direction, anatomical location and dry or wet condition must be mentioned. [6]

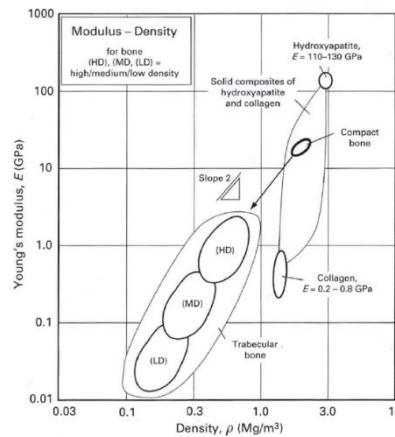


Figure I - 5 Variation of Young's modulus with density of human bone [13]

Ashby et al. [13] provided a graphical representation of variation of Young's modulus with density of bone as shown in Fig. I – 5. Wang et al. [3] has compiled a data base for the mechanical properties of cortical and trabecular bone by considering the effect of various parameters such as species, location, age and loading direction.

### 1.1.3. Bone tissue repair and role of implants

As mentioned earlier, human skeletal system experiences complex loads and the bones model and remodel themselves based on the mechanical load applied. Despite the strength and stiffness of the bone, they are vulnerable to fractures or breaks. But human bone has the ability to repair and grow on its own based on the extent of damage the bone has suffered. The first step in the fracture treatment involves realignment of broken bone ends to their initial position, this sometimes involves external

alignment manually or securing them with the help of nails and plates surgically. After the realignment, the bone repair occurs in four stages: (1) Formation of blood clot (hematoma) (2) Formation of granulation tissue which leads to generation of collagen fibres joining the broken bone (fibrocartilaginous callus) (3) Gradual formation of trabecular bone forming a bony callus (4) Conversion of bony callus into hard cortical bone [8].

Another treatment method that is adopted in case of complex fractures is bone grafting. Bone grafting is used when the bone does not respond to the natural repair treatment or when the present bone is infected/lost due to disease. Bone grafts not only work as a replacement, but they should also induce osseointegration [4]. The main grafting procedures are,

1. Autografting: This procedure involves replacing the infected or the damaged bone with a bone from another anatomical location. The limitation is the availability of the graft from another location.
2. Allografting: This procedure involves obtaining the graft from a cadaver. Some of the risks of allograft involve bacterial infection or rejection from the recipient [10].

With the above-mentioned grafting techniques having its own limitations, research, and developments of new materials to be used as replacement for human bone and tissue was initiated.

Tissue engineering '*Tissue engineering is the creation of new tissue for the therapeutic reconstruction of the human body, by the deliberate and controlled stimulation of selected target cells through a systematic combination of molecular and mechanical signals*' [14]. Tissue engineering involves development of scaffolds that are implanted inside the human body for the purpose of healing damaged tissue. This involves development of biocompatible materials that guide cells and promote growth of new tissues. Temporary scaffolds are designed to perform the functions mentioned above and degrade at the same time without leaving any traces. Long term or permanent implants are used in situations where the mechanical support is provided along with inducing tissue growth as that of tissue engineered scaffolds. Tissue engineered scaffolds are usually highly porous material manufactured using degradable polymers (synthetic or natural) or ceramics with high calcium content to ensure there are no traces of the scaffolds once the tissue is complete replaced [3, 10, 13–15].

The main challenge when it comes implants for bone replacement is the load bearing capacity of the implants. Permanent metallic implants are a better choice since they have better mechanical stability when compared to polymer or ceramic implants. For an implant to work as effectively as a bone, the implants should be able to withstand the cyclic loads that are experienced in the day-to-day activities, provide motion, and ensure biocompatibility with the surrounding bone/tissue. The implants should ensure that it does not corrode or react with the surrounding to create release degraded particle [7]. Metal implants such as plates or rods that are used to support bone growth are removed or in some cases metal implants are replaced time to time [3]. The next section provides a detailed discussion on the biomaterials and their properties used in orthopaedic implants.

#### **1.1.4. Biomaterials and their biocompatibility**

Initially biomaterials were defined as '*A non-viable material used in a medical device, intended to interact with the biological systems*' or as '*a material intended to interface with the biological systems to evaluate, treat, augment or replace any tissue or organ or function of the body*' [16]. Therefore, the factor that differentiates any material with the biomaterial is its ability to adapt to the biological environment once it is inserted. With the development of materials and medical technology, biomaterials can be defined as follows, '*A biomaterial is a substance that has been engineered to take a form which, alone or as part of a complex system, is used to direct, by control of interactions with components of living systems, the course of any therapeutic or diagnostic procedure, in human or veterinary medicine*'. Various materials such as metals, ceramics and polymers can be used as biomaterials if their interaction with the surrounding tissue does not create undesirable effects in the

host. In metals, alloys of titanium and stainless steel, noble metals such as gold and platinum are viable options to be used as biomaterials. Ceramics such as alumina, zirconia and polymeric materials such as polyolefins and polyacrylates are some of the non-metallic biomaterials [17]. Regardless of kind of the materials that used for implants, some of the material properties that influence their behavior with the host are, bulk material composition, mechanical properties, surface morphology, corrosion resistance, wear debris release, and degradation profile [14].

*‘Biocompatibility refers to the ability of a biomaterial to perform its desired function with respect to a medical therapy, without eliciting any undesirable local or systemic effects in the recipient or beneficiary of that therapy, but generating the most appropriate beneficial cellular or tissue response in that specific situation, and optimizing the clinically relevant performance of that therapy’* [14]. The response/biocompatibility of a particular biomaterials can be categorized as follows,

- Protein absorption, this includes the initial reaction that happens as soon as the implant is inserted in the host. During this the surface of the implant is covered with a layer of protein. The ability of the biomaterial to sustain this protein layer plays a major role.
- Material degradation, biomaterials are inserted in an aqueous environment which make is susceptible to degradation. The by-products of the degradation process such as wear debris, release of toxic chemicals due to reaction are of prime concern.
- Identification of effects caused by the degradation of material. Inflammation, pain and loosening of the implants over a period has to be monitored. The impact of the implant may not be local. Due to the presence of aqueous environment, the effect of the material can be sometimes observed at locations away from the implant as well.
- The implants can be host specific and depend on the anatomical location. Biomaterial that is compatible with the local tissue at a particular location may not respond well when used in another location [17].

A detailed discussion on biomaterials used in implants and their properties are discussed in the next section.

#### ***1.1.4.1. Polymers***

The basic building block of a tissue or bone is collagen, which is a natural polymer. This leads to idea of polymers being used as biomaterials in implants. Since polymers can be easily fabricated in different forms and tuned, they possess a wide range of mechanical properties. Apart from the mechanical properties, most of the polymers are biodegradable and biocompatible. The polymers used as biomaterials can be either synthetic or natural polymer depending on the application, location and mechanical loads experienced by the implant [3]. Synthetic polymers that are commonly used include polyethylene, polypropylene, polymethylmethacrylate (PMMA), polyurethane (PU), silicone [18]. Natural polymers include collagen, keratin, cellulose, silk, elastin, and chitosan. Synthetic polymers can be highly rigid (Ultra high molecular weight polyethylene) or highly deformable (Silicone) based on the application. They can also be stable or biodegradable. It is observed that the mechanical properties of the polymers are inversely related to the biodegradability. Some of the implants and medical devices that use polymers are catheters, pacemakers, artificial blood vessels, sutures, and scaffolds for tissue engineering [3, 18, 19]. One of the main drawbacks for polymers is their low mechanical strength when compared to metals and ceramics. This makes them inappropriate for load bearing applications [10].

Despite their low mechanical properties, some of the high-density polymers are used in orthopaedic applications. Nonabsorbable polymers like polyethylene, polyetherketone, UHMWPE are used in load bearing applications. Despite their properties, wear and release of wear debris is a major concern. Studies have indicated that wear debris leads to osteolysis and loosening of implants over a period. Some of the application of nonabsorbable polymers includes fusion cages, screws, plates and inner lining material for knee and hip implants. Another widely used nonabsorbable polymer is PMMA which

acts a cement or a bonding between prostheses and bone. Addition of monomer and antibiotics helps in polymerization and to treat infections [20].

Absorbable polymers are being used in orthopaedic implants to reduce stress shielding and promote tissue regeneration. These polymers can be used in locations which do not undergo mechanical stress since they possess very low mechanical properties. Some of the absorbable polymers include polylactide (PLA), polyglycolide (PGA). The degradation and new tissue development takes place simultaneously, this process can take weeks or months depending on the polymer. Absorbable polymers are mainly used in developments of scaffolds for tissue regeneration and in screws and plates as fixtures for bone fracture [3, 20].

#### 1.1.4.2. Ceramics

Ceramics are compounds that are usually inorganic, they contain various metallic oxides, silicates, and refractory materials such as hydrides and sulfides. They have gained attention in development of implants due to the inertness to body fluid, high compressive strength. Also, ceramics are difficult to shear plastically under shear loading due to their ionic bond [12]. The ceramics used in implants can be divided into three categories. The first are the structural ceramics (Alumina, Zirconia), they are highly stiff, hard and have good wear resistance. The second category are calcium phosphate-based ceramics which are used to replace bone. They have excellent osteoconductive properties, hence they are applied as coatings for metallic implants and in bone grafts. The third category of ceramics are bioactive glass, they have excellent biocompatibility properties. Their surface undergoes dissolution to form a high strength interfacial bond with the bone [21].

Bio ceramics do not undergo corrosion or degradation in biological environment unlike metals and plastics. Various *in vivo* and *in vitro* studies have indicated that ceramic implants are easily accepted by the surrounding tissue. Alumina and zirconia have been used extensively in dental implants such as dental crowns, dental post and in endosteal screws. When it comes to application in orthopaedic implants, alumina and zirconia are extensively used in hip implants as balls and as cups in total femoral prosthesis [23]. Bioactive glass or bioactive ceramics form a bond with the bone as mentioned before. The surface of these materials develops hydroxy carbonate apatite (HCA) when they encounter body fluids, this HCA bonds with the collagen fibres to form an interface. The interfacial strength of the adhesion formed between the ceramics implants and bone is usually higher than or equal to the natural bone. The interfacial strength or cohesive strength of bioactive ceramics and the non-bioactive ceramics is as shown in Fig. I-6. It can be clearly seen that the cohesive strength of alumina is very less when compared to bioactive materials like bioglass and cerabone [22].

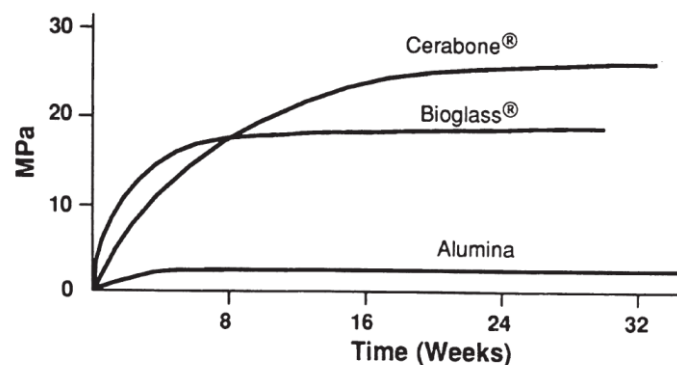


Figure I - 6 Pull off test to obtain cohesive strength. Comparison of non-bioactive and bioactive ceramics[22]

#### 1.1.4.3. Metals

Metals have better mechanical properties such as strength and stiffness when compared to ceramics and polymers. These advantages make metals a suitable candidate for application in load bearing implants. Some of the examples of load bearing implants are knee and hip implants, screws and plates. One of the main drawbacks of using metals are biocompatibility, corrosion, and bulk material properties [3]. Corrosion of metals can lead to loosening of implants, and release of wear debris into the local tissue and lead to infection and inflammation [24].

Metals used in biomedical applications the ability to develop a thin and stable protective oxide layer that prevent the corrosion of bulk material. This layer acts as an inert layer similar to the one seen in alumina or zirconia. Stainless steel, Cobalt – Chromium alloy (Co-Cr), and Titanium alloys are among the metals that are widely used in biomedical applications [12, 25].

One of the first metallic implants were manufactured using “Sherman Vanadium steel”, they were used to produce screws and plates for bone fracture. The corrosion resistance of vanadium was not sufficient for implants used for long term applications. The development of alloys provided a range of metals that can be used for biomedical applications. Stainless steel such as 316L is stronger and has better corrosion resistance. The presence of molybdenum and nickel improves the corrosion resistance but in highly stressed and oxygen – depleted regions, they are susceptible to corrosion. Hence, stainless steel is used in temporary fixations such as plates, screws, and nails [12, 24]. Cobalt based alloys or cobalt-chromium alloys (Co-Cr) have high corrosion resistance even under stress. There are two main cobalt alloys that are used in biomedical applications. The first one is cast CoCrMo alloy that is widely used in dental implants and joints. The second alloy is CoNiCrMo, this is used in load bearing prosthesis such as hip and knee implants. One of the disadvantages of these alloys is their frictional behavior and the wear resistance which can release chromium leading to undesirable reaction. The Young’s moduli of cobalt-based alloys (220-234 GPa) is higher when compared to stainless steels(200GPa) and clearly very high when compared to the properties of the surrounding bone. This higher stiffness of stainless steel and co-based alloys led to use of titanium-based alloys for biomedical applications. Titanium and its alloy have a density of 4.42g/cc which is almost half of the density of stainless steel (7.9g/cc) and co-based alloys (8.3-9.4g/cc), and the stiffness is 110GPa which is half of the cobalt-based alloys. Also, titanium alloys have better corrosion resistance when compared to stainless steel and cobalt based alloys due to the formation of titanium oxide layer on the surface of the implants. One of the widely used titanium alloys is Ti6Al4V. The other titanium-based alloy which has a unique property of shape-memory effect is nickel-titanium alloy. These alloys recover their original shape when subjected to heat. These alloys are used in orthodontic wires, stents, and aneurysm clips [7, 12, 26].

One of the main concerns of metallic implants is the lower magnitude of osteoinductive properties. In order to obtain better osteointegration of metallic implants with the surrounding tissues, the surface of metallic implants is modified. The physical modification involves increasing the porosity and roughness of the surface by providing a nano or macroscopic trabecular metal coating or nano scale protrusion to increase the adhesion. The pores in the coating also ensure bone ingrowth which helps for better fixation of implants [27]. The other route that is extensively used in coating of metallic implants with a layer of Hydroxyapatite (HA) coating that induces that promote osteointegration. HA coating with a thickness of ~50-75  $\mu\text{m}$  is used in commercially available orthopaedic implants. The studies have indicated that HA coating provides good fixation properties but their effect on cementless implants is still conflicting. The coating process parameters influence the crystallinity and the phase purity of the coating, which further influences the effectiveness of the coating. Therefore, extensive studies are necessary to obtain effective and approved HA coatings for long term application in implants [28].

### **1.1.5. Joint replacement implants and their performance**

Joint degeneration is the last stage of destruction in articular cartilage which can be due to trauma, age or disease which leads to loss in mobility, pain, and deformity. Recent developments in the implant

technology and surgery helps in replacement of these degenerate joints with permanent implants. The requirements and issue related to this replacement are discussed below:

### *1.1.5.1. Requirements and issues of joint replacement*

The removal of large amount of cartilage and bone during the implantation process makes the joint replacement an irreversible process. Therefore, designing effective implants is of prime importance. Some of the design consideration for the implants are as listed below [7, 29]:

- The design is primarily based on the complex load distribution (Kinematic and dynamic loads) experienced during daily activities. The load experienced by the joints depend on the location, age, and the amount of physical activity of the host.
- Materials, shape, mechanical properties, and the fixation method used in the surgery also play an important role in the load distribution on the implant.
- Overloading of the implant should be avoided to ensure there is no bone resorption that leads to implant loosening.
- The design of the implant should ensure complete range of motion while maintaining its stability.
- The material used and the surface finish of the implant should ensure osteointegration leading to better fixation of implant.
- The implant should be designed to ensure the fixation involves a minimum invasive surgery.

The implant fixation method is a crucial part of the complete joint replacement process. As mentioned in the reference [29] following three methods are used:

- Mechanical Interlock, this is accomplished by press-fitting the implant using bone cement (PMMA) or by using threaded components.
- Biological fixation, using implants with porous or textured surface helps in bone in growth which leads to better implant fixation.
- Chemical bonding, in this method, the implant is coated with an optimized amount of hydroxyapatite (HA) to create a chemical bond between the implant and the surrounding tissue.

Each of the above-mentioned mechanisms have its own distinctive behavior. Therefore, using more than one fixation method in complex joint replacements can lead to further complications, nevertheless it can help in customized load distribution.

Failure of implants can be due to various biomechanical events, that occur once the implant is placed and encounters the physiological environment. Some of the failure scenarios are as mentioned below [7]:

- Fatigue failure: The day-to-day activities leads to dynamic cyclic loading on the implant. This leads to damage accumulation over a period, leading to crack formation. The continuous bending and torsional loads further enhance the crack propagation leading to critical failure of the implant or failure of the interface.
- Stress shielding: The ability of the bone to vary its density with the load it experiences has to be considered in designing implants. Overloading the implant leads to underloading the bone. As this continues the bone loses its density and weakens around the implant. A bad prostheses design can lead to extreme stress shielding known as “Stress bypass”. Stress bypass leads to unwanted/undesirable localized osteointegration.
- Failed ingrowth: Inability of an implant to promote osteointegration leads to excessive micromotion, and implant weakening. Presence of large gaps between bone and prosthesis and the absence of porous or coated surface are the main causes of failed ingrowth.
- Particulate reaction: The abrasion between the implant and the bone surface or between the different surfaces of an implant or fretting on the surface of metal implants lead to release of

particulate matter into the host body. In certain cases, this particulate matter may lead to localized inflammation.

- Destructive wear: The bearing surface used to provide motion in the implants (usually made of UHMWPE) can proceed to a complete wear out stage.

There are two methods that are used to fix the implants, with cement and without cement. In cemented implants, a layer of PMMA is introduced to provide fixation between bone and protheses. While in uncemented implants the fixation is managed without any cement to provide better fixation.

#### **1.1.5.2. Cemented Implants**

Fixing of implants using cements provides immediate stability, allowing the host to apply complete weight at once, since the cement provides the adequate shear strength within one hour of implantation. The cements are viscoelastic in nature and act as shock absorbers and distribute the load between the implant and bone. PMMA bone cement acts as a glue by creating an interface between bone-cement and cement-implant. However, bone cements are considered to be toxic and the exothermic reaction removes a layer of the bone tissue. This layer ensures that the implant has a long life since the layer does not undergo resorption. A fibrous membrane in bone cement interface increases in width with time and results in micromotion, bone loss and implant loosening [30].

#### **1.1.5.3. Cementless Implants**

In cementless implants, the fixation between the bone and the implant takes place naturally. But the recovery time needed for the implant is higher since the fixation takes a longer time to ensure safe loading (3 – 12 weeks) depending on the host [30, 31]. To have a better fixation, there are two processes that make this possible, bone ingrowth and osseointegration. Bone ingrowth involves development of bone on the macroscopic irregularities of the implant surface forming a geometrical interlock. While osseointegration involves bone growth in microscopic irregularities or forms a direct chemical bond [31]. The amount of fixation between the implant and the bone is dependent on various properties of the implants such as porosity, surface roughness and biocompatibility of the material. Other parameters involve state of the bone tissue, surgery technique and gap between the bone and the implant. However, development of implant with porous mesh on the outer surface provides a better fixation [31]. Some of the macroscopic porous structures shown in Fig. I-7, include plasma spray coating, sintered wire mesh, sintered beads and porous cellular structure [32].

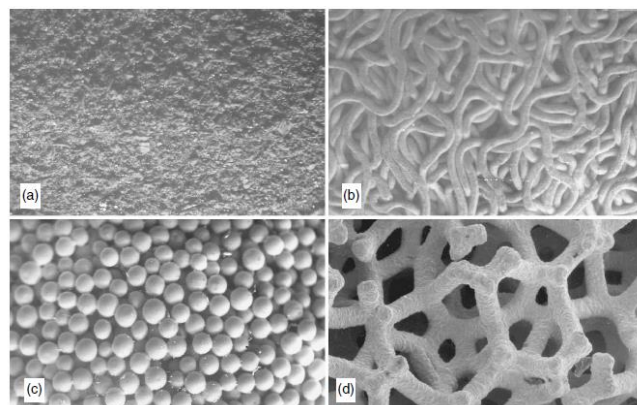


Figure I - 7 Different macroscopic surface irregularities (a) Plasma spray coating (b) Sintered wire mesh coating (c) Sintered beads and (d) Porous cellular tantalum [32]

*Osseointegration* is a technique where the implant fixation is achieved from tissue growth on the microscopic features of the implant. Some of these features include roughness on a smooth implant surface, HA coating, bioactive ceramics and bio glass. In osseointegration, two types of interfaces can be created, chemical bonding and mechanical interdigitation. In chemical bonding, a layer of bone tissue is sufficient while in interdigitation mature bone elements are required for proper functioning.

The process of osseointegration occurs only in the presence of osteoinduction and osteoconduction phenomenon. Osteoinduction is the process of engaging mesenchymal cells to generate pre-osteoblasts which later transform into osteoblasts. This a naturally occurring process and is essential for fixation of the implant. Osteoconduction is the ability of the bone to grow on a surface, such as implants. This process is dependent on the presence of differentiated bone cells. These bone cells maybe present due to the osteoblast process from a trauma or from the osteoinduction process. The process of osteoconduction is highly dependent on the surface properties of the implant and the biocompatibility of the surface, biomaterials have shown better performance compared to other material [33].

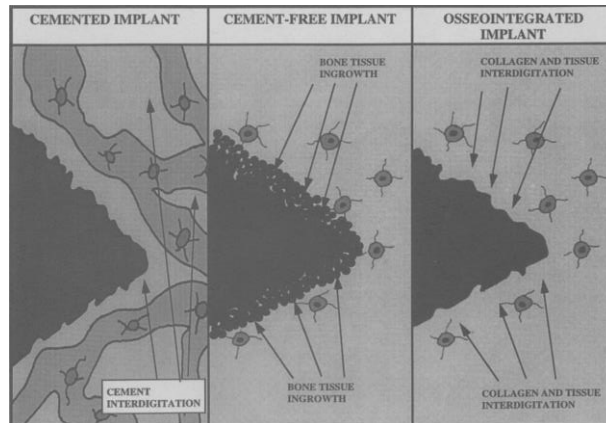


Figure I - 8 Fixation mechanism in cemented, cementless, and osseointegrated implants [31]

A complete fixation of the implant for its effective functioning involves, bone ingrowth on the macroscopic irregularities on the surface, followed by osseointegration with the assistance of a bioactive surface. HA coatings on porous titanium surface has proved be a good option for achieving the above-mentioned process. The interaction between bone and implant for different fixation process is describe is Fig. I-8.

#### 1.1.5.4. Total joint replacement : Hip, Knee, and Vertebral implants

*Hip Joint:* The development of implants and minimal invasive surgery has given the opportunity to conduct total arthroplasty or total replacement of joint. Total hip arthroplasty is one of the largely performed procedures and is a largely studied joint. The forces experienced by hip and knee joint during daily activities is tabulated in Table I-3.

Table I - 3 Load on hip and knee joint due to daily activities [7]

| Activity       | Maximum joint force ( times body weight) |      |
|----------------|--|------|
|                | Hip                                      | Knee |
| Slow walking   | 4.9                                      | 2.7  |
| Normal walking | 4.9                                      | 2.8  |
| Fast walking   | 7.6                                      | 4.3  |
| Stairs – Up    | 7.2                                      | 4.4  |
| Stairs – Down  | 7.1                                      | 4.4  |
| Ramp – Up      | 5.9                                      | 3.7  |
| Ramp – Down    | 5.1                                      | 4.4  |

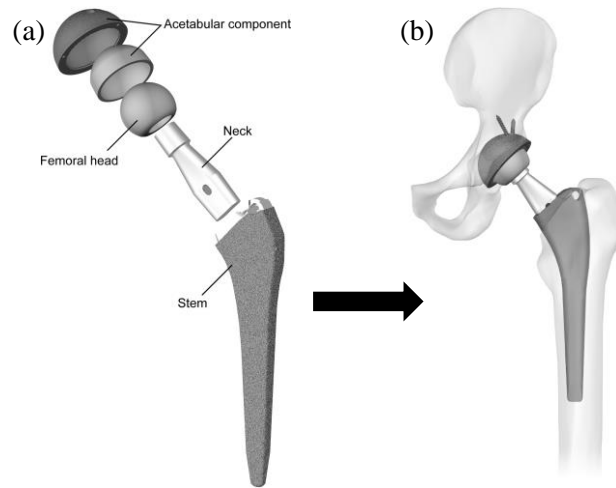


Figure I - 9 (a) Components of total hip arthroplasty (b) Stem inserted in intramedullary cavity of femur and acetabular component inserted in hip [37]

The hip joint is one of the critical bone joint due to the high loads and its involvement in all day-to-day activities. The loads on the hip-femur joint are complex but has been investigated since Galileo, but the first out-and-out study was carried out by Wolff at the end of 19<sup>th</sup> century. The major issue regarding the loads experienced by the joint is dependent on the severity of the activity and also on the host (age, sex, condition of the bone, etc.). The femur experiences cyclic load in all the activities and the load is distributed in all the directions. Sometimes, activities such as extreme sports, a sudden fall can lead to impact load on the joint. Therefore, a common loading mechanism cannot be assumed while studying the hip-femur joint. Upto 17 million cycles of load is experienced by hip-femur joint in a span of 10 years [30]. Also, stumbling during an activity can increase the peak load by almost 13 times the body weight [34]. Therefore, high peak loads and fatigue loads have to be considered while designing an implant for hip joint. Apart from the external loads (hip contact load) experienced by the femur, muscle attached to femur also transmit loads [35, 36]. These muscles ensure that the femur is subjected to compressive loads, thereby ensuring that the femur does not fail due to the tensile stress since bone is stronger under compression load compared to tensile load.

The components of the hip-femur implant consist of the acetabular component, femoral head, neck and stem as shown in Fig I-9a. The femoral head is connected to the stem by means of a neck. The size of the head and neck play a major role in the range of motion from the reconstruction [7]. The implant might be monolithic (one part) or modular (two or more parts), modular implants are available for customization according to the requirements of the host [30, 32]. The stem being the longest component of the implant, it should be strong and tough, therefore, it is made of metals such as Ti alloy, CoCr alloy, or, more rarely, 316L stainless steel. The stem part of the implant is inserted into the intramedullary cavity of the femur as shown in Fig I-9b either through cementation technique or press-fitting technique followed by bone ingrowth/osseointegration. The head is subjected to friction during its motion therefore materials such as CoCr and ceramics such as alumina and zirconia are used. The acetabular component of the implant should have low friction and also possess the ability to absorb shock loads experienced by the implant therefore this part is made up of UHMWPE (monolithic design). In case of modular design, the acetabular component is made up of a metallic shell with a UHMWPE insert. In order to reduce wear, a low wear UHMWPE is developed using a cross-linking polyethylene molecular chain. Under normal circumstances, despite the low friction of UHMWPE, they generate a high amount of wear debris between the acetabular and femoral head and between acetabular and its metallic shell [12, 30].

*Knee joint:* Due to the complicated loads and biomechanics involved in knee joint, the development and approval of knee prostheses was slower compared to the highly studied hip joint. Also, the complicated load and the high incidence makes the knee joint unstable compared to hip joints. The load

experienced by the knee joint in day-to-day activities is mentioned in Table I-3. The components of the total knee replacement (TKR) prostheses consists of knee femoral component (attached to femoral bone), stemmed tibial plate (attached to tibial bone) and the intermediate polyethylene articulate surface [29]. The load experienced by the knee joint is highly complex and varies with respect to the activity and the host (sex, age, disease) similar to hip joints. A detailed study on the load experience by the knee joint is carried out in the following reference [38].

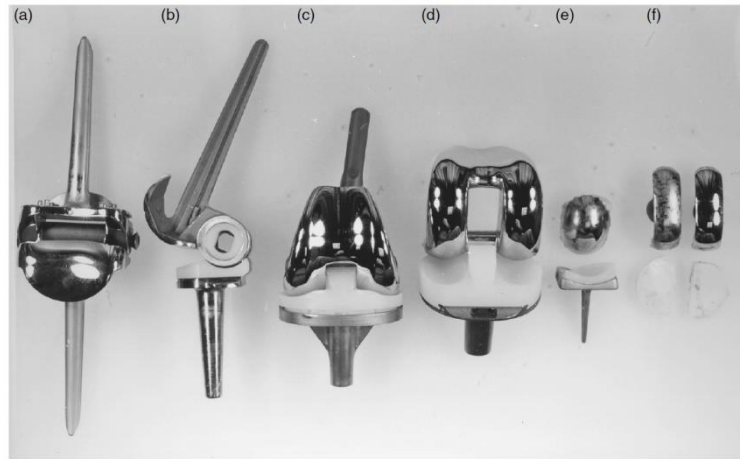


Figure I - 10 Different types of knee prostheses (a) Hinged (metal) (b) Hinged design (Plastic liner) (c) semi constrained (d) replacement for surface (e) uni-compartmental (f) bi-compartmental replacement [29]

Depending on the extent of damage at the knee joint, different types of knee replacement prostheses are considered. The TKR prostheses can be categorized into the following: (1) *Constrained*: These consist of a hinged articulation and have limited or fixed axis rotation. They are used when the damage at the knee is extreme and the ligament is absent. (2) *Semi-constrained*: These control the posterior displacement of tibia on femur and medial-lateral angulation of the knee. These are used when the deformation in the host is extreme. (3) *Non-constrained*: These provide minimum constrain and have used in situation when the ligament damage is less. Fig I-10 shows different types of TKR prostheses. TKR implants can be cemented or uncemented, in the case of uncemented implants a porous coating is provided to ensure proper fixation. The femoral and the tibial component are made up of metals such as Ti-alloys and CoCr alloys since they act as load bearing components while the intermediate articulate plate is made up of UHMWPE to reduce friction between the femoral and stemmed tibial component due to rotation [29].

*Spinal implants/spinal fusion cages*: The spine is the most important part of the human skeleton system as they act as a supporting structure. They also protect the delicate nerves that travel from the brain. Therefore, a stable and balanced spine is required to have 100% functionality of human body. However, injury, disease, genetic conditions, and age can lead to deterioration of the spinal cord. This led to development of spinal implants that can be used to replace these deteriorated components to restore balance in the spine. Major types of implants used in spine include spinal cages (interbody implants) and total disc replacement. The intervertebral disc (IVD) between adjacent vertebrae is shown in Fig. I-11(a). IVD undergoes a compression load during operation which creates a hydrostatic pressure on nucleus pulposus which induces tensile load on the fibrosus as shown in Fig. I-11(b) [39].

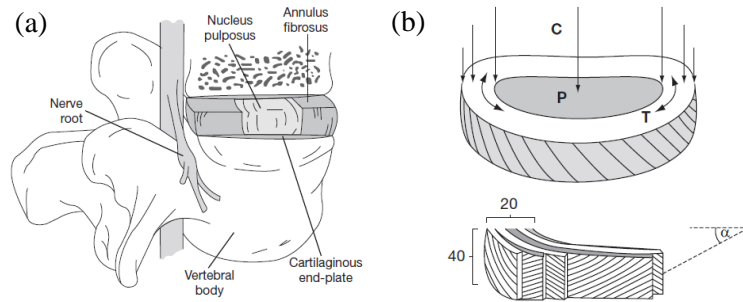


Figure I - 11 (a) Representation of intervertebral disc between two vertebrae (b) Load distribution in intervertebral disc[39]

Spinal cages should be designed to sustain compression loads without collapsing and to create a biological environment to incorporate grafts. Material such as PEEK, titanium and tantalum have been used in for spinal cages, along with PEEK implants with titanium coatings. Metals implants must be altered to match the stiffness of the implant to the surrounding bone. The surface of the metal implants must be modified in order to influence both on-growth and in-growth of the bone. While PEEK implants are treated with titanium or HA coatings for better biocompatibility. An example of PEEK and titanium alloy is provided in Fig. I-12 [39–41].

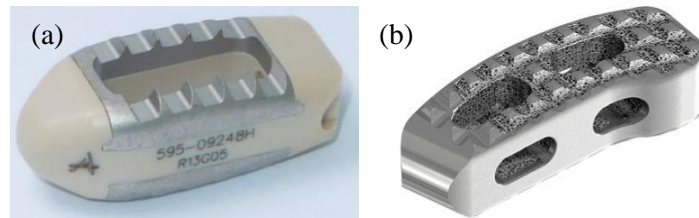


Figure I - 12 (a) PEEK spinal cage with Ti between bone and implant surface[40] (b) Porous titanium spinal cage[42]

Total disc arthroplasty (TDA) is gaining importance due to its high success rate. TDA involves replacing the damaged IVD with an implant connecting the two adjacent vertebrae. The TDA involves two endplates and a bearing surface between the endplates to provide mobility as shown in Fig.I-13. The endplates are generally made of metals such as cobalt chromium and titanium alloys. The endplates are attached to the bone using screws, fins, or serration. Bearing surfaces decide the stability of the TDA implant. The material used for bearing surfaces should have good wear resistance. UHMWPE has been extensively used as bearing material [39, 43]



Figure I - 13 TDA implant: Prodisc-C with metal on polymer articulation[43]

### 1.1.6. Stress shielding

The ability of bone to remodel and adapt to the external forces helps in maintaining the stability in the human skeletal system. Bone remodelling involves two steps, bone resorption followed by bone replacement. This is a continuous process that occurs throughout the life of an individual. The extent of bone remodelling depends on various factors such as age, gender and mainly on the extent of physical activity. During the bone remodelling at high stress regions leads to formation of denser tissue while in locations with low stress, bone resorbs. The bone resorption phenomenon can be due to variation in lifestyle (sedentary lifestyle leads to weaker bone) or due to presence of fixations such as plates, or other permanent implants which reduce the load carried by the bone i.e., stress shielding occurs. The phenomenon of stress shielding is a major concern in the case in joint implants. These implants are intended for long term usage (years), therefore the load carried by the surrounding bone is reduced for a long term. Therefore, the stress experienced by the bone is considerable low which leads to bone remodelling [44, 45]. Engineers and orthopaedic surgeons are working towards designing implants to avoid or reduce stress shielding. Stress shielding does not inflict any pain or restrict the motion. However, it reduces the bone mass density which leads to weaker bone. Loss in bone density and weaker bone leads to loosening of implants, misalignment, and increases the complexity of subsequent implant revision [45, 46]. A vital factor that determines the extent of stress shielding is the relative stiffness of the implant and the surrounding bone. While the stiffness of the bone is dependent on the age, anatomical location, gender, etc, the stiffness of the implant depends on the base material, design, and geometry. Apart from the bone and implant stiffness, the stiffness of their interface and the direction of load experienced by the bone-implant have an influence on stress shielding [45, 46]. The bone-implant system is similar to a parallel spring setup, when load is applied, the stiffer component (implant) of the bone-implant interface takes the maximum share of the load. In case on hip implants, the stem has a higher stiffness and is thicker, which allows it to carry maximum load and yield a better implant fixation. The amount of bone resorption is different for cemented and noncemented implants. In cemented implants the viscoelastic cement helps in even distribution of load which reduces the stress shielding. In case on noncemented implants, the extensive bone ingrowth and osseointegration increases the bone resorption. Apart from the properties of the implant, the bone density of the host also influences bone resorption. Higher bone density reduces the difference in stiffness between bone and implant there by reducing stress shielding. An implantation in different individuals can lead to different levels of bone resorption depending on the initial bone mass density of the host [45]. As the most common implant replacement is total hip replacement, maximum stress shielding, and bone resorption is seen in the proximal part of the femur due to the presence of thicker stem. Stress shielding around the stem is as shown in Fig.I-14, the bone resorption occurs between 6-24 months after the implantation and can reach upto 30% [47].

Various designs for hip implant have been proposed to reduce stress shielding [45, 47]. The main idea is to increase in the bone ingrowth on the surface using porous coatings to ensure load distribution and to reduce the stiffness of the stem by changing its design/geometry or by providing a porous polymer or metal coating. Metallic stems which are completely solid are either made of CoCr alloy Ti alloy which have a stiffness of 230 GPa and 110 GPa respectively, but the stiffness of a healthy cortical bone is close to 20 GPa. Using a material with low modulus will reduce bone loss but increases the interfacial stress between bone and the implant. These stresses lead to interface failure and possible loosening of the implant [46, 48]. Therefore, using a stiff stem under-loads the bone leading to bone loss and a complaint stem increases the interfacial shear stress. Hence, developing an ideal implant is a complicated process, since it requires us to balance the stress shielding effect as well as the interfacial stress [48–50]. Kuiper et al. [50] concluded that a non-homogenous (functionally graded) stem is a viable option to balance the stress shielding and interfacial stress experienced due to implantation. Functionally graded materials have a continuous transition in their properties from one location to another depending on the application. Example of a natural functionally graded material is bone. The properties of the bone vary continuously from a low stiffness trabecular bone on the inside to a high

stiffness cortical bone on the outside. The application of functionally graded materials for orthopaedics has been studied by Sola et al. [51]. Progress in functionally graded materials has led to the development of fully porous, non-homogeneous implants with optimized relative density [54-56]. A detailed study and in-depth information on stress shielding phenomenon can be obtained from the following references [44-48, 52].



Figure I - 14 Stress shielding in the proximal part of the femur due to bone-implant stiffness mismatch. Radiography compares the bone after 5 years of implantation (locations are highlighted)[45]

#### ***1.1.6.1. Porous orthopedic implants***

Porous implants have been used in orthopaedic applications. Porous coatings mentioned in the previous sections help in better fixation of the implant and support bone in growth in cementless implants [53]. As mentioned earlier using a porous implant reduces the stress shielding due to implantation [13, 25]. Materials such as porous polymers and ceramics are not used in load bearing locations due to the lack of material stiffness [25] but coating a metallic implant with bioactive ceramics or bio-glass increases the biocompatibility of the implant [28, 54]. There are different types of metallic coatings that are used on implants, (i) fibre metal coatings, they are obtained by pressing and diffusing randomly oriented CoCr alloy or Ti-alloy wires. (ii) Bead coatings, obtained by sintering beads of CrCo alloy or Ti-alloy into the implant surface of CrCo alloy or Ti-alloy respectively (iii) Plasma spray coating, this involves blowing metal alloy powder on the surface through gas plasma at high velocity. CP titanium and titanium alloys are used in plasma spray coating (iv) open-cell porous tantalum coating obtained by chemical vapor deposition (CVD) [53, 55]. The pore size obtained from the above-mentioned process vary between 100 – 1000  $\mu\text{m}$  with a porosity of 40-50%. But in the porous tantalum foam mentioned the porosity of 75-85% and a uniform pore size of 550  $\mu\text{m}$ , which is closer to the pore in trabecular bone [53]. The trabecular formation obtained from the porous tantalum (trabecular metal) has its elastic modulus between cortical and trabecular bone. Uniform and high porosity of trabecular metal provides excellent bone ingrowth and can be used as a main component in spinal cages. This leads to the conclusion that porous structures can be used in load bearing implants as well [13, 53, 55].

Porous coatings have the above-mentioned advantages but also have some drawbacks such as introduction of notches on the metal substrate during the coating process which acts as stress concentration points. This can lead to a reduction in the fatigue strength of the implant, which has to be

considered during the design phase. Next, the coating on the metal substrate can detach overtime if not considered [53]. As mentioned earlier, solid implants lead to stress shielding and hence bone loss while using a compliant design leads to high stresses at the bone-implant interface. The above-mentioned disadvantages led to the idea of fully porous implants instead to just a porous coating [57–59]. These porous materials (cellular materials) possess high porosity and low modulus and hence an optimized design process is required to develop a full porous load bearing implant. An example of a fully porous stem is as shown in Fig.I-15. Recent developments in manufacturing process such additive manufacturing using, Laser powder bed fusion (L-PBF) or Electron beam powder bed fusion (EB-PBF) makes it possible to produce complex, intricate, and highly porous structures. Various geometries with functional grading can be obtained with minimum effort and material loss [58, 60].

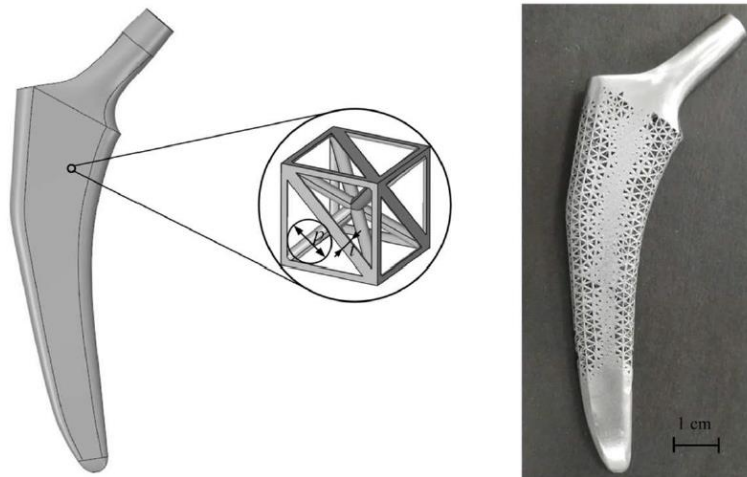


Figure I - 15 Fully porous stem developed by a tetrahedron unit cell [56]

The following sections provide a detailed discussion on cellular materials, additive manufacturing process and titanium alloy.

## 1.2. Introduction to cellular materials

Cellular structures are a class of materials made up of two phases, one is solid, and the other is empty/fluid. Cellular materials are formed from an interconnected network of plate, solid struts which form faces and edges of cell. A variety of cellular structures are observed in nature, such as wood, cork, bone and coral [11, 61, 62]. The properties of cellular materials are mainly influenced by three factors [63]:

- The base material properties used for cellular structures. For example, metals, polymers, and ceramics.
- The topology parameters such as cell wall thickness and the shape formed by the cell edges and faces.
- Relative density or the porosity of the structure.

The thickness values of the cell edges/walls in the unit cells vary between millimeters to micrometers. Therefore, cellular structures can be viewed as material which are made up of unit cells. Cellular structures exhibit their own mechanical properties such as strength and stiffness at macroscopic level. Hence cellular structures are also called as *cellular materials* in many scenarios [61]. In future discussions, the term *cellular material* has been used.

There are different types of cellular materials and can be classified under different categories:

- Natural and man-made.
- Closed and open pore.
- Foam based and lattice structure.

If the cellular materials are composed of only solid edges it is called open cellular materials and if it consists of solid edges as well as faces it is referred to as closed cellular material. Foam based structures, can be open foam or closed foam cellular material [62]. Foam based structures are composed of randomly oriented struts and faces, while lattice-based structures are made up of periodic, repetitive unit cells leading to highly regular form. Lattice based cellular structures can be further divided into, strut based, triply periodic minimal surface (TPMS) and sheet-based lattice structures. Depending on the mechanical behavior they can be classified as bending dominated and stretching dominated, a detailed explanation of the same is provided in the next section [64]. Various topologies of cellular structures are as shown in Fig. I-16. The areas of application for cellular materials vary from aerospace, automobile to biomedical industry. Fig I-17 shows the application areas of cellular materials based on their porosity.

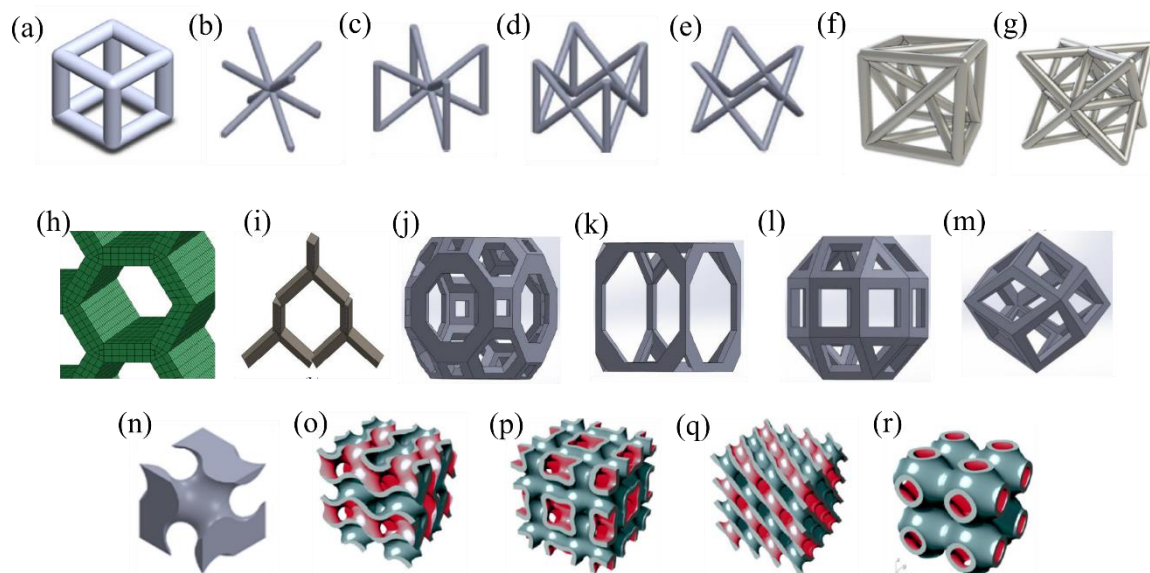


Figure I - 16 Representation of various unit cells (a) Cubic (b) BCC (c) BCC-Z (d) FCC (e) FCC-Z (f) Tetrahedron (g) Octet truss (h) Honeycomb (i) Diamond (j) Truncated cuboctahedron (k) Truncated cube (l) Rhombic cuboctahedron (m) Rhombic dodecahedron (n) Skeletal gyroid (o) Sheet gyroid (p) I-WP (q) Sheet diamond (r) Primitive. (a) [65] (b-e) [66] (f-g) [67] (h) [68] (i-m)[69] (n)[70] (o-r)[71]

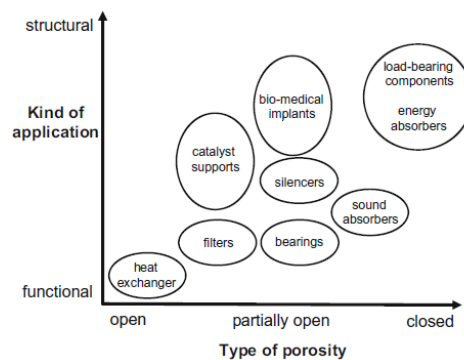


Figure I - 17 Application of cellular material with respect to porosity[62]

### 1.2.1. Stretching and bending dominated cellular material

As mentioned, one of the classifications of cellular material is the stretching and bending-dominated cellular materials. The classification is dependent on the nodal connectivity in the unit cell and they influence the mechanical properties of cellular material on a macroscopic level.

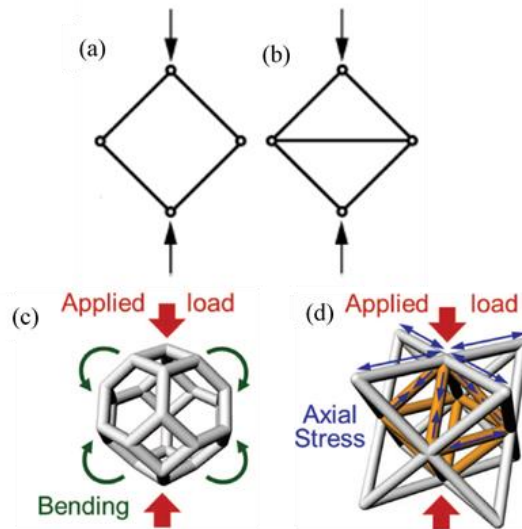


Figure I - 18 Pin jointed frame for illustrating (a) Bending dominated mechanism (b) Stretching dominated – structure [63]  
 (c) Loading in bending dominated unit cell (d) Loading in stretching dominated unit cell[62]

Fig.I-18 can be used to explain the difference between the bending and stretching dominated structures. Consider the struts are joined at the nodes by means of a rotating pin instead of welds and loaded in the direction depicted by the arrows. In Fig. I-15(a) when load is applied, the other two unloaded joints rotate and form a mechanism. Therefore, when joints are welded in Fig. I-15(a), the struts undergo bending and hence is bending-dominated. Adding an extra strut as shown in Fig. I5(b) restricts the rotation of joints and acts as a structure. In this case the struts experience axial loading when joints are welded and hence called stretching dominated. Fig. I-15(c) and (d) represent an example of bending and stretching dominated unit cell respectively. Foam based cellular materials exhibit bending dominated behavior while the behavior of lattice based cellular material depends on the cell shape [63, 72, 73]. Maxwell’s stability criterion is used to establish a mathematical relation between the number of struts, joints and the bending/stretching dominated behavior, a detailed explanation of the same is provided in the following reference [63]. Stretching dominated cellular materials are loaded in axial direction (compression and tensile) and exhibit higher strength and stiffness when compared to bending dominated cellular materials. Mechanical behavior of these structures are discussed in section 1.2.6.

### 1.2.2. Relative density of cellular material

Relative density ( $\rho$ ) is the main parameter that can be used to relate any property of the cellular material from mechanical to thermal properties. It is defined as the ratio of density of the cellular material ( $\rho^*$ ) to the density of the solid/bulk/base material ( $\rho_s$ ) as shown in the Eq. I-1.

$$\rho = \frac{\rho^*}{\rho_s} \quad \dots\dots \text{Eq. I-1}$$

If the mass of the material filling the void in cellular material is negligible when compared to the mass of the solid material, the relative density can be calculated by taking the volume as a parameter. Relative density depicts the amount of solid material present in a considered volume of the cellular material. The contrary of relative density is the porosity of cellular material and calculated as  $(1 - \rho)$ .

In general, cellular materials are considered to have a relative density lesser than 0.3. Relative density is dependent on the cell topology and the geometrical parameters of the strut. A review on the analytical relationship to find the effect of cell topology and strut cross-section was provided by Zadpoor et al. [74].

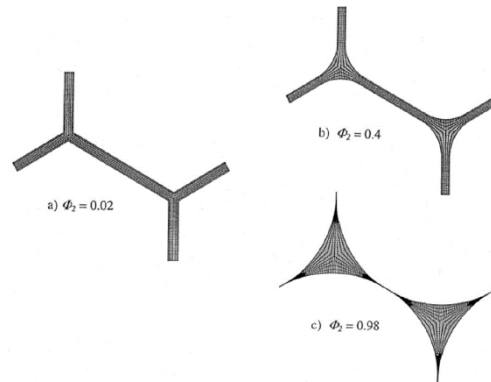


Figure I - 19 Planar lattice with same relative density, but different fraction of material between joints[75]

Even though the mechanical properties are dependent on the relative density, other parameters such as cell shape, cell size influence the mechanical behavior. For example, a square unit cell based cellular materials has different mechanical properties when compared to a honeycomb based or foam based cellular material with the same relative density. Even for cellular materials with the same unit cell and relative density, the amount of material between the nodes also influences the mechanical properties. Fig. I-19 depicts the relative material distribution between nodes for same relative density. The parameter  $\Phi$  is used to depict this material distribution [75]. The mechanical behavior also depends on the stretching and bending dominated behavior of cellular materials as discussed in the next section.

### 1.2.3. Mechanical properties of cellular material

The mechanical behavior of cellular materials is generally obtained from compressive stress-strain curves. A typical stress-strain curve for both bending dominated and stretching dominated cellular materials is as shown in Fig. I-20. The stress-strain curve can be divided into three regions: Elastic region, plastic deformation, and densification. In the elastic region, the material behavior is linear, however, Gibson et al. [11] suggested to measure the Young's modulus of the cellular materials during the unloading as shown in Fig. I-20. Once the cellular material is past the elastic region, the plastic deformation occurs due to yielding or buckling. In the plastic region, the samples undergo deformation under constant stress, called as *plateau stress* for bending dominated structures. While for stretching dominated structures, there is a post-yield softening that is observed, and the plateau region is composed of peaks and valleys as indicated in Fig. I-20. The final densification region is reached when the failed components of the cellular material collapse and come in contact with the next layer, thereby constraining further deformation. An illustration of FCC-Z unit cell under compression is as shown in Fig. I-21. The stress in the material increases steeply during the densification stage and its slope tends to the elastic modulus of the base material. Stretching dominated structures have high strength and stiffness when compared to bending dominated structures with same relative density. However, stretching dominated structures are prone to sudden failure while bending dominated, structures are more complaint [13, 63, 64]. Studies have indicated that depending on the lattice structure and relative density, the failure is layer-by-layer for stretching-dominated cellular materials and failure is usually due to shear failure for bending dominated cellular materials [76, 77].

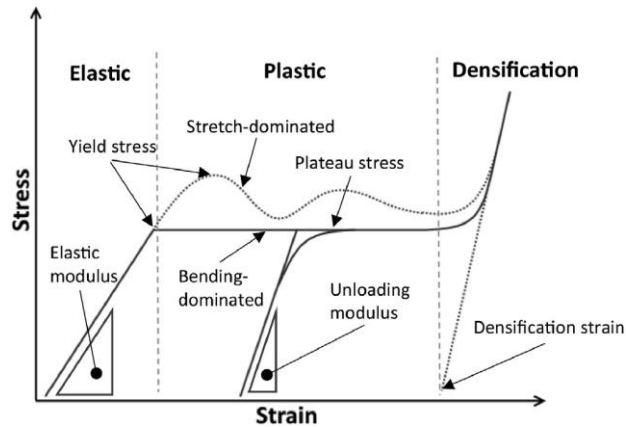


Figure I - 20 Illustration of compressive stress-strain curve for bending and stretching dominated cellular material[64]

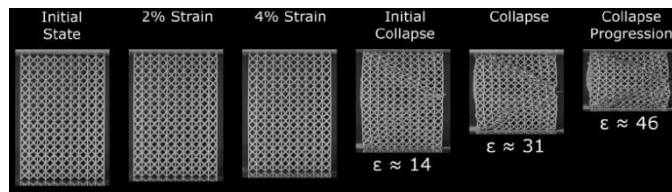


Figure I - 21 Deformation of FCC-Z cellular material under compression load[78]

Testing of cellular material under tensile loading is still a developing area of research. However, the tensile stress-strain curve for cellular material is similar compressive curve in the elastic region, after yielding the struts tend to orient towards the loading direction and finally undergo failure. Depending on the properties of the base material, the failure under tensile loading can be ductile or brittle. The elongation in the structures also depend on the unit cell used in the cellular material [11].

The flowchart in Fig. I-22 gives a clear direction on the parameters to be considered for designing the cellular material to obtain the required properties.

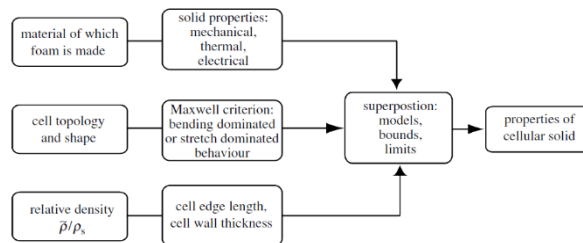


Figure I - 22 Design variables that influence the behavior of cellular materials[63]

### 1.2.4. Mechanical modelling of cellular materials

Cellular materials are made of several number of unit cells, using the complete structure for modelling is difficult due to computational constraints. Over the past few decades, various numerical and theoretical models have been developed to understand and predict the behavior of cellular materials. The properties are calculated as a function of the cell topology, relative density, and the base material. These properties are further used in designing components composed of cellular material.

The basic building block for cellular material is the Representative Volume Element (RVE). The RVE should be able to represent the properties of the complete cellular material with lesser computational complexity. For lattice based cellular materials the RVE is the unit cell that has been repeated in all the three directions to form the complete structure. While in case of foams and non-periodic cellular materials, the selection of RVE size is not a direct task. Different sizes of the RVE are

tested until a convergence is observed in the properties. Even in this case the computational limitation has to be considered [79–81].

One of the most used theoretical solutions for the mechanical properties of cellular materials was developed by Gibson et al. The model was developed for lattice based cellular materials, with model is applicable for 2D and 3D lattice based cellular materials. The model was developed by assuming the struts obey Euler – Bernoulli theorem for beams [11, 82]. The model finally relates the elastic modulus and strength to the relative density of the cellular material using a power law as indicated below:

$$\frac{E^*}{E_s} = C_1 \left( \frac{\rho^*}{\rho_s} \right)^{n_1} \quad \dots\dots \text{Eq. I-2}$$

$$\frac{\sigma^*}{\sigma_s} = C_2 \left( \frac{\rho^*}{\rho_s} \right)^{n_2} \quad \dots\dots \text{Eq. I-3}$$

The  $E^*$ ,  $\sigma^*$  are the elastic modulus and the strength value of the cellular material while  $E_s$  and  $\sigma_s$  represent the elastic modulus and the strength values of the base material. The constants  $C_1$ ,  $C_2$ ,  $n_1$ , and  $n_2$  are dependent on the unit cell and can be obtained from theoretical calculation or from fitting the experimental data. Fig. I-23 (a) gives the relation between the relative density and relative Young's modulus. The value of  $n_1$  is 1 for ideal stretching dominated behavior and 2 for ideal bending dominated behavior as indicated by the graph. Fig I-23 (b) gives the relation between the relative strength and the relative density of the cellular materials, the curves indicate that the value of  $n_2$  is 1 for ideal stretching dominated behavior and 1.5 for ideal bending dominated behavior. Similar relations have been derived for other elastic constants, fracture toughness and plastic buckling with respect to relative density [11].

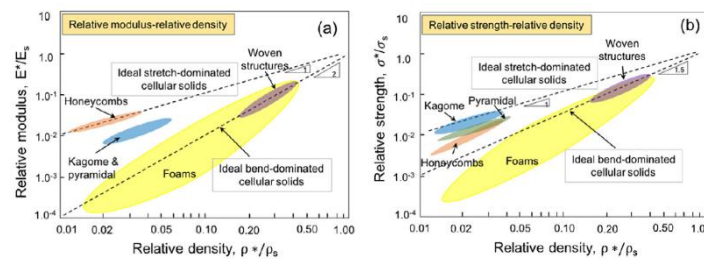


Figure I - 23 (a) Relative density vs relative Young's modulus (b) Relative density vs relative strength for different cellular solids, indicating ideal behavior [61]

The above-mentioned approach directly relates the relative density, this helps in relating the geometrical parameters of the unit cell such as strut thickness and strut length to the mechanical properties. However, theoretical calculation is limited to simple lattice structures and is not recommended for complex lattice structure. For the beam theory to accurately predict the properties, the lattice should be composed of slender struts. The accuracy of the Gibson -Ashby model decreases with increase in the relative density, the model works best when the relative density is less than 0.3 [83]. In most of the cases, the struts in the cellular material undergo geometrical deviation due to the manufacturing process, which influence the mechanical properties. Therefore, the mechanical properties predicted from the above model might be different from the ones obtained experimentally [84, 85].

To overcome the disadvantages of the previously mentioned model, various numerical homogenization methods have been proposed [86]. In these techniques, RVE of the cellular material is considered, this can include the irregularity of the cell topology and is independent of the relative density of the cellular material under study. The assumptions in this method include a length scale

separation between the domain and the microstructure, and the presence of spatial periodicity. The field variables associated with the model are periodic in small scales but are smooth on the macroscopic scale [79, 81]. From the literature [81, 86–88], asymptotic homogenization has been used extensively in many instances [83, 89]. Some of the applications include study of topology optimization and manufacturing irregularities [56, 90]. This method has certain drawbacks due to the assumptions. The length scale separation is difficult to verify for lesser number of unit cells that contribute to the domain under study, stress in certain critical locations and effect of defects on the local stress state are lost due to the homogenized approach.

The other technique that has been used widely to model the behavior of cellular materials is Finite Element (FE) method. This covers all the drawbacks from the theoretical Gibson-Ashby model and homogenization technique. This method provides us with the ability to understand the finest details without simplifying the model for complex geometries and without any assumptions. But the computational capacity available limits the size of the FE model. Lattice based cellular materials can be modeled using two methods, beam elements and continuum elements while foam based cellular materials can be modeled by continuum elements only [86]. The advantage of using beam elements is faster modelling and computation time, it is useful in obtaining the overall behavior of the cellular material, and to capture the failure mechanism [91, 92]. Beam elements can be used to study the effect of geometrical parameters and deviation such as strut thickness, fillet radius and geometrical deviations on the strength and stiffness of cellular materials [93–96]. Beam elements were used by Alkhader et al. [97] to show the transition of stretching dominated behavior to bending dominated behavior due to change in periodicity, which reduced the stiffness. Beam models have also been used to study the effect of cell geometry, and manufacturing irregularities on the fatigue properties of cellular materials [98, 99], however, beam models cannot be used to study the effect at the local level. Continuum models on the other hand have the ability to reproduce the finest details of the morphology but require higher computation capacity. Various studies in literature have used continuum elements to study the behavior of cellular material [86, 100, 101]. The effect of surface irregularities were studied for CoCr lattice based cellular materials manufactured using LPBF [102] and polymer based cellular materials [103]. Experimental results are compared with the FE analysis results obtained using continuum elements, the results indicated a clear overlap of the curves [76]. The effect of loading direction on the mechanical behavior [65] and modeling of multi-material to study the effect of ingrowth [104] has also been carried out using continuum method. The development of X-ray tomography technology to obtain detailed information on the morphology of the manufacture structure has helped to obtain the mechanical behavior of as-built cellular material [105, 106]. Depending on the base material the cellular materials can be manufactured using different processes. Production of lattice-based or periodic cellular materials is complex process, however development of additive manufacturing process has made it feasible. The further discussion will be based on metallic cellular materials manufactured using PBF process.

## **1.2.5. Defects found in AM manufactured cellular materials**

### ***1.2.5.1. Internal Porosity***

The internal porosity in LPBF manufactured samples can be categorized into two types, spherical and irregular-shaped pores. Spherical pores are formed due to gas entrapment during the process and irregular shaped pores are due to incomplete melting of metallic powder. Spherical pores are influenced by the high specific energy during the process which increases the melting phenomenon. On the contrary low specific energy leads to uneven or incomplete melting leading to irregular pores [107]. The percentage of porosity in bulk structures varies between 0.5-0.1%. Fig. I-24 illustrates both the types of porosity. Studies have shown that HIPing reduces the porosity in cellular materials [108, 109]. The inclination of the struts with respect to the printing plane influences the internal porosity, as the angle of inclination increases the internal porosity also increases [109, 110].

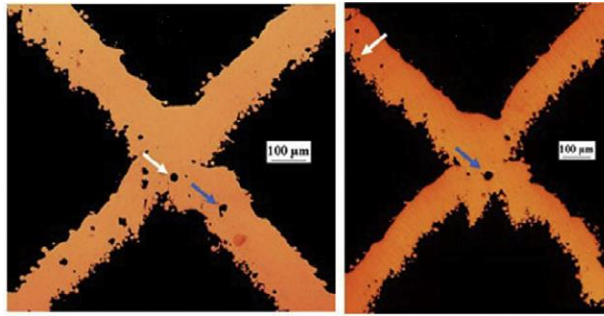


Figure I - 24 Internal porosity from the PBF process, spherical pores (indicated by white arrow), irregular pores (indicated by blue arrows) [111]

### 1.2.5.2. Unmelted particles

In PBF process, the heat used to melt the powder particles radiates and melts the surrounding particles. These particles adhere to the solid surface, depending on the heat dissipated, the particles can be attached strongly or loosely. Increasing the power of heat source increases the number of particles attached [77]. This increases the surface roughness of the solid part [86]. The extent of particle attachment depends also on the orientation of the struts in the cellular material, as shown in Fig I-25. Lateral surfaces have lower particle attachment compared to horizontal and inclined surfaces [112, 113]. Post manufacturing treatment such as chemical etching can be used to remove these particles [112, 114, 115].

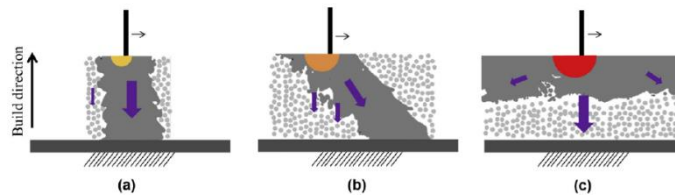


Figure I - 25 Illustration of effect of building direction on surface roughness of struts[116]

### 1.2.5.3. Geometrical deviation: As-designed vs As-built

The difference between the as-designed geometry (CAD) and the as-built geometry is a well know observation. This difference is predominant in cellular structure with thin struts and influences the properties of the cellular structures [86]. The accuracy with which the as-designed geometry is replicated in LPBF process is determined form the melt pool size. Bigger melt pools are not suggested for cellular structures since they do not reproduce fine details. The melt pool size is dependent on the thermal properties of the powder/solid interface and the energy of the melt source (laser). Large melt pool is obtained is obtained in the high energy is provided and the heat is not carried away, else smaller melt pool is obtained. The other parameters that effect the geometry are laser power, scanning speed, hatching distance and particle size [77, 117, 118].

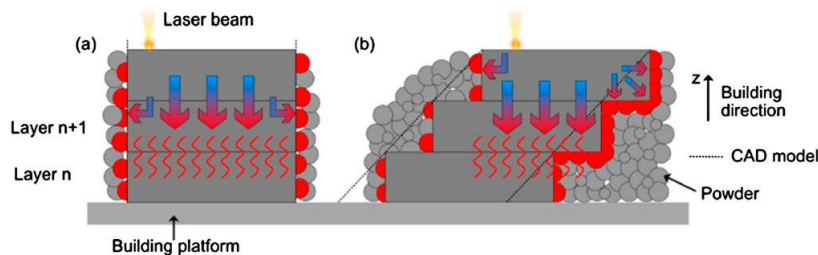


Figure I - 26 Effect of strut orientation on strut morphology (a) heat is carried away more evenly (b) heat is conducted in other directions in inclined struts due to formation of stair-case effect and to lower layer in horizontal struts[119]

Apart from the above-mentioned parameters, the building orientation also plays a major role in the geometrical deviation. Furthermore, the amount of solid present in the powder layer below and packing

density of the powder influence the heat transfer properties locally. Since the powder is less conductive than a solid layer, heat dissipation is faster in the presence of solid layer thereby reducing the melt pool size. For example, horizontal struts do not have any solid support therefore has a larger melt pool. Additionally, the gravitational and capillary effects the molten material sags and flows into the powder leading to increased strut thickness and formation of irregular struts with varying thickness and loose particles [112, 113, 118, 120]. On the contrary, melt pool of vertical strut is completely supported by solid material and hence is smaller. This leads to a better reproduction of CAD dimensions, as shown in Fig. I-26(a). Studies have shown that horizontal struts have the largest geometrical deviation, the deviation decreases with increasing the angle (building orientation) [121, 122]. In case of inclined struts, the presence of partial solid support leads to the “staircase effect”. There is a partial offset in the solid part with respect to each layer, as shown in Fig. I-26(b) [112, 113]. The aforementioned phenomenon is applicable of other parts manufactured using LPBF process which consists of overhanging components [123, 124]. The materials properties such a solidification and material shrinkage further increase the complexity of the study of geometrical mismatch [125].

The geometrical defects in cellular materials that arise from the LPBF process can be categorized as follows [94, 95]:

- *Strut waviness*: For a given strut, the center of the cross-section at various points misaligns with respect to the designed axis of the strut. This center offset induces a wavy effect to the strut as shown in Fig. I-27(b) [94, 120].
- *Strut section irregularity*: The melting of adjacent powder particle and the staircase effect deviate the as-built cross section from the as-designed cross-section. For examples, a circular cross section may be printed as elliptical [94, 122].
- *Strut thickness variation*: The process parameters and building orientation can increase or decrease the thickness/diameter of the strut from the designed value [69, 77, 120, 121]. Struts perpendicular to the build plane (vertical struts) have a uniform thickness comparable to the designed values while horizontal struts and struts with smaller inclinations are relatively thicker, as shown in Fig. I-27(a).

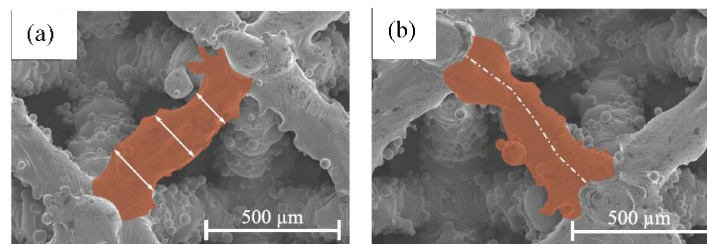


Figure I - 27 Deviations in struts (a) Thickness variation in strut (b) Strut waviness[126]

The rapid cooling in the LPBF process induces stress in the cellular structures, these stresses are not relieved completely even after the stress relieving process. The residual stresses not only influence the mechanical properties, but also instigates distortion of stresses. The measurement of residual stresses is a complicated process, but the presence of tensile residual stress is detrimental to the fatigue resistance of structures [127].

For biomedical orthopaedic implants, elastic modulus plays a major role. The Young’s modulus of the cellular structure influences the bone regeneration and stress shielding as discussed in section 1.1.3. In orthopaedic implants, the elastic modulus is often the single most important parameter to determine the suitability of the material, given its relation to stress shielding and bone regeneration (see Section 1.1). Since cellular structures can be used for load bearing orthopaedic applications, their yield stress and strength have to be considered. The strength and stiffness of cellular structures are measured using

compressive test and sometimes using tensile test. The other most used testing procedure involves fatigue testing, but they require more samples. The quasi-static properties are dependent on the cell topology (type of cell, wall thickness, pore size), base material, and strut defects (geometrical deviations and surface roughness). Geometrical deviations can increase the mechanical properties depending on the increase in the strut thickness compared to the as-designed thickness. Manufacturing defects such as strut waviness, strut irregularity decrease the mechanical competency of the cellular structures. Strut defects have a greater influence in struts which are directly loaded compared to struts which are indirectly loaded [86][80]. Struts parallel to the building plane have less support as explained previously and are weak. Hence, loading these struts can lead to lower mechanical properties. Due to the high dependency of mechanical properties on as-built geometry, a considerable amount of scatter is observed for the same [95, 128]. As a general rule, struts laying in the building plane should be avoided because, especially if oriented in loading direction, can considerably alter the mechanical properties of the lattice [110].

### **1.2.6. Static and fatigue properties of cellular materials**

As discussed in the previous section 1.2.3, the mechanical properties of cellular material is dependent on various geometrical and material parameters. This section provides insight on the static and fatigue behavior of metallic cellular material manufactured using PBF process. Effect of parameters such as cell type, porosity, manufacturing defects and post manufacturing process obtained from the literature are discussed below.

#### ***1.2.6.1. Effect of cell type and porosity on quasi-static properties***

As mentioned in the general discussion on cellular materials, the development of AM process has given the freedom to design new lattice structures which could not be manufactured using conventional manufacturing processes. Different cell types ranging from lattice based to TPMS based, with uniform porosity to graded porosity, and with porosity ranging from 50% to 90% have been studied. Some of which are discussed below.

Parthasarathy et al. [129] studies EB-PBF manufacture Ti6Al4V cubic cellular material under compression loading. The study considered samples with porosity varying between 49.75 – 70.32%, the porosity was varied by changing their strut thickness and pore size. The stiffness values obtained from the study were in the range of 0.57-2.92 GPa and strength between 7 – 160 MPa. The values indicated that the cellular material is suitable for craniofacial applications. The decrease in the strut thickness had very less effect on the overall porosity but reduced the stiffness by 80% and strength by 93% when compared to the thickest strut. Subsequently, three different cell types, Cubic, G7 and rhombic dodecahedron were considered by Li et al. [130]. The samples were manufactured EB-PBF process with porosity in the range of 58-88%. The compression test results indicated that cubic and rhombic dodecahedron structures displayed high collapse strength and brittle characteristics, while G7 structures exhibited bending dominated behavior. The mechanical properties were in the range of 0.5 – 15GPa and compressive strength in the range of 10-300MPa. Xiao et al. [105] studied the behavior of rhombic dodecahedron titanium cellular materials manufactured using EB-PBF. The experimental results were compared with the FE analysis of model generated using X-ray tomography data of the samples. The deformation mode and the maximum strength match well with the experimental data.

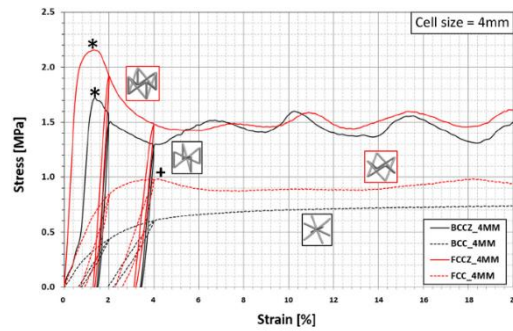


Figure I - 28 Stress-strain curves for different cell types indicating the effect in vertical struts, that introduces peaks and valleys in plateau region[78]

As discussed previously, the orientation of struts with respect to the building direction decides if the cellular material is bending dominated or stretching dominated. The study carried out by Gümrük et al. [131] provided a clear idea about the same. The study involved stainless steel cellular material formed using three cell types, BCC, BCC-Z (Extra vertical strut) and  $F_2$ BCC (Two BCC unit cell from one node) using LB-PBF process. The presence of vertical strut in BCC-Z increased the stiffness and strength of the cellular materials compared to other configurations for all porosity values. The effect of strut in the Z-direction was also studied by Leary et al. [78] by comparing the properties of BCC, BCC-Z, FCC, FCC-Z. The fitting of experimental results using power law showed that the inclusion of vertical strut helps in transitioning from bending dominated behavior to stretching dominated behavior. The plateau region from stress-strain curves shown in Fig. I-28 also indicates the same. Similar results were obtained by Mazur et al. [132] for Ti6Al4V based cellular materials.

Ahmadi et al. [69] conducted a detailed study on the effect of both cell types and the porosity of Ti6Al4V cellular materials manufactured using LB-PBF. The study considered six cell types, cubic, diamond, truncated cube, truncated cuboctahedron, rhombic dodecahedron, and rhombic cuboctahedron. The cell types consisted manufactured with various strut thickness and pore size to vary their porosity. The strength and stiffness values obtained were well fitted using the power law as suggested by the Gibson-Ashby law. Out of the six cell types, truncated cube exhibited high stiffness. Cube based cell types such as truncated cube, cube, truncated cuboctahedron, and rhombic cuboctahedron were categorized as stronger unit cells compared to diamond and rhombic dodecahedron. Further, Kadkhodapour et al. [76] investigated the failure mechanism under compression for cubic and diamond unit cell studied by Ahmadi et al. [69]. The experimental data was validated using FE analysis of RVE model with 125 – unit cell. Johnson-Cook damage model was used to predict the failure mechanism. Acceptable results were obtained from the FE analysis, with a relative error of 18% in the first peak stress. The study concluded that FE analysis can be successfully used to predict the failure mechanism of cellular materials using RVE models. Similar studies were carried out for AlSi10Mg cellular materials with BCC, truncated octahedron, and hexagon unit cell [133].

Arabnejad et al. [67] studied the compression behavior of two stretching dominated structures, octet truss and tetrahedron Ti6Al4V cellular material. The study took into consideration the effect of porosity, geometrical deviation, and the ability for bone ingrowth. For both the unit cells, the increase in porosity decreased the strength and stiffness. However, when comparing the mechanical properties between the unit cells, octet truss had higher strength and stiffness compared to tetrahedron unit cell at lower porosity. However, a drastic decrease in the strength and stiffness was observed for octet truss unit cell at higher porosity. This is attributed to the manufacturing defects that affected the deformation mechanism at higher porosity. Cuadrado et al. [65] studied the compression and torsional response of cube, BCC and cross (cube printed with 45° inclination). The study also included the effect of inclined loading on the strength and stiffness, inclination of 22.5°, 45°, 67.5°, and 90° with respect to the horizontal were considered for different porosities. The results indicated that cubic samples performed well under compression load, while BCC structures have better performance under torsional load.

Inclined load induces bending in the cubic structure and change the failure from buckling in vertical loads to bending in inclined loads.

Similar to the strut based cellular material discussed above, different triply periodic minimal surfaces (TPMS) have been studied under compression loading. Yan et al. [113] studied the gyroid based, stainless steel cellular material manufactured using LPBF method. Variation in porosity and the effect of orientation of the strut angles ( $0^\circ$  and  $45^\circ$ ) was studied. The LPBF process reduced the porosity of the sample due to the staircase effect, which adds extra material. The results indicated that samples produced with struts oriented at  $0^\circ$  orientation have higher mechanical properties. Bobbert et al. [71] studies four different types of Ti6Al4V TPMS unit cell: primitive, I-WP, gyroid and diamond. The Young's modulus of all the structures were in between 3 – 6.5GPa and the strength was in between 92 – 276MPa. The obtained properties were close to properties of various bones from the literature. Kadkhodapour et al. [134] studied the failure mechanism of I-WP and F-RD TPMS unit cell based cellular materials for different porosity values. The failure was layer-by-layer crushing of micro-struts for all the porosities of I-WP structures and most of F-RD structures. The failure mechanism analysis indicated that the unit cells considered were more of stretching dominated due to the presence of columnar configuration. Yanez et al. [135] conducted an uncommon study on the compressive properties of Ti6Al4V gyroid structures. The study involved comparing the properties of normal gyroid cellular material with the deformed gyroid cellular material. The pores in the deformed gyroid cellular material were elliptical rather than circular. The study concluded that the deformed configuration performed better when loads were applied along the longitudinal direction. But normal gyroid had a homogenous behavior when inclined loads ( $45^\circ$ , FE analysis) were applied. Zaharin et al. [136] compared the compressive properties of Ti6Al4V gyroid and cubic unit cell based cellular materials, with pore size between the range 0.3 – 0.6mm. The stiffness values for all the structures are between the range of 3 – 17GPa, which is suitable for biomedical applications.

Functionally graded (FG) cellular materials are of interest since the mechanical properties can be tailored according to the mechanical and biological requirements (pore size for bone ingrowth). Functional gradient can be induced by varying the strut thickness, varying the strut thickness and the pore size, by using multiple materials and or by using different unit cells in the same sample [137]. Surmeneva et al. [138] studied the compression behavior of FG-BCC and FG-diamond cellular materials under compression loading. Two-layer and three-layer gradients with gradient along the radial direction was studied. The experimental results concluded that the presence of gradient helps in transforming the brittle behavior in diamond based cellular materials to ductile behavior. Zhang et al. [137] studied the variation in the compressive and permeability properties of FG-diamond cellular material. The gradient in the porosity was, linear, exponential and based on sigmoidal function. The strength and stiffness values obtained were in the range of cancellous and cortical bone values, making them a viable option for biomedical applications. Zhang et al. [139] compared the properties of uniform and functionally graded rhombic dodecahedron cellular materials. The study indicated that FG cellular materials have low stiffness similar to uniform structures, but higher strength and energy absorption compared to uniform structures.

*Tensile testing:* In the present literature, extensive study is carried out the compression testing of cellular materials. However, few studies have focused on the tensile properties of cellular materials. Some of the discrepancy observed for tensile testing is the specimen design. Different types tensile testing samples for cellular material are as shown in Fig. I-26.

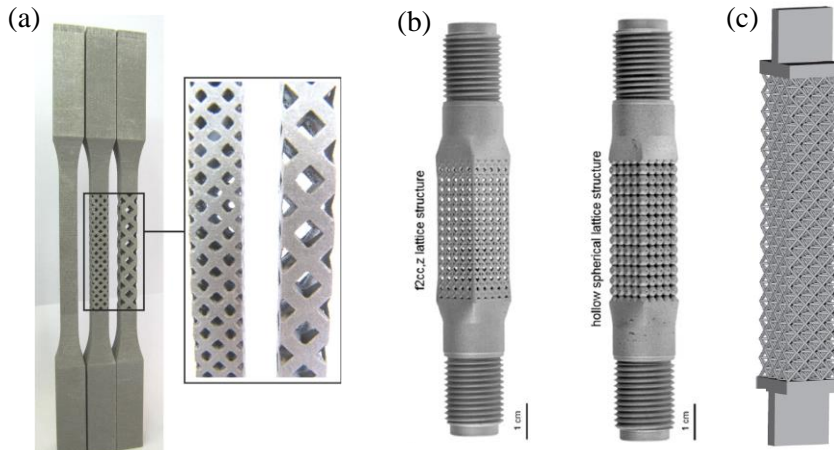


Figure I - 29 Different types of tensile cellular specimens. (a)[140] (b)[141] (c)[142]

Maskery et al. [140] studied the tensile properties of BCC cellular structure based on the cell size. The cellular part was embedded in the gauge length region of the dog-bone shaped tensile specimen as shown in Fig.I-29(a). The results indicated that the strength and stiffness values followed the power law and decrease with increase in the cell size. Köhnen et al. [142] studied the tensile behavior of FCC-Z and hollow-spherical unit cell based cellular material. The tensile specimens had cellular materials attached to a solid transition followed by grips at the end as shown in Fig. I-29(b). The results indicated that FCC-Z cellular material had the highest strength and stiffness and displayed higher % of elongation due to stretching-dominated behavior of FCC-Z unit cell. Ferrigno et al. [141] studied the tensile behavior along with compression behavior for octet based cellular material. The sample is as indicated in Fig. I-29(c). The failure analysis indicated that the failure was along the orthogonal plane with respect to the loading direction.

Along with the static properties obtained from compression and tensile test, understanding of fatigue behavior of cellular materials is important for application in biomedical field.

#### ***1.2.6.2. Effect of cell type and porosity on fatigue properties***

Cellular materials for application in implants undergo cyclic loading during their complete life. Therefore, it is important for characterization of cellular materials under fatigue loading. Many studies have been carried out to understand and improve the fatigue properties of cellular materials.

The fatigue behavior of cellular materials can be divided into three regions: The first stage consists of constant plastic strain accumulation, followed by crack initiation and crack propagation in the struts. The fatigue behavior depends on the plastic strain accumulated and fatigue crack propagation. The final stage is crack coalescence stage, where the fatigue crack propagation drastically and fatigue failure occurs with crack in the macroscopic scale [143, 144]. Representation of three stages of fatigue failure in porous structures is indicated in Fig. I-30 [145]. Literature survey of some of the studies on fatigue behavior is given below.

The fatigue behavior of EB-PBF manufactured cellular materials were studied by Li et al. [146] and Zhao et al. [147]. The studies involved cubic, G7 and rhombic dodecahedron unit cells manufactured using Ti6Al4V alloy. The cubic unit cell had the highest fatigue strength followed by rhombic dodecahedron and G7. The failure in cubic samples as mainly due to buckling of struts and failure was orthogonal to the applied load. But in G7 and rhombic dodecahedron the failure was due to bending and fracture was along a shear plane. Li et al. [146] obtained a relation between the fatigue strength and the relative density from the Gibson-Ashby law for strength [11]. The value of the exponential  $n_2$  in the study was 2.7 which is slightly higher than 1.5 of ideal foams. Zhao et al. [147] indicated that the fatigue

failure was initiated due to surface defects and/or internal defects from EB-PBF process. Liu et al. [144] also studied the fatigue properties of  $\beta$ -type Ti2448 alloy, rhombic dodecahedron cellular material manufactured using EB-PBF. The results were compared with the fatigue properties of Ti6Al4V alloy under same configuration and porosity. The results indicated that, in fatigue, crack initiation depends on surface properties and applied stress while crack propagation depends on material properties and stress levels. It was observed that crack propagation was faster in Ti6Al4V compared to Ti2448 alloy.

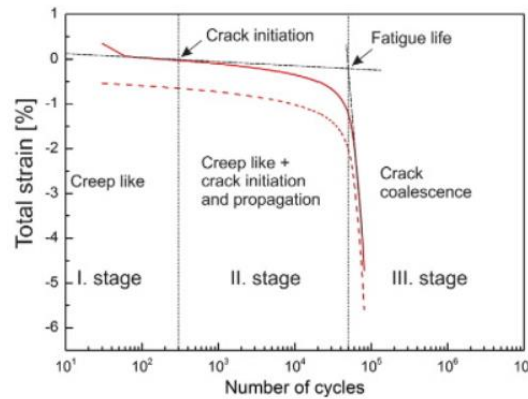


Figure I - 30 Representation of three stages of fatigue failure in porous cellular material[145]

Yavari et al. [148] studied the effect of porosity on fatigue properties on one type of unit cell manufactured using LPBF process. Fatigue test was carried out under a stress ratio of 0.1 and for loads between 0.2-0.8 of yield stress. Samples were assumed to be failed once they lost their initial stiffness by 90%. Absolute and normalized S-N curves were plotted and fitted using the power law. The results indicated that the fatigue strength decreases with increase in porosity and follows the power law. Large deformation is observed at struts with lower thickness or defects from the manufacturing process. Another extensive study was conducted by Yavari et al. [149] which included the study of compression-compression fatigue behavior of cubic, diamond and truncated cuboctahedron cellular materials (Ti6Al4V, LPBF) with four porosity varying from 89-65%. Cubic specimens did not fail and sustained for  $10^6$  cycles even at the highest loads of  $0.8 \times$  yield stress for all the porosities. Tests were stopped once the samples exceeded  $10^6$  cycles since it is considered as endurance limit of materials. Cubic cells develop only compressive stress, while the other two have both compression and tension due to bending in the struts, which is necessary for fatigue failure. Both the studies indicated that if the unit cell type is same, the normalized S-N curves follow a single power law for different porosities. Absolute and normalized S-N curve for truncated cuboctahedron is as shown in Fig. I-31.

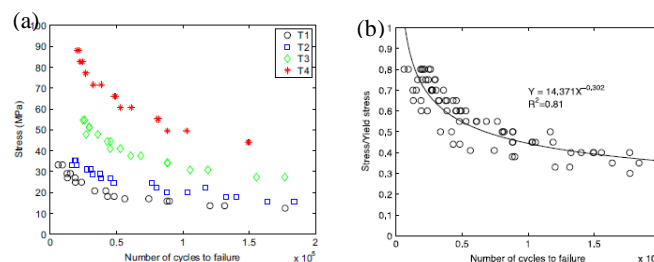


Figure I - 31 (a) Absolute S-N curve with varying porosity (b) Normalized S-N curve for truncated cuboctahedron[149]

Speirs et al. [150] compared the fatigue properties Ni – Ti based cellular materials composed of truss-based octahedron, TPMS based gyroid and sheet gyroid unit cells. The absolute and normalized S-N curves indicated that TPMS based unit cells performed better under fatigue compared to octahedron unit cell. The S-N curve is as shown in Fig. I-32. The better performance of gyroid was attributed to the absence of nodes and reduced geometrical defects from LPBF process.

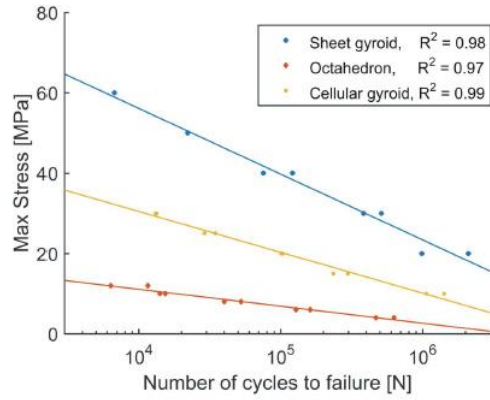


Figure I - 32 S-N curve differentiating struts based and TPMS based cellular material[150]

Liu et al. [151] investigated the fatigue properties of topology optimized and rhombic dodecahedron-based CP -Ti cellular materials manufactured using LPBF. The topology optimized cellular materials displayed better mechanical properties. Further the optimization reduced the stress concentration in the materials and delayed the strut damage, leading to a better fatigue life. Boniotti et al. [152] investigated bending dominated ( $45^\circ$  rotated SC) and stretching dominated (SC-BCC, SC-FCC) under compressive fatigue. High scatter in the fatigue data was observed for SC-BCC and SC-FCC when compared to  $45^\circ$  SC. This scatter was significantly reduced when S-N curve was plotted using real strains. The fracture analysis indicated that surface irregularity has more effect on the fatigue properties, while internal defects and microstructure have a lower effect. A detailed study on the effect of base material on the compression-compression fatigue properties was carried out by Ahmadi et al. [153]. The study compared the fatigue properties of three different unit cell based cellular materials manufactured using CoCr, CP-Ti, tantalum, and Ti6Al4V base material. Fig.I-33 indicates the effect of material on the normalized S-N curve for rhombic dodecahedron cellular materials. A large scatter was observed for CoCr based cellular material; this behavior is due to the post-elastic behavior of CoCr. CoCr bulk material shows strain hardening which increases its fatigue strength. As the porosity in CoCr cellular material increases, the fatigue behavior transitions towards that of the bulk material. Further the effect of material, topology and imperfections has different effect in LCF and HCF regions.

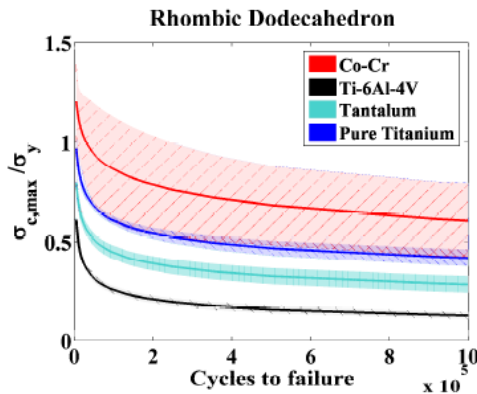


Figure I - 33 Normalized S-N curve indicating the effect of base material on rhombic-dodecahedron cellular material[153]

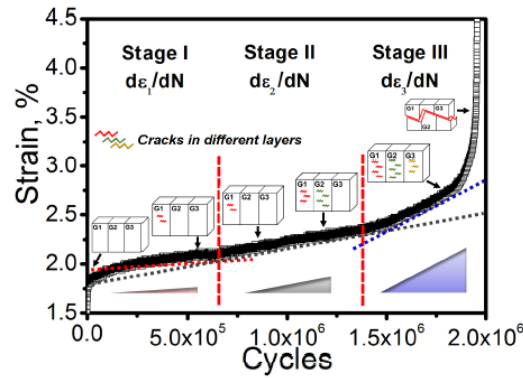


Figure I - 34 Representation of variation in accumulated strain in graded cellular material with number of cycles[154]

The influence of functionally graded porosity on the fatigue behavior was studied by Zhao et al. [154]. Different regions of fatigue failure are as shown in the above Fig. I-34. The FG cellular materials have better fatigue properties due to continuous redistribution of stresses and crack formation in constituent meshes retard the fatigue failure. The study also expressed the fatigue life using an equation which was in close to the experimentally determined values.

Numerical simulations have been used to predict the fatigue failure behavior of cellular materials. Zargarian et al. [98] conducted finite element analysis of diamond, rhombic dodecahedron and truncated cuboctahedron modelled using Timoshenko beam elements. The failure was predicted using a failure event-based algorithm explained in detail in the study. The results were well fitted using power law, a slight difference between the experimental and numerical simulation were seen. This is attributed to the exclusion of strut irregularity and microstructural parameters into the finite element modelling. Peng et al. [155] also carried out FE analysis on SC, BCC, FCC and SC-BCC unit cell based cellular materials. The fatigue life predication using Brown – Miller theory was employed in the study. The normalized S-N curves indicated that BCC and FCC unit cells are sensitive to relative density, while SC and SC – BCC are not influenced by relative density.

Apart from the cell topology and the porosity in cellular materials, other factors such as heat treatments, surface finish and PBF process parameters also effect the mechanical behavior of cellular materials. The next section deals with the effect of above-mentioned parameters on the static and fatigue behavior of cellular materials.

### 1.2.6.3. Effect of process parameters on mechanical properties

The process and the process parameters used to manufacture cellular materials influence their mechanical properties. The relative density, strut thickness, and pore size are not only dependent on cell topology but also on process parameters such as line spacing, layer thickness, power of energy source and scanning strategy. Studies have suggested that printing horizontal struts is difficult when compared to inclined or vertical struts [110]. Leva et al. [156] compared the static behavior of Ti6Al4V cubic cellular materials manufactured using LPBF with the behavior of same geometry manufactured using EB-PBF by Parthasarathy et al. [129]. The comparison indicated that LPBF yielded thinner struts, while EB-PBF yielded thicker struts when compared to designed CAD thickness. As-built LPBF yielded  $\alpha'$  martensitic microstructure while EB-PBF yielded a  $\alpha+\beta$  phase. LPBF yielded better mechanical properties when compared to EB-PBF cellular material. Zhang et al. [157] studied the effect of line spacing on the porosity of LPBF cellular structures, increasing the line spacing increases the porosity thereby decreasing the mechanical strength and stiffness. The line spacing is fixed based on the topology, required pore size and strut thickness. Qiu et al. [77] studied the effect of laser power, scanning speed on LPBF manufactured AlSi10Mg cellular materials. Strut diameter and irregularity increased with increase in the laser power due to the formation of a larger melt pool. Strut thickness was increased at slow rates of scanning, porosity was highest at intermediate speed (4000mm/s) and at

laser power of 200W. Manufacturing at intermediate scan speed and low power leads to larger grains in the microstructure. Sing et al. [117] also concluded that laser power has higher influence on geometrical and mechanical properties of lattice structures compared to scan speed or layer thickness. With respect to the effect of parameters on the fatigue behavior, Ghouse et al. [158] studied porous stochastic cellular materials. The study considered four different materials, three scanning strategies (point, contour, and pulsing). Pulsing strategy was carried out at two power levels (50W and 200W). Optimizing the laser parameter increased the fatigue strength by 7% while contour printing strategy increased the fatigue strength by 8%, when compared to pulsing and points strategy.

#### ***1.2.6.4. Effect of post manufacturing treatments on mechanical properties***

Post-manufacturing treatments such as heat treatment, stress relieving, hot-isostatic pressing (HIP), and surface preparation are used to improve the mechanical properties, either by changing the microstructure or by changing the surface and internal defects [159]. Wauthle et al. [110] studied the effect of stress relieving and HIP on the mechanical properties of diamond cellular material. The former tends to increase the strength but induces brittles, while the later changes the microstructure of Ti6Al4V to  $\alpha+\beta$  phase thereby increasing ductility at the cost of strength. Maskery et al. [160] carried out heat treatment (solution treatment) followed by water quenching and artificial aging on gyroid cellular material. The study concluded that the stress-strain curves obtained were closer to the ideal cellular solid deformation as indicated by Gibson-Ashby model [11]. Heat treatment reduced the collapse strength and the peak stress reached in the cellular material. However, Köhnen et al.[142] concluded that annealing had not positive influence on the tensile and fatigue properties of 316L stainless steel cellular materials.

Studies on the effect of these post-manufacturing treatments on fatigue behavior were also carried out. Hooreweder et al. [161] studied the effect of stress relieving (SR), HIP and chemical etching (CE) on the fatigue strength of Ti6Al4V diamond unit cell based cellular material. The SR and HIP treatment increase the fatigue strength to a considerable extent. However, a combination of HIP and CE significantly increases the fatigue strength. This is because HIP increases the ductility and CE reduces the stress concentration, especially at the nodes. Yuan et al. [162] performed annealing treatment at 750°C, 850°C, and 950°C on Ti6Al4V cellular material manufactured using EB-PBF. The results indicated that at 950°C, the  $\alpha'$  martensitic microstructure was transformed into a more ductile  $\alpha+\beta$  phase. This transformation increased the fatigue endurance ratio to ~0.6 which is similar to bulk material. Similar increase in fatigue endurance ratio was obtained by Wei Wu et al. [163] from HIP treatment carried out 1000°C and 150MPa. du Plessis et al. [164] compared the fatigue properties of gyroid cellular material manufactured at different process parameters and subjected to SR and HIP. The HIP treated samples showed promising results compared to SR samples. HIP treatment reduced the internal porosity and increased ductility which enhanced the fatigue performance.

A comprehensive review on the various aspects related to static and fatigue properties of metallic cellular materials is provided in the following reference [64, 143].

### **1.3. Additive Manufacturing of Metals**

Conversely to the subtractive manufacturing, additive manufacturing (AM) is a process which involves layer-by-layer deposition of material to obtain the final product. AM process can produce complex geometries such a cellular material, which is a difficult task using traditional machining techniques. Initially AM process was used only for rapid prototyping, with the development of technology and improvement in the design process led to using AM process in serial manufacturing. The optimization of component design and the AM process parameters can lead to consumption of less materials and helps reduce wastage. The AM process involves different steps as shown in Fig. I-35. The steps involves (1) Generation of CAD (2) Conversion of CAD to STL format, STL format is used as input for AM machine (3) File manipulation, slicing and positioning of STL file using AM software (4)

Input process parameters such as energy, layer thickness, line spacing, etc. (5) Building of part inside machine (6) Removal of the built part after production (7) Post – processing, cleaning, heat treatment and surface preparation (8) Final part available for usage [107, 165].

According to ASTM the AM techniques involve, binder jetting, direct energy deposition, material extrusion, material jetting, powder bed fusion, sheet lamination and vat photopolymerization. The process selected for the AM of part depends on the material (ceramics, metals, and polymers), available technology and the quantity to be produced [Harun et al]. In AM of metals, powder bed fusion (PBF) and direct energy deposition (DED) are the most used processes. In PBF, a thermal energy source such as laser and electron beam to melt and fuse the powder material based on the CAD input. In DED, the metal/material in the form of powder, filament or wire is melted and directly deposited to form the final product. The current thesis focuses on the PBF AM process. Further information regarding different AM process can be obtained from the following references [166, 167].

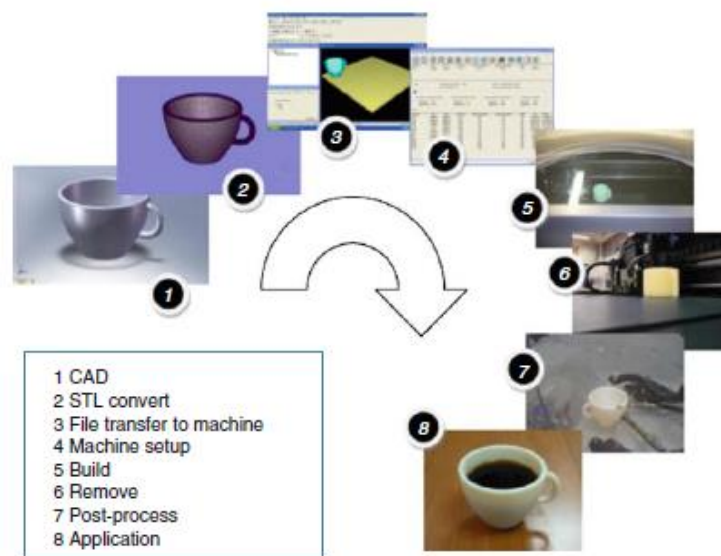


Figure I - 35 Steps involved in AM process : CAD to Part.[165]

Powder bed fusion (PBF) is a process that can be used for a range of materials such as ceramics, polymers, and metals. Extensively used PBF process includes selective laser melting (SLM) or Laser powder bed fusion (LPBF) and Electron beam melting (EBM) or Electron-beam powder bed fusion (EB-PBF). The process involves layer-by-layer addition formation of component using metal powder. As the name suggests, the fusion of metal powder takes place in a powder bed. A beam of thermal energy in the form of laser or electron beam is used to melt the metal powder to form a layer. This solid metal layer is lowered, and a new coating of metal powder is introduced. Now, this new layer of powder is melted, and the process repeats until the complete part is obtained. In production of complex parts, other inclusion such as providing extra support for unsupported locations, for even dissipation of thermal energy, to avoid undesirable deformations must be made. The detailed discussion of EB-PBF and L-PBF is provided in the next section.

### 1.3.1. Electron beam – powder bed fusion (EB – PBF)

EB – PBF process uses stationary electron beam as the source of energy to melt the powder. A schematic representation of EB – PBF process is as shown in Fig.I-36. The system consists of a rake, build platform, powder hoopers, lens, and electron beam gun. The electron beam emitted by the gun is focuses and accelerated to a voltage of 60 kV using electromagnetic lens and directed using magnetic coils [168]. Some essential characteristics of the electron beam requires EB – PBF to be carried out

under high vacuum conditions. The vacuum is used to ensure that the part maintains its integrity [Harun]. The building platform is pre-heated and maintained at elevated temperature to reduce shrinkage stress and distortion upon cooling and to minimize formation of non – equilibrium phases which can lead to formation of cracks [169]. A powder layer of 50 – 200  $\mu\text{m}$  is deposited, a scan speed of  $10^4$  mm/s, current of 30 mA and temperatures  $> 700^\circ\text{C}$  are used for Ti6Al4V powder. The power, focus and scanning speed is dependent on the current, focus offset and the speed of production [107].

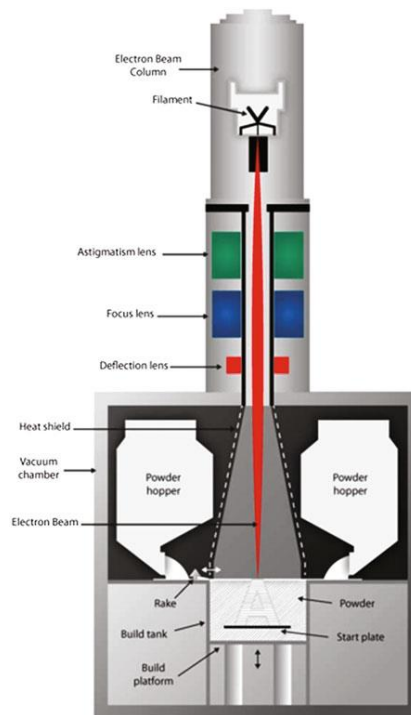


Figure I - 36 Schematic representation of EB-PBF process ([www.arcam.com](http://www.arcam.com))

### 1.3.2. Laser powder bed fusion (LPBF)

Like the EB – PBF process, the part is produced by layer-by-layer melting of powder but used laser beam instead of electron beam. A schematic representation of LPBF process is as shown in Fig.I-37. The laser beam is directed on the powder bed to melt and fuse the powder particles. The input for the melting process is obtained from the sliced CAD part.

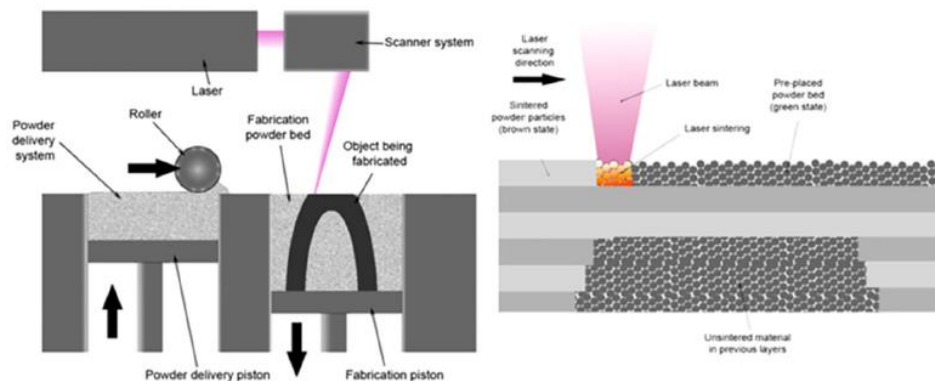


Figure I - 37 Schematic representation of L - PBF process

Once a layer is produced, the powder bed and the metal layer are lowered in steps. A new layer or powdered metal is rolled on to the surface using a roller and powder delivery system as shown in Fig.I-

37 [169]. A powder with a particle size in the range of 20 – 60 μm is used, spherical particles with a narrow distribution in the particle size is desirable to obtain steady flow of molten material [61]. The specific energy  $E_v$  transferred to the powder and responsible for melting the powder and heating the adjacent area is defined as follows:

$$E_v = \frac{P_L}{v_s h_s D_s} \quad \dots \text{Eq.I-4}$$

Where,  $P_L$  is the laser power (20 – 1000W),  $v_s$  is the scanning speed (up to 15m/s) and spot size between 50 – 180 μm,  $D_s$  is the layer thickness (20 – 100 μm), and the distance between adjacent layers of laser path called hatching distance ( $h_s$ ). The thermal gradient between the melted metal and unmelted powder leads to distortion, this is reduced by preheating the building platform. Apart from this support structures are provided to the parts to help in heat dissipation, fixing of part and supporting overhanging surfaces [107]. The presence of oxygen in the chamber can lead to oxidation and formation of impurities in the parts. To prevent the same, the chamber atmosphere for LPBF process is made inert using nitrogen or argon (argon is used for Ti alloys) [57, 61].

### 1.3.3. Comparison of LPBF and EB – PBF

The main difference between LPBF and EB – PBF process is the energy sources used, the former uses a laser source while the latter uses electron beam. The electron beam in EB – PBF process negatively charges the powder particles creating repulsive force between them. Therefore, the particle size cannot be very small, it ranges from 45 – 105 μm. Smaller particles may lead to expulsion of particles from the powder bed. This phenomenon decreased with increase in conductivity of the powder material, hence the EB – PBF process is limited to metals and metallic composites [61, 169]. Since the particle size is on the higher side for EB – PBF when compared to LPBF, the spot size is higher in the former to avoid local charge build-up. This further leads to a large melt pool and decreased geometrical accuracy [165].

Electron beams when passed through an atmosphere, the electrons interact with the atmosphere and deflect, therefore it is essential to maintain vacuum in the chamber. While on the contrary, laser beam is unaffected by the atmosphere but maintain an inert atmosphere reduces the impurities and prevents oxidation of parts. The electron beam heats the surrounding powder to a higher temperature when compared to laser beam, therefore the temperature gradient in EB – PBF is higher when compared to LPBF process. Therefore, the powder beds in E -PBF process are pre-heated and maintained at higher temperature when compared to LPBF process to reduce the temperature gradient in the chamber. The magnetic coils in EB – PBF process moves the beam instantaneously from one point to another. While, in LPBF process to move the laser beam, the mirrors are adjusted by the galvanometers which take more time. This is the reason the production rate is higher in EB -PBF when compared to LPBF process. The microstructure of the material obtained from both the process depend on the process parameters and material [61, 117, 165]. Parts fabricated using both the process are subjected to post processing such as removal of supports, surface cleaning to remove loose particles (ultrasound, sand blasting, shot-peening), heat treatment to change the microstructures, Hot – isostatic pressing to reduce internal porosity [170]. A summary of the difference between E -PBF and L – PBF is tabulated in Table I-4.

Table I - 4 Comparison of process parameters between EB - PBF and LPBF [57, 61, 107, 165]

| Parameters                    | EB - PBF  | LPBF  |
|-------------------------------|---|---|
| <b>Power Source</b>           | Electron beam (3 kW)  | Laser beam (up to 1kW)                                |
| <b>Atmosphere</b>             | High vacuum   | Inert gas (Ar or N <sub>2</sub> )                     |
| <b>Scanning</b>               | Deflection coils  | Galvanometers   |
| <b>Energy absorption</b>      | Conductivity – limited  | Absorptivity – limited                                |
| <b>Powder preheating</b>      | High, using beam (0.8T <sub>m</sub> )   | Low, using heaters (~200°C)                           |
| <b>Scan speeds</b>            | Very fast, magnetically driven (up to 10m/s during pre-heat, 0.1m/s during melting) | Limited by galvanometer inertia (up to 0.8 – 1.2 m/s) |
| <b>Energy costs</b>           | Moderate  | High  |
| <b>Spot size</b>              | -   | 50 – 180 μm   |
| <b>Surface finish</b>         | Moderate to poor  | Excellent to moderate                                 |
| <b>Feature resolution</b>     | Moderate  | Excellent   |
| <b>Materials</b>              | Metals and metallic based composites  | Metals, polymers, ceramics                            |
| <b>Powder particle size</b>   | Medium (45 – 105 μm)  | Fine (20 – 60 μm)                                     |
| <b>Powder layer thickness</b> | 50 μm   | 20-100 μm   |
| <b>Build rate</b>             | Fast  | Slow  |
| <b>Residual stresses</b>      | Low   | High  |

#### 1.3.4. Design for additive manufacturing

Compared to design for manufacturing (DFM), the objective of design for additive manufacturing (DFAM) is to “*maximize product performance through the synthesis of shapes, sizes, hierarchical structures, and material compositions, subject to the capabilities of AM technologies*”. The mentioned objectives can be achieved by taking into consideration the following points [165],

- AM permits the use of complex geometry to obtain the desired design goals.
- AM helps in production of customized parts by taking direct inputs form 3D CAD data.
- AM process can help in consolidating many parts and reduce the assembly process.
- AM process further provides new level of freedom from the constraints imposed from traditional manufacturing process.

Besides the above-mentioned advantages from AM process, there are certain constraints that are specific to the AM process considered for manufacturing. Since AM process is a layer wise deposition of material, the geometrical properties such as thickness, resolution, surface finish are highly affected by the layer thickness. Some AM systems can build materials with a layer thickness of 20 μm, this leads to a better geometrical accuracy but other factors such as production time, particle size must be considered during the production process. The features along the building direction are generated with a better geometrical accuracy when compared to angled features due to staircase effect. In case of AM process based on powder bed fusion, additional powder is attached to the parts due to the sintering process. Furthermore, the shrinkage in the parts due to melting – solidification process is dependent on the powder bed and must be considered for DFAM. Another major design aspect to be considered for AM process is support structure designs. Addition of support structure to a component not only increases the material used and time but also requires post processing to remove the supports. As mentioned before, support structures not only act as support for unsupported, horizontal, and overhanging parts but also reduce distortion due shrinkage and reduce the thermal gradient. DFAM

should also consider the orientation of printing, this may reduce the support structures required but might introduce other complexities [168, 171].

#### **1.3.4.1. Design for additive manufacturing : cellular structures**

As mentioned before, designed cellular structure/materials is instigated by the desire to apply them for certain applications. They offer high strength to weight ratio and can be designed to sustain loads along a particular direction. These cellular materials are characterized by their relative density, which depends on the cell wall thickness or strut thickness. The morphological properties of cellular materials manufactured using AM process are determined by the process parameters such as laser power, layer thickness, scan speed and on the orientation of the strut with respect to the building direction. The difference between the as-designed and as-built strut thickness is influenced by all the above-mentioned parameters. Since struts are oriented in different direction in cellular materials, optimizing the process parameters does not eliminate the difference between the as-designed and the as-built strut thickness. Conversely, studies have indicated that the difference between the as-designed and the as-built strut thickness follows a linear relation, which makes it possible to adjust the thickness accordingly [112, 120, 172]. Two different methods have been proposed by various studies, (i) chemical etching to reduce the thickness (*post processing*) [112, 114, 115] (ii) adjust the input CAD to obtain a desired output (*pre-processing*) [121]. In the second process, the difference between the as-designed and as-built strut thickness is compensated in the input CAD model. This process does not involve any post processing. However, an initial batch of specimens have to be produced to obtain the thickness difference after manufacturing. This difference is used to obtain a correlation between the as-designed and as-built struts. The input for the consecutive batches of specimens is the *compensated CAD model*. This method helps in better prediction of mechanical properties using FE analysis [126]. The compensation approach can be further used to optimize the model and design fully porous biomedical implants [56, 173]. This approach uses techniques such as X-ray microtomography ( $\mu$ CT) to provide accurate metrological measurements and to evaluate strut defects [94]. The data are imported to into FE and CAD software to evaluate their mechanical properties and compare the same with the desired or experimentally determined mechanical properties to study the effect of defects [126].

### **1.4. Titanium and its alloy for biomedical applications**

#### **1.4.1. Titanium vs other metal alloys**

Titanium and its alloys have been extensively used in biomedical field when compared to other metal alloys (CoCr, steel). From the available range of titanium and its alloys, Ti6Al4V is the most extensively used. Properties such as biocompatibility, corrosion resistance, bio-adhesion, excellent mechanical properties-to-weight ratio and low modulus are desirable from metals alloys, all of which are satisfied by titanium. One of the disadvantages of titanium when compared to CoCr is their low wear resistance. [174, 175]. A comparison of the mechanical properties of commonly used biomaterials is tabulated in Table I-5.

Pure titanium has displayed better biocompatibility and is used in stents and wires, but their low mechanical strength is below the required value for hard tissue or load bearing applications. Therefore, Ti6Al4V is used for load bearing implants despite the possibility of cytotoxicity from Vanadium. Finally, the formation of a stable  $\text{TiO}_2$  oxide layer aid in obtaining high biocompatibility of titanium alloy [175]. Some of the characteristics, advantages and disadvantages of different biomedical metal alloys are as shown in Table I-6.

Table I - 5 Mechanical properties of most common biomedical metal alloys [12, 176]

| Metal                    | $\rho$<br>(g/cc) | E<br>(GPa) | Y.S<br>(MPa) | Y.S / $\rho$ | Fatigue<br>strength<br>(MPa) | %<br>El |
|--------------------------|------------------|------------|--------------|--------------|------------------------------|---------|
| 316L SS                  | 7.9              | 210        | 450          | 57           | 250                          | 40      |
| CoCr<br>(as cast)        | 8.3              | 200        | 500          | 60           | 300                          | 8       |
| CoNiCrMo<br>(as wrought) | 9.2              | 220        | 850          | 92           | 500                          | 20      |
| Ti6Al4V                  | 4.5              | 105        | 900          | 200          | 500                          | 13      |
| Cp – Ti                  | 4.5              | 100        | 300          | 67           | 200                          | 40      |

Table I - 6 Characteristics of most common biomedical metal alloys[175]

|  | Stainless Steels                               | Cobalt based<br>alloys   | Ti and Ti based<br>Alloys  |
|--|--|--|--|
| <b>Designation</b>                       | ASTM F-138                                     | ASTM F-75<br>ASTM F-799<br>ASTM F-1537<br>(Cast and wrought)     | ASTM F-67<br>ASTM F-136<br>ASTM F-1295<br>(Cast and wrought)     |
| <b>Principal alloying elements (wt%)</b> | Fe (bal.)<br>Cr(17-20)<br>Ni(12-14)<br>Mo(2-4) | Co(bal.)<br>Cr(19-30)<br>Mo(0-10)<br>Ni(0-37)                    | Ti(bal.)<br>Al(6)<br>V(4)<br>Nb(7)                               |
| <b>Advantages</b>                        | Cost<br>Availability<br>Processing             | Wear resistance<br>Corrosion resistance<br>Fatigue strength      | Biocompatibility<br>Corrosion<br>Low modulus<br>Fatigue strength |
| <b>Disadvantages</b>                     | Long term behavior<br>High modulus             | High modulus<br>Biocompatibility                                 | Low shear strength<br>Power wear resistance                      |
| <b>Primary utilization</b>               | Temporary devices (plates, screws, nails)      | Dentistry castings<br>Prostheses stem<br>Load-bearing components | Used in THRs<br>Long-term implants<br>Permanent devices          |

### 1.4.2. Metallurgy

The metallurgical properties of most used titanium alloy (Ti6Al4V) are discussed in this section. There are two variation of Ti6Al4V alloy ( $T_m = 1650^\circ\text{C}$ ): the standard grade 5 and the Extra Low Interstitial (ELI), also known as Grade 23. The composition of Grade % Ti6Al4V is as shown in Table I- 7. The only difference between the above-mentioned grades is the maximum allowable %wt of oxygen, it is 0.2%wt for grade 5 while it is 0.13% for grade 23. The decrease in oxygen content increases the fracture toughness and ductility of titanium alloy [177].

Table I - 7 Composition of Ti6Al4V (Grade 5) alloy in %wt [27]

| Alloy | Al        | V         | N     | C     | H       | Fe    | O    | Others |     |
|-------|-----------|-----------|-------|-------|---------|-------|------|--------|-----|
|       |           |           |       |       |         |       |      | Single | Sum |
| %wt   | 5.50-6.50 | 3.50-4.50 | <0.05 | <0.08 | <0.0125 | <0.25 | <0.2 | 0.1    | 0.4 |

Like other metals, titanium also has various crystal structures. Pure titanium and its alloys crystallize at low temperatures are generally in a hexagonal close packed (HCP) structure, mentioned as  $\alpha$  – titanium. However, at high temperatures, the titanium acquires a more stable body-centered cubic (BCC) structure called as  $\beta$  – titanium. The transformation temperature is  $882\pm 2^\circ\text{C}$  for titanium and is referred as  $\beta$  – transus temperature [178]. Depending on the phase present in titanium alloys, they can be classified into  $\alpha$ , near  $\alpha$ ,  $\alpha+\beta$ , metastable  $\beta$ . To stabilize the mentioned phases, various alloying elements are added. Elements such as Al, O, N, C are used as  $\alpha$  – stabilizers, they help by increasing the transformation temperature required to obtain  $\beta$  – phase. They next category of elements are Cr, Co, V, Fe, Nb, which stabilize the  $\beta$  – phase by lowering the transformation temperature. The last category of elements are those that do not affect the transformation but help in strengthening the room temperature phase, Sn and Zr are some of the neutral stabilizers.  $\beta$  titanium alloys are a composition that produces 100%  $\beta$  when quenched from above transformation temperature, however aging of metastable  $\beta$  alloys can lead to the formation of  $\alpha+\beta$ . On the contrary, quenching (fast cooling) of  $\alpha+\beta$  alloys leads to the formation of a metastable martensitic  $\alpha'$  phase. A phase transformation diagram of Ti6Al [178] alloy with variable V content is as shown in Fig.I-38.

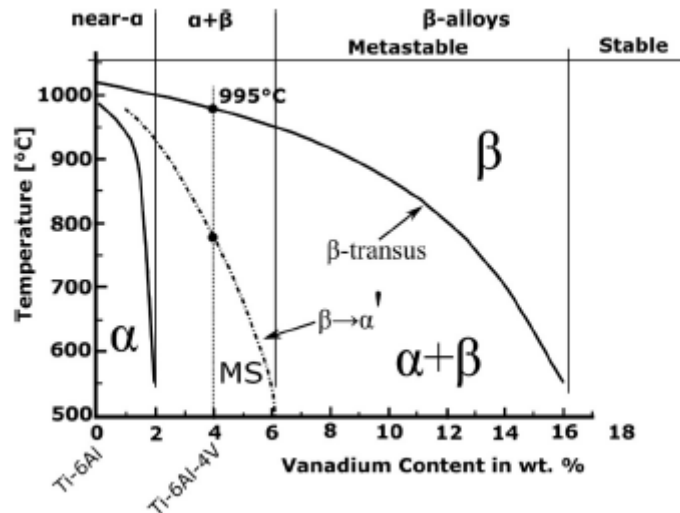


Figure I - 38 Phase transformation of titanium alloy with variation in % of V [178]

Fig.I-38 indicates that Ti6Al4V is a  $\alpha+\beta$  alloy. The mechanical properties and corrosion resistance of Ti6Al4V are well balanced between the single phases of  $\alpha$  and  $\beta$ . The effect of different phases on the properties of titanium alloys is as shown in Table I-8. However, the mechanical properties of titanium alloys are highly dependent on their thermal and mechanical properties [12, 175].

Table I - 8 Variation of properties in  $\alpha$ ,  $\alpha+\beta$  and  $\beta$  Ti alloys [178]

|                           | $\alpha$ | $\alpha+\beta$ | $\beta$ |
|---------------------------|----------|----------------|---------|
| <b>Density</b>            | +        | +              | -       |
| <b>Strength</b>           | -        | +              | ++      |
| <b>Ductility</b>          | -/+      | +              | +/-     |
| <b>Fracture toughness</b> | +        | -/+            | +/-     |
| <b>Creep strength</b>     | +        | +/-            | -       |
| <b>Corrosion behavior</b> | ++       | +              | +/-     |
| <b>Oxidation behavior</b> | ++       | +/-            | -       |
| <b>Weldability</b>        | +        | +/-            | -       |
| <b>Cold formability</b>   | --       | -              | -/+     |

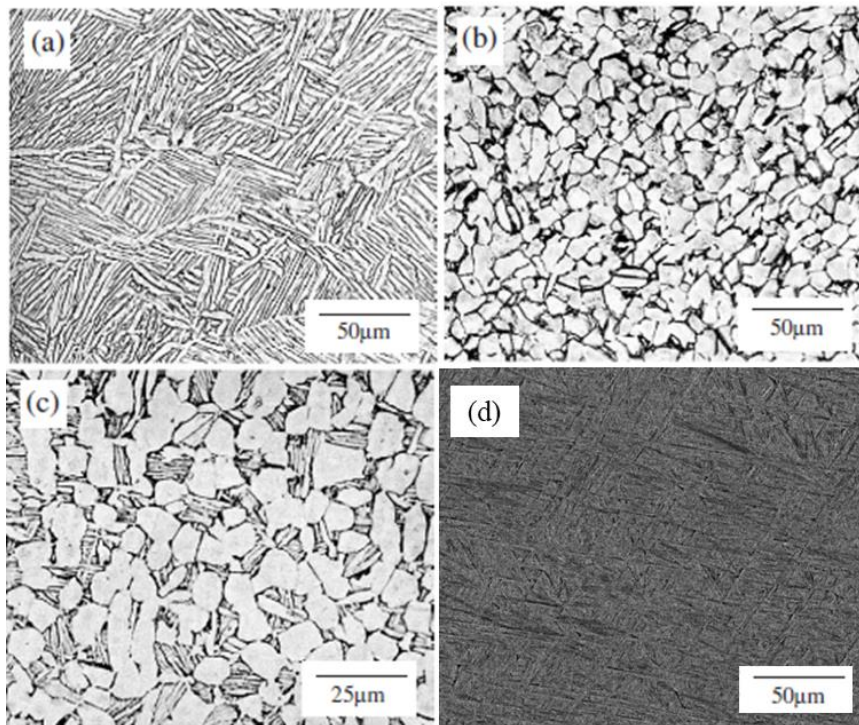


Figure I - 39 (a - c) microstructure of  $\alpha+\beta$  phase titanium alloy [179] (d) microstructure in  $\alpha'$  martensitic phase[180]

As mentioned before, the properties of titanium alloys are dependent on their microstructure and the arrangement of  $\alpha$  and  $\beta$  phases in the microstructure. The microstructure depends on the thermal or thermo-mechanical processes that alter the microstructure. In titanium alloys, these processes involve deformation, heat treatment and ageing.

There are two broad types of microstructure observed in titanium alloys: lamellar and equiaxed. The grain size can be fine or coarse depending on the initial microstructures and the thermo-mechanical treatment employed. For any composition, the parameter that influences the phase transformation is the  $\beta$  – transus temperature (995°C for standard grade 5 Ti6Al4V and 975°C for ELI Ti6Al4V). Pure lamellar microstructure is as shown in Fig. I-39(a), it is obtained by carrying out a solution treatment

above  $\beta$  – transus temperature, followed by slow cooling and aging between 700-800 °C. A faster cooling can lead to finer lamellae, quenching provides a  $\alpha'$  martensitic lamellae as shown in Fig. I-39(d). The equiaxed microstructure shown in Fig.I-39(b) is obtained by performing solution annealing below  $\beta$  – transus temperature, between 800 and 925 °C. Another microstructure is bimodal and is as shown in Fig. I-39(c). This is developed by solution treatment below  $\beta$  – transus (900 - 950°C) followed by aging below 700°C. It consists of equiaxed  $\alpha$  grains in a  $\alpha+\beta$  lamellar matrix [174, 179].

The microstructure influences mechanical properties such as strength, stiffness, and oxidation behavior. Table I-9 indicates the influence of microstructure on various mechanical properties. It indicates that equiaxed microstructure improve strength, ductility, while lamellar microstructure improves fracture toughness, creep strength and oxidation behavior. However, bimodal microstructure is a balance between the advantages of equiaxed and lamellar microstructure. Also, bimodal microstructure has the highest high cycle fatigue (HCF) resistance while lamellar has the lowest HCF resistance [178, 179]. Apart from the microstructure, grain size also has an influence on the mechanical properties. Finer microstructure improves strength, ductility and detains fatigue crack initiation. On the contrary, coarse microstructure improves fracture toughness, creep strength and retards fatigue crack propagation [178]. A detailed explanation on the microstructure of  $\alpha+\beta$  titanium alloys in provided in chapter 5 in the reference [174].

Table I - 9 Influence of microstructure on properties of Ti alloys [178]

| <b>Fine</b> | <b>Coarse</b> | <b>Property</b>                  | <b>Lamellar</b> | <b>Equiaxed</b> |
|-------------|---------------|----------------------------------|-----------------|-----------------|
| O           | O             | <b>Elastic modulus</b>           | O               | +/-             |
| +           | -             | <b>Strength</b>                  | -               | +               |
| +           | -             | <b>Ductility</b>                 | -               | +               |
| -           | +             | <b>Fracture toughness</b>        | +               | -               |
| +           | -             | <b>Fatigue crack initiation</b>  | -               | +               |
| -           | +             | <b>Fatigue crack propagation</b> | +               | -               |
| -           | +             | <b>Creep strength</b>            | +               | -               |
| +           | -             | <b>Super elasticity</b>          | -               | +               |
| +           | -             | <b>Oxidation behavior</b>        | +               | -               |

### 1.4.3. Mechanical properties of Ti6Al4V

Previous section discussed the effect of microstructure and grain size on the mechanical properties of Ti6Al4V. However, the effect was indicated in a qualitative manner. The mechanical properties depend not only on the microstructure but also on the thermo-mechanical treatment employed. Therefore, it is not possible to obtain the exact numerical values for the mechanical properties. Table I-10 provides the representative values of the mechanical properties. The values indicate that equiaxed microstructure provides higher ductility and strength, while lamellar microstructure has higher toughness. As discussed before, bimodal has properties between lamellar and equiaxed microstructure. The table also indicated values of  $\alpha'$  martensitic microstructure. They possess the highest strength

compared to others and have a high hardness value. However, they have the lowest ductility in comparison to other microstructures. Also, the Young's modulus of titanium is least affected by the microstructure.

Table I - 10 Mechanical Properties of Ti6Al4V alloy for various microstructures (Note: d, is for mill annealed condition which is similar to equiaxed microstructure)

|  | <b>E</b><br>(GPa)        | <b>YS</b><br>(MPa)                             | <b>UTS</b><br>(MPa)                            | <b>%El</b>                                  | <b>Hardness</b>    | <b>KIC</b><br>(MPa√m)                   |
|--|--------------------------|--|--|---|--------------------|---|
| <b>Ti6Al4V ELI</b><br><b>(Equiaxed)</b>            | 101-<br>109 <sup>d</sup> | 830 <sup>b</sup> ;<br>795-<br>875 <sup>d</sup> | 903 <sup>b</sup> ;<br>860-<br>965 <sup>d</sup> | 17 <sup>b</sup> ;<br>10-<br>15 <sup>d</sup> | -                  | 91 <sup>b</sup>                         |
| <b>Ti6Al4V ELI</b><br><b>(SLM, α' martensitic)</b> | 113 <sup>c</sup>         | 1015 <sup>c</sup>                              | 1090 <sup>c</sup>                              | 10 <sup>c</sup>                             | 380HV <sup>c</sup> | -                                       |
| <b>Ti6Al4V</b><br><b>(Equiaxed)</b>                | -                        | 910 <sup>a</sup> ;<br>951 <sup>b</sup>         | 1020 <sup>b</sup>                              | 15 <sup>b</sup>                             | -                  | 44-66 <sup>a</sup> ;<br>61 <sup>b</sup> |
| <b>Ti6Al4V</b><br><b>(Bimodal)</b>                 | -                        | 875 <sup>a</sup>                               | -  | -   | -                  | 88-110 <sup>a</sup>                     |
| <b>Ti6Al4V</b><br><b>(Lamellar)</b>                | 110-<br>114 <sup>d</sup> | 884 <sup>d</sup>                               | 949 <sup>b</sup>                               | 13 <sup>b</sup>                             | -                  | 78 <sup>b</sup>                         |

<sup>a</sup>[181];<sup>b</sup>[179];<sup>c</sup>[182];<sup>d</sup>[177]

Similar to other mechanical properties, fatigue performance of Ti6Al4V alloys is related to the microstructure, the grain size (width of lamellae), prior thermo-mechanical treatments and the oxygen content. Apart from the metallurgical properties, surface finish also plays a major since Ti6Al4V has a high notch sensitivity [175, 183].

The effect of different microstructures on the fatigue behavior is clearly represented in the S-N curve shown in Fig. I-40. Studies on high cycle fatigue behavior have shown that decreasing the lamellar size from 10 to 0.5μm increases the fatigue strength from 480 – 675 MPa. Likewise, decreasing the grain size from 12 to 2μm in equiaxed structures, increases the fatigue strength from 560 -720 MPa. For bimodal microstructures, decreasing the lamellae width from 1 to 0.5μm increases the fatigue strength from 480 – 575 MPa [183]. The above increase in the fatigue strength is attributed to the fact that finer microstructure retards the crack initiation and has lower short crack propagation rate. However, having coarse grains help in decelerating the crack propagation rates. From the Fig. I-40 it can be observed that under HCF, bimodal has the best performance followed by fine equiaxed and fine lamellar.

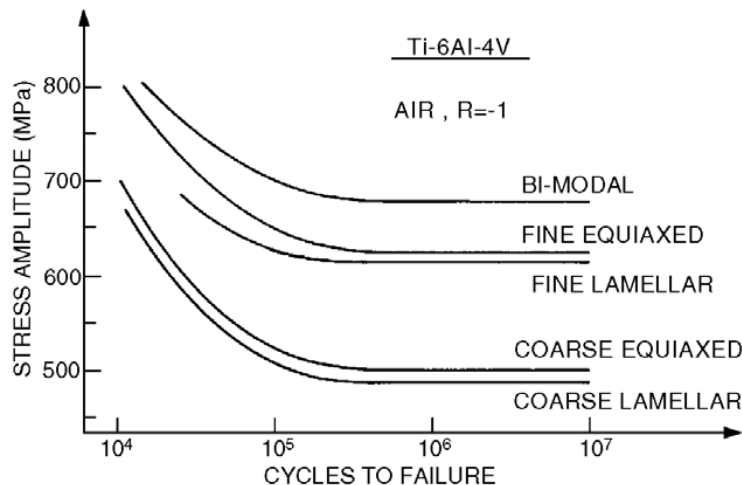


Figure I - 40 S-N curve for different Ti6Al4V microstructure under fully reversed condition [179]

Table I - 11 Rotating bending fatigue strength (R = -1) of Ti6Al4V - Equiaxed[184]

| Surface condition                      | Fatigue strength [MPa] |
|--|------------------------|
| Electrically polished                  | 610                    |
| Shot peened                            | 710                    |
| Shot peened + 1h 500°C                 | 390                    |
| Shot peened + 1h 500 °C + 20µm removed | 800                    |
| Shot peened + 20µm removed             | 820                    |

As the fatigue properties depend on the surface roughness, surface treatments are used to enhance the fatigue performance on titanium alloys. Due to the high notch sensitivity of titanium, roughness is a critical parameter when considering their fatigue life. Consequently, use of porous coatings on implants, and use of rough surface to provide better osseointegration may affect the fatigue life of the titanium implant and hence they must be considered during the design phase. Fatigue resistance of titanium alloys can be enhanced by using polished surfaces, inducing compressive state of stress, and cold working the surface.

One such cold working process is shot peening. This process involves bombarding the surface of titanium with small hard beads to induce compressive residual stresses. The process parameters should be carefully controlled since it increases the surface roughness. Shot peening followed by stress relieving process decreases the fatigue strength as shown in Table I-11. However, polishing after shot peening or after shot peening and stress relieving further enhances the fatigue strength [175, 183].

#### 1.4.4. Corrosion behavior of titanium

Under normal circumstances in a human body, the body fluid is a NaCl solution (0.9%) with a pH level of 7.4. This pH level increases to maximum of 7.8 and drops to 5.5 during a surgery. The presence of salt-based fluid initiates corrosion in case of implants. Therefore, corrosion resistance becomes a desirable property for metals used in implants. Breakdown potential and repassivation time in Hank's solution for various metals used in biomedical application is as shown in Table I-12. Comparing the values, of breakdown potential, cp-Ti and Ti6Al4V have the highest values of 2.4 and 2.0 V compared to steel and CoCr. High values of breakdown potential indicate that the metals do not undergo passivity breakdown. Another parameter listed in Table I-12 is the repassivation time. This indicates the time taken by the metal to regenerate the passive oxide layer to prevent corrosion. The values indicate that the repassivation time is lowest for cp-Ti followed by Ti6Al4V, revealing that the oxide layer regenerates quickly in titanium and its alloys [176]. The oxide layer formed by Ti6Al4V consists of TiO<sub>2</sub> and small traces of Al<sub>2</sub>O<sub>3</sub> [175].

Table I - 12 Breakdown potential (Hank's solution) and repassivation times (in 0.9% NaCl solution with pH=7.4) for most common biomedical alloys[176]

| Material                      | Breakdown potential (V) | Repassivation time ( $10^{-3}$ s) |        |            |        |
|-------------------------------|-------------------------|-----------------------------------|--------|------------|--------|
|                               |                         | $t_e$                             |        | $t_{0.05}$ |        |
|                               |                         | -0.5 V                            | +0.5 V | -0.5 V     | +0.5 V |
| <b>316L</b>                   | 0.2-0.3                 | > 72000                           | 35     | >> 7200    | > 6000 |
| <b>CoCr</b><br>(as cast)      | +0.42                   | 44.4                              | 36     | >> 6000    | > 6000 |
| <b>CoNiCr</b><br>(as wrought) | +0.42                   | 35.5                              | 41     | > 6000     | 5300   |
| <b>Ti6Al4V</b>                | +2.0                    | 37                                | 41     | 43.4       | 45.8   |
| <b>cp -Ti</b>                 | +2.4                    | 43                                | 44.4   | 47.4       | 49     |
| <b>cp – Ta</b>                | +2.25                   | 41                                | 40     | 43         | 45     |
| <b>cp – Nb</b>                | +2.5                    | 47.6                              | 43.1   | 47         | 85     |

The main reason for the rapid oxidation of titanium is its affinity to oxygen (higher than titanium and nitrogen). Oxygen has a high solubility of 14.5% in titanium which results in rapid oxidation and formation of a continuous oxide layer. The oxygen rich layer is called as  $\alpha$  – case as it consists of a stabilized  $\alpha$  phase. The  $\alpha$  – case reduces the ductility of bulk titanium alloy, induce surface cracks under tensile loading, and reduce fatigue strength by initiating early crack nucleation. Since maximum oxygen solubility is obtained at 550°C, use of titanium alloys in high temperature conditions is limited [174].

#### 1.4.5. Biocompatibility

As mentioned in the previous sections, titanium and its alloys have good biocompatibility. The formation of a stable oxide layer helps in preventing corrosion and the following inflammatory response of body that leads to implant loosening [185]. It was observed that a good amount of bone growth was observed on the interface between bone and the titanium interface, which also increase the shear strength of the interface. Also, for Ti alloys, osseointegration is achieved without the aid on any bioactive coating. However, bioactive coatings have further increased the performance on titanium alloy implants [176]. A general representation of interaction between titanium implant and body fluid is shown in Fig. I-41.

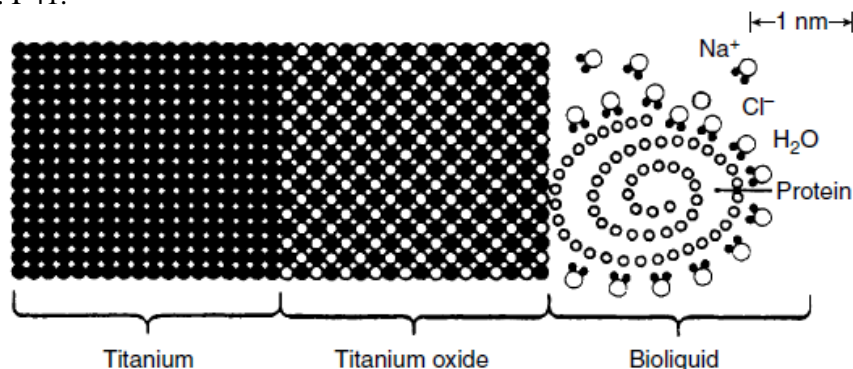


Figure I - 41 Schematic representation of interaction between titanium implant and body fluid[185]

Other parameters such as microstructure and surface roughness also influence osseointegration, formation of osteoblasts and the pull-out strength [179]. Studies have indicated that increasing the average roughness from 0.5 to 5.9  $\mu\text{m}$  increases the interfacial strength from 0.48 to 3.5MPa. Also increasing the surface roughness provides better osseointegration due to an increased contact surface [176, 185].

### 1.4.6. Additive manufacturing of Ti6Al4V: Laser powder bed fusion

As mentioned before Ti6Al4V manufactured using different AM process have different metallurgical and mechanical properties. In this section a brief discussion on the effect of AM process (LPBF) on the Ti6Al4V alloy is presented. Various studies have discussed in detail the effect of (EB-PBF) process in the following references [61, 107, 167, 170]. As discussed before, PBF process involves rapid cooling, directional melting of material and repeated thermal cycles which impact the material properties. Apart from these, process parameters such as laser powers, line spacing and particle size influence the mechanical properties and defects introduced during the process.

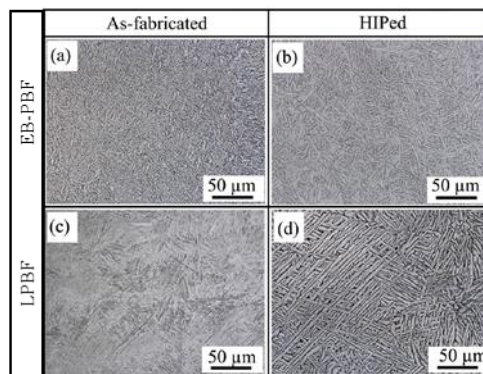


Figure I - 42 Microstructure of Ti6Al4V alloy (a) As-built EB-PBF (b) HIPed EB-PBF (C) As-built LPBF and (d) HIPed LPBF process [186]

In microstructure of LPBF Ti6Al4V is characterized by the rapid cooling rates and the directional heat flow which influence the formation of metastable phases and orientation of grains [167]. The cooling rates in LPBF and EB-PBF process is dependent in the pre-heating of the powder bed, which is 200°C for LPBF and 700 °C for EB-PBF process of Ti6Al4V. Therefore, the cooling rates are on the higher side in LPBF process. As a result, the as-built microstructure from LPBF process is a fine  $\alpha'$  acicular martensitic phase as shown in Fig.I-42(c), while microstructure from EB-PBF consists of coarse  $\beta$  grain transformed to lamellar  $\alpha$  yielding a fine  $\alpha + \beta$  lamellar as shown in Fig.I-42(b) [107, 186, 187]. In LPBF process, during scanning  $\beta$  – columnar grains are generated and aligned along the building direction, due to the cooling during the manufacturing process, these  $\beta$  grains are converted into  $\alpha'$  martensitic phase. The grain size obtained exceeds the layer thickness significantly, but the width of the grain was proportional to the width of the scan track. A finer grain size reflects faster cooling rates. Also, studies have concluded that the grain size is not affected by the part size in LPBF, but grain size decreases with decrease in part size for EB-PBF process [107, 186]. The properties improved from the as-built microstructure are strength and hardness but have low ductility. This makes in unsuitable for load bearing biomedical applications. Therefore, post manufacturing treatments are employed to relieve stresses and increase the ductility. Heat treatments are carried out between 700 -1000°C, solution treatment at 1000°C transforms the martensitic microstructure into  $\alpha + \beta$  phase enhancing the ductility and fatigue performance [107, 188].

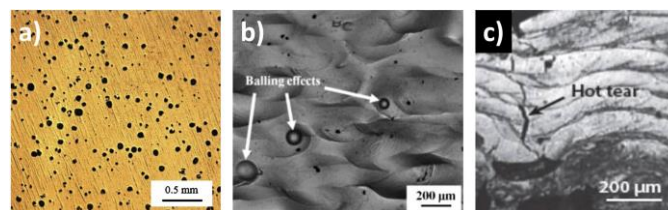


Figure I - 43 Defects from AM process (a) Internal porosity (b) Entrapped unmelted powder particles (c) formation of internal cracks [188]

As discussed, the LPBF process parameters influence the microstructure which further affect the mechanical properties, but defects arising from the process also influence the mechanical properties.

One of the advantages of PBF process is its ability to produce parts with a density greater than 99.5%. However, defects such as spherical pores (from trapped gases), unmelted powder, cracks as shown in Fig. I-43 are observed and are dependent on the volume energy of the process, line spacing and particle size [110, 189]. These defects decrease the mechanical properties and act as stress concentrators.

Due to the presence of  $\alpha'$  martensite in as-built structures, they have higher strength values when compared to wrought/ cast titanium but have very low ductility as indicated in the following reference [190]. As introduced in the previous paragraph, heat treatments can be used to enhance the properties of as-built LPBF parts. Process such as HIP (Hot Isostatic Pressing) can be used to reduce the internal pores and change the microstructure. The effect of HIP on the microstructure is as shown in Fig. I-42(b) and Fig. I-42(d) for EB-PBF and LPBF process respectively. In LPBF process, HIP transforms the microstructure from martensitic to  $\alpha+\beta$  phase, while from EB-PBF process, HIP increases the grain size of lamellae. Fatigue properties are also influenced by the pores and the surface roughness of the part. Presence of pores closer to the surface act as crack initiation sites and as-built LPBF parts have better surface finish but are susceptible to internal pores and lower ductility. On the contrary EB-PBF parts are more ductile, have rough surface and less internal porosity. Therefore, the fatigue life of LPBF parts is lower when compared to EB-PBF and cast or wrought Ti6Al4V alloys [107, 186]. A details study on the effect LPBF and E-PBF process on mechanical properties and their comparison with cast or wrought counter parts are provided in the following references [170, 186, 188, 190, 191].

## 1.5. References

1. Khurana JS (2009) Bone Pathology. Humana Press, Totowa, NJ
2. Wang X, Xu S, Zhou S, et al (2016) Topological design and additive manufacturing of porous metals for bone scaffolds and orthopaedic implants: A review. *Biomaterials* 83:127–141. <https://doi.org/10.1016/j.biomaterials.2016.01.012>
3. Wang X, Nyman JS, Dong X, et al (2010) *Fundamental Biomechanics in Bone Tissue Engineering*
4. Hing KA (2004) Bone repair in the twenty-first century: biology, chemistry or engineering. *Philos Trans R Soc London Ser A Math Phys Eng Sci* 362:2821–2850. <https://doi.org/10.1098/rsta.2004.1466>
5. Wegst UGK, Bai H, Saiz E, et al (2015) Bioinspired structural materials. *Nat Mater* 14:23–36. <https://doi.org/10.1038/nmat4089>
6. Syahrom A, Al-Fatihhi M, Szali M, et al (2018) Cancellous Bone - Mechanical Characterization and Finite Element Simulation
7. Cowin, S, Telega, J (2003) *Bone Mechanics Handbook*, 2nd Edition. -
8. Tortora, G.J. and Derrickson BH (2010) *Principles of Anatomy and Physiology*, 13th Edition
9. Morgan EF, Unnikrisnan GU, Hussein AI (2018) Bone Mechanical Properties in Healthy and Diseased States. *Annu Rev Biomed Eng* 20:119–143. <https://doi.org/10.1146/annurev-bioeng-062117-121139>
10. Wu S, Liu X, Yeung KWK, et al (2014) Biomimetic porous scaffolds for bone tissue engineering. *Mater Sci Eng R Reports* 80:1–36. <https://doi.org/10.1016/j.mser.2014.04.001>
11. Gibson LJ, Ashby MF (1997) *Cellular Solids*. Cambridge University Press
12. Park J, Lakes RS (2007) *Biomaterials: An introduction*, 3rd ed. Springer New York, New York, NY
13. Gibson LJ, Harley BA, Ashby MF (2010) *Cellular materials in nature and medicine*. Cambridge University Press
14. Williams DF (2008) On the mechanisms of biocompatibility. *Biomaterials* 29:2941–2953. <https://doi.org/10.1016/j.biomaterials.2008.04.023>

15. Zhao P, Gu H, Mi H, et al (2018) Fabrication of scaffolds in tissue engineering: A review. *Front Mech Eng* 13:107–119. <https://doi.org/10.1007/s11465-018-0496-8>
16. Williams DF (2009) On the nature of biomaterials. *Biomaterials* 30:5897–5909. <https://doi.org/10.1016/j.biomaterials.2009.07.027>
17. Williams DF (2016) General concepts of biocompatibility. In: *Handbook of Biomaterial Properties, Second Edition*
18. Teo AJT, Mishra A, Park I, et al (2016) Polymeric Biomaterials for Medical Implants and Devices. *ACS Biomater Sci Eng* 2:454–472. <https://doi.org/10.1021/acsbiomaterials.5b00429>
19. Vert M (2007) Polymeric biomaterials: Strategies of the past vs. strategies of the future. *Prog Polym Sci* 32:755–761. <https://doi.org/10.1016/j.progpolymsci.2007.05.006>
20. Ambrose CG, Hartline BE, Clanton TO, et al (2015) *Advanced Polymers in Medicine*. *Adv Polym Med*. <https://doi.org/10.1007/978-3-319-12478-0>
21. Patrick J. Prendergast, Der MCH van, Meulen Mechanics of bone regeneration. In: *Bone Mechanics Handbook, 2nd Edition*. CRC Press
22. L.L. Hench and T. Kokubo (2016) Properties of bioactive glasses and glass-ceramics. In: *Handbook of Biomaterial Properties, Second Edition, 2nd ed*. Springer-Verlag New York, pp 355–363
23. J. Li and G.W. Hastings (2016) Oxide bioceramics: inert ceramic materials in medicine and dentistry. In: *Handbook of Biomaterial Properties, Second Edition, 2nd ed*. Springer-Verlag New York, pp 340–354
24. Breme J, Biehl V (1998) *Metallic Biomaterials*. In: *Handbook of Biomaterial Properties*. Springer US, Boston, MA, pp 135–144
25. Ryan G, Pandit A, Apatsidis DP (2006) Fabrication methods of porous metals for use in orthopaedic applications. *Biomaterials* 27:2651–2670. <https://doi.org/10.1016/j.biomaterials.2005.12.002>
26. Zaman HA, Sharif S, Idris MH, Kamarudin A (2015) *Metallic Biomaterials for Medical Implant Applications: A Review*. *Appl Mech Mater* 735:19–25. <https://doi.org/10.4028/www.scientific.net/amm.735.19>
27. Breme H, Biehl V, Reger N GE (2016) *Metallic biomaterials: Introduction*. In: *Handbook of Biomaterial Properties*. pp 151–158
28. Bose S, Tarafde S BA (2015) Hydroxyapatite coatings for metallic implants. In: *Hydroxyapatite (HAp) for biomedical applications*. Woodhead Publishing Series in Biomaterials
29. Park S-H, Llinas A, Park S-H, Llinás A, Goel VK KJ *Hard tissue replacements*. In: *Biomaterials, 2nd ed*
30. Park S-H, Llinás A, Goel VK KJ (2006) *Hard tissue replacment*. In: *Biomedical Engineering fundamentals, 1st ed*. CRC Press
31. Albrektsson T (2016) *Hard tissue response*. In: *Handbook of Biomaterial Properties, 2nd ed*. Springer-Verlag New York
32. Wong JY, Bronzino JD (2007) *Biomaterials*. CRC Press
33. Albrektsson T, Johansson C (2001) Osteoinduction, osteoconduction and osseointegration. *Eur Spine J* 10:S96–S101. <https://doi.org/10.1007/s005860100282>
34. Bergmann G, Graichen F, Rohlmann A, et al (2010) Realistic loads for testing hip implants. *Biomed Mater Eng* 20:65–75. <https://doi.org/10.3233/bme-2010-0616>
35. Taylor ME, Tanner KE, Freeman MAR, Yettram AL (1996) Stress and strain distribution within the intact femur: compression or bending? *Med Eng Phys* 18:122–131. [https://doi.org/https://doi.org/10.1016/1350-4533\(95\)00031-3](https://doi.org/https://doi.org/10.1016/1350-4533(95)00031-3)
36. Lu T-W, Taylor SJG, O'Connor JJ, Walker PS (1997) Influence of muscle activity on the forces in the femur: An in vivo study. *J Biomech* 30:1101–1106. [https://doi.org/https://doi.org/10.1016/S0021-9290\(97\)00090-0](https://doi.org/https://doi.org/10.1016/S0021-9290(97)00090-0)

37. Saverio Affatato (2014) *Perspectives in Total Hip Arthroplasty*, 1st ed. Woodhead publishing
38. Zhang L, Liu G, Han B, et al (2020) *Knee Joint Biomechanics in Physiological Conditions and How Pathologies Can Affect It: A Systematic Review*. *Appl Bionics Biomech* 2020:.  
<https://doi.org/10.1155/2020/7451683>
39. Marcolongo M, Sarkar S, Ganesh N (2017) 7.11 Trends in materials for spine surgery. Elsevier Ltd.
40. Rao PJ, Pelletier MH, Walsh WR, Mobbs RJ (2014) Spine Interbody Implants: Material Selection and Modification, Functionalization and Bioactivation of Surfaces to Improve Osseointegration. *Orthop Surg* 6:81–89. <https://doi.org/10.1111/os.12098>
41. Warburton A, Girdler SJ, Mikhail CM, et al (2020) Biomaterials in spinal implants: A review. *Neurospine* 17:101–110. <https://doi.org/10.14245/ns.1938296.148>
42. No Title. <https://www.stryker.com/it/en/spine/products/tritanium-tl.html>
43. Hallab NJ, Singh V (2014) *Intervertebral disc joint replacement technology*
44. Goodship AE, Cunningham JL (2001) Pathophysiology of functional adaptation of bone in remodelling and repair in-vivo. In: *Bone Mechanics Handbook* (2nd Ed.). CRC Press, USA United States, pp 26.1--26.31
45. Arun Shanbhag, Harry E. Rubash JJJ (2005) *Joint Replacement and Bone Resorption Pathology, Biomaterials and Clinical Practice*. CRC Press
46. Sumner DR (2015) Long-term implant fixation and stress-shielding in total hip replacement. *J Biomech* 48:797–800. <https://doi.org/https://doi.org/10.1016/j.jbiomech.2014.12.021>
47. Glassman AH, Bobyn JD, Tanzer M (2006) New femoral designs: do they influence stress shielding. *Clin Orthop Relat Res* 453:64–74. <https://doi.org/10.1097/01.blo.0000246541.41951.20>
48. Huiskes R, Weinans H, Van Rietbergen B (1992) The relationship between stress shielding and bone resorption around total hip stems and the effects of flexible materials. *Clin Orthop Relat Res* 124–134. <https://doi.org/10.1097/00003086-199201000-00014>
49. Huiskes R, Weinans H, Dalstra M (1989) Adaptive bone remodeling and biomechanical design considerations for noncemented total hip arthroplasty. *Orthopedics* 12:1255–1267
50. Kuiper JH, Huiskes R (1997) Mathematical optimization of elastic properties: application to cementless hip stem design. *J Biomech Eng* 119:166–174. <https://doi.org/10.1115/1.2796076>
51. Sola A, Bellucci D, Cannillo V (2016) Functionally graded materials for orthopedic applications – an update on design and manufacturing. *Biotechnol Adv* 34:504–531.  
<https://doi.org/https://doi.org/10.1016/j.biotechadv.2015.12.013>
52. Cristofolini L (1997) A critical analysis of stress shielding evaluation of hip prostheses. *Crit Rev Biomed Eng* 25:409–483. <https://doi.org/10.1615/critrevbiomedeng.v25.i4-5.30>
53. Cheryl R. Blanchard, Dana J. Medlin and RS (2005) *Advances in metals*. In: Arun Shanbhag, Harry E. Rubash JJJ (ed) *Joint replacement and Bone resorption pathology, Biomaterials and clinical practice*. Taylor & Francis
54. Epinette J-A, Manley MT (2004) *Fifteen Years of Clinical Experience with Hydroxyapatite Coatings in Joint Arthroplasty*. Springer Paris, Paris
55. Levine B (2008) A New Era in Porous Metals: Applications in Orthopaedics. *Adv Eng Mater* 10:788–792. <https://doi.org/10.1002/adem.200800215>
56. Moussa A, Tanzer M, Pasini D (2018) Cervical fusion cage computationally optimized with porous architected Titanium for minimized subsidence. *J Mech Behav Biomed Mater* 85:134–151.  
<https://doi.org/10.1016/j.jmbbm.2018.05.040>
57. Murr LE, Gaytan SM, Medina F, et al (2009) Additive Layered Manufacturing of Reticulated Ti-6Al-4V Biomedical Mesh Structures by Electron Beam Melting. pp 23–28
58. Murr LE, Gaytan SM, Medina F, et al (2010) Next-generation biomedical implants using additive

- manufacturing of complex, cellular and functional mesh arrays. *Philos Trans R Soc A Math Phys Eng Sci* 368:1999–2032. <https://doi.org/10.1098/rsta.2010.0010>
59. Harrysson OLA, Cansizoglu O, Marcellin-Little DJ, et al (2008) Direct metal fabrication of titanium implants with tailored materials and mechanical properties using electron beam melting technology. *Mater Sci Eng C* 28:366–373. <https://doi.org/10.1016/j.msec.2007.04.022>
  60. Arabnejad S, Johnston B, Tanzer M, Pasini D (2017) Fully porous 3D printed titanium femoral stem to reduce stress-shielding following total hip arthroplasty. *J Orthop Res* 35:1774–1783. <https://doi.org/10.1002/jor.23445>
  61. Tan XP, Tan YJ, Chow CSL, et al (2017) Metallic powder-bed based 3D printing of cellular scaffolds for orthopaedic implants: A state-of-the-art review on manufacturing, topological design, mechanical properties and biocompatibility. *Mater Sci Eng C* 76:1328–1343. <https://doi.org/10.1016/j.msec.2017.02.094>
  62. Nazir A, Abate KM, Kumar A, Jeng JY (2019) A state-of-the-art review on types, design, optimization, and additive manufacturing of cellular structures. *Int J Adv Manuf Technol* 104:3489–3510. <https://doi.org/10.1007/s00170-019-04085-3>
  63. Ashby MF (2006) The properties of foams and lattices. *Philos Trans R Soc A Math Phys Eng Sci* 364:15–30. <https://doi.org/10.1098/rsta.2005.1678>
  64. Maconachie T, Leary M, Lozanovski B, et al (2019) SLM lattice structures: Properties, performance, applications and challenges. *Mater Des* 183:108137. <https://doi.org/10.1016/j.matdes.2019.108137>
  65. Cuadrado A, Yáñez A, Martel O, et al (2017) Influence of load orientation and of types of loads on the mechanical properties of porous Ti6Al4V biomaterials. *Mater Des* 135:309–318. <https://doi.org/10.1016/j.matdes.2017.09.045>
  66. Leary M, Mazur M, Elambasseril J, et al (2016) Selective laser melting (SLM) of AlSi12Mg lattice structures. *Mater Des* 98:344–357. <https://doi.org/10.1016/j.matdes.2016.02.127>
  67. Arabnejad S, Burnett Johnston R, Pura JA, et al (2016) High-strength porous biomaterials for bone replacement: A strategy to assess the interplay between cell morphology, mechanical properties, bone ingrowth and manufacturing constraints. *Acta Biomater* 30:345–356. <https://doi.org/10.1016/j.actbio.2015.10.048>
  68. Kucwicz M, Baranowski P, Małachowski J, et al (2018) Modelling, and characterization of 3D printed cellular structures. *Mater Des* 142:177–189. <https://doi.org/10.1016/j.matdes.2018.01.028>
  69. Ahmadi SM, Yavari SA, Wauthle R, et al (2015) Additively manufactured open-cell porous biomaterials made from six different space-filling unit cells: The mechanical and morphological properties. *Materials (Basel)* 8:1871–1896. <https://doi.org/10.3390/ma8041871>
  70. Yáñez A, Herrera A, Martel O, et al (2016) Compressive behaviour of gyroid lattice structures for human cancellous bone implant applications. *Mater Sci Eng C* 68:445–448. <https://doi.org/10.1016/j.msec.2016.06.016>
  71. Bobbert FSL, Lietaert K, Eftekhari AA, et al (2017) Additively manufactured metallic porous biomaterials based on minimal surfaces: A unique combination of topological, mechanical, and mass transport properties. *Acta Biomater* 53:572–584. <https://doi.org/10.1016/j.actbio.2017.02.024>
  72. Fleck NA, Deshpande VS, Ashby MF (2010) Micro-architected materials: past, present and future. *Proc R Soc A Math Phys Eng Sci* 466:2495–2516. <https://doi.org/10.1098/rspa.2010.0215>
  73. Deshpande VS, Ashby MF, Fleck NA (2001) Foam topology: Bending versus stretching dominated architectures. *Acta Mater* 49:1035–1040. [https://doi.org/10.1016/S1359-6454\(00\)00379-7](https://doi.org/10.1016/S1359-6454(00)00379-7)
  74. Zadpoor AA, Hedayati R (2016) Analytical relationships for prediction of the mechanical properties of additively manufactured porous biomaterials. *J Biomed Mater Res - Part A* 104:3164–3174. <https://doi.org/10.1002/jbm.a.35855>
  75. Simone AE, Gibson LJ (1998) Effects of solid distribution on the stiffness and strength of metallic foams. *Acta Mater* 46:2139–2150. [https://doi.org/10.1016/S1359-6454\(97\)00421-7](https://doi.org/10.1016/S1359-6454(97)00421-7)

76. Kadkhodapour J, Montazerian H, Darabi AC, et al (2015) Failure mechanisms of additively manufactured porous biomaterials: Effects of porosity and type of unit cell. *J Mech Behav Biomed Mater* 50:180–191. <https://doi.org/10.1016/j.jmbbm.2015.06.012>
77. Qiu C, Yue S, Adkins NJE, et al (2015) Influence of processing conditions on strut structure and compressive properties of cellular lattice structures fabricated by selective laser melting. *Mater Sci Eng A* 628:188–197. <https://doi.org/10.1016/j.msea.2015.01.031>
78. Leary M, Mazur M, Williams H, et al (2018) Inconel 625 lattice structures manufactured by selective laser melting (SLM): Mechanical properties, deformation and failure modes. *Mater Des* 157:179–199. <https://doi.org/10.1016/j.matdes.2018.06.010>
79. Hashin Z (1983) Analysis of Composite Materials—A Survey. *J Appl Mech* 50:481–505. <https://doi.org/10.1115/1.3167081>
80. Shahzamanian MM, Tadepalli T, Rajendran AM, et al (2014) Representative Volume Element Based Modeling of Cementitious Materials. *J Eng Mater Technol* 136:011007. <https://doi.org/10.1115/1.4025916>
81. Hollister SJ, Kikuchi N (1992) A comparison of homogenization and standard mechanics analyses for periodic porous composites. *Comput Mech* 10:73–95. <https://doi.org/10.1007/BF00369853>
82. Gibson, L. J.; Ashby, M. F.; Schajer, G. S.; Robertson CI (1982) The mechanics of two-dimensional cellular materials. *Proc R Soc London A Math Phys Sci* 382:25–42. <https://doi.org/10.1098/rspa.1982.0087>
83. Arabnejad S, Pasini D (2013) Mechanical properties of lattice materials via asymptotic homogenization and comparison with alternative homogenization methods. *Int J Mech Sci* 77:249–262. <https://doi.org/10.1016/j.ijmecsci.2013.10.003>
84. Kim HS (2001) A morphological elastic model of general hexagonal columnar structures. 43:
85. Warren WE, Kraynik AM (1987) Foam mechanics: the linear elastic response of two-dimensional spatially periodic cellular materials. *Mech Mater* 6:27–37. [https://doi.org/10.1016/0167-6636\(87\)90020-2](https://doi.org/10.1016/0167-6636(87)90020-2)
86. Dong G, Tang Y, Zhao YF (2017) A Survey of Modeling of Lattice Structures Fabricated by Additive Manufacturing. *J Mech Des* 139:. <https://doi.org/10.1115/1.4037305>
87. Hassani B, Hinton E (1998) A review of homogenization and topology optimization II—analytical and numerical solution of homogenization equations. *Comput Struct* 69:719–738. [https://doi.org/10.1016/S0045-7949\(98\)00132-1](https://doi.org/10.1016/S0045-7949(98)00132-1)
88. Hassani B, Hinton E (1998) A review of homogenization and topology optimization I—homogenization theory for media with periodic structure. *Comput Struct* 69:707–717. [https://doi.org/10.1016/S0045-7949\(98\)00131-X](https://doi.org/10.1016/S0045-7949(98)00131-X)
89. Masoumi Khalil Abad E, Arabnejad Khanoki S, Pasini D (2013) Fatigue design of lattice materials via computational mechanics: Application to lattices with smooth transitions in cell geometry. *Int J Fatigue* 47:126–136. <https://doi.org/10.1016/j.ijfatigue.2012.08.003>
90. Arabnejad Khanoki S, Pasini D (2012) Multiscale Design and Multiobjective Optimization of Orthopedic Hip Implants with Functionally Graded Cellular Material. *J Biomech Eng* 134:. <https://doi.org/10.1115/1.4006115>
91. Smith M, Guan Z, Cantwell WJ (2013) Finite element modelling of the compressive response of lattice structures manufactured using the selective laser melting technique. *Int J Mech Sci* 67:28–41. <https://doi.org/10.1016/j.ijmecsci.2012.12.004>
92. Luxner MH, Stampfl J, Pettermann HE (2005) Finite element modeling concepts and linear analyses of 3D regular open cell structures. *J Mater Sci* 40:5859–5866. <https://doi.org/10.1007/s10853-005-5020-y>
93. Zhu HX, Thorpe SM, Windle AH (2006) The effect of cell irregularity on the high strain compression of 2D Voronoi honeycombs. *Int J Solids Struct* 43:1061–1078. <https://doi.org/10.1016/j.ijsolstr.2005.05.008>

94. Liu L, Kamm P, García-Moreno F, et al (2017) Elastic and failure response of imperfect three-dimensional metallic lattices: the role of geometric defects induced by Selective Laser Melting. *J Mech Phys Solids* 107:160–184. <https://doi.org/10.1016/j.jmps.2017.07.003>
95. Campoli G, Borleffs MS, Amin Yavari S, et al (2013) Mechanical properties of open-cell metallic biomaterials manufactured using additive manufacturing. *Mater Des* 49:957–965. <https://doi.org/10.1016/j.matdes.2013.01.071>
96. Latture RM, Rodriguez RX, Holmes LR, Zok FW (2018) Effects of nodal fillets and external boundaries on compressive response of an octet truss. *Acta Mater* 149:78–87. <https://doi.org/10.1016/j.actamat.2017.12.060>
97. Alkhader M, Vural M (2008) Mechanical response of cellular solids: Role of cellular topology and microstructural irregularity. *Int J Eng Sci* 46:1035–1051. <https://doi.org/10.1016/j.ijengsci.2008.03.012>
98. Zargarian A, Esfahanian M, Kadkhodapour J, et al (2016) Numerical simulation of the fatigue behavior of additive manufactured titanium porous lattice structures. *Mater Sci Eng C* 60:339–347. <https://doi.org/10.1016/j.msec.2015.11.054>
99. Hedayati R, Hosseini-Toudeshky H, Sadighi M, et al (2016) Computational prediction of the fatigue behavior of additively manufactured porous metallic biomaterials. *Int J Fatigue* 84:67–79. <https://doi.org/10.1016/j.ijfatigue.2015.11.017>
100. Kim HS, Al-Hassani STS (2003) Effective elastic constants of two-dimensional cellular materials with deep and thick cell walls. *Int J Mech Sci* 45:1999–2016. <https://doi.org/10.1016/j.ijmecsci.2004.02.002>
101. Webb DC, Kormi K, Al-Hassani STS (1995) Use of FEM in performance assessment of perforated plates subject to general loading conditions. *Int J Press Vessel Pip* 64:137–152. [https://doi.org/10.1016/0308-0161\(94\)00078-W](https://doi.org/10.1016/0308-0161(94)00078-W)
102. Hazlehurst K, Wang CJ, Stanford M (2013) Evaluation of the stiffness characteristics of square pore CoCrMo cellular structures manufactured using laser melting technology for potential orthopaedic applications. *Mater Des* 51:949–955. <https://doi.org/10.1016/j.matdes.2013.05.009>
103. Cahill S, Lohfeld S, McHugh PE (2009) Finite element predictions compared to experimental results for the effective modulus of bone tissue engineering scaffolds fabricated by selective laser sintering. *J Mater Sci Mater Med* 20:1255–1262. <https://doi.org/10.1007/s10856-009-3693-5>
104. Hedayati R, Janbaz S, Sadighi M, et al (2017) How does tissue regeneration influence the mechanical behavior of additively manufactured porous biomaterials? *J Mech Behav Biomed Mater* 65:831–841. <https://doi.org/10.1016/j.jmbbm.2016.10.003>
105. Xiao L, Song W, Wang C, et al (2017) Mechanical properties of open-cell rhombic dodecahedron titanium alloy lattice structure manufactured using electron beam melting under dynamic loading. *Int J Impact Eng* 100:75–89. <https://doi.org/10.1016/j.ijimpeng.2016.10.006>
106. Veyhl C, Belova IV, Murch GE, Fiedler T (2011) Finite element analysis of the mechanical properties of cellular aluminium based on micro-computed tomography. *Mater Sci Eng A* 528:4550–4555. <https://doi.org/10.1016/j.msea.2011.02.031>
107. Herzog D, Seyda V, Wycisk E, Emmelmann C (2016) Additive manufacturing of metals. *Acta Mater* 117:371–392. <https://doi.org/10.1016/j.actamat.2016.07.019>
108. Dallago M, Fontanari V, Torresani E, et al (2018) Fatigue and biological properties of Ti-6Al-4V ELI cellular structures with variously arranged cubic cells made by selective laser melting. *J Mech Behav Biomed Mater* 78:381–394. <https://doi.org/10.1016/j.jmbbm.2017.11.044>
109. Qiu C, Adkins NJE, Attallah MM (2013) Microstructure and tensile properties of selectively laser-melted and of HIPed laser-melted Ti-6Al-4V. *Mater Sci Eng A* 578:230–239. <https://doi.org/10.1016/j.msea.2013.04.099>
110. Wauthle R, Vrancken B, Beynaerts B, et al (2015) Effects of build orientation and heat treatment on the microstructure and mechanical properties of selective laser melted Ti6Al4V lattice structures. *Addit Manuf* 5:77–84. <https://doi.org/10.1016/j.addma.2014.12.008>

111. Salem H, Carter LN, Attallah MM, Salem HG (2019) Influence of processing parameters on internal porosity and types of defects formed in Ti6Al4V lattice structure fabricated by selective laser melting. *Mater Sci Eng A* 767:138387. <https://doi.org/10.1016/j.msea.2019.138387>
112. Pyka G, Kerckhofs G, Papantoniou I, et al (2013) Surface Roughness and Morphology Customization of Additive Manufactured Open Porous Ti6Al4V Structures. *Materials (Basel)* 6:4737–4757. <https://doi.org/10.3390/ma6104737>
113. Yan C, Hao L, Hussein A, et al (2014) Advanced lightweight 316L stainless steel cellular lattice structures fabricated via selective laser melting. *Mater Des* 55:533–541. <https://doi.org/10.1016/j.matdes.2013.10.027>
114. de Formanoir C, Suard M, Dendievel R, et al (2016) Improving the mechanical efficiency of electron beam melted titanium lattice structures by chemical etching. *Addit Manuf* 11:71–76. <https://doi.org/10.1016/j.addma.2016.05.001>
115. Lhuissier P, de Formanoir C, Martin G, et al (2016) Geometrical control of lattice structures produced by EBM through chemical etching: Investigations at the scale of individual struts. *Mater Des* 110:485–493. <https://doi.org/10.1016/j.matdes.2016.08.029>
116. Suard M, Martin G, Lhuissier P, et al (2015) Mechanical equivalent diameter of single struts for the stiffness prediction of lattice structures produced by Electron Beam Melting. *Addit Manuf* 8:124–131. <https://doi.org/10.1016/j.addma.2015.10.002>
117. Sing SL, Wiria FE, Yeong WY (2018) Selective laser melting of lattice structures: A statistical approach to manufacturability and mechanical behavior. *Robot Comput Integr Manuf* 49:170–180. <https://doi.org/10.1016/j.rcim.2017.06.006>
118. Mullen L, Stamp RC, Fox P, et al (2010) Selective laser melting: A unit cell approach for the manufacture of porous, titanium, bone in-growth constructs, suitable for orthopedic applications. II. Randomized structures. *J Biomed Mater Res Part B Appl Biomater* 92B:178–188. <https://doi.org/10.1002/jbm.b.31504>
119. Calignano F (2018) Investigation of the accuracy and roughness in the laser powder bed fusion process. *Virtual Phys Prototyp* 13:97–104. <https://doi.org/10.1080/17452759.2018.1426368>
120. Van Bael S, Kerckhofs G, Moesen M, et al (2011) Micro-CT-based improvement of geometrical and mechanical controllability of selective laser melted Ti6Al4V porous structures. *Mater Sci Eng A* 528:7423–7431. <https://doi.org/10.1016/j.msea.2011.06.045>
121. Bagheri ZS, Melancon D, Liu L, et al (2017) Compensation strategy to reduce geometry and mechanics mismatches in porous biomaterials built with Selective Laser Melting. *J Mech Behav Biomed Mater* 70:17–27. <https://doi.org/10.1016/j.jmbbm.2016.04.041>
122. Kessler J, Balc N, Gebhardt A, Abbas K (2017) Basic design rules of unit cells for additive manufactured lattice structures. *MATEC Web Conf* 137:. <https://doi.org/10.1051/mateconf/201713702005>
123. Kranz J, Herzog D, Emmelmann C (2015) Design guidelines for laser additive manufacturing of lightweight structures in TiAl6V4. *J Laser Appl* 27:S14001. <https://doi.org/10.2351/1.4885235>
124. Calignano F (2014) Design optimization of supports for overhanging structures in aluminum and titanium alloys by selective laser melting. *Mater Des* 64:203–213. <https://doi.org/10.1016/j.matdes.2014.07.043>
125. Zhu Z, Anwer N, Mathieu L (2017) Deviation Modeling and Shape Transformation in Design for Additive Manufacturing. *Procedia CIRP* 60:211–216. <https://doi.org/10.1016/j.procir.2017.01.023>
126. Melancon D, Bagheri ZS, Johnston RB, et al (2017) Acta Biomaterialia Mechanical characterization of structurally porous biomaterials built via additive manufacturing : experiments , predictive models , and design maps for load-bearing bone replacement implants. *Acta Biomater*. <https://doi.org/10.1016/j.actbio.2017.09.013>
127. Zadpoor AA (2017) Mechanics of additively manufactured biomaterials. *J Mech Behav Biomed Mater* 70:1–6. <https://doi.org/10.1016/j.jmbbm.2017.03.018>

128. Torries B, Imandoust A, Beretta S, et al (2018) Overview on Microstructure- and Defect-Sensitive Fatigue Modeling of Additively Manufactured Materials. *JOM* 70:1853–1862. <https://doi.org/10.1007/s11837-018-2987-9>
129. Parthasarathy J, Starly B, Raman S, Christensen A (2010) Mechanical evaluation of porous titanium (Ti6Al4V) structures with electron beam melting (EBM). *J Mech Behav Biomed Mater* 3:249–259. <https://doi.org/10.1016/j.jmbbm.2009.10.006>
130. Li SJ, Xu QS, Wang Z, et al (2014) Influence of cell shape on mechanical properties of Ti-6Al-4V meshes fabricated by electron beam melting method. *Acta Biomater* 10:4537–4547. <https://doi.org/10.1016/j.actbio.2014.06.010>
131. Gümruk R, Mines RAW, Karadeniz S (2013) Static mechanical behaviours of stainless steel micro-lattice structures under different loading conditions. *Mater Sci Eng A* 586:392–406. <https://doi.org/10.1016/j.msea.2013.07.070>
132. Mazur M, Leary M, Sun S, et al (2016) Deformation and failure behaviour of Ti-6Al-4V lattice structures manufactured by selective laser melting (SLM). *Int J Adv Manuf Technol* 84:1391–1411. <https://doi.org/10.1007/s00170-015-7655-4>
133. Liu X, Sekizawa K, Suzuki A, et al (2020) Compressive properties of Al-Si alloy lattice structures with three different unit cells fabricated via laser powder bed fusion. *Materials (Basel)* 13:1–16. <https://doi.org/10.3390/ma13132902>
134. Kadkhodapour J, Montazerian H, Darabi AC, Zargarian A (2017) The relationships between deformation mechanisms and mechanical properties of additively manufactured porous biomaterials. *J Mech Behav Biomed Mater* 70:28–42. <https://doi.org/10.1016/j.jmbbm.2016.09.018>
135. Yáñez A, Cuadrado A, Martel O, et al (2018) Gyroid porous titanium structures: A versatile solution to be used as scaffolds in bone defect reconstruction. *Mater Des* 140:21–29. <https://doi.org/10.1016/j.matdes.2017.11.050>
136. Zaharin H, Abdul Rani A, Azam F, et al (2018) Effect of Unit Cell Type and Pore Size on Porosity and Mechanical Behavior of Additively Manufactured Ti6Al4V Scaffolds. *Materials (Basel)* 11:2402. <https://doi.org/10.3390/ma11122402>
137. Zhang XY, Fang G, Xing LL, et al (2018) Effect of porosity variation strategy on the performance of functionally graded Ti-6Al-4V scaffolds for bone tissue engineering. *Mater Des* 157:523–538. <https://doi.org/10.1016/j.matdes.2018.07.064>
138. Surmeneva MA, Surmenev RA, Chudinova EA, et al (2017) Fabrication of multiple-layered gradient cellular metal scaffold via electron beam melting for segmental bone reconstruction. *Mater Des* 133:195–204. <https://doi.org/10.1016/j.matdes.2017.07.059>
139. Zhang S, Li C, Hou W, et al (2016) Longitudinal Compression Behavior of Functionally Graded Ti-6Al-4V Meshes. *J Mater Sci Technol* 32:1098–1104. <https://doi.org/10.1016/j.jmst.2016.02.008>
140. Maskery I, Aremu AO, Simonelli M, et al (2015) Mechanical Properties of Ti-6Al-4V Selectively Laser Melted Parts with Body-Centred-Cubic Lattices of Varying cell size. *Exp Mech* 55:1261–1272. <https://doi.org/10.1007/s11340-015-0021-5>
141. Ferrigno A, Di Caprio F, Borrelli R, et al (2019) The mechanical strength of Ti-6Al-4V columns with regular octet microstructure manufactured by electron beam melting. *Materialia* 5:100232. <https://doi.org/10.1016/j.mtla.2019.100232>
142. Köhnen P, Haase C, Bültmann J, et al (2018) Mechanical properties and deformation behavior of additively manufactured lattice structures of stainless steel. *Mater Des* 145:205–217. <https://doi.org/10.1016/j.matdes.2018.02.062>
143. Ren D, Li S, Wang H, et al (2019) Fatigue behavior of Ti-6Al-4V cellular structures fabricated by additive manufacturing technique. *J Mater Sci Technol* 35:285–294. <https://doi.org/10.1016/j.jmst.2018.09.066>
144. Liu YJ, Wang HL, Li SJ, et al (2017) Compressive and fatigue behavior of beta-type titanium porous structures fabricated by electron beam melting. *Acta Mater* 126:58–66.

- <https://doi.org/10.1016/j.actamat.2016.12.052>
145. Özbilen S, Liebert D, Beck T, Bram M (2016) Fatigue behavior of highly porous titanium produced by powder metallurgy with temporary space holders. *Mater Sci Eng C* 60:446–457. <https://doi.org/10.1016/j.msec.2015.11.050>
  146. Li SJ, Murr LE, Cheng XY, et al (2012) Compression fatigue behavior of Ti-6Al-4V mesh arrays fabricated by electron beam melting. *Acta Mater* 60:793–802. <https://doi.org/10.1016/j.actamat.2011.10.051>
  147. Zhao S, Li SJ, Hou WT, et al (2016) The influence of cell morphology on the compressive fatigue behavior of Ti-6Al-4V meshes fabricated by electron beam melting. *J Mech Behav Biomed Mater* 59:251–264. <https://doi.org/10.1016/j.jmbbm.2016.01.034>
  148. Amin Yavari S, Wauthle R, Van Der Stok J, et al (2013) Fatigue behavior of porous biomaterials manufactured using selective laser melting. *Mater Sci Eng C* 33:4849–4858. <https://doi.org/10.1016/j.msec.2013.08.006>
  149. Amin Yavari S, Ahmadi SMM, Wauthle R, et al (2015) Relationship between unit cell type and porosity and the fatigue behavior of selective laser melted meta-biomaterials. *J Mech Behav Biomed Mater* 43:91–100. <https://doi.org/10.1016/j.jmbbm.2014.12.015>
  150. Speirs M, Van Hooreweder B, Van Humbeek J, Kruth JP (2017) Fatigue behaviour of NiTi shape memory alloy scaffolds produced by SLM, a unit cell design comparison. *J Mech Behav Biomed Mater* 70:53–59. <https://doi.org/10.1016/j.jmbbm.2017.01.016>
  151. Liu YJ, Ren DC, Li SJ, et al (2020) Enhanced fatigue characteristics of a topology-optimized porous titanium structure produced by selective laser melting. *Addit Manuf* 32:. <https://doi.org/10.1016/j.addma.2020.101060>
  152. Boniotti L, Beretta S, Patriarca L, et al (2019) Experimental and numerical investigation on compressive fatigue strength of lattice structures of AlSi7Mg manufactured by SLM. *Int J Fatigue* 128:105181. <https://doi.org/10.1016/j.ijfatigue.2019.06.041>
  153. Ahmadi SM, Hedayati R, Li Y, et al (2018) Fatigue performance of additively manufactured meta-biomaterials: The effects of topology and material type. *Acta Biomater* 65:292–304. <https://doi.org/10.1016/j.actbio.2017.11.014>
  154. Zhao S, Li SJ, Wang SG, et al (2018) Compressive and fatigue behavior of functionally graded Ti-6Al-4V meshes fabricated by electron beam melting. *Acta Mater* 150:1–15. <https://doi.org/10.1016/j.actamat.2018.02.060>
  155. Peng C, Tran P, Nguyen-Xuan H, Ferreira AJM (2020) Mechanical performance and fatigue life prediction of lattice structures: Parametric computational approach. *Compos Struct* 235:111821. <https://doi.org/10.1016/j.compstruct.2019.111821>
  156. Sallica-Leva E, Jardini AL, Fogagnolo JB (2013) Microstructure and mechanical behavior of porous Ti-6Al-4V parts obtained by selective laser melting. *J Mech Behav Biomed Mater* 26:98–108. <https://doi.org/10.1016/j.jmbbm.2013.05.011>
  157. Zhang S, Wei Q, Cheng L, et al (2014) Effects of scan line spacing on pore characteristics and mechanical properties of porous Ti6Al4V implants fabricated by selective laser melting. *Mater Des* 63:185–193. <https://doi.org/10.1016/j.matdes.2014.05.021>
  158. Ghouse S, Babu S, Nai K, et al (2018) The influence of laser parameters, scanning strategies and material on the fatigue strength of a stochastic porous structure. *Addit Manuf* 22:290–301. <https://doi.org/10.1016/j.addma.2018.05.024>
  159. Zadpoor AA (2019) Mechanical performance of additively manufactured meta-biomaterials. *Acta Biomater* 85:41–59. <https://doi.org/10.1016/j.actbio.2018.12.038>
  160. Maskery I, Aremu AO, Parry L, et al (2018) Effective design and simulation of surface-based lattice structures featuring volume fraction and cell type grading. *Mater Des* 155:220–232. <https://doi.org/10.1016/j.matdes.2018.05.058>

161. Van Hooreweder B, Apers Y, Lietaert K, Kruth JP (2017) Improving the fatigue performance of porous metallic biomaterials produced by Selective Laser Melting. *Acta Biomater* 47:193–202. <https://doi.org/10.1016/j.actbio.2016.10.005>
162. Yuan W, Hou W, Li S, et al (2018) Heat treatment enhancing the compressive fatigue properties of open-cellular Ti-6Al-4V alloy prototypes fabricated by electron beam melting. *J Mater Sci Technol* 34:1127–1131. <https://doi.org/10.1016/j.jmst.2017.12.003>
163. Wu MW, Chen JK, Lin BH, et al (2020) Compressive fatigue properties of additive-manufactured Ti-6Al-4V cellular material with different porosities. *Mater Sci Eng A* 790:139695. <https://doi.org/10.1016/j.msea.2020.139695>
164. du Plessis A, Razavi SMJ, Berto F (2020) The effects of microporosity in struts of gyroid lattice structures produced by laser powder bed fusion. *Mater Des* 194:108899. <https://doi.org/10.1016/j.matdes.2020.108899>
165. Gibson I, Rosen DW, Stucker B (2010) *Additive Manufacturing Technologies*. Springer US, Boston, MA
166. Harun WSW, Kamariah MSIN, Muhamad N, et al (2018) A review of powder additive manufacturing processes for metallic biomaterials. *Powder Technol* 327:128–151. <https://doi.org/10.1016/j.powtec.2017.12.058>
167. Frazier WE (2014) Metal additive manufacturing: A review. *J Mater Eng Perform* 23:1917–1928. <https://doi.org/10.1007/s11665-014-0958-z>
168. Yang L, Hsu K, Baughman B, et al (2017) *Additive Manufacturing of Metals: The Technology, Materials, Design and Production*
169. Milewski JO (2017) *Additive Manufacturing of Metals*. Springer International Publishing, Cham
170. B. Dutta FHF (2017) *Additive Manufacturing Handbook Product Development for the Defense Industry*. pp 263–274
171. Thompson MK, Moroni G, Vaneker T, et al (2016) Design for Additive Manufacturing: Trends, opportunities, considerations, and constraints. *CIRP Ann - Manuf Technol* 65:737–760. <https://doi.org/10.1016/j.cirp.2016.05.004>
172. Weißmann V, Drescher P, Bader R, et al (2017) Comparison of Single Ti6Al4V Struts Made Using Selective Laser Melting and Electron Beam Melting Subject to Part Orientation. *Metals (Basel)* 7:91. <https://doi.org/10.3390/met7030091>
173. Wang Y, Arabnejad S, Tanzer M, Pasini D (2018) Hip Implant Design With Three-Dimensional Porous Architecture of Optimized Graded Density. *J Mech Des* 140:. <https://doi.org/10.1115/1.4041208>
174. Lütjering, Gerd, Williams JC (2007) *Titanium*. Springer Berlin Heidelberg, Berlin, Heidelberg
175. Mark Long, Rack HJ (1998) Titanium alloys in total joint replacement - a materials science perspective. *Biomaterials* 19:1621–1639. [https://doi.org/10.1016/S0142-9612\(97\)00146-4](https://doi.org/10.1016/S0142-9612(97)00146-4)
176. Breme J, Eisenbarth E, Biehl V (2005) *Titanium and its Alloys for Medical Applications*. In: *Titanium and Titanium Alloys*. Wiley-VCH Verlag GmbH & Co. KGaA, Weinheim, FRG, pp 423–451
177. Niinomi M, Boehlert CJ (2015) *Titanium alloys for biomedical applications*. Springer Ser Biomater Sci Eng 3:179–213. [https://doi.org/10.1007/978-3-662-46836-4\\_8](https://doi.org/10.1007/978-3-662-46836-4_8)
178. M. Peters, J. Hemptenmacher JK and CL (2003) *Structure and Properties of Titanium and Titanium Alloys*. In: *Leyens C, Peters M (eds) Titanium and Titanium Alloys*. Wiley
179. Rack HJ, Qazi JI (2006) *Titanium alloys for biomedical applications*. *Mater Sci Eng C* 26:1269–1277. <https://doi.org/10.1016/j.msec.2005.08.032>
180. Zhang ZX, Qu SJ, Feng AH, et al (2017) Hot deformation behavior of Ti-6Al-4V alloy: Effect of initial microstructure. *J Alloys Compd* 718:170–181. <https://doi.org/10.1016/j.jallcom.2017.05.097>
181. Freese HL, Volas MG, Wood JR (2001) *Metallurgy and Technological Properties of Titanium and*

Titanium Alloys. pp 25–51

182. Benedetti M, Torresani E, Leoni M, et al (2017) The effect of post-sintering treatments on the fatigue and biological behavior of Ti-6Al-4V ELI parts made by selective laser melting. *J Mech Behav Biomed Mater* 71:295–306. <https://doi.org/10.1016/j.jmbbm.2017.03.024>
183. Wagner L, Bigoney JK (2005) Fatigue of Titanium Alloys. In: Leyens C, Peters M (eds) *Titanium and Titanium Alloys*. Wiley-VCH Verlag GmbH & Co. KGaA, Weinheim, FRG, pp 153–185
184. Murphy W, Black J, Hastings G (2016) *Handbook of biomaterial properties*, second edition
185. Joon B. Park YKK (2007) *Metallic Biomaterials*. In: Wong JY, Bronzino JD. (eds) *Biomaterials*. CRC Press
186. Zhao X, Li S, Zhang M, et al (2016) Comparison of the microstructures and mechanical properties of Ti-6Al-4V fabricated by selective laser melting and electron beam melting. *Mater Des* 95:21–31. <https://doi.org/10.1016/j.matdes.2015.12.135>
187. Murr LE, Gaytan SM, Ramirez DA, et al (2012) Metal Fabrication by Additive Manufacturing Using Laser and Electron Beam Melting Technologies. *J Mater Sci Technol* 28:1–14. [https://doi.org/10.1016/S1005-0302\(12\)60016-4](https://doi.org/10.1016/S1005-0302(12)60016-4)
188. Gorsse S, Hutchinson C, Gouné M, Banerjee R (2017) Additive manufacturing of metals: a brief review of the characteristic microstructures and properties of steels, Ti-6Al-4V and high-entropy alloys. *Sci Technol Adv Mater* 18:584–610. <https://doi.org/10.1080/14686996.2017.1361305>
189. Thijs L, Verhaeghe F, Craeghs T, et al (2010) A study of the microstructural evolution during selective laser melting of Ti-6Al-4V. *Acta Mater* 58:3303–3312. <https://doi.org/10.1016/j.actamat.2010.02.004>
190. Shunmugavel M, Polishetty A, Littlefair G (2015) Microstructure and Mechanical Properties of Wrought and Additive Manufactured Ti-6Al-4V Cylindrical Bars | Elsevier Enhanced Reader. *Procedia Technol* 20:231–263
191. Shunmugavel M, Polishetty A, Goldberg M, et al (2017) A comparative study of mechanical properties and machinability of wrought and additive manufactured (selective laser melting) titanium alloy - Ti-6Al-4V. *Rapid Prototyp J* 23:1051–1056. <https://doi.org/10.1108/RPJ-08-2015-0105>

---

## Chapter 2

# Tensile and Compression Properties of Cubic Regular, Cubic Irregular and Trabecular Cellular Materials

---

The difference between the stiffness of the bone and the implants leads to stress shielding phenomenon that reduces the density of the surrounding bone and ultimately leading to implant loosening. Therefore, development of porous structures with properties closer to human bone is necessary. The development of additive manufacturing process has made it possible to develop porous structures for biomedical applications. The porous cellular materials used in implants undergo compression load most of the times, but in certain cases of loose implants and overweight patients, tensile properties of these materials should also be considered.

This chapter incorporates a novel tensile test with conventional compression test for titanium alloys (Ti6Al4V) cellular materials to obtain their mechanical properties. Three different types of cellular materials (cubic regular, cubic irregular and trabecular) at three different porosity levels were manufactured using LPBF process. A misalignment in the compression test specimens led to an asymmetric behavior between tensile and compression properties of the specimen. The effect of irregularity and a comparison between the trabecular inspired cellular material is provided. Also, the LPBF process induces a difference between the as-designed and the as-built geometry. Also, simple methods were used to recreate the as-built geometry for cubic regular cellular materials. With a focus on the tensile behavior, FEM analysis has been used to compare the as-designed and the as-built FE results with the experimental values. FE results from  $\mu$ CT FE models are compared with the experimental results of different types of cellular material. The last part of the study provides an empirical relation between the as-designed and the as-built Young's modulus for the three cell topologies.

A part of this chapter has been published in:

Raghavendra S, Molinari A, Fontanari V, Dallago M, Luchin V, Zappini G, Benedetti M. *Effect of strut cross section and strut defect on tensile properties of cubic cellular structure*. Mater Des Process Commun. 2020;2: 1–6.

Raghavendra S, Molinari A, Fontanari V, Dallago M, Luchin V, Zappini G, Benedetti M. *Tension-compression asymmetric mechanical behaviour of lattice cellular structures produced by selective laser melting*. Proc Inst Mech Eng Part C J Mech Eng Sci. 2020;234: 3241–3256.

Raghavendra S, Molinari A, Fontanari V, Luchin V, Zappini G, Benedetti M, Johansson F, Klarin J. *Tensile and compression properties of variously arranged porous Ti-6Al-4V additively manufactured structures via SLM*. Procedia Struct Integr. 2018;13: 149–154.

Raghavendra S, Molinari A, Fontanari V, Luchin V, Zappini G, Benedetti M. *Effect of Porosity and Cell Topology on Elastic-Plastic Behavior of Cellular Structures*. Procedia Struct Integr. 2019;18: 93–100.

## 2.1. Introduction

At present, metallic materials have been extensively used in biomedical implants due to their load bearing abilities compared to ceramic and polymer materials. Among different metallic materials available for biomedical applications, titanium and its alloys have been used extensively. Titanium and its alloys have a high strength-to-weight ratio and excellent corrosion resistance[1–3]. The biocompatibility of titanium alloys is due to the formation of a natural oxide layer on the surface of the titanium alloy[4].

Despite the advantages of metallic materials, prostheses made of solid material induces certain instability in the host and the surrounding of the prostheses. The reasons for instability are as discussed below.

- i. Young's modulus values of titanium alloys range from 40 GPa (metastable  $\beta$ -Ti alloys) to 110 GPa ( $\alpha$ -Ti alloys). These values are on the higher side when compared to the Young's modulus of the bone. The compact exterior part of the bone, called cortical bone has a Young's modulus of 10-20GPa. While the inner porous trabecular bone has a Young's modulus in the range of 0.3 – 5GPa depending on the anatomical location. The stiffness mismatch between the implant and the surrounding bone leads to underloading of the bone leading to *stress shielding*. The low loads on the bone makes the bone weak due to resorption of the bone leading to implant loosening [5–9].
- ii. Further, solid implant has less bone/tissue interaction which leads to poor bone regeneration after implantation. Lower mechanical interlocking at the bone-implant interface leads to implant loosening [10].

To reduce the above-mentioned problems in solid implants, extensive research is being carried out to reduce the mismatch between bone and implant. Efforts to replace the solid implants with porous implants with reduced stiffness, required load bearing capability, and better bone ingrowth is being carried out [3, 11]. Bone ingrowth in porous implants is dependent on certain factors such as cell topology, pore size, and surface roughness [12]. Rahmanian et al. [13] mentioned that a porosity greater than 50% and pore size of 800  $\mu\text{m}$  is recommended for bone ingrowth from the study conducted on NiTi porous material.

The development of additive manufacturing (AM) technology has made the production of complex porous cellular materials possible. Out of the various AM process, Laser powder bed fusion (LPBF) and Electron-beam powder bed fusion (EB-PBF) are widely used in the production of cellular materials. LPBF has shown greater accuracy but was time consuming when compared to EB-PBF [7, 14]. Some of the drawbacks from the AM process are the residual stress, surface roughness, geometrical deviation, and internal defects. Various post manufacturing process have been studied to reduce the effect of above-mentioned drawbacks on the mechanical properties. Heat treatment has been employed to transform the as-built  $\alpha$ -martensitic stage to a more stable  $\alpha+\beta$  phase at 800°C, which transforms the brittle failure to ductile failure [15]. Other post manufacturing process such as hot isostatic pressing (HIP), stress relieving with heat treatment, shot peening, and electropolishing used alone or in combination have shown to reduced internal porosity and improve the static and dynamic performance [16, 17]. LPBF and EB-PBF process parameters have influenced the internal defects, surface finish and the struts thickness in the case of cellular/lattice materials. Increasing the power of the energy source increases the strut thickness due to a larger melt pool, while internal porosity decreases [18, 19]. Studies have shown that the final strut thickness in the case of cellular materials is higher and or lower than the as-designed value depending on the orientation of the struts and the process parameters [20–22].

Different categories of cellular materials such as bending dominated, stretching dominated, functionally graded and auxetic cellular materials have been studied. The mechanical properties of

cellular materials are highly influenced by the cell topology and the porosity of the cellular materials. Various cell topologies such as cubic, BCC, BCC-Z, diamond, and Triply periodic minimum surface (TPMS) based gyroid cellular materials have been subjected to static and fatigue loads [23–31]. The effect of manufacturing defects such as internal porosity, geometrical deviation has also been studied. It is suggested that geometrical deviations such as strut waviness, eccentricity and missing struts reduce the stiffness of the cellular material by introducing bending in the cellular materials [32, 33]. Meanwhile, in the case of metal foams a difference between the tensile and compression behavior has been observed [34, 35]. This difference could be due to the response of defects induced in the manufacturing process and geometrical irregularity in foams to the tensile and compression loading mechanism [36]. Analytical model such as Gibson–Ashby model has been widely used for cellular materials [37, 38], for complex cell topologies and to understand their behavior at a local scale, finite element analysis has been carried out using beam and brick elements [39, 40]. To reduce the computational costs, Representative volume elements (RVE) have been used. Tomography based FE models are used to capture the minute details of the cellular material and to study their effect on both local and macroscopic scale [41–44].

For biomedical applications, under ideal implant loading conditions, implants are subjected to compression loading. Therefore, majority of the work carried out is to study the compression properties of cellular materials. However, some of the failure analysis of unexpected fractures of implants indicated that prostheses experience tensile loading due to excessive patient weight, extreme physical activity, improper positioning of implants, no osseointegration and loosening of implants [45, 46]. Therefore, the main aim of this study is to characterize cellular materials under tensile loading along with the conventional compression test for application in biomedical as well as other fields. The study is carried out by considering three different topologies: (i) Cubic regular: designed by arranging cubic unit cells in 3D space (ii) Cubic irregular: designed by considering the cubic regular topology and misaligning the nodes to induce irregularity. (iii) Trabecular: designed by connecting 4-6 struts at a node in random directions to replicate the trabecular bone. The samples were manufactured for different strut thickness and pore size to obtain various porosity levels. The samples were subjected to tensile and compression loading conditions to obtain their mechanical properties. Morphological analysis was carried out using stereomicroscope to measure geometrical deviation from as-designed values. Finite elements analysis was carried out under tensile loading to understand the effect of geometrical deviation by comparing the as-designed and as-built properties. Gibson-Ashby model was used to obtain theoretical validation for the finite element as well as the experimental results. The last part of the study focuses on correlating the experimental data obtained from the partner company and the finite element results of the as-designed cellular materials to obtain an empirical relation between the as-designed and as-built Young's modulus.

## **2.2. Materials and methods**

This section provides detailed information on the materials and methods used in the study. Information on the LPBF process, specimen design, and experimentation carried out is provided.

### **2.2.1. LPBF process and specimen details**

The cellular materials were manufactured by using a Renishaw AM250 LPBF machine at Lincotek medical, Italy. The specimens were manufactured using a biomedical grade, atomized Ti6Al4V powder with particle size in the range of 15-45  $\mu\text{m}$ . A layer thickness of 60  $\mu\text{m}$  and a laser power of 200W was employed in the process. Specimens were subjected to heat treatment in vacuum for 1.5 hours to transform the as-built  $\alpha'$  – martensitic stage to a more stable  $\alpha+\beta$  phase. The process was also used to relieve residual stresses. The LPBF process parameters and the post manufacturing treatments were decided by the partner company. Further information on the same is confidential and proprietary.

Table II - 1 Designed strut thickness and pore size for different batches

| Batch | Sample designation | Pore Size ( $\mu\text{m}$ ) | Strut thickness( $\mu\text{m}$ ) |
|-------|--------------------|-----------------------------|----------------------------------|
| A     | 1550               | 1500                        | 500                              |
| B     | 0720               | 700                         | 200                              |
| C     | 1520               | 1500                        | 200                              |

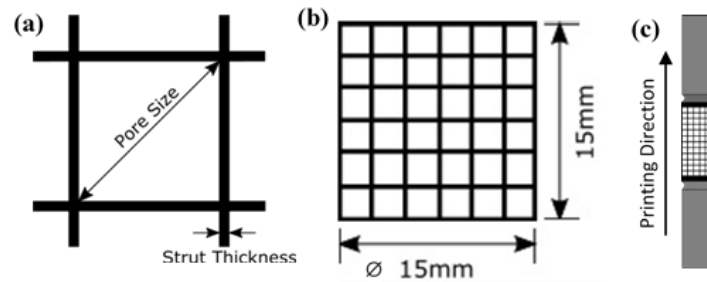


Figure II - 1 Schematic representation of (a) Pore size and strut thickness (b) compression test sample (c) tensile test sample

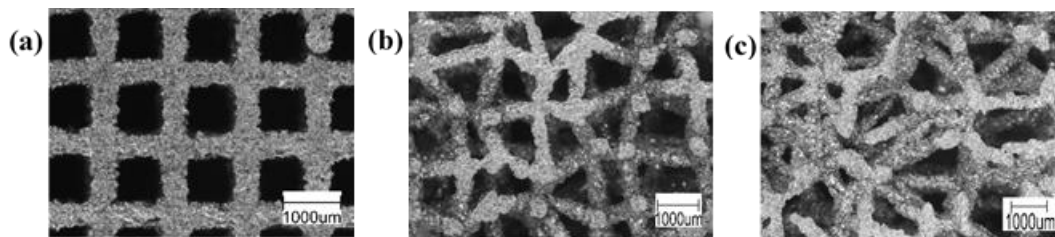


Figure II - 2 Cell topologies considered in the study (a) cubic regular (b) cubic irregular (c) trabecular

Three batches of specimen were considered for the study by varying their pore size and strut thickness. A schematic representation of strut thickness and pore size is as shown in Fig. II-1(a). The strut thickness and pore size of the three batches are as shown in Table-II.1. Batch A (1550) had large pore size and thick struts, batch B(0720) had small pore size and thin struts and batch C(1520) had large pore size and thin struts. The combination of small pores size and thick strut was not considered as it would result in lack of interconnections between pores which not ideal for bone in-growth. For easy representation batch A, batch B and batch C are used instead of sample designation in the future discussions.

Based on the study from the partner company, irregular distribution of pores helps in better osseointegration compared to regular lattice structure. Therefore, two structures with irregular pore structure and distribution were also considered along with regular lattice structure. A total of three different cell topologies were considered in each batch of specimen. The three structures include: *cubic regular*, *cubic irregular* and *trabecular*. The STL files of these configuration were obtained from Materialise MAGICS 21.1® software by the Lincotek medical. Fig. II-1 illustrates the cellular materials for all the three topologies of batch A. Cubic regular (Fig.II-2(a)) was obtained by repeating the cubic unit cell in 3 directions. Cubic irregular (Fig.II-2(b)) was obtained by misaligning the nodes of the cubic regular to induce irregularity. Trabecular samples (Fig.II-2(c)) did not possess any repeating unit cell and were obtained by joining 4-6 randomly oriented struts at a node to mimic a trabecular bone.

A schematic diagram on compression and tensile test samples are as shown in Fig.II-1(b) and (c) respectively. It is assumed that samples are produced with an acceptable repeatability from the LPBF process. Compression test specimens were cylindrical in shape and had length: diameter (L:D) ratio of

one. The test specimens were special designed with the cellular material in the center with solid part connect to it (indicated in black in Fig. II-1(c)). This was connected to the solid grips with a stress relief groove in between the grip and the cellular material. A total of five specimens were considered for mechanical testing. Three specimens were subjected to monotonic testing and two specimens were subjected to cyclic testing.

As described in the subsequent sections, a marked tension-compression asymmetry was recorded in the apparent Young's modulus. This was due to a tiny misalignment between loading axis and specimen axis, because of the inaccurate EDM cutting taken from the building platform. Hence, another batch of regular C sample (named as Ci) were produced to improve the alignment between loading directions and vertical struts. This was produced by precisely sectioning the end-planes of the cylindrical samples through a micro-cutting equipment, which secured the specimens tightly during the cutting operation, using a custom-made fixture.

### 2.2.2. Microstructure

The microstructure analysis was carried out for specimens to see if the heat treatment carried out was able to transform the as-built  $\alpha'$ -martensitic phase to a  $\alpha+\beta$  phase. A cylindrical specimen was cut along longitudinal and transverse direction using a Struers Secotom – 50 cutting machine. The samples were cold mounted in resin (Struers EPOFIX) and subjected to polishing process. The sectioned specimens were ground in a Struers ABRAMIN polishing machine using silicon carbide grinding papers with grit size starting from 180, 220, 500, 800, 1200, and 4000. After grinding, the samples were polished on a polishing cloth by using diamond abrasive of particle size  $3\mu\text{m}$  and  $1\mu\text{m}$  along with a lubricant. Finally, the process was finished by using OP-S 0.04 colloidal silica suspension to obtain a mirror finish. The specimens were next etched using Kroll's reagent to reveal the microstructure.

### 2.2.3. Porosity measurement

The LPBF process has the tendency to vary the porosity of the specimens from the designed porosity values. The porosity measurement was carried out for manufactured specimens and compared with the designed porosity values. The designed porosity of the specimens was directly obtained from the software while designing the STL files.

Cylindrical specimens of  $\text{Ø}15 \times 30$  mm dimension were considered to calculate the porosity. Six specimens in each batch were considered. The specimens were subjected to cleaning using an ultrasonic bath for 5 minutes in acetone, followed by blow drying to remove loosely attached powder particles from the manufacturing process. To calculate the density, the specimens were first weighed using a gravimetric precision balance (Ohaus) with a precision upto four decimal places. Then the length and diameter of the samples was measured at six different locations, the average of the same was used to calculate the volume of the sample. The density of the cellular material ( $\rho$ ) specimen was obtained by dividing its mass by the volume. The porosity of the specimen is calculated using the below formula provided by [36], where  $\rho_c$  is calculated as mentioned before and  $\rho_o$  is the theoretical density of Ti6Al4V alloys ( $4.42 \text{ g/cm}^3$ ). Another way of expressing porosity of the sample is the relative density of the sample ( $\rho/\rho_o$ ) as explained in previous chapter.

$$\text{Porosity}(\%) = \frac{\rho_o - \rho}{\rho_o} * 100 \quad \dots\dots\dots\text{Eq. II-1}$$

### 2.2.4. Morphological analysis

The morphological analysis of the specimens was performed to measure the strut thickness and pore size. One specimen was analyzed in each batch under JEOL JSM-IT300LV scanning electron microscope (SEM) and Nikon stereomicroscope. Strut thickness and pore size/void diameter was calculated on both longitudinal (parallel to printing direction) and transverse plane (perpendicular to

printing direction). The strut thickness was calculated from the images obtained and the pore size was calculated using the feret diameter. Feret diameter is the distance between the two parallel tangents of the pore/void [22]. Marking the pore boundary on the NIS-Element software of the stereomicroscope directly provides the maximum and minimum feret diameter, and equivalent diameter of the pore. For this study, the minimum feret diameter has been used to compare with the designed pore size. Further, the measurement of the strut thickness and the feret diameter on the longitudinal plane was difficult due to the curvature when compared to the transverse plane which is flat. Due to the complexity of the cubic irregular and trabecular specimens, more measurements are carried out when compared to cubic regular. Strut thickness was calculated at more than 50 locations in the specimen for each plane. A statistical analysis of the measured values was performed by calculating the mean and standard deviation and comparing with the as-designed values of the specimen.

### 2.2.5. X-ray computed tomography

In cubic regular, cubic irregular and trabecular cell configurations, one compression specimen was subjected to X-ray computed tomography at the University of Padua, Italy. The  $\mu$ CT was carried out using a metrological  $\mu$ CT system (Nikon Metrology MCT225). The system is composed of a micro-focus X-ray tube, high-precision linear guideways, 16-bit detector with 2000×2000 pixels, and controlled cabinet temperature maintained at  $20\pm 0.5$  °C. The metrological systems have provided highly accurate scans compared to conventional  $\mu$ CT [47]. The output of the scanning was a 3D voxel-based model of the specimen with a voxel size of 8.3  $\mu$ m. A high-density point cloud was obtained after the reconstruction and surface determination carried out using an adaptive algorithm in the visualization software VG Studio MAX 3.2 (Volume Graphics GmbH, Germany). The voxel-based model was used to compute the struts thickness using the “wall – thickness analysis” module in the visualization software. The point cloud was used to obtain a solid FE model for further analysis.

### 2.2.6. Compression and tensile test

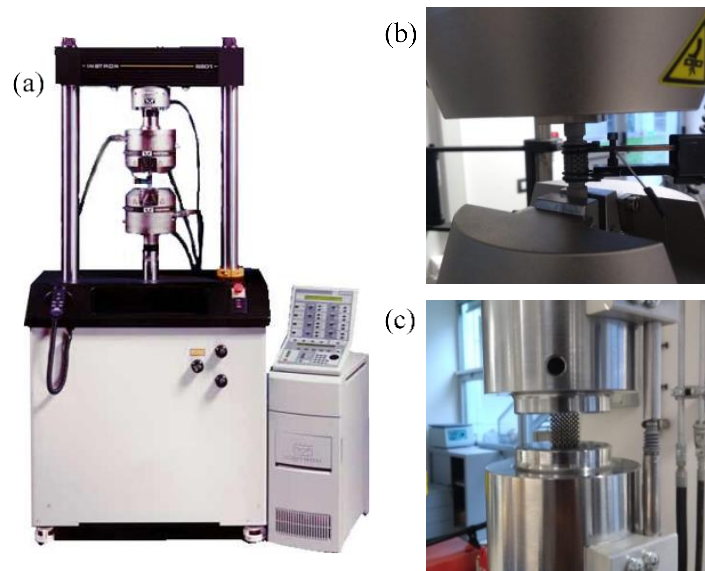


Figure II - 3 (a) Intron universal testing machine (b) tensile test of cellular specimen (c) compression test of cellular specimen

Compression test: The compression test of the cellular materials is carried out according to the standard ISO 13314:2011 specifically formulated for porous cellular materials [48]. A typical stress-strain curve for cellular materials is as shown in Fig. II-4(a). and the parameters that can be derived from the curve are explained in detail in ISO 13314:2011. The slope of the line 1 indicates quasi-elastic gradient (referred

as monotonic Young's modulus in the future discussion), slope of line 2 indicates the elastic gradient (referred as cyclic Young's modulus in the future discussion), plateau stress, offset yield strength and maximum compressive strength can be obtained from the curve.

In this study the compression test was carried out under two conditions, monotonic and cyclic loading conditions. In monotonic test the axial load is applied continuously, and a stress-strain curve is obtained. The slope of the linear region of the stress-strain curve is used to calculate the monotonic Young's modulus, offset yield strength and maximum compressive strength as described above. The cyclic test was carried out to obtain the elastic gradient/cyclic Young's modulus (line 2) by loading the specimen between 20-70% of yield load obtained from monotonic tests. The cyclic test stabilizes the specimen and yields stabilized Young's modulus. The cyclic test was carried out under load-controlled condition using a triangular wave shape for five cycles. The test was performed in an Instron 8516 universal testing machine (Fig. II-3(a)) under room temperature. The samples were loaded with a constant cross head speed of 1mm/min and a data sampling frequency of 1 kHz. The displacement in the sample was measured using an Instron LVDT gauge fixed to the lower grip of the machine (Fig. II-3(c)). Series IX and SAX V9.3 software was used for data acquisition in monotonic and cyclic test, respectively.

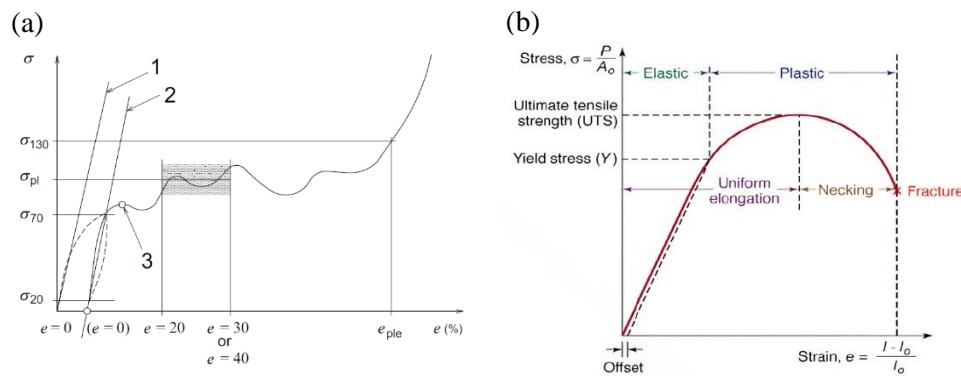


Figure II - 4 (a) Typical compression stress-strain curve for cellular material[48] (b) Typical tensile stress-strain curve[49]

Tensile test: A typical tensile stress-strain curves is as shown in Fig. II-4(b), the parameters such as Young's modulus, 0.2% offset yield strength and ultimate tensile strength are obtained from the stress strain curve. The tensile test of cellular materials is carried out on the specifically designed test specimens mentioned in the section 2.2.1. Given the novelty of the study and the unavailability of testing standards, the test was carried out just like the tensile test of dog bone shaped specimens. In this study, the tensile test was carried out under two conditions monotonic and cyclic, similar to the compression test. The test was carried out on an Instron 8516 universal testing machine under the similar testing conditions employed for compression test. The displacement of the specimen was measured using the 12.5mm Instron extensometer (Fig. II-3(b)). The ends of the extensometer were attached to the end of the cellular material region of the specimen. The data acquisition was carried out using Series IX and SAX V9.3 software for monotonic and cyclic tests.

### 2.2.7. Finite element analysis

In this study the finite element (FE) analysis of the cellular materials is carried out to understand the behavior of as-built samples and as-designed samples. The FE analysis are compared with the theoretical and experimental results. The FE analysis is carried on under different stages:

- FE analysis in elastic region to obtain the Young's modulus.
- FE analysis in elastic-plastic region to obtain the Young's modulus and stress-strain curve.
- FE analysis with strut defects to understand the effect of geometrical deviation.

- FE analysis of the model generated from the tomography data.

### 2.2.7.1. FE analysis elastic region

The FE analysis in elastic region was first carried out for all the three topologies, cubic regular, cubic irregular and trabecular in all the three batches. The analysis was carried out only for the as-designed configuration and the Young's modulus obtained from the FE analysis was fitted using the power law and compared with the ideal behavior according to Gibson-Ashby law [37]. The STL files used for the LPBF process were considered. The STL files were converted into a 3D solid model made up of 10-noded tetrahedron (SOLID187) elements using the software HyperMesh (Altair Engineering Inc.). A 5x5x5mm RVE model was used for all the configurations with atleast 5 junctions in each direction. An example of RVE model is shown in Fig. II-5(a). A mesh convergence analysis was carried out to select the element size, an example of the same is provided in Fig. II-A1 of Appendix 2.7.1, based on which an element size between 0.04 – 0.08mm was used depending on the strut thickness. The number of elements in the FE model varied between 430,000 – 620,000 depending on the strut thickness. An example of a meshed unit cell is as shown in Fig. II-5(b). The boundary conditions for all the three topologies are as shown in Table II-2. For cubic regular structures, top face (side 1) is subjected to displacement, the bottom face (side 3) is constrained in all the DOFs. The cubic irregular and trabecular structures were analyzed using periodic boundary conditions, as listed in Table 2. The material data required for the analysis was the Young's modulus of the bulk material (110GPa) and Poisson's ratio of 0.3. The analysis and the post processing were performed in ANSYS V16®.

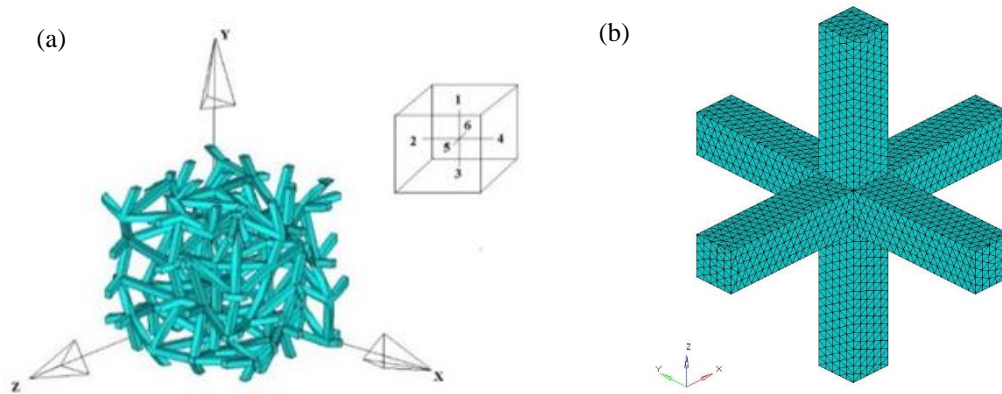


Figure II - 5 (a) RVE model of cubic irregular and description of sides (b) FE model indicating the mesh

Table II - 2 Boundary conditions used in FE elastic analysis

| Sample                         | Side 1 | Side 2         | Side 3             | Side 4                  | Side 5         | Side 6                  |
|--------------------------------|--------|----------------|--------------------|-------------------------|----------------|-------------------------|
| Cubic regular                  | Loaded | Free           | $\delta_{all} = 0$ | Free                    | Free           | Free                    |
| Cubic irregular and trabecular | Loaded | $\delta_x = 0$ | $\delta_y = 0$     | Free <sup>Coupled</sup> | $\delta_z = 0$ | Free <sup>Coupled</sup> |

### 2.2.7.2. FE analysis elastic-plastic region

This section deals with the elastic-plastic response of cellular materials. The outcome of this study was to compare the difference in the mechanical properties of as-designed and as-built cellular materials. The finite element analysis was carried out under both tensile and compression loading conditions. The as-designed STL files were converted to 3D solid mesh models as described in section 2.2.6.1. The analysis and post processing were carried out using ANSYS V16®. The material model used for the elastic-plastic simulation is the Multilinear Isotropic model (MISO) available in ANSYS. The data for MISO material model was obtained from the tensile testing of a standard dog bone

specimen manufactured using the same LPBF process and subjected to similar heat treatment as that of the cellular materials. The stress strain curve of the same is as shown in Fig. II-6 For cubic regular cellular materials, 5x5x5 RVE model consisting of 125-unit cells was considered and for cubic irregular and trabecular, a 5x5x5mm RVE model was considered after a convergence analysis [50]. The number of elements in the FE model was similar to that explained in section 2.2.6.1 and was also dependent on the computation capacity of the system. The RVE model was considered by conducting a convergence analysis by considered different sizes of the RVE model. A representation of RVE size convergence analysis is provided in Fig. II-A2 of Appendix 2.7.2. To replicate the testing conditions, the bottom face of the sample is constrained in all DOFs and the top face is subjected to tensile and compressive displacement loads to reduce the computation time. The displacement values used in based on the experimental stress-strain curves and the cell topology. The displacement values used ensured that the specimens undergo certain deformation after yielding. The stress-strain curves from the FE analysis are compared with the experimental results. The codes used for the elastic and elastic-plastic analysis of RVE models are provided in Appendix I.

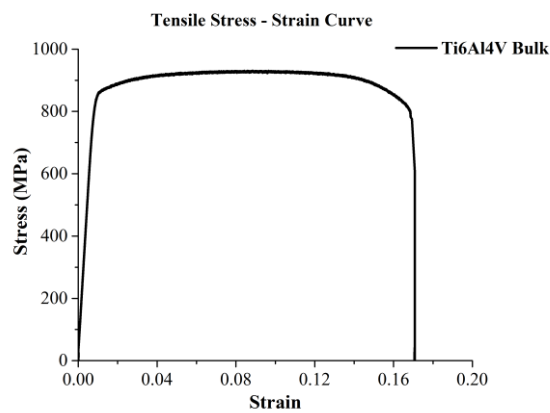


Figure II - 6 Tensile stress-strain curve for bulk Ti6Al4V manufactured using LPBF process used for cellular material

The next step in the analysis was to check the effect of inclined loading on the samples that caused the asymmetric behavior between compression and tensile. To obtain a comparable result, the as-built thickness was considered. Since increasing the as-built strut thickness in cubic irregular and trabecular cellular materials was not easy to replicate, only cubic regular cellular materials were considered in all the three batches. The strut thickness in cubic regular topology was increased by  $\sim 220\mu\text{m}$  in order to match the porosity of the FE model to the as-built cellular materials. Strut defects arising from the LPBF process have not been considered at this stage to reduce the complexity. However, these defects influence the mechanical properties (Dallago et al., 2019). The tensile loading is applied as shown in Fig. II-7(a), and the compression load is applied by increasing the inclination in steps of  $5^\circ$  as shown in Fig. II-7(b). The stress-strain curves obtained are compared with the corresponding experimental curves.

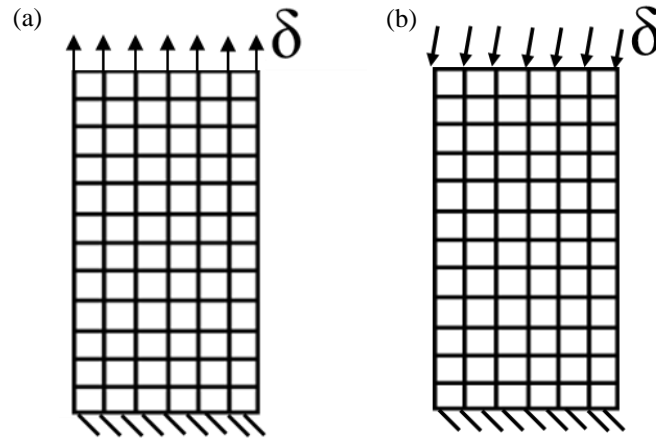


Figure II - 7 Boundary conditions used for FE elastic-plastic analysis (a) tensile loading (b) compression loading with inclined load

### 2.2.7.3. FE analysis with strut defects

The next step in the finite element analysis was to introduce the strut defects in the as-designed FE models. Studies have shown the strut defects not only influence the elastic properties but also the plastic behavior of cellular materials. The FE analysis with strut defects was carried out only for batch C (1520) cubic regular samples since their mechanical properties were of high interest. Also, the FE analysis was carried out only for tensile loading since it is the novelty of the current study.

Before modeling the strut defects, the measurement of the parameters required to produce the FE model was carried by using multiple images of the sample captured using SEM.

*Measurement of strut defects:* The as-designed parameters of the considered topology were strut thickness of 200  $\mu\text{m}$ , a pore size of 1500  $\mu\text{m}$  and a strut cross-section was rectangular cross-section as shown in Figure 1(a). The SEM image of a small region of the sample is as shown in Fig. II-8. The image indicates a clear deviation in the geometrical parameters. The other strut defects that are shown include strut waviness, strut oversizing, varying strut thickness and deviation in the cross-section of the strut.

The geometrical parameters that are used to generate the FE models are tabulated in Table. II-3. The strut oversizing is obtained from the strut thickness values and waviness is obtained from the center offset along the strut. Measurements were carried out for more than 10 struts in each plane to obtain a statistically considerable data. The strut thickness values along the X and Y direction (vertical struts) are approximately twice the thickness value of the as-built structures. Maximum strut thickness was measured along Z – direction in the struts that are printed parallel to the printing direction. This is deviation is due to the absence of support structure while printing horizontal struts.

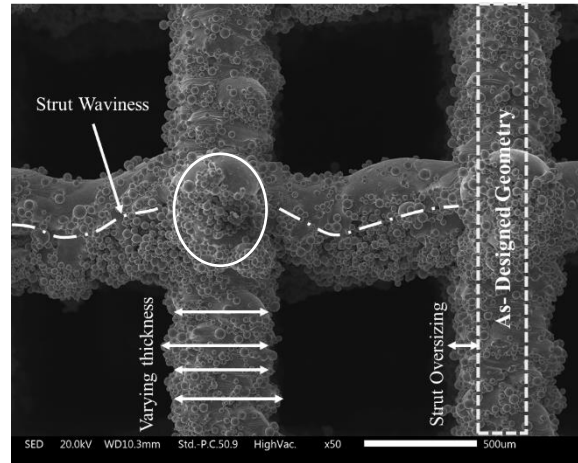


Figure II - 8 Defects in LPBF manufactured cubic regular cellular material

Table II - 3 Measured strut thickness and center offset in all the three directions measured for struts in cubic regular cellular material

| Direction                 | Measured Thickness ( $\mu\text{m}$ ) |        |        | Offset in Center( $\mu\text{m}$ ) |       |       |
|---------------------------|--------------------------------------|--------|--------|-----------------------------------|-------|-------|
|                           | X                                    | Y      | Z      | X                                 | Y     | Z     |
| <b>Average</b>            | 447.44                               | 409.96 | 504.26 | 11.08                             | 6.66  | 19.50 |
| <b>Standard Deviation</b> | 26.27                                | 55.13  | 77.40  | 7.66                              | 4.27  | 9.94  |
| <b>Max value</b>          | 493.90                               | 547.25 | 664.63 | 21.80                             | 11.00 | 34.00 |
| <b>Min Value</b>          | 389.57                               | 297.80 | 334.36 | 2.00                              | 0.19  | 10.00 |

*FE models with strut defects:* The FE models are generated by first developing 3D CAD models with defects using Autodesk Inventor®. This section provides details on the different models generated using the geometrical deviations tabulated above. Initially, a unit cell as shown in Fig. II-9(b-d) is generated. Later the unit cell is repeated in all three directions to generate an RVE model with 125-unit cells for the analysis. Three different models were generated based on the different defects introduced.

- *Average dimensions (AD):* The struts had a uniform cross-section with average strut thickness values from Table II-3. The unit cell of the CAD model is as shown in Fig. II-9(b). The struts perpendicular to the printing plane are thinner when compared to the struts parallel to the printing plane.
- *Varying cross-section (VCS):* The model considers the varying strut thickness in a single strut. The strut thickness was measured at 10 different locations of a single strut. These thickness values were used to generate different sections as shown in Fig. II-9(a) and joined using the loft option to obtain the CAD model shown in Fig. II-9(c).
- *Varying cross-section with offset (VCS with offset):* This model introduces all the three defects mentioned, strut oversizing, varying thickness, and strut waviness. The center offset measured for different sections in the strut is considered along with the varying thickness mentioned in the above paragraph to generate different sections as shown in Fig. II-9(a) and the generated CAD model is as shown in Fig. II-9(d).

All three models are generated using rectangular and elliptical cross-sections to incorporate the effect of cross-section shape. The difference between the AD samples and VCS with offset is indicated by overlapping the CAD files as shown in Fig. II-9(e).

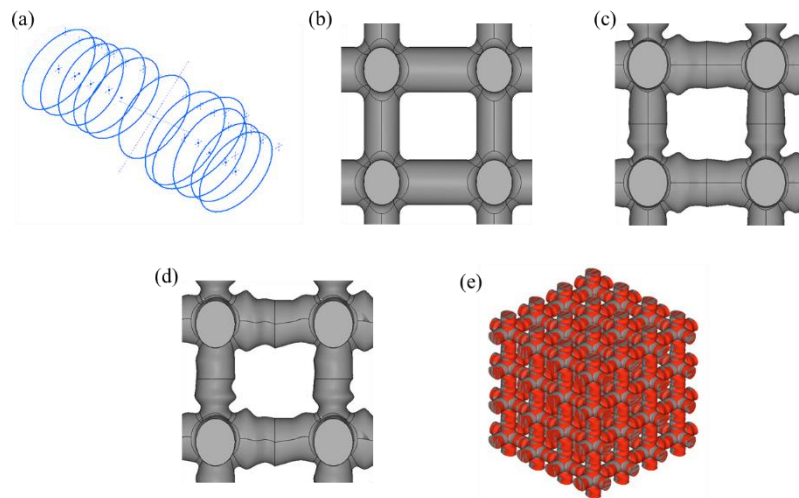


Figure II - 9 Representation of elliptical cross-section used to study defects (a) varying cross-section used to generate struts (b) AD model with uniform thickness along strut (c) VCS model with thickness variation along a strut (d) VCS with offset considering strut waviness (e) overlap of AD and VCS with offset CAD model

The procedure followed for the FE analysis is similar to the procedure explained in section 2.2.6.2. The stress-strain curves are compared with the tensile experimental results.

#### 2.2.7.4. Tomography FE model

As mentioned in section 2.2.5,  $\mu$ CT data of cubic regular, cubic irregular, and trabecular specimens were used to generate FE models for elastic-plastic analysis under tensile loading.

Prior to the FE analysis, the generation of the FE model from the point cloud involves certain steps; (i) down sampling of the high-density point cloud, carried out using MeshLab® (ii) generation of STL files (2D surface) using triangular elements (iii) generation of the solid 3D model with 10-noded tetrahedron elements. Steps (i) and (ii) were carried out using MeshLab® and the (iii) step was carried out using the shrink-wrap option in Hypermesh®, the steps are shown in Fig. II-10.

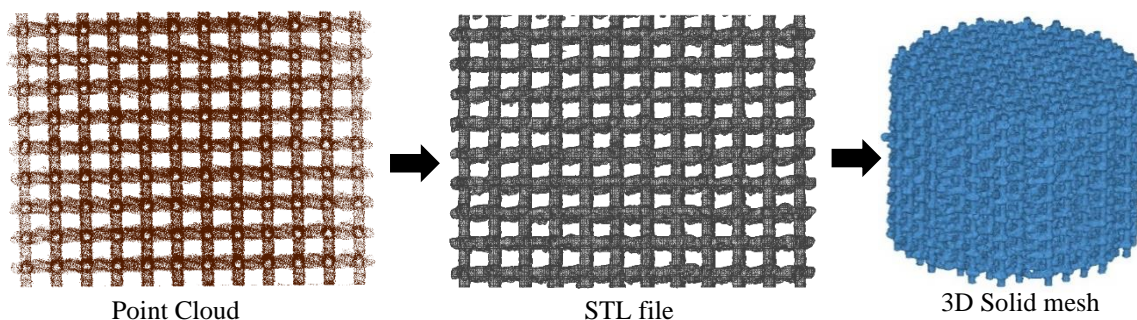


Figure II - 10 Conversion of point cloud to FE model

Since the analysis of the full FE model shown in Fig. II-10 was not feasible due to computational limitations, an RVE model was generated for all three configurations as shown in Fig. II-11. The size of the cubic regular was selected in order to have 125-unit cells as mentioned in the previous chapter. For cubic irregular and trabecular configurations, an RVE size was selected to have at least 4-6 nodes in each direction similar to the cubic regular configurations and also based on RVE models for foams [52–55]. A RVE size convergence analysis shown in Fig. II-A2 of Appendix 2.7.2 was carried out. 10

– noded tetrahedron element was used similar to the as-designed FE models and the number of elements was also in between 800,000 -1,500,000 due to thicker struts despite using RVE models. The equivalent plastic strain plots were used to evaluate the failure in the tomography FE models.

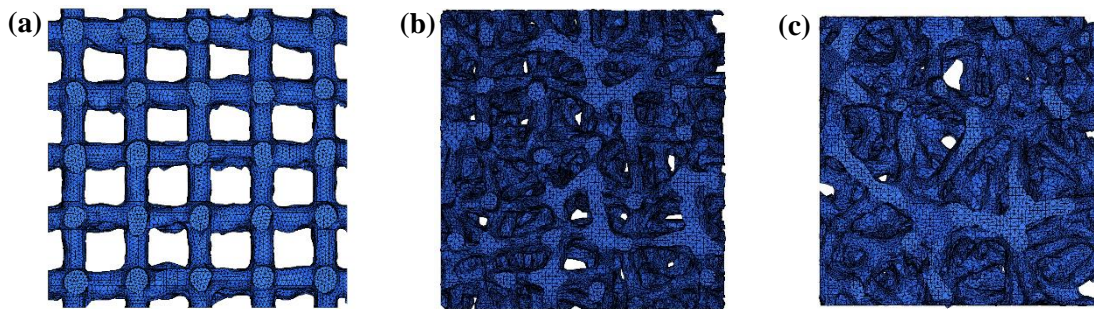


Figure II - 11 RVE FE models of (a) Cubic regular (b) Cubic irregular (c) Trabecular

## 2.3. Results and discussion

### 2.3.1. Microstructure

In general, Ti6Al4V components manufactured using the LPBF process have an as-built  $\alpha'$ -martensitic phase [56]. The  $\alpha'$ -martensitic phase is brittle in nature, which is detrimental to mechanical properties. The samples are subjected to heat treatment as described in section 2.2.1. The microstructure is transformed into the  $\alpha+\beta$  phase. The microstructure of the specimen is as shown in Fig. II-12. A uniform basket weave microstructure with  $\alpha+\beta$  lamellae phase is observed in both planes. Small traces of coarse  $\alpha$  phase are also observed. The lamellae tend to orient themselves towards the building direction in the lateral plane as shown in Fig. II-12(b).

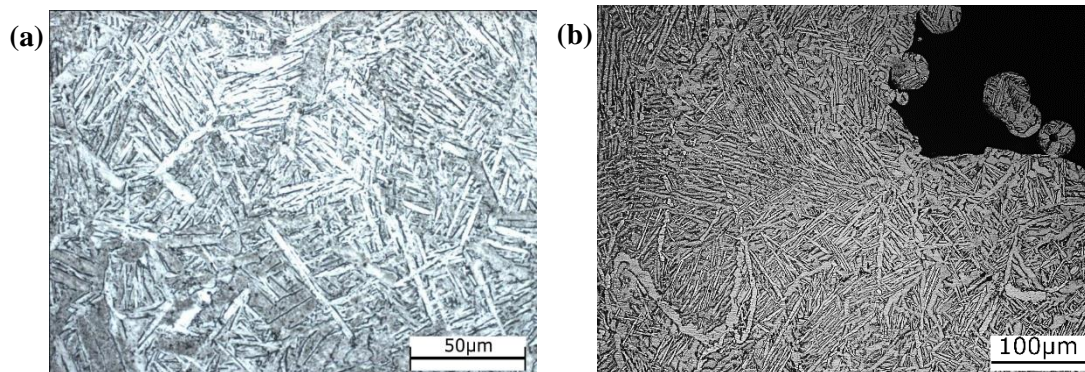


Figure II - 12 Microstructure (a) horizontal plane; perpendicular to printing direction (b) lateral plane; parallel to printing direction

### 2.3.2. Porosity analysis

The results from the porosity calculate for manufactured specimens and the designed porosity are tabulated in Table. II-4. A clear difference between the designed porosity and measured porosity is seen. Comparing the different batches of specimen, a maximum relative error of ~50% was observed in the batch B specimens for cubic irregular configuration. Batch A specimens had relative error in the range of 20-25%, however trabecular specimens in batch A had very small deviation. Batch C samples had the highest designed porosity >90% but has least relative error when compared to batch A and B.

Table II - 4 Measured and designed porosity with relative error for all batches and topology

|                | Sample          | Measured Porosity (%) | Designed Porosity (%) | Relative Error (%) |
|----------------|-----------------|-----------------------|-----------------------|--------------------|
| <b>Batch A</b> | Cubic regular   | 59(8)                 | 75                    | 21.16              |
|                | Cubic irregular | 57(7)                 | 75                    | 24.27              |
|                | Trabecular      | 59(3)                 | 63                    | 7.42               |
| <b>Batch B</b> | Cubic regular   | 44(5)                 | 80                    | 44.63              |
|                | Cubic irregular | 39(3)                 | 79                    | 50.45              |
|                | Trabecular      | 46(6)                 | 72                    | 36.72              |
| <b>Batch C</b> | Cubic regular   | 77(1)                 | 93                    | 17.06              |
|                | Cubic irregular | 76(2)                 | 93                    | 18.62              |
|                | Trabecular      | 76(2)                 | 92                    | 17.42              |

Comparing the porosity by taking the cell topology into consideration, the trabecular specimens had the lowest relative error in all the batches. Further explanation on the same is provided by taking the morphological measurements into consideration in the section 2.3.3.

### 2.3.3. Morphological analysis

The morphological analysis includes thickness measurement and pore size measurement in the manufactured cellular materials. An example of SEM image used for thickness measurement is as shown in Fig.II-13(a) and pore size measurement using stereomicroscope is shown in Fig. II-13(b). The thickness and pore size measurement are carried out along two planes and values are tabulated in Table. II-5 and 6.

A clear increase in the strut thickness is observed for all the topologies in both the planes. This increase in thickness is responsible for the decrease in the porosity of the specimens indicated in Table. II-4. The difference between the designed strut thickness and the measured average strut thickness was more than 200 $\mu\text{m}$  for all the topologies and batches. The presence of satellite powder particles on the strut increases the strut thickness. The powder particles attach to the strut surface due to the dissipation of heat from the solid strut to the powder bed. Also, the increase in the strut thickness is attributed to the LPBF process parameter such as power of the energy source which influences the melt pool, building layer thickness, and slicing of the input STL file.

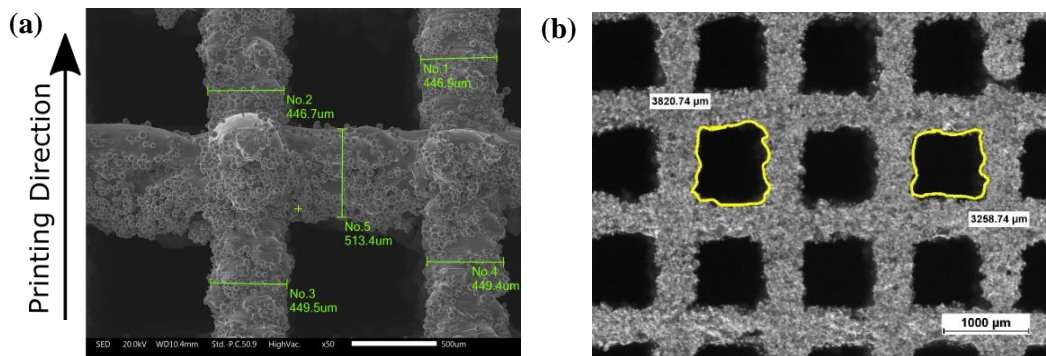


Figure II - 13 (a) SEM image showing the strut thickness (b) stereomicroscope image indicating the pore outline

Table II - 5 Strut thickness and feret diameter along lateral plane; parallel to printing direction

|                | Cubic regular                 |                           | Cubic irregular               |                           | Trabecular                    |                           |
|----------------|-------------------------------|---------------------------|-------------------------------|---------------------------|-------------------------------|---------------------------|
|                | Min. Feret Diameter (Std Dev) | Strut thickness (Std Dev) | Min. Feret Diameter (Std Dev) | Strut thickness (Std Dev) | Min. Feret Diameter (Std Dev) | Strut thickness (Std Dev) |
|                | [ $\mu\text{m}$ ]             | [ $\mu\text{m}$ ]         | [ $\mu\text{m}$ ]             | [ $\mu\text{m}$ ]         | [ $\mu\text{m}$ ]             | [ $\mu\text{m}$ ]         |
| <b>Batch A</b> | 1140(70)                      | 760(60)                   | 1380(230)                     | 780(109)                  | 1430(300)                     | 900(70)                   |
| <b>Batch B</b> | 350(6)                        | 460(50)                   | 440(70)                       | 480(80)                   | 560(120)                      | 490(40)                   |
| <b>Batch C</b> | 1100(60)                      | 460(30)                   | 1130(260)                     | 490(40)                   | 1320(240)                     | 480(80)                   |

Table II - 6 Strut thickness and feret diameter along horizontal plane; perpendicular to printing direction

|                | Cubic regular                 |                           | Cubic irregular               |                           | Trabecular                    |                           |
|----------------|-------------------------------|---------------------------|-------------------------------|---------------------------|-------------------------------|---------------------------|
|                | Min. Feret Diameter (Std Dev) | Strut thickness (Std Dev) | Min. Feret Diameter (Std Dev) | Strut thickness (Std Dev) | Min. Feret Diameter (Std Dev) | Strut thickness (Std Dev) |
|                | [ $\mu\text{m}$ ]             | [ $\mu\text{m}$ ]         | [ $\mu\text{m}$ ]             | [ $\mu\text{m}$ ]         | [ $\mu\text{m}$ ]             | [ $\mu\text{m}$ ]         |
| <b>Batch A</b> | 1060(20)                      | 760(20)                   | 980 (250)                     | 760(30)                   | 1250(320)                     | 700(240)                  |
| <b>Batch B</b> | 350(30)                       | 290(40)                   | 660(90)                       | 360(40)                   | 850(130)                      | 450(50)                   |
| <b>Batch C</b> | 1030(10)                      | 440(30)                   | 1400(600)                     | 390(30)                   | 1500(230)                     | 440(30)                   |

The comparison of strut thickness from the lateral and horizontal plane indicated that the strut thickness is higher in struts seen lateral plane. The decrease in the pore size is directly related to the increase in the strut thickness in all the samples.

#### 2.3.4. Morphological analysis using tomography data

The tomography analysis of the specimens provided information on strut thickness, thickness variation, and overall porosity. An example of the strut thickness variation in cubic regular specimens is shown in Fig. II-14. This indicates that vertical struts are uniform compared to horizontal struts, which indicated uneven struts due to thickness variation and center offset. The strut thickness distribution for all the cell topologies is shown in Fig. II-14(b-d). The distribution indicated that maximum surface area has thickness values between 350 – 400  $\mu\text{m}$ ., this is close to the thickness values evaluated from the spectroscopy images from section 2.3.3. The uneven thickness of horizontal struts is due to the lack of support during the LPBF process that leads to melting of excess material below the first layer that increases thickness and attach loose particles.

The center offset is calculated by taking the difference between the center of as-designed struts and sections of the as-built struts shown in Fig. II-14(e). The normalized center offset from Fig. II-14(f) gives a clear relation between the orientation of struts and the waviness in the struts. The results indicate that the vertical struts had the least offset and reproduced well compared to irregular and horizontal struts as indicated by the width of the distribution.

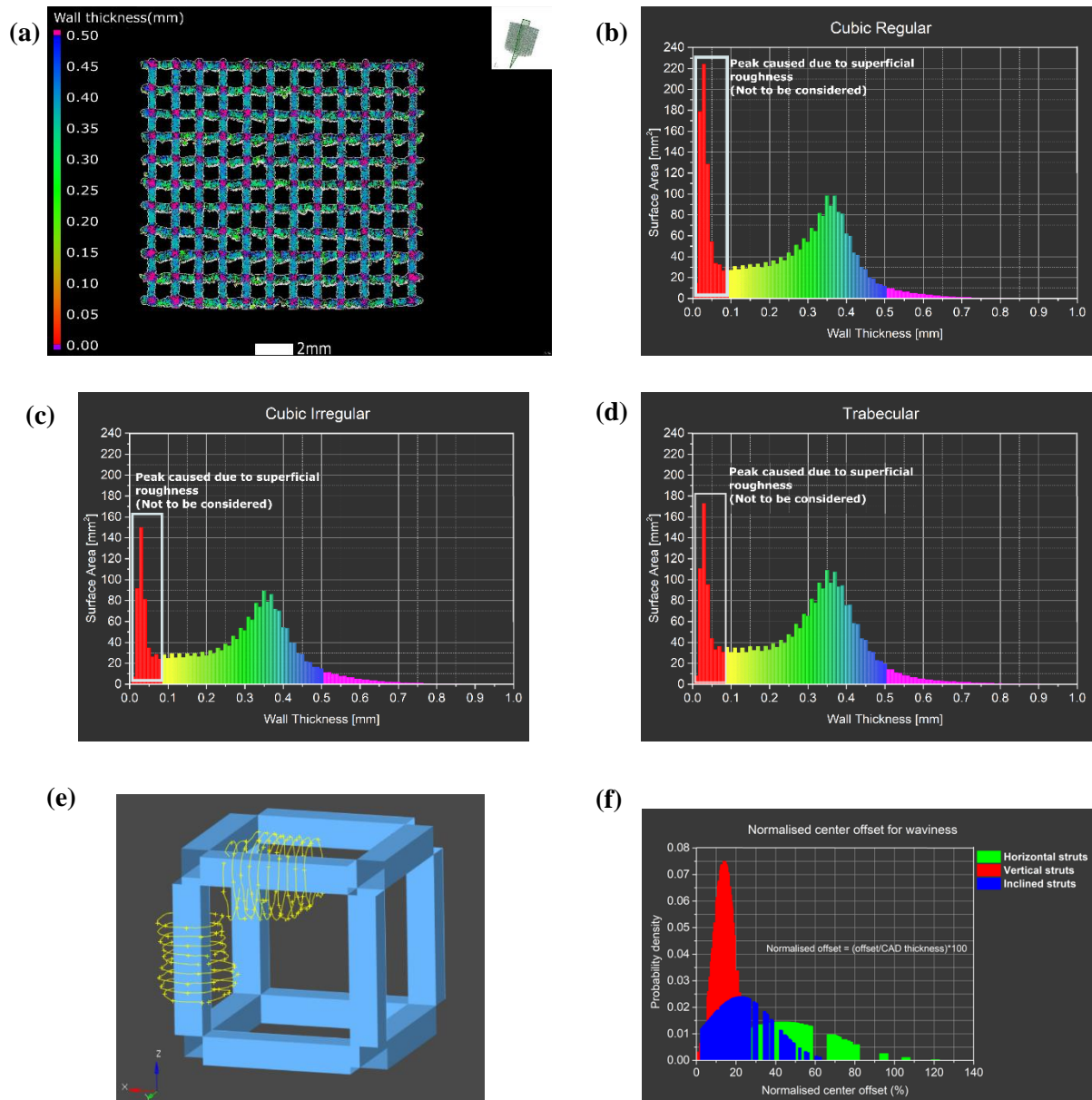


Figure II - 14 Evaluation of strut thickness using tomography data (a) Representation of strut thickness variation in cubic regular (b-d) Strut thickness variation in cubic regular, cubic irregular, and trabecular structure respectively (red peaks is due to the complex topography of the strut surfaces as explained by Zanini et al.[57], hence it is not considered); (e) Difference between as-built and as-designed strut (f) Normalized center offset for different strut orientation

## 2.3.5. Experimental results

### 2.3.5.1. Compression test

The compression test was carried out under two loading conditions, monotonic and cyclic. Three specimens were tested under monotonic test and two specimens under cyclic loading. The stress-strain curve obtained from monotonic test of one specimen in each batch is shown in Figure. II-15(a). The compression test was carried out until a failure was observed in the specimen. The stress-strain curve of batch B shows an increase the stress with the strain after the elastic region, this is due to the high relative density/low porosity of the batch B specimens. The load required to see a complete failure in the specimen exceeds the load capacity of the machine (100 kN). A rapid densification was observed in the batch B specimens without any plateau region. The batch A specimens did not exhibit a clear plateau region as seen in batch C specimens. From the three batches, the batch C specimens reached

higher strain values when compared to other two batches. In batch C, the cubic regular samples reached strain values of 0.1 and trabecular samples reached strain values as high as 0.4.

The variation of strength and stiffness with respect to the porosity for all the batches and topologies is plotted in Fig. II-15 and 16. As per the Gibson-Ashby law, the strength and stiffness of cellular materials reduce with decrease in the porosity. Fig. II-15(b) and Fig. II-16(c) indicates the 0.2% offset yield strength and monotonic Young's modulus respectively. The batch B specimens had the lowest porosity in the range of 35 – 45%. Their monotonic Young's modulus was in between 10 – 20 GPa and yield strength of 250 -220 MPa. The batch A specimens had porosity in the range of 55–60% for all the cell topologies. The monotonic Young's modulus was between 7 – 13 GPa and the yield strength was between 120 – 150 MPa. The last batch of specimens, batch C had the highest porosity greater than 75%. Hence, they had the lowest Young's modulus and yield strength that varied between 1.2 – 3 GPa and 40 – 60 MPa respectively. The cyclic Young's modulus values shown in Fig. II-16(b) an increase when compared to monotonic Young's modulus by 3 – 6 GPa depending on the cell topology and the porosity. This increase in the stiffness in cyclic loading is due to the stabilization of the structure after first unloading cycle. The stabilization is achieved due to compaction and local plasticization at the junctions during the first loading cycle. The graph in Fig. II-20(b) indicates the stabilization in the Young's modulus after first cycle and the modulus remains constant from second cycle to the fifth cycle.

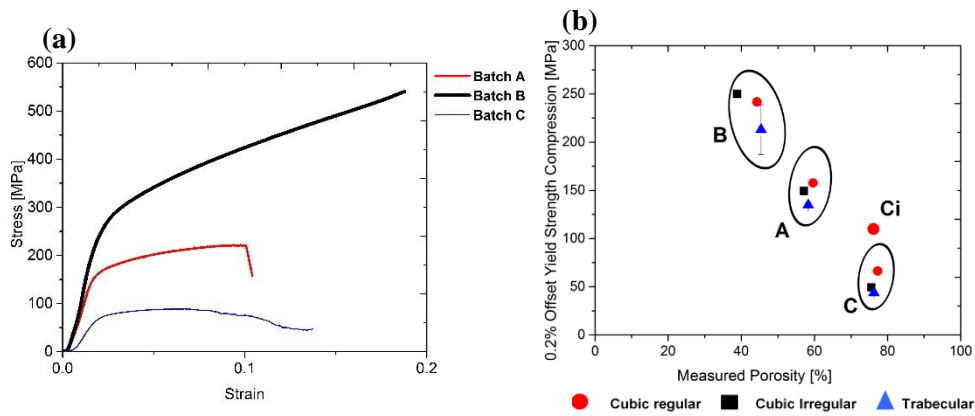


Figure II - 15 (a) General stress-strain curve obtained for different batches (b) 0.2% offset yield strength in compression

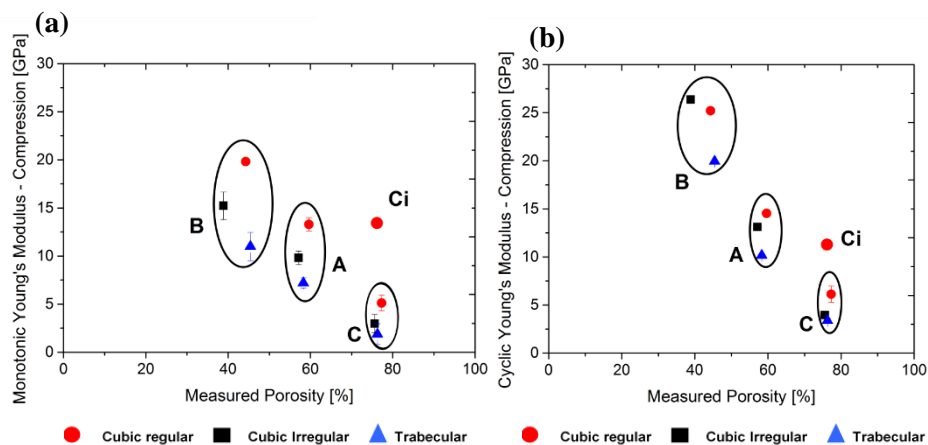


Figure II - 16 Variation of compression Young's modulus with porosity (a) monotonic Young's modulus (b) Cyclic Young's modulus

As discussed before, the compression test was repeated for another batch of regular specimens, batch Ci which had porosity value similar to batch C specimen. The strength and stiffness values of batch Ci

are compared with batch C values in the graphs shown above. The batch Ci specimens had a monotonic Young's modulus of 13.43 GPa which is almost twice the value obtained for batch C specimen. The cyclic Young's modulus was 11.3 GPa which is higher than the batch C specimen but was slightly lower than the monotonic Young's modulus of batch Ci. This decrease in the cyclic Young's modulus is also due to the stabilization of the cellular materials as explain previously.

By considering the cell topology as a criterion, the cubic regular specimens had the highest strength and stiffness in compression despite the misalignment, followed by cubic irregular and trabecular. The presence of struts along the loading direction in cubic regular specimens increases the stiffness of the cellular material. In all the batches, the trabecular specimens had the lowest strength and stiffness. The effect of irregularity was highest in the batch with highest porosity and the effect was not seen in batch B specimens which had the lowest porosity.

### 2.3.5.2. Tensile test

Similar to the compression test, tensile test was also carried out under two loading conditions, monotonic and cyclic. Three specimens were tested under monotonic loading and two specimens under cyclic loading. The general stress-strain curve obtained from the monotonic test is as shown in Fig. II-17(a), the curves indicate the behavior of the specimens in all the three batches. The curve indicate that batch B specimens reached higher stress values for a given strain when compared to batch A and batch C due to their low porosity and high density. A sudden failure was observed in batch B specimens, while in batch A and batch C the stress gradually decreases after reaching a maximum value.

The monotonic Young's modulus and the 0.2% offset yield strength are obtained from the stress-strain curves. The variation in the properties with respect to the specimen porosity and the cell topology is shown in the Fig. II-17(b) and 18(a). Considering just the porosity as the criteria, the batch B specimens which has the lowest porosity values had the highest monotonic Young's modulus between the range 40 – 45 GPa, and yield strength of 225 – 250 MPa. The batch A specimens with the porosity between 55 – 60% had a Young's modulus of 15 – 20 GPa and yield strength in the range of 80 – 120 MPa. The batch C specimens which had the highest porosity values greater than 75% had stiffness between 5 – 12 GPa and yield strength between 80 – 120 MPa. The cyclic Young's modulus obtained from the unloading cycle is shown in Fig. II-18(b). The cyclic Young's modulus values are in close agreement with the monotonic Young's modulus values. The stabilization in the cyclic tensile test is shown in Fig. II-20(b), the stabilization in the structure is obtained from the 2<sup>nd</sup> cycle. Similar to the compression test, another batch of specimen (batch Ci, cubic regular) was tested even for tensile loading. The Young's modulus and the yield strength for batch Ci are 13.8 GPa and 80 MPa respectively. These values are in close agreement with the strength and stiffness of batch C, cubic regular specimens.

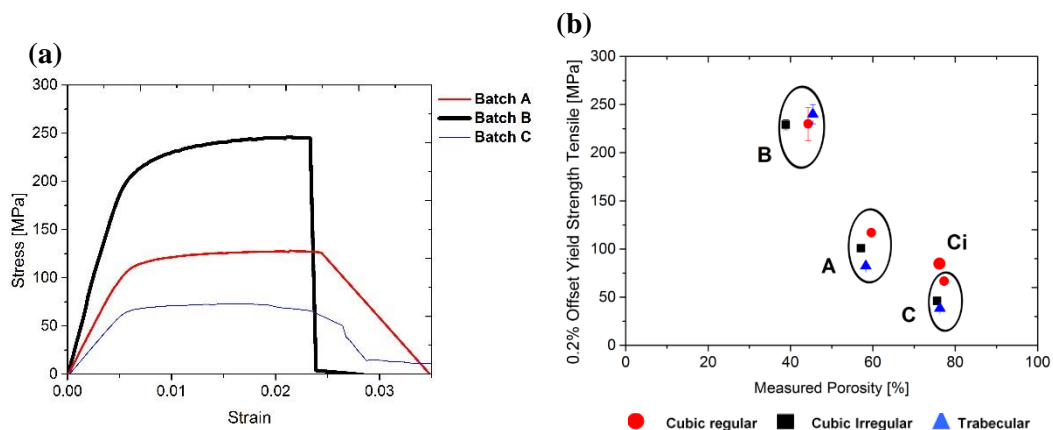


Figure II - 17 (a) General stress-strain curve obtained for different batches (b) 0.2% offset yield strength in tensile

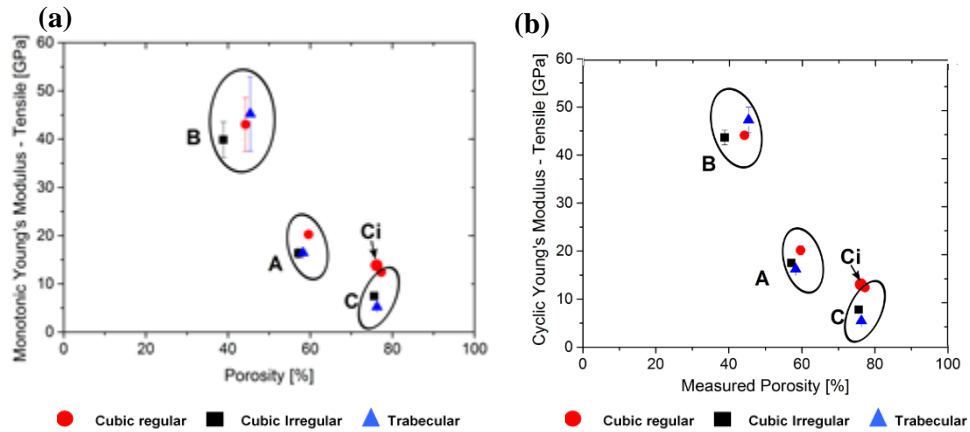


Figure II - 18 Variation of tensile Young's modulus with porosity (a) monotonic Young's modulus (b) Cyclic Young's modulus

Taking the cell topology as a criterion for comparison, the cubic regular specimens had the highest strength and stiffness in batch A and batch C, followed by cubic irregular and trabecular. However, in batch B, trabecular specimens had the highest strength and stiffness compared to the cubic regular and cubic irregular. This is due to the high density of batch B specimens and especially trabecular specimens which has thick nodes due to random arrangement of struts. These thick nodes behave differently under tensile loading, making this cell topology and porosity the stiffest of the considered lot.

### 2.3.5.3. Comparison of compression and tensile test

This section compares the strength and stiffness from the compression and tensile test. The asymmetry between the compression and tensile loading is clearly seen in this section. A study on the NiTi alloy [58] for compression and tensile loading displayed a higher modulus in compression. However, in this study, a higher Young's modulus is observed under tensile loading. A comparison of the Young's modulus under monotonic and cyclic loading is as shown in Fig. II-19(a) and (b) and the 0.2% offset yield strength is compared in Fig. II-20(a). The yield strength values are closer to the bisector line for batch B and batch C and was slightly higher in compression for batch A specimens. The modulus comparison shows that a higher modulus in tension is observed for all the batches and all the cell topologies. But as mentioned in the previous section 2.3.4.1, a change in the Young's modulus is observed between monotonic and cyclic loading, and this difference is higher for compression loading. The change in the Young's modulus with each cycle is as shown in Fig. II-20(b). The graph indicates a clear jump for compression specimens, while in tensile the graph is almost a straight line.

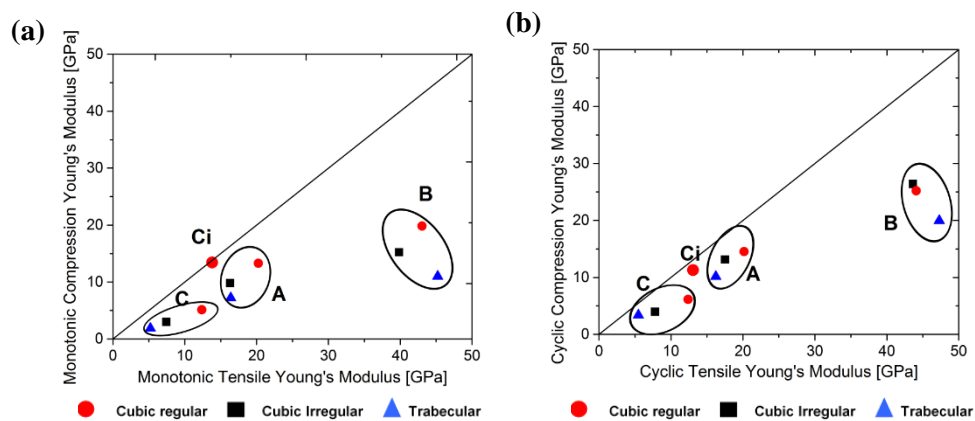


Figure II - 19 Comparison of tensile and compression (a) monotonic Young's modulus (b) cyclic Young's modulus

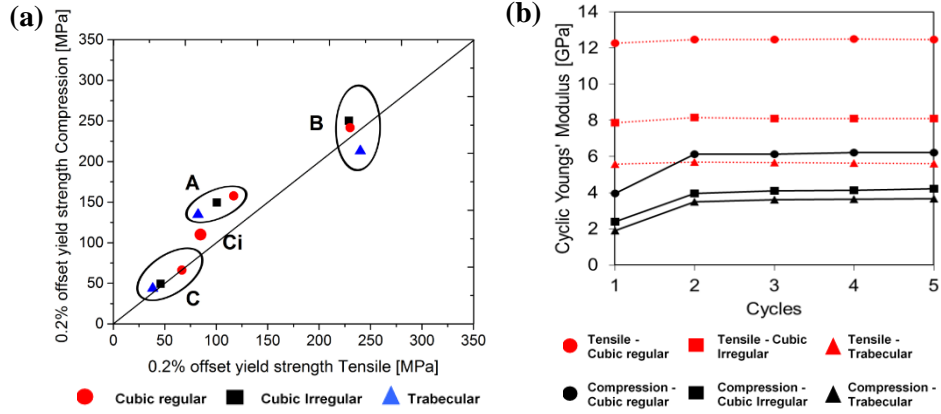


Figure II - 20 (a) Comparison of offset yield strength in tensile and compression (b) variation of cyclic Young's modulus with each cycle

The values of batch Ci (samples with no inclination) are also plotted in the graphs Fig. II-19(a) and (b) and Fig. II-20(a), the values are closer to the bisector line, indicating that no difference is observed between compression and tensile loading. The results of the cubic regular specimens of batch C and batch Ci are tabulated in Table. II-7 for better comparison. The Young's modulus in tensile loading are closer to each other, while the increase in the Young's modulus in compression is due to the strut inclination in the compression specimens. The results indicate that inclined struts influence the mechanical properties to a considerable extent. The uniform behavior displayed by batch Ci cubic regular structures under tensile and compression was due to the accurate alignment of struts in the loading direction. FE analysis was carried out to further study the behavior of as-designed and as-built cellular materials in the next sections. A part of the study also includes the effect of inclination on the Young's modulus.

Table II - 7 Comparison of Young's modulus for batch C and batch Ci

| Loading type | Loading condition | Young's Modulus (GPa) |          |
|--------------|-------------------|-----------------------|----------|
|              |                   | Batch C               | Batch Ci |
| Compression  | Monotonic         | 5.12                  | 13.43    |
|              | Cyclic            | 6.14                  | 11.28    |
| Tensile      | Monotonic         | 12.38                 | 13.82    |
|              | Cyclic            | 12.38                 | 13.10    |

## 2.3.6. FE analysis

### 2.3.6.1. FE analysis elastic region

The results discussed in the section deals with the FE analysis in the elastic regime that provides the Young's modulus of the cellular materials. The FE results are compared with the theoretical predication of the Gibson-Ashby model for cellular materials considering the relative density [37]. The results of the as-designed Young's modulus are compared with the theoretical predications as shown in Fig. II-21(a). The slope of the curve is closer to 2 for cubic irregular and trabecular specimens indicating a bending dominated behavior and slope is closer to 1 for cubic regular specimens indicating a stretching dominated behavior. However, the results did not change when the FE models were tested with and without the periodic boundary conditions.

To evaluate the experimental results for all the as-built cellular materials i.e., cubic regular, cubic irregular and trabecular theoretical calculations from Gibson – Ashby model was carried out.

For as-built structures, to evaluate the experimental results, theoretical calculations have been considered for all the structures. Due to the deviation in the compression test results, the theoretical calculations were compared with the tensile test results only, as shown in Fig. II-21(b). An overlap between the theoretical and experimental results was observed for cubic irregular and trabecular specimens was seen. These results also confirmed the bending dominate behavior of cubic irregular and trabecular specimens. However, a difference between the theoretical and experimental results was observed for cubic regular samples. The experimental results show that the specimens are not purely stretching dominated in this case. Also, the Gibson – Ashby model works well for porosity values > 70%. Therefore, some of the discrepancy between the experimental and theoretical results can be attributed to this limitation as well.

FE analysis of as-built cellular materials is carried out only for cubic regular structures since it was easy to create CAD models with increasing the strut thickness as mentioned in section 2.2.6.2. A vertical load in terms of displacement was applied for tensile loading analysis. Fig. II-22(b) clearly indicates that the Young’s modulus from the FE analysis overlap with the experimental results of tensile cyclic loading. But in order to compensate for the lower compression Young’s modulus measured through experiments, a relative inclination between the struts and loading axis was used. To confirm the hypothesis of decreased Young’s modulus in compression loading due to inclined load, the FE analysis in compression was carried out under inclined loading with increasing the inclination in steps of 5° (w.r.t vertical direction) until a value closer to the experimental results was obtained. The variation of Young’s modulus with respect to inclination is as shown in Fig. II-22(a). The decrease in Young’s modulus with increase in the inclination is compared with the experimental values of both batch C and batch Ci. The modulus at 0° inclination matches with the batch Ci results and the batch C results are in closer agreement with the values obtained for an inclination of ~10°. The effects of strut defects such as waviness and varying thickness are not considered in the elastic region analysis. The elastic – plastic analysis of as-designed and as-built cellular materials is discussed in the next section to understand the effect of increased porosity on the overall behavior of the cellular materials. A part of the study also includes inclined loading to compare the stress-strain curves obtained from the compression test. Furthermore, strut defects such as strut waviness and varying thickness are also studied for cubic regular specimens of batch C.

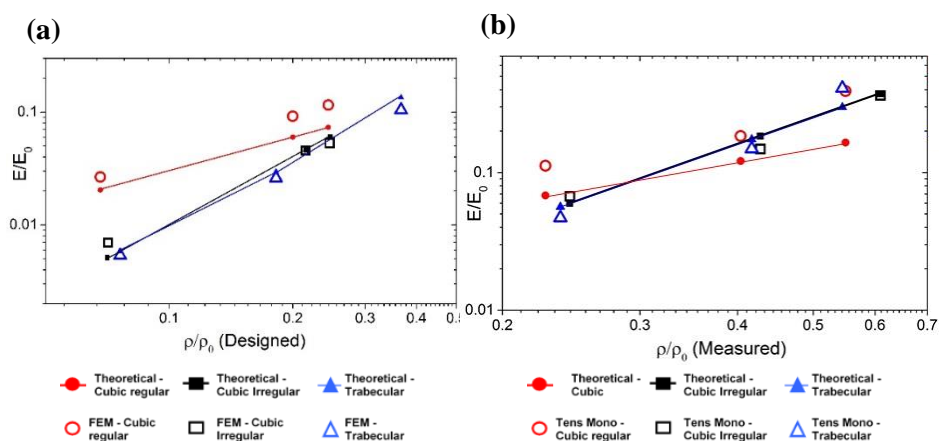


Figure II - 21 (a) Comparison of FEM and theoretical Young’s modulus for designed porosity samples (b) Comparison of monotonic tensile Young’s modulus with theoretical Young’s modulus

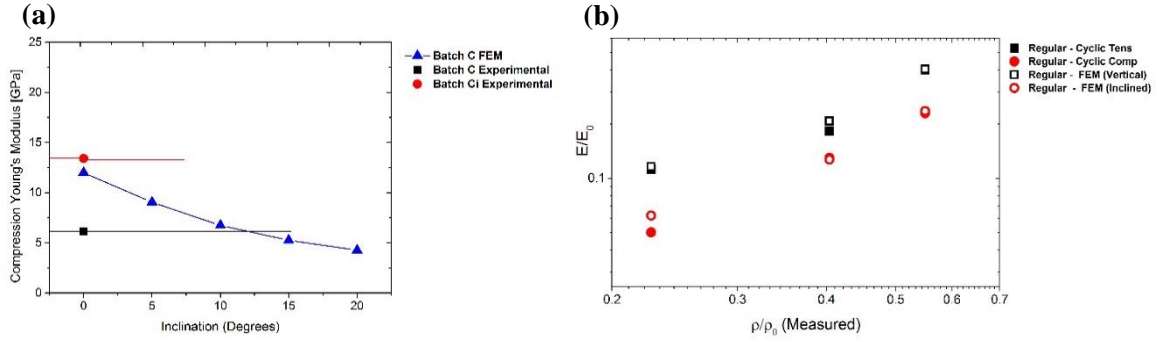
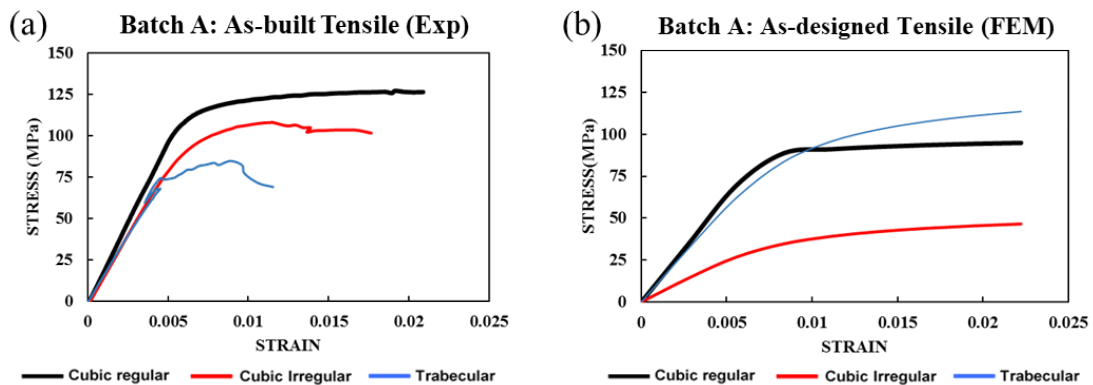


Figure II - 22 (a) Effect of inclination on measured stiffness values (b) Comparison of cyclic compression Young's modulus in compression and tensile Young's modulus with FEM (vertical and inclined loading)

### 2.3.6.2. FE analysis elastic-plastic region

The FE analysis in the elastic-plastic region was carried in three stages: (i) Tensile test of as-designed cellular materials for all topologies (ii) Compression test of as-designed cellular materials and (iii) Compression test with inclination and tensile test for as-built cubic regular structures.

*Tensile test of as-designed cellular material:* The FE analysis is carried out in elastic-plastic region as mentioned in section BBB. The tensile loading is applied on the top face using a displacement. The strain values applied in the FE analysis is similar to the experimental values for all the batches. Due to the decrease in the porosity values after the LPBF process, the mechanical properties of the specimens obtained from the experiment are higher than the expected values [26, 53]. A comparison of as-designed and as-built stress-strain curves as shown in Fig. II-23. The FE results indicate that the cubic regular specimens had the highest strength and stiffness compared to cubic irregular and trabecular in as-designed and as-built curves, except for the batch A FE results. This behavior of trabecular specimens in batch A is highly dependent on the section of the RVE model considered for the study. However, for batch C specimens, the effect of irregularity is predominant when compared to batch A and batch B due to their low porosity values. This is further confirmed when we compare the curves of batch B (as-built) shown in Fig. II-23(c) with batch B (as-designed) shown in Fig. II-23(d). An overlap of experimental curves is seen in the experimental curves, while a clear effect of topology is seen for FE curves of as-designed configuration.



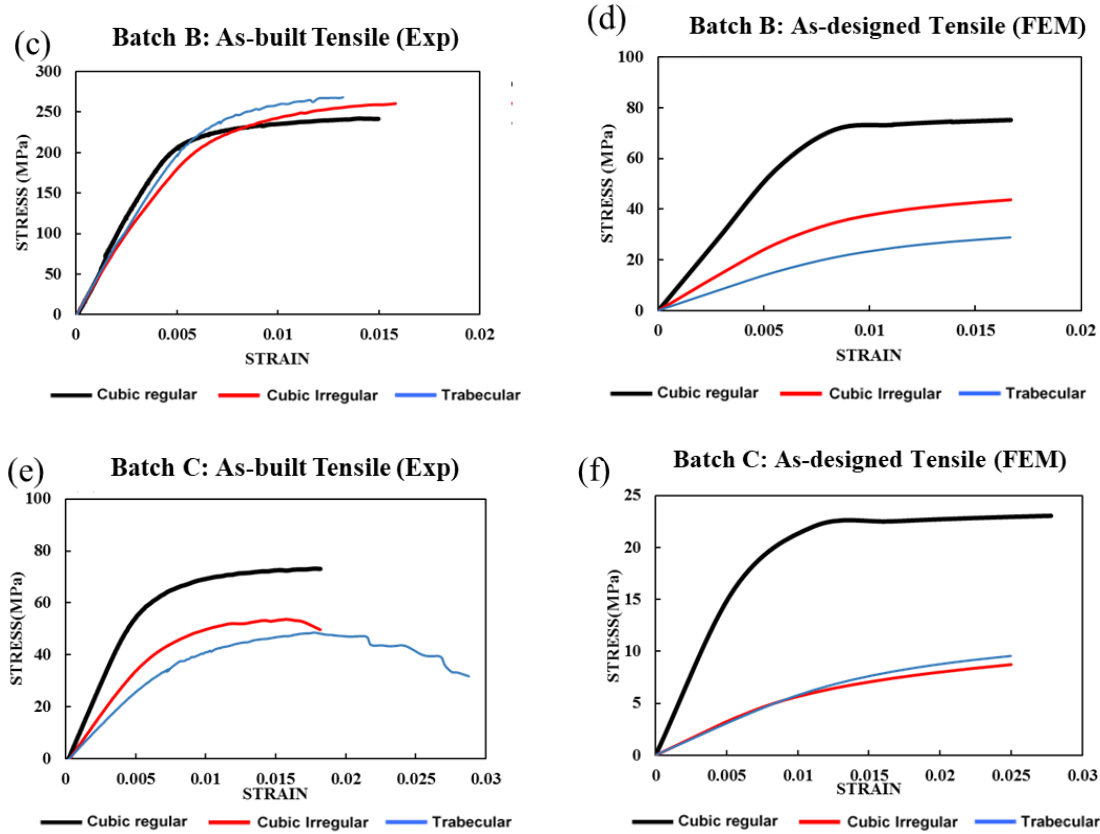


Figure II - 23 Tensile stress-strain curves in experimental (as-built) and FEM (as-designed): (a) and (b) batch A, (c) and (d) batch B, (e) and (f) batch C

*Compression test of as-designed cellular materials:* The compression loading of as-designed specimen is carried out without any inclination. To initiate the compression loading in the FE models, a small displacement was provided in the horizontal direction along with the vertical displacement. Since the porosity of the as-designed specimens were higher than the as-built values, the FE analysis were carried out for strain values  $<0.1$ . The stress in the specimens was obtained by considering the nominal area of the RVE model. The stress-strain curves are obtained and are shown along with the experimental stress-strain curves in Fig. II-24. The stress values reached by the as-designed samples is lower than the as-built samples due to their higher porosity. Despite the decrease in the porosity after manufacturing, the overall behavior of different cell topologies remains the same. Comparing the Fig. II-24(c) and (d) the batch B specimens had the lowest porosity and therefore we do not see any decrease in the stress for as-designed as well as for as-built configurations. The curves of batch C specimens shown in Fig. II-24(d) and (e) for as-built and as-designed configuration show a similar behavior. The cubic regular specimen of batch C show a decrease at very low strain values just like in the experiments, this is due to the thin struts that undergo buckling and initiate failure in one layer. In batch A specimens, the curves shown in Fig. II-24(b) indicate that the trabecular specimens have higher strength and stiffness, this is due to some of dense nodes found in the considered RVE model. Apart from the batch C cubic regular specimen, all the other as-designed configurations indicated a plateau region. Some discrepancy is seen when comparing the experimental and as-built FE curves. This could be due to the presence of internal and surface defects in struts for manufactured specimens. Also, the effect of irregularity on the mechanical properties is higher for batch C due to their high porosity.

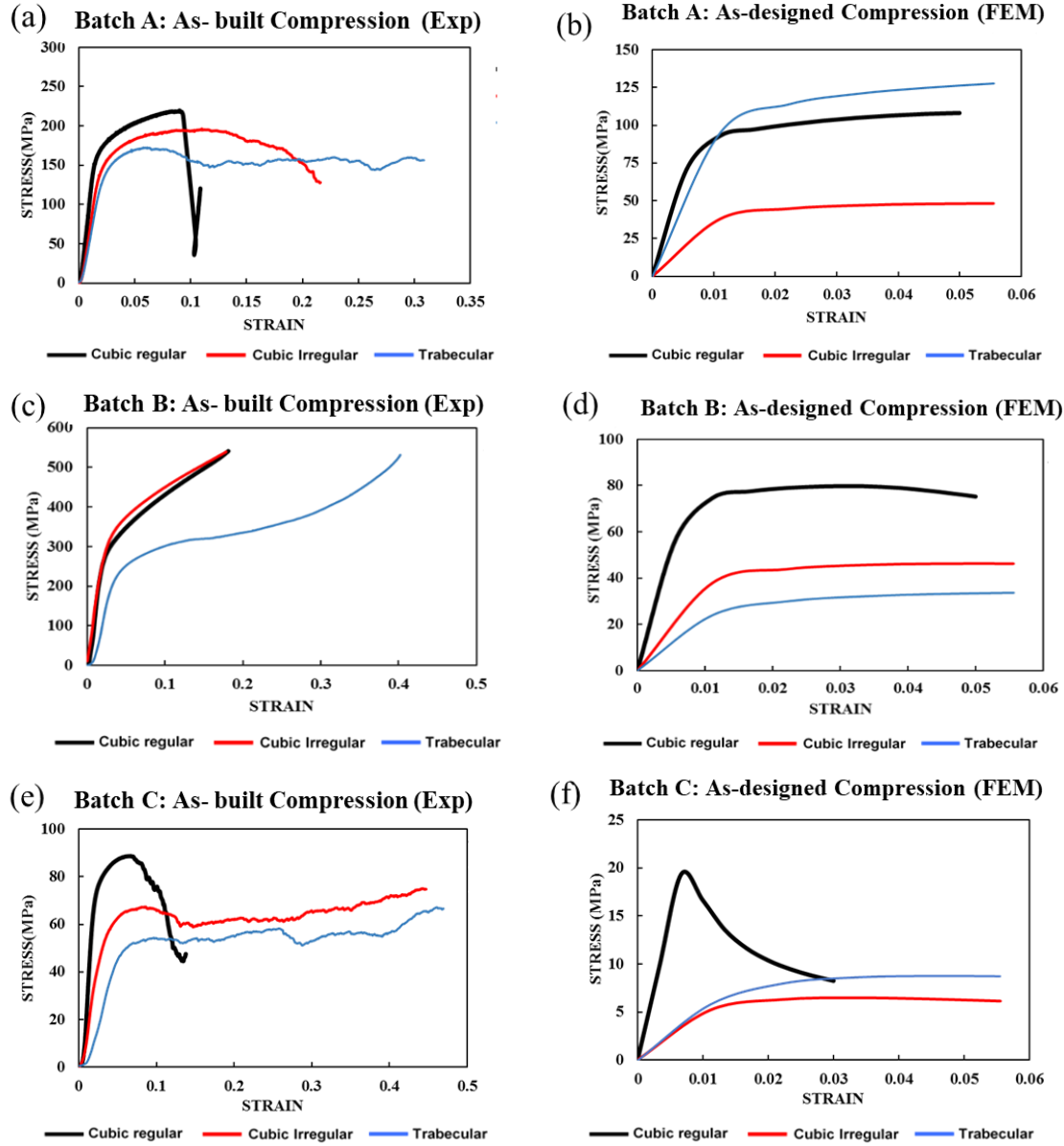


Figure II - 24 Compression stress-strain curves in experimental (as-built) and FEM (as-designed): (a) and (b) batch A, (c) and (d) batch B, (e) and (f) batch C

As discussed in the experimental results, a difference is seen when comparing the compression and tensile Young's modulus of the considered cellular materials. The hypothesis that misalignment of struts with respect to loading direction leads to decreased stiffness was confirmed from the FE analysis discussed in section 2.3.5.1. The study of as-built FE models in elastic region is extended to the elastic-plastic region and compared with the experimental curves in the next section.

*Comparison of experimental and finite element results of as-built regular structures:* The FE model of cubic regular cellular material with increased strut thickness to match porosity of the manufactured specimens was considered. The tensile loading analysis was carried out with vertical displacement and the stress-strain curves obtained are compared with the tensile experimental curves as shown in Fig. II-25(a). The curves show an acceptable overlap in the linear region. However, the FE models yield at higher loads compared to the experimental yield stress. This behavior is observed at all the three porosity levels. Similar difference in the FE analysis and experimental curves was seen for cubic and diamond based cellular materials in the reference [59]. The maximum difference between the yield stress in the FE model and obtained from the experiment is  $\sim 30\%$  for batch B more than the yield stress

from the experiment. The early yielding and the behavior in the plastic region of the manufactured samples is due to the presence of defects such as missing struts, strut waviness, varying cross-section and internal defects which have not been considered in the FE model.

The compression test was carried out for as-built FE model as discussed before, an inclination of  $10^\circ$  was provided in order to simulate the elastic-plastic behavior. The comparison of the stress-strain curves is shown in Fig. II-25(b). A perfect overlap was observed for batch A when compared to batch B and batch C. For batch B, a difference of  $\sim 15\%$  was observed in yield strength and stiffness when comparing the FE and experimental results. As mentioned before, the absence of defects in the FE model influences the mechanical behavior under tensile as well as compression loading.

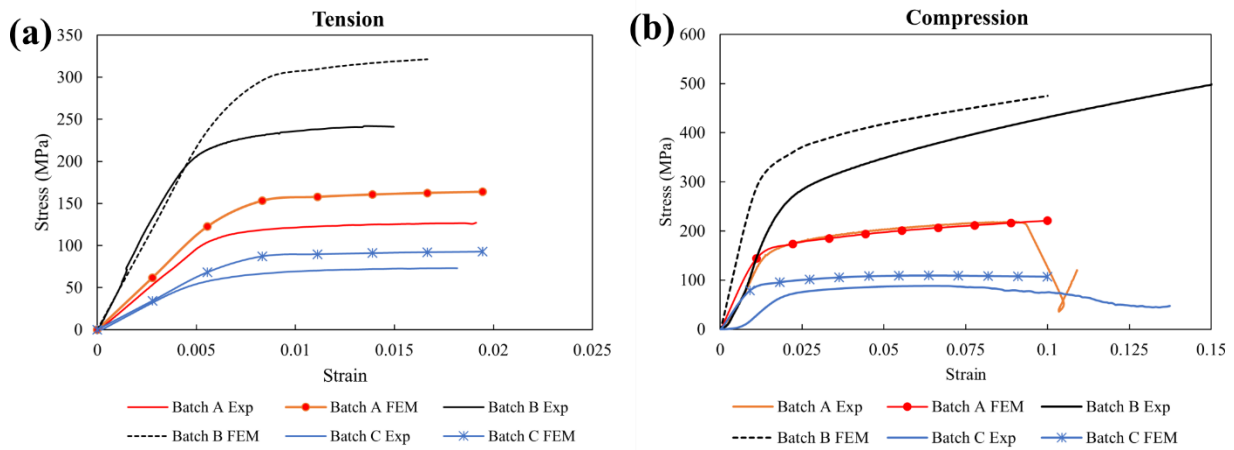


Figure II - 25 Comparison of FEM and experimental behavior of as-built regular structures (a) Tensile loading (b) Compression loading - Inclined

The Young's modulus of the batch C specimens is in the desired range for application in implants despite the increase in the porosity after LPBF process. Since the tensile test results from the experiment are more reliable and is the novelty of this work, the FE analysis on the effect of strut defects is carried out only for cubic regular specimens of batch C under tensile loading.

### 2.3.6.3. FE analysis with strut defects

The FE analysis of the model described in this section 2.2.6.3 is discussed here. The parameters compared in this study are the Young's modulus and the ultimate tensile strength. The FE results of as-designed, AD, VCS and VCS with offset models are compared with the experimental results.

To obtain a complete picture on the effect of strut defect modeling on the mechanical properties, both Young's modulus and UTS are compared as shown in Fig. II-26(a) and (b) respectively. The comparison considers both elliptical and rectangular cross-section FE models. The results indicate that the elliptical cross-section underestimates the Young's modulus when compared to rectangular cross-section. However, despite the cross-section considered, the stiffness of the material decreases with increase in the extent of defects considered in the FE model, similar behavior for other cellular materials was seen the following reference [43, 60]. The lowest modulus in elliptical cross-section was 10.37 GPa, and in rectangular cross-section was 13.14 GPa. The experimental value is 12.38 GPa which lies between the two cross-sections considered. However, the as-designed values of 2.88 GPa is very low compared to the other tabulated values.

The stress-strain curves obtained from the FE analysis are compared with the experimental results in Fig. II-27(a) and (b). The yielding point in rectangular cross-section is higher than the experimental curves, while a clear overlap between the VCS, VCS with offset and experimental curves is seen. It is seen that the varying cross-section has a greater effect on the mechanical properties compared to the

center offset considered in *VCS with offset model*. The difference between the yield strength in experimental and rectangular cross-section is 23%, while the difference is reduced to 2% in elliptical cross-section. However, the models considered in the study were built by repeating a unit cell in all the three directions. But in manufactured specimens the defects are not periodic and vary from one specimen to another. Additionally, there are certain defects such as disconnected struts, missing struts which have not been considered. Nevertheless, a good correlation between the strut defects and mechanical properties has been demonstrated in the study.

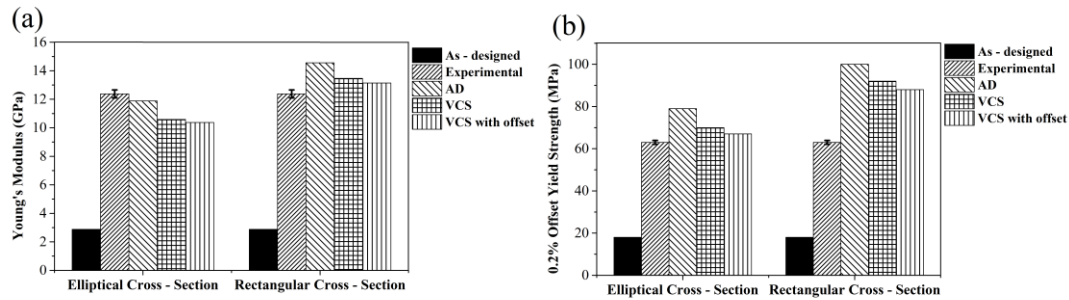


Figure II - 26 Comparison of (a) Tensile Young's modulus and (b) offset yield strength in elliptical and rectangular cross-section models compared with as-designed FE and experimental values

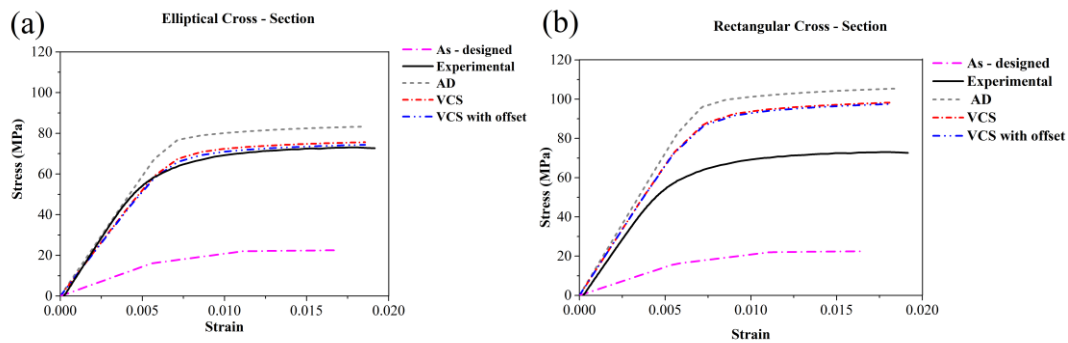


Figure II - 27 Comparison of stress-strain curves of different FE models with experimental curve (a) elliptical cross-section (b) rectangular cross-section

#### 2.3.6.4. FE analysis of tomography model

The FE analysis was carried out on the tomography RVE models as mentioned in section 2.2.7.4. The stress-strain curves are compared in the Fig. II-28. The curves of the tomography FE models are above the experimental curves for all the three cell topologies indicating higher strength and stiffness. The porosity and the mechanical properties of the tomography FE analysis and experimental results are tabulated in Table II - 8. The porosity of the FE models was lower than the specimens, this is due to the down sampling of the point cloud from the tomography analysis. This increases the strength and stiffness compared to the experimental values. Also, the material data used for the FE analysis was from the bulk specimen which might slightly impact the difference between the FE and the experimental results. The damage locations in the FE model are obtained from the equivalent plastic strain plots as shown in Fig. II- 29, indicating that the failure in cubic regular is at the struts, in cubic irregular the failure is at the struts as well as the junctions, while in trabecular the failure is generally at the junctions/nodes.

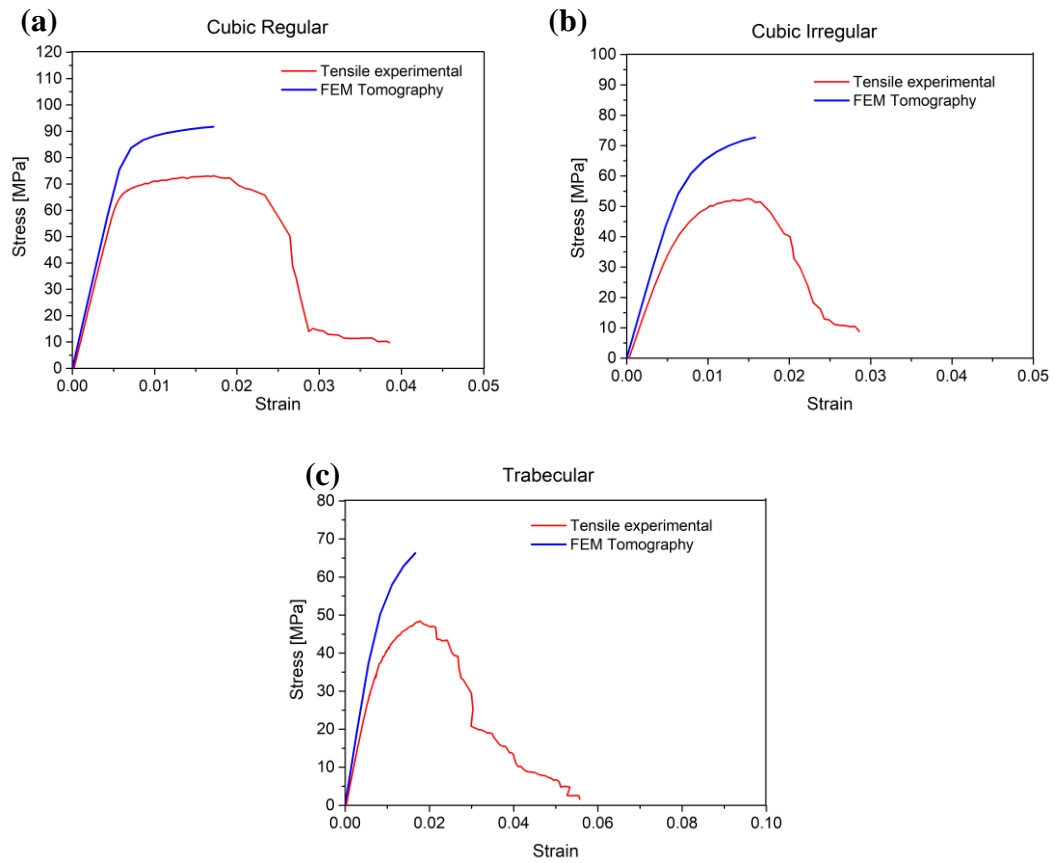


Figure II - 28 Comparison of tensile experimental curves with tomography FE analysis (a) Cubic regular (b) Cubic irregular (c) Trabecular

Table II - 8 Comparison of properties from tensile experimental and tomography FE models

|                        | Porosity (%) |          | Young's modulus (GPa) |          | 0.2% offset yield strength |          |
|------------------------|--------------|----------|-----------------------|----------|----------------------------|----------|
|                        | Experimental | $\mu$ CT | Experimental          | $\mu$ CT | Experimental               | $\mu$ CT |
| <b>Cubic regular</b>   | 77           | 74       | 12.38                 | 13.56    | 67                         | 86       |
| <b>Cubic irregular</b> | 76           | 70       | 7.44                  | 9.13     | 46                         | 60       |
| <b>Trabecular</b>      | 76           | 73       | 5.21                  | 6.72     | 38                         | 55       |

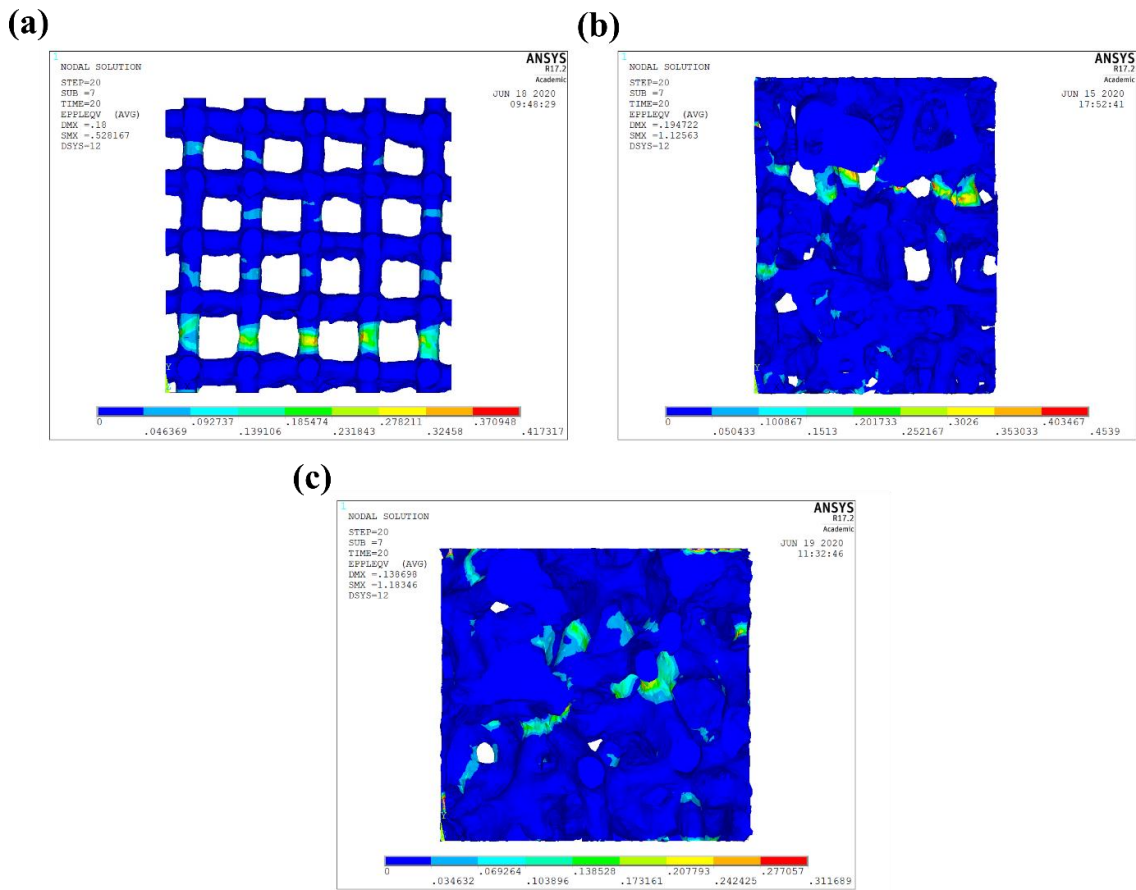


Figure II - 29 Failure location in tomography FE models obtained from the equivalent plastic strain plots (a) Cubic regular (b) Cubic irregular (c) Trabecular

### 2.3.7. Fractography

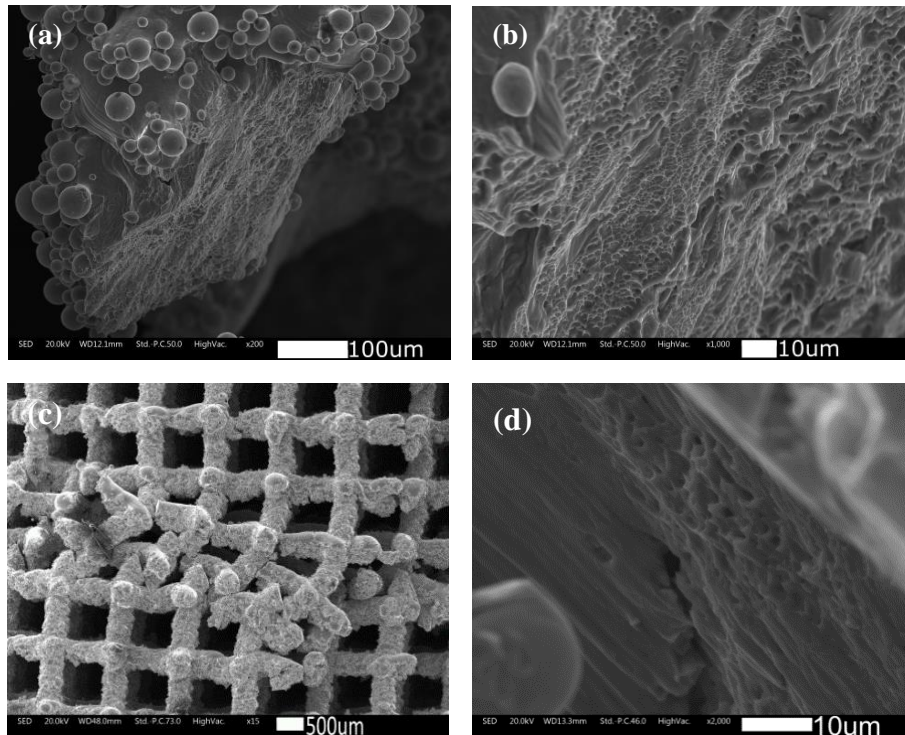


Figure II - 30 Fracture surface images of cubic regular specimen (a),(b) Tensile test fracture surface (c) compression test failure (d) compression test fracture surface

The fracture surface analysis of the tested specimens was carried out using SEM. The Fig. II-28 indicate the fracture surface if tensile sample. The Fig. II-30(b) indicates the formation of dimples similar to cup and cone failure indicating ductile failure. An image of batch C specimen under compression is shown in Fig. II-30(c) and (d). The Fig. II-30(c) indicates that the failure occurs at one layer of the cellular material and is mainly due to buckling of vertical struts. The failure of the struts is generally initiated at the nodes or junctions since they act as stress concentration locations. The Fig. II-30(d) clearly shows the formation of smooth shear bands followed by a small portion of dimples indicating ductile failure.

## 2.4. Empirical relation between as-designed and as-built cellular materials

### 2.4.1. Specimen details

This section of the study provides a relationship between the as-designed and the as-built Young's modulus of cubic regular, cubic irregular and trabecular cell topologies. The main of this study is to provide an empirical relation between the designed and obtained Young's modulus in order to create a database for future reference.

Table II - 9 Designed strut thickness and pore size

| Strut thickness<br>( $\mu\text{m}$ ) | Pore size ( $\mu\text{m}$ ) | Sample<br>designation |
|--------------------------------------|-----------------------------|-----------------------|
| 50                                   | 700                         | 0705                  |
|                                      | 1000                        | 1005                  |
|                                      | 1500                        | 1505                  |
|                                      | 2000                        | 2005                  |
| 100                                  | 700                         | 0710                  |
|                                      | 1000                        | 1010                  |
|                                      | 1500                        | 1510                  |
|                                      | 2000                        | 2010                  |
| 200                                  | 700                         | 0720                  |
|                                      | 1000                        | 1020                  |
|                                      | 1500                        | 1520                  |
|                                      | 2000                        | 2020                  |

Each cell topology has 12 porosity values in between the range 80 – 99.5%. The porosity level has been achieved with varying the pore size as well as the strut thickness. Therefore, considering all the three topologies, 36 configurations (12 for each pore type) have been considered. The as-built Young's modulus values under tensile and compression cyclic test were obtained from the partner company, Lincotek Medical. FE analysis for the as-designed cellular materials was carried out as discussed in the section 2.2.6.1. Details of the designed strut thickness and pore size are provided in the Table II-9 along with the sample designation. For example, 0705 indicates a pore size of 700  $\mu\text{m}$  and strut thickness of 50  $\mu\text{m}$ . In some of the graphs presented in the next section designation of xx05, xx10, and xx20 are used to represent specimens with same pore size and varying thickness.

### 2.4.2. Relation between relative density and relative Young's modulus

The porosity and the Young's modulus from the experimental data and FE analysis are converted to relative density and the relative Young's modulus respectively. The relative Young's modulus is obtained by dividing the Young's modulus of cellular material with the Young's modulus of Ti6Al4V alloy (110 GPa). The points are fitted using the power law in order to represent the Gibson – Ashby equation [37] shown below. The parameter  $C$  and  $n$  are obtained from the curve fitting.  $E$  is the Young's modulus from cyclic test,  $E_0$  is the bulk Young's modulus (110 GPa),  $\rho$  is the density of the cellular

material, and  $\rho_0$  is the density of Ti6Al4V alloy (4.42 g/cm<sup>3</sup>). The value of  $n$  indicates the slope of the curve in log-log graph.

$$\frac{E}{E_0} = C \left( \frac{\rho}{\rho_0} \right)^n \quad \dots\dots \text{Eq. II-2}$$

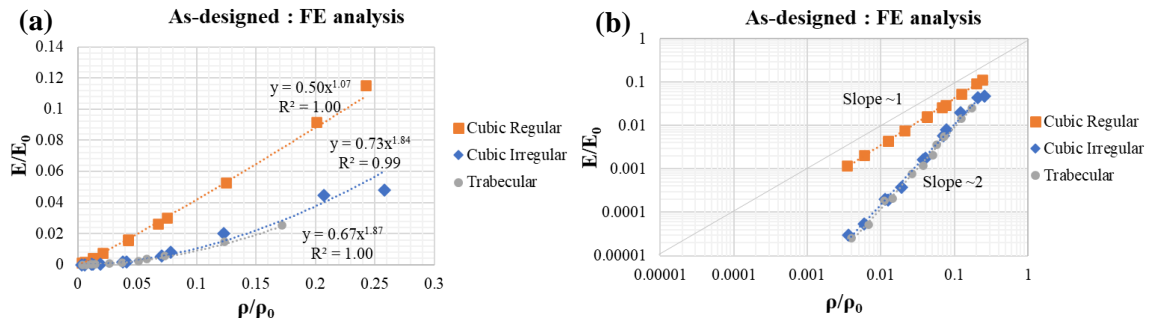


Figure II - 31 (a) Variation of relative Young's modulus with relative density (b) log-log curve indicating the behavior of cell topology

The as-designed Young's modulus values are plotted in Fig. II-31(a) and (b). The curve of the cubic irregular and trabecular specimens overlap indicating a similar behavior. The log-log graph of the FE models is shown in Fig. II-31(b) shows that cubic regular specimens have a slope of 1 indicating a purely stretching dominated behavior. However, the cubic irregular and trabecular specimen curves overlap with a slope of 1.9, indicating a bending dominated behavior. The misalignment in the nodes in cubic irregular transform the stretching dominated behavior of cubic regular into bending dominated behavior.

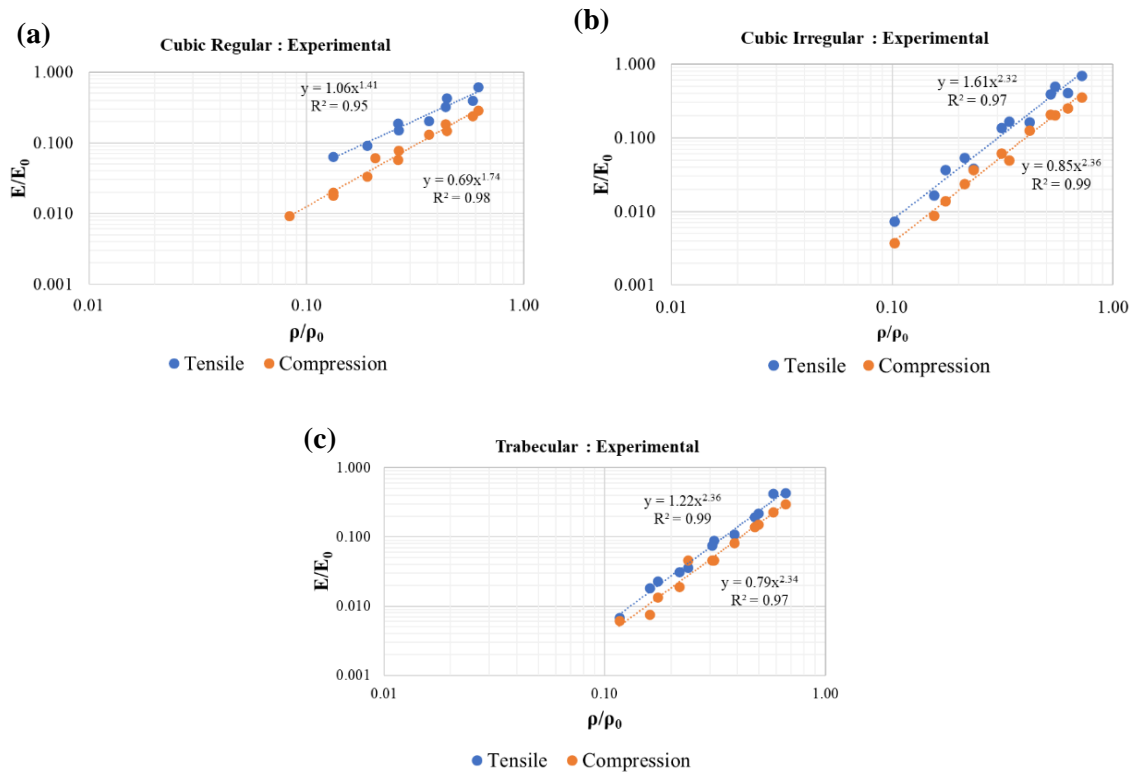


Figure II - 32 Power law fitting for tensile and compression Young's modulus (a) cubic regular (b) cubic irregular and (c) trabecular

Fig. II-32 provides the relationship between relative density and relative Young's modulus for as-built specimens. The graph considers compression and tensile test data. A variation in the tensile and compression Young's modulus was reported for the specimens. However, the slope of the curves in log-log graphs are similar for tensile and compression. The slope of cubic irregular and trabecular are greater than 2, while the slope of cubic regular is greater than 1.

Table II - 10 Gibson - Ashby parameter for relative Young's modulus

| Sample          | As-designed FE |      | Compression - Exp |      | Tensile - Exp |      |
|-----------------|----------------|------|-------------------|------|---------------|------|
|                 | C              | n    | C                 | n    | C             | n    |
| Cubic regular   | 0.5            | 1    | 0.69              | 1.74 | 1.06          | 1.41 |
| Cubic irregular | 0.9            | 1.93 | 0.85              | 2.36 | 1.61          | 2.32 |
| Trabecular      | 0.67           | 1.87 | 0.79              | 2.34 | 1.07          | 2.18 |

The Gibson – Ashby parameters of as-designed FE results and experimental results are tabulated in Table. II-10. The values in compression and tensile are compared in Fig. II-33(a) and (b) respectively. The slope of the as-designed specimens is closer to the ideal values of Gibson – Ashby since the model works well for cellular materials with porosity > 65 – 70%. Therefore, the value of n is away from the bisector line in Fig. II-33 when we compare the experimental and FE values.

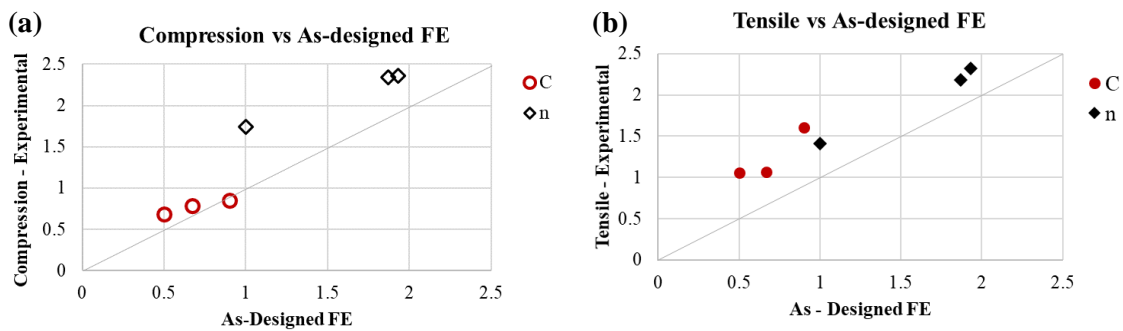


Figure II - 33 Comparison of Gibson - Ashby parameters C and n in (a) compression (b) tensile

### 2.4.3. Correlation between as-designed and as-built Young's modulus

To obtain a linear relationship between the as-designed and the as-built Young's modulus the log values of the Young's modulus is plotted since the data showed a normal distribution in log-log scale. The relation is as shown in the equation below.

$$\text{Log}(E_{as\_built}) = A \times \text{Log}(E_{as\_designed}) + B \quad \dots\dots \text{Eq.II-3}$$

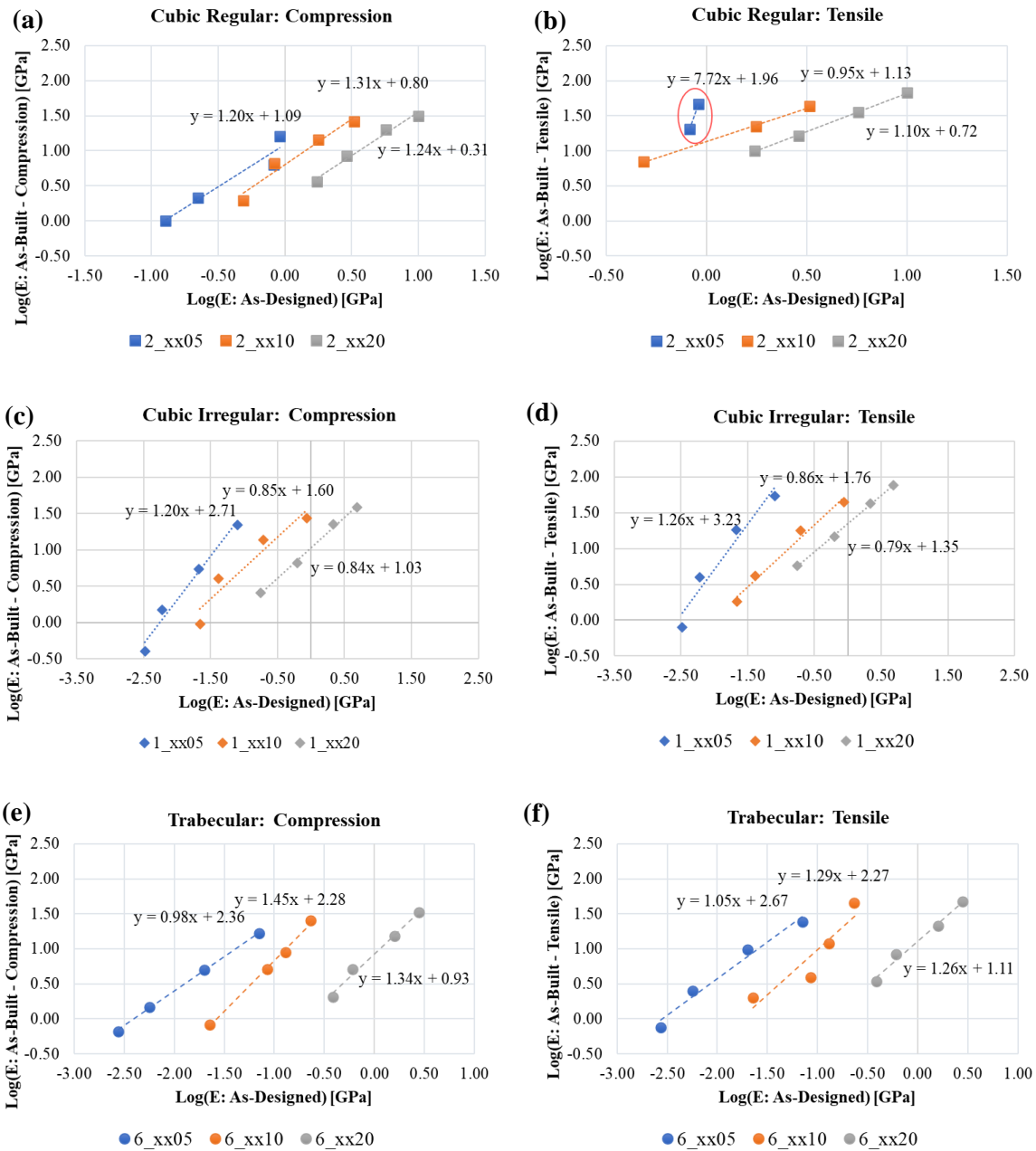


Figure II - 34 Relation between as-designed Young's modulus with as-built Young's modulus based on pore size and loading (a) cubic regular compression (b) cubic regular tension (c) cubic irregular compression (d) cubic irregular tension (e) trabecular tension (f) trabecular compression

The Fig. II-34 provides the relation between as-designed and as-built modulus for all the specimens and topologies considered in the study. The data is separated for based on the strut thickness of the specimens and fitted using linear equation. Three to four points are considered for the curve fitting, however, for the configuration 2\_xx05-tensile (marked in red) the fitting is not satisfactory since two points are eliminated as the specimens gave very low modulus compared to the expected value. The correlation is useful in designing the porosity values to obtain the required Young's modulus after manufacturing using LPBF process for the three topologies considered in the study. The empirical equations provided by the study is applicable for relating the as-designed specimens with porosity between 79 – 99.4 % to their corresponding as-built configuration with porosity between 30 – 91%.

## 2.5. Section summary

This study deals with the mechanical characterization of three types of cellular materials, cubic regular, cubic irregular and trabecular with varying porosity. The samples were manufactured using LPBF process and mainly subjected to compression and tensile tests. The samples were also subjected to porosity analysis and morphological analysis. FE analysis was carried out on three different stage to understand and replicate the mechanical behavior of these cellular materials. The following interpretation can be obtained from the study:

- The porosity of the as-built specimens was lower than the designed porosity values. The increase in the strut thickness by  $\sim 220 \mu\text{m}$  proportionally decreases the porosity. This indicates that the use of a compensated CAD model for manufacturing can decrease the difference between the as-designed and as-built strut thickness and porosity.
- An inclination of struts was observed in compression test samples, later a new batch of specimen Ci were manufactured in the cubic regular configuration with improved alignment.
- As expected, the strength and stiffness of the specimen decreased with increase in the porosity. Cubic regular specimens had the highest strength and stiffness compared to cubic irregular and trabecular, due to the presence of vertical struts along the loading direction.
- Comparison of Young's modulus in compression and tensile indicated lower modulus in compression. Further comparison of batch C results with batch Ci indicated the asymmetric behavior between compression and tensile loading.
- The FE analysis in elastic regime to and the analytical results from the Gibson – Ashby model also confirm the effect of off – axis in compression. The FE results provide a clear idea about the extent of off-axis loading experienced by the specimen.
- The results from the tensile test which is the novelty of this work indicates that they can be used as an alternative to compression test for evaluating the stiffness of the cellular materials.
- Comparison of the FE stress-strain curves of the as-designed configuration and the as-built experimental results indicate the effect of porosity on the plastic behavior of the cellular materials. The results also indicated that the effect of cell topology is prominent at higher porosity values compared to lower porosity values.
- The compression test simulations indicate that cubic regular specimens tend to fail due to buckling of the vertical struts, while cubic irregular and trabecular fail due to bending induced from node misalignment and random distribution of struts.
- The FE analysis of as-built cubic regular indicate that, matching the porosity of the FE model with the manufactured specimens yield comparable results for the Young's modulus. However, an increase yield stress was observed in FE models.
- The elliptical cross-section underestimates the Young's modulus but has a good correlation in the plastic region of the stress-strain curve.
- The FE analysis of as-built structures with strut defects indicate that the varying cross-section in the struts has greater effect on the mechanical properties compared to strut waviness for cubic regular specimens.
- The analysis of a large database of cubic regular, cubic irregular and trabecular specimens indicates that the ideal parameters of the Gibson – Ashby law was obtained for specimens with the porosity values  $> 70\%$ .

- A linear equation is obtained to relate the as – built Young’s modulus with the as – designed Young’s modulus. The relation depends in the pore size and the cell topology. This empirical relation can be used to predict the Young’s modulus before manufacturing and to optimize the CAD input for the LPBF process depending on the required stiffness. The study can be further used to relate the mechanical properties of as-built specimens with lower porosity to the as-designed specimens that obey the Gibson-Ashby law directly.

## 2.6. References

1. Li SJ, Xu QS, Wang Z, et al (2014) Influence of cell shape on mechanical properties of Ti-6Al-4V meshes fabricated by electron beam melting method. *Acta Biomater* 10:4537–4547. <https://doi.org/10.1016/j.actbio.2014.06.010>
2. Mark Long, Rack HJ (1998) Titanium alloys in total joint replacement - a materials science perspective. *Biomaterials* 19:1621–1639. [https://doi.org/10.1016/S0142-9612\(97\)00146-4](https://doi.org/10.1016/S0142-9612(97)00146-4)
3. Murr LE, Gaytan SM, Medina F, et al (2010) Characterization of Ti-6Al-4V open cellular foams fabricated by additive manufacturing using electron beam melting. *Mater Sci Eng A* 527:1861–1868. <https://doi.org/10.1016/j.msea.2009.11.015>
4. Singh, R., Lee, P.D., Dashwood, R.J., Lindley, T.C. (2010) Titanium foams for biomedical applications: a review. *Mater Technol* 25:127–136. <https://doi.org/10.1179/175355510X12744412709403>
5. Cheng XY, Li SJ, Murr LE, et al (2012) Compression deformation behavior of Ti-6Al-4V alloy with cellular structures fabricated by electron beam melting. *J Mech Behav Biomed Mater* 16:153–162. <https://doi.org/10.1016/j.jmbbm.2012.10.005>
6. Ryan G, Pandit A, Apatsidis DP (2006) Fabrication methods of porous metals for use in orthopaedic applications. *Biomaterials* 27:2651–2670. <https://doi.org/10.1016/j.biomaterials.2005.12.002>
7. Tan XP, Tan YJ, Chow CSL, et al (2017) Metallic powder-bed based 3D printing of cellular scaffolds for orthopaedic implants: A state-of-the-art review on manufacturing, topological design, mechanical properties and biocompatibility. *Mater Sci Eng C* 76:1328–1343. <https://doi.org/10.1016/j.msec.2017.02.094>
8. Arabnejad Khanoki S, Pasini D (2013) Fatigue design of a mechanically biocompatible lattice for a proof-of-concept femoral stem. *J Mech Behav Biomed Mater* 22:65–83. <https://doi.org/10.1016/j.jmbbm.2013.03.002>
9. Arabnejad S, Burnett Johnston R, Pura JA, et al (2016) High-strength porous biomaterials for bone replacement: A strategy to assess the interplay between cell morphology, mechanical properties, bone ingrowth and manufacturing constraints. *Acta Biomater* 30:345–356. <https://doi.org/10.1016/j.actbio.2015.10.048>
10. Albrektsson T, Johansson C (2001) Osteoinduction, osteoconduction and osseointegration. *Eur Spine J* 10:S96–S101. <https://doi.org/10.1007/s005860100282>
11. Dabrowski B, Swieszkowski W, Godlinski D, Kurzydowski KJ (2010) Highly porous titanium scaffolds for orthopaedic applications. *J Biomed Mater Res - Part B Appl Biomater* 95:53–61. <https://doi.org/10.1002/jbm.b.31682>
12. Jones AC, Arns CH, Hutmacher DW, et al (2009) The correlation of pore morphology, interconnectivity and physical properties of 3D ceramic scaffolds with bone ingrowth. *Biomaterials* 30:1440–1451. <https://doi.org/10.1016/j.biomaterials.2008.10.056>
13. Rahmanian R, Shayesteh Moghaddam N, Haberland C, et al (2014) Load bearing and stiffness tailored NiTi implants produced by additive manufacturing: a simulation study. *Behav Mech Multifunct Mater Compos* 2014 9058:905814. <https://doi.org/10.1117/12.2048948>
14. Kruth JP, Levy G, Klocke F, Childs THC (2007) Consolidation phenomena in laser and powder-bed based layered manufacturing. *CIRP Ann - Manuf Technol* 56:730–759. <https://doi.org/10.1016/j.cirp.2007.10.004>

15. Zhang M, Yang Y, Wang D, et al (2018) Effect of heat treatment on the microstructure and mechanical properties of Ti6Al4V gradient structures manufactured by selective laser melting. *Mater Sci Eng A* 736:288–297. <https://doi.org/10.1016/j.msea.2018.08.084>
16. Benedetti M, Torresani E, Leoni M, et al (2017) The effect of post-sintering treatments on the fatigue and biological behavior of Ti-6Al-4V ELI parts made by selective laser melting. *J Mech Behav Biomed Mater* 71:295–306. <https://doi.org/10.1016/j.jmbbm.2017.03.024>
17. Wauthle R, Vrancken B, Beynaerts B, et al (2015) Effects of build orientation and heat treatment on the microstructure and mechanical properties of selective laser melted Ti6Al4V lattice structures. *Addit Manuf* 5:77–84. <https://doi.org/10.1016/j.addma.2014.12.008>
18. Qiu C, Yue S, Adkins NJE, et al (2015) Influence of processing conditions on strut structure and compressive properties of cellular lattice structures fabricated by selective laser melting. *Mater Sci Eng A* 628:188–197. <https://doi.org/10.1016/j.msea.2015.01.031>
19. Salem H, Carter LN, Attallah MM, Salem HG (2019) Influence of processing parameters on internal porosity and types of defects formed in Ti6Al4V lattice structure fabricated by selective laser melting. *Mater Sci Eng A* 767:138387. <https://doi.org/10.1016/j.msea.2019.138387>
20. Dallago M, Fontanari V, Winiarski B, et al (2017) Fatigue properties of Ti6Al4V cellular specimens fabricated via SLM: CAD vs real geometry. *Procedia Struct Integr* 7:116–123. <https://doi.org/10.1016/j.prostr.2017.11.068>
21. Van Bael S, Kerckhofs G, Moesen M, et al (2011) Micro-CT-based improvement of geometrical and mechanical controllability of selective laser melted Ti6Al4V porous structures. *Mater Sci Eng A* 528:7423–7431. <https://doi.org/10.1016/j.msea.2011.06.045>
22. Kasperovich G, Hausmann J (2015) Journal of Materials Processing Technology Improvement of fatigue resistance and ductility of TiAl6V4 processed by selective laser melting. *J Mater Process Tech* 220:202–214. <https://doi.org/10.1016/j.jmatprotec.2015.01.025>
23. Kelly CN, Francovich J, Julmi S, et al (2019) Fatigue behavior of As-built selective laser melted titanium scaffolds with sheet-based gyroid microarchitecture for bone tissue engineering. *Acta Biomater* 94:610–626. <https://doi.org/10.1016/j.actbio.2019.05.046>
24. Maskery I, Aremu AO, Simonelli M, et al (2015) Mechanical Properties of Ti-6Al-4V Selectively Laser Melted Parts with Body-Centred-Cubic Lattices of Varying cell size. *Exp Mech* 55:1261–1272. <https://doi.org/10.1007/s11340-015-0021-5>
25. Ahmadi SM, Yavari SA, Wauthle R, et al (2015) Additively manufactured open-cell porous biomaterials made from six different space-filling unit cells: The mechanical and morphological properties. *Materials (Basel)* 8:1871–1896. <https://doi.org/10.3390/ma8041871>
26. Amin Yavari S, Ahmadi SMM, Wauthle R, et al (2015) Relationship between unit cell type and porosity and the fatigue behavior of selective laser melted meta-biomaterials. *J Mech Behav Biomed Mater* 43:91–100. <https://doi.org/10.1016/j.jmbbm.2014.12.015>
27. Dallago M, Fontanari V, Torresani E, et al (2018) Fatigue and biological properties of Ti-6Al-4V ELI cellular structures with variously arranged cubic cells made by selective laser melting. *J Mech Behav Biomed Mater* 78:381–394. <https://doi.org/10.1016/j.jmbbm.2017.11.044>
28. Wei K, Yang Q, Yang X, et al (2020) Mechanical analysis and modeling of metallic lattice sandwich additively fabricated by selective laser melting. *Thin-Walled Struct* 146:106189. <https://doi.org/10.1016/j.tws.2019.106189>
29. Wei K, Yang Q, Ling B, et al (2018) Mechanical responses of titanium 3D kagome lattice structure manufactured by selective laser melting. *Extrem Mech Lett* 23:41–48. <https://doi.org/10.1016/j.eml.2018.07.001>
30. Choy SY, Sun CN, Leong KF, Wei J (2017) Compressive properties of functionally graded lattice structures manufactured by selective laser melting. *Mater Des* 131:112–120. <https://doi.org/10.1016/j.matdes.2017.06.006>
31. Zhang XY, Fang G, Xing LL, et al (2018) Effect of porosity variation strategy on the performance of

- functionally graded Ti-6Al-4V scaffolds for bone tissue engineering. *Mater Des* 157:523–538. <https://doi.org/10.1016/j.matdes.2018.07.064>
32. Hernández-Nava E, Smith CJ, Derguti F, et al (2016) The effect of defects on the mechanical response of Ti-6Al-4V cubic lattice structures fabricated by electron beam melting. *Acta Mater* 108:279–292. <https://doi.org/10.1016/j.actamat.2016.02.029>
  33. Dallago M, Winiarski B, Zanini F, et al (2019) On the effect of geometrical imperfections and defects on the fatigue strength of cellular lattice structures additively manufactured via Selective Laser Melting. *Int J Fatigue* 124:348–360. <https://doi.org/10.1016/j.ijfatigue.2019.03.019>
  34. Simoneau C, Brailovski V, Terriault P (2016) Design, manufacture and tensile properties of stochastic porous metallic structures. *Mech Mater* 94:26–37. <https://doi.org/10.1016/j.mechmat.2015.11.010>
  35. Yeni YN, Dong XN, Fyhrie DP, Les CM (2004) The dependence between the strength and stiffness of cancellous and cortical bone tissue for tension and compression: extension of a unifying principle. *Biomed Mater Eng*
  36. Mullen L, Stamp RC, Fox P, et al (2010) Selective laser melting: A unit cell approach for the manufacture of porous, titanium, bone in-growth constructs, suitable for orthopedic applications. II. Randomized structures. *J Biomed Mater Res Part B Appl Biomater* 92B:178–188. <https://doi.org/10.1002/jbm.b.31504>
  37. Gibson LJ, Ashby MF (1997) *Cellular Solids*, Second. Cambridge University Press
  38. Ahmadi SM, Campoli G, Yavari SA, et al (2014) Mechanical behavior of regular open-cell porous biomaterials made of diamond lattice unit cells. *J Mech Behav Biomed Mater* 34:106–115. <https://doi.org/10.1016/j.jmbbm.2014.02.003>
  39. Campoli G, Borleffs MS, Amin Yavari S, et al (2013) Mechanical properties of open-cell metallic biomaterials manufactured using additive manufacturing. *Mater Des* 49:957–965. <https://doi.org/10.1016/j.matdes.2013.01.071>
  40. Karamooz Ravari MR, Kadkhodaei M, Badrossamay M, Rezaei R (2014) Numerical investigation on mechanical properties of cellular lattice structures fabricated by fused deposition modeling. *Int J Mech Sci* 88:154–161. <https://doi.org/10.1016/j.ijmecsci.2014.08.009>
  41. Bagheri ZS, Melancon D, Liu L, et al (2017) Compensation strategy to reduce geometry and mechanics mismatches in porous biomaterials built with Selective Laser Melting. *J Mech Behav Biomed Mater* 70:17–27. <https://doi.org/10.1016/j.jmbbm.2016.04.041>
  42. Epasto G, Palomba G, D’Andrea D, et al (2019) Ti-6Al-4V ELI microlattice structures manufactured by electron beam melting: Effect of unit cell dimensions and morphology on mechanical behaviour. *Mater Sci Eng A* 753:31–41. <https://doi.org/10.1016/j.msea.2019.03.014>
  43. Lozanovski B, Leary M, Tran P, et al (2019) Computational modelling of strut defects in SLM manufactured lattice structures. *Mater Des* 171:107671. <https://doi.org/10.1016/j.matdes.2019.107671>
  44. Ashrafi MJ, Amerinatanzi A, Saebi Z, et al (2018) Shape memory response of cellular lattice structures: Unit cell finite element prediction. *Mech Mater* 125:26–34. <https://doi.org/10.1016/j.mechmat.2018.06.008>
  45. Pazzaglia UE, Ghisellini F, Barbieri D, Ceciliani L (1988) Failure of the stem in total hip replacement - A study of aetiology and mechanism of failure in 13 cases. *Arch Orthop Trauma Surg* 107:195–202. <https://doi.org/10.1007/BF00449667>
  46. Andriacchi TP, Galante JO, Belytschko T, Hampton SJ (1976) A stress analysis of the femoral stem in total hip prostheses. *J Bone Joint Surg Am* 58 5:618–624
  47. Carmignato, Simone, Dewulf, Wim, Leach R (Eds. . (2018) *Industrial X-Ray Computed Tomography*. Springer International Publishing, Cham
  48. ISO 13314 (2011) ISO 13314 Mechanical testing of metals, ductility testing, compression test for porous and cellular metals. Ref number ISO 13314:1–7
  49. Kalpakjian S, Schmid SR (2013) *Manufacturing Engineering and Technology*, 7th ed. Pearson

50. Yang L (2016) A study about size effects of 3D periodic cellular structures. *Solid Free Fabr* 2016 2181–2193
51. Helou M, Vongbunyong S, Kara S (2016) Finite Element Analysis and Validation of Cellular Structures. *Procedia CIRP* 50:94–99. <https://doi.org/10.1016/j.procir.2016.05.018>
52. Raghavendra S, Molinari A, Fontanari V, et al (2020) Effect of strut cross section and strut defect on tensile properties of cubic cellular structure. *Mater Des Process Commun* 2:1–6. <https://doi.org/10.1002/mdp2.118>
53. Cuadrado A, Yáñez A, Martel O, et al (2017) Influence of load orientation and of types of loads on the mechanical properties of porous Ti6Al4V biomaterials. *Mater Des* 135:309–318. <https://doi.org/10.1016/j.matdes.2017.09.045>
54. Brun E, Vicente J, Topin F, et al (2009) Microstructure and transport properties of cellular materials: Representative volume element. *Adv Eng Mater* 11:805–810. <https://doi.org/10.1002/adem.200900131>
55. Youssef S, Maire E, Gaertner R (2005) Finite element modelling of the actual structure of cellular materials determined by X-ray tomography. *Acta Mater* 53:719–730. <https://doi.org/10.1016/j.actamat.2004.10.024>
56. Simonelli M, Tse YY, Tuck C (2012) Microstructure of Ti-6Al-4V produced by selective laser melting. *J Phys Conf Ser* 371:. <https://doi.org/10.1088/1742-6596/371/1/012084>
57. Zanini F, Sbettega E, Carmignato S (2018) X-ray computed tomography for metal additive manufacturing: Challenges and solutions for accuracy enhancement. *Procedia CIRP* 75:114–118. <https://doi.org/10.1016/j.procir.2018.04.050>
58. Karamooz Ravari MR, Nasr Esfahani S, Taheri Andani M, et al (2016) On the effects of geometry, defects, and material asymmetry on the mechanical response of shape memory alloy cellular lattice structures. *Smart Mater Struct* 25:. <https://doi.org/10.1088/0964-1726/25/2/025008>
59. Kadkhodapour J, Montazerian H, Darabi AC, et al (2015) Failure mechanisms of additively manufactured porous biomaterials: Effects of porosity and type of unit cell. *J Mech Behav Biomed Mater* 50:180–191. <https://doi.org/10.1016/j.jmbbm.2015.06.012>
60. Liu L, Kamm P, García-Moreno F, et al (2017) Elastic and failure response of imperfect three-dimensional metallic lattices: the role of geometric defects induced by Selective Laser Melting. *J Mech Phys Solids* 107:160–184. <https://doi.org/10.1016/j.jmps.2017.07.003>

## 2.7. Appendix 2

### 2.7.1. An example of mesh convergence

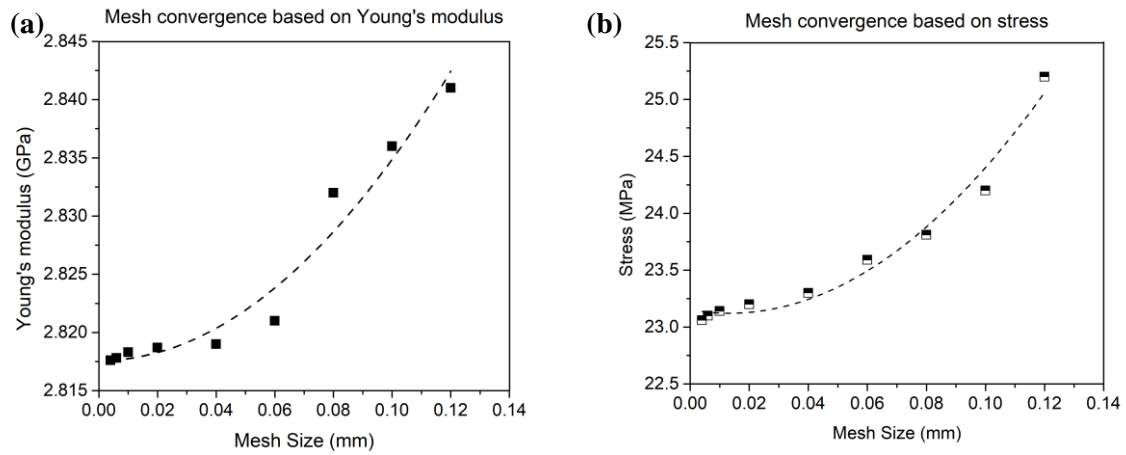


Figure II - A 1 Representation of mesh convergence analysis shown for batch C cubic regular (as-designed) (a) convergence for elastic analysis (b)convergence for elastic-plastic analysis

### 2.7.2. An example of effect of RVE size on stress values

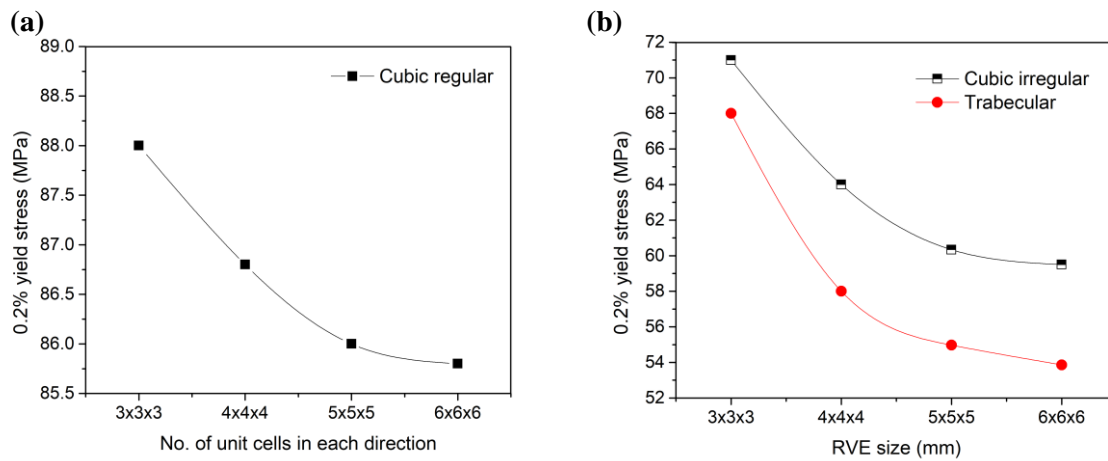


Figure II - A 2 Representation of effect of RVE size variation shown for tomography models for (a) cubic regular, based on number of unit cells in each direction (b) cubic irregular and trabecular based on RVE size in mm

---

## Chapter 3

### Static and compression – compression fatigue properties of different cellular materials

---

Biomedical implants experience fatigue loads due to daily activities along with the compression load and in some cases tensile load. Therefore, understanding the fatigue behaviour of the cellular materials is an important aspect for implant design. The previous chapter dealt with the just the static and compression properties by varying the porosity of three different cellular materials. The results also indicated that tensile test used for the cellular materials yielded satisfactory results. Moving forward with the results of the highest porosity specimens of chapter 2, this current chapter was developed.

This current chapter aims at developing and analysing seven different types of cellular materials for application in completely porous implants or as a coating to induce osseointegration. The Ti6Al4V cellular specimens were manufactured using the LPBF process. The cellular materials were designed to obtain properties between the highly stiff cubic regular unit cell and highly compliant cross based specimens. The tensile and the compression test evaluated the static properties, and the results indicate the stretching and dominated behavior of these specimens. The compression-compression fatigue results give a clear demarcation between the properties based on the type of unit cell and the irregularity. The final outcome of the study indicates that all the considered configurations can be used in biomedical applications. Also, a combination of different unit cells can be used to design a completely porous implant for vertebral prosthesis.

A part of this chapter has been published in:

Raghavendra S, Molinari A, Fontanari V, Zappini G, Benedetti M. *Evaluation of Static and Fatigue Properties of Regular Lattice and Trabecular Cellular Structures*. *Procedia Struct Integr*. 2020;28: 517–524.

Raghavendra S, Molinari A, Cao A, Gao C, Berto F, Zappini G, Benedetti M. *Quasi – Static Compression and Compression – Compression Fatigue Behavior of Regular and Irregular Cellular Biomaterials*. *Fatigue Fract Eng Mater Struct*. (under publication)

### 3.1.Introduction

The mechanical properties of cellular materials are mainly dependent on the base material, cell architecture and the relative density. At present mechanical characterization of cellular materials is mainly carried through static compression test, fatigue test and in some studies tensile tests are carried out. The compressive properties of periodic lattice based cellular materials were compared against the foam based cellular materials by Cheng et al. [1]. Furthermore, many studies have been carried out on different cell topologies under compression loading [2–9]. These studies indicate that the behavior of the cellular materials are dependent on the relative density as indicated by the Gibson-Ashby law [10].

Most of the components used in biomedical and aerospace industry are subjected to fatigue loading during their operation. Especially implants undergo fatigue loading during the day-to-day activities of the host. Therefore, the fatigue performance of cellular material is of prime importance if they must be considered for biomedical applications. Compression - compression fatigue behavior of cellular materials is influenced by various parameters such as base material, cell topology, stress ratio, processing parameters and post processing treatments similar to the static mechanical properties [8, 11–19]. The fatigue failure mechanism consists of three stages, strain accumulation due to cyclic ratcheting, crack initiation and propagation. However, the failure first starts at individual struts, then multiple struts fail leading to crack propagation through the complete sample [12, 20]. External defects such as surface defects, base material and microstructure influence the fatigue behavior of cellular materials [15, 21]. A combination of heat treatment and surface treatment has shown to increase the fatigue performance of cellular materials [13, 22].

A lot of research on cellular materials is focused on their compression behavior since the implants mainly undergo compression loading during their operation. However, the study reported in this chapter focuses on the behavior of different cell topologies under static tensile, static compression and compression - compression fatigue loads. The following points from the literature and the research carried out in the previous chapter was the motivation for the current investigation:

- i. To understand the compressive behavior of cellular materials to be used in vertebral prosthesis and as coatings for solid implants that experience compressive loads.
- ii. Tensile test was carried out since some of the implant failure studies have shown that the implants in hosts who perform high physical activity and/or are overweight failed due to tensile loading. Also, improper positioning and loosening of implants leads to generation of tensile stresses in prostheses [23, 24]. Further, the results from the previous chapter indicated that stiffness is better measured in tension with respect to compression.
- iii. The fatigue strength was assessed for the cellular materials to relate to the realistic loading conditions.

This study focuses on the static properties from compression and tensile test, and the fatigue properties from compression-compression fatigue test for seven different topologies of cellular materials. Ti6Al4V alloy is used as the base material and the specimens are manufactured using LPBF process. The considered cell architecture can be divided into three categories.

- i. Regular structures: Formed by repeating a lattice-based unit cell in three direction (#1: Cubic regular, #2: Star regular and #3:Cross regular).
- ii. Irregular structures: These structures are obtained by misaligning/ skewing the junctions of regular structures (#4: Cubic irregular, #5: Star irregular and #6: Cross irregular).
- iii. Trabecular (#7): These are obtained by randomly arranging 4 – 6 struts at a node to mimic trabecular bone.

The specimens were investigated for porosity, strut thickness deviation, compression and tensile test, and fatigue test. The compression and tensile test were carried out under monotonic and cyclic loading conditions to obtain their strength and stiffness. Apart from the experimental study, FE analysis was also carried out. Since the novelty of this work involves tensile testing of cellular material, FE analysis was carried out on as-designed cellular materials and compared with the experimental results. Further, tomography was carried out on a part of the cubic regular, cubic irregular and trabecular specimens. The tomography data was used to obtain a better comparison of the morphological parameters, FE models generated from tomography data were subjected to tensile loading and the results were compared with the experimental values. The fatigue tests were carried out in compression with a stress ratio of 0.1. One specimen in each topology was tested to capture the deformation pattern under fatigue loading. The effect of irregularity is captured in static as well as fatigue tests. The results of regular and irregular cellular materials are compared with the trabecular based cellular materials to obtain suitable cellular materials for future biomedical applications.

## 3.2. Materials and Methods

### 3.2.1. LPBF process

The cellular materials specimens were fabricated via LPBF technology, similar to the process explained in section 2.2.1. However, the machine and the parameters were different. An EOS LPBF machine with a laser power of 400W was used, with a layer thickness of 60  $\mu\text{m}$ . Similar to the study from chapter 2, biomedical grade Ti6Al4V alloys powder with particle size between 15-45  $\mu\text{m}$  was used. The manufactured specimens were subjected to heat treatment after manufacturing as mentioned in section 2.2.1. Additionally, the mechanical properties of the bulk material manufactured using the same process are in accordance with the ASTM standard F2924 [25] for the LPBF manufactured components.

### 3.2.2. Specimen Design

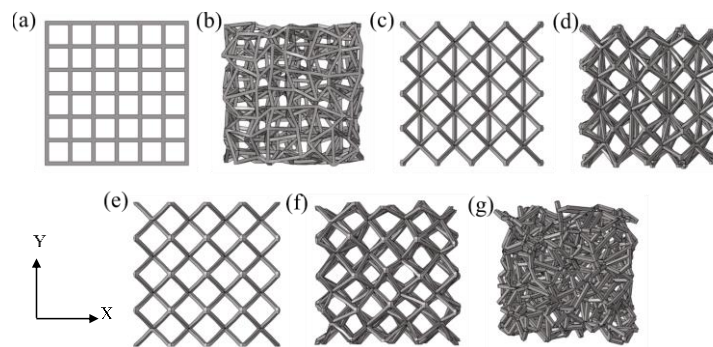


Figure III - 1 Schematic representation of the topology using STL files; (a) Cubic regular, (b) Cubic irregular, (c) Star regular, (d) Star irregular, (e) Cross regular, (f) Cross irregular, (g) Trabecular

As mentioned before, the study considers seven different topologies with a designed strut thickness of 200  $\mu\text{m}$  and pore size of 1200  $\mu\text{m}$ . The as-designed values were selected in order to reach a target strut thickness of 500  $\mu\text{m}$  and a pore size of 1100  $\mu\text{m}$  after the LPBF process. A schematic representation of the STL files used in the manufacturing process with designed values is shown in Fig. III-1. The STL files were generated using the MAGICS 21.1®, Materialise software and printed along the Y – direction. The regular structures are, cubic regular, star regular and cross regular shown in Fig. III-1(a), (c) and (e) respectively. The irregular structures are, cubic irregular, star irregular and cross irregular shown in Fig. III-1(b), (d) and (f) respectively. The nodes/junctions of the irregular structures are misaligned with respect to each other in random directions. The irregularity is obtained by an algorithm, the details of which is under proprietary conditions. The trabecular configuration is shown in Fig. III-1(g), this is a modification of the Voronoi tessellation, with narrow pore size and 4-6 struts

randomly joined at a node to mimic the trabecular bone. The number of struts per node and their orientation vary depending on the cell topology. The ability of the irregular/trabecular structures to provide better osseointegration is the main rationale behind their design and consideration for mechanical testing.

The different types of specimens produced were: (i) Cylindrical specimens shown in Fig. III-2(a) with a diameter of 15mm and length of 17mm ( $l/d > 1$ ). These specimens were used for static compression and compression-compression fatigue tests. (ii) Tensile specimens with cellular part in the center and solid grips in the end as discussed in section 2.2.1. However, the cellular part of the tensile specimen (Fig. III-2(b)) consists of transition region (Fig. III-2(c)) at the ends with a gradual increase in the struts thickness. The STL files of the tensile specimen are shown in Fig. III-A1 provided in Appendix 3.6.1. The length and the diameter of the cellular part is 14 mm and 10 mm respectively. The thickness was gradually increase by  $\sim 1.8$  times at the end of the cellular part. The transitions were used to avoid any stress concentration between the cellular part and the solid grip.

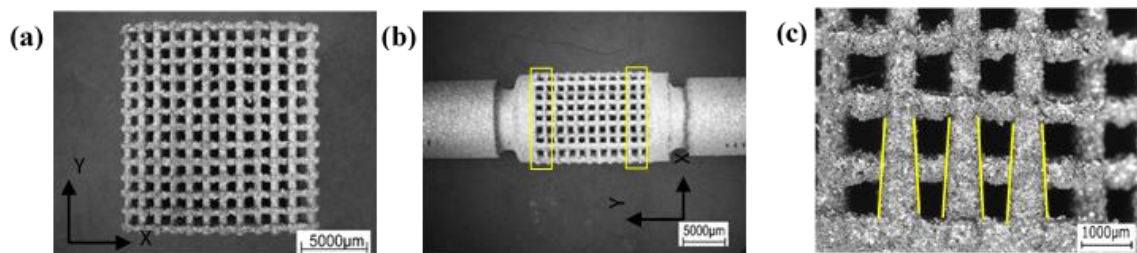


Figure III - 2 (a) Compression and fatigue test specimen (b) Tensile test specimen with transition highlighted and (c) Thickness increase in tensile specimens.

### 3.2.3. Microstructure and porosity

The microstructure observation was carried out on one specimen along both the directions to observe the microstructure after manufacturing and the heat treatment. The porosity analysis was carried out to calculate the deviation in the porosity values of the specimens from the designed porosity values. The procedure for microstructure porosity analysis is provided in section 2.2.2 and 2.2.3 respectively.

### 3.2.4. Strut thickness analysis

The morphological analysis was mainly carried out to obtain the variation in strut thickness values from the designed values. The variation of the strut thickness is based on the orientation of the struts, the thickness values consider the powder particles attached to the surface since the specimens were not subjected to any treatment such as chemical etching to remove the attached particles. In this, all the seven topologies were considered. The struts in all the seven topologies were broadly categorized as horizontal struts, vertical struts, inclined/oblique struts for regular struts, and irregular and random struts for irregular and trabecular configuration. The images are captured using Nikon stereo optical microscope (Nikon SMZ25), a representation of the same is shown in Fig. III-3. The strut thickness is calculated considering the rough edges as well using ImageJ®. More than 100 measurements are obtained from the images to have a statistically accurate data.

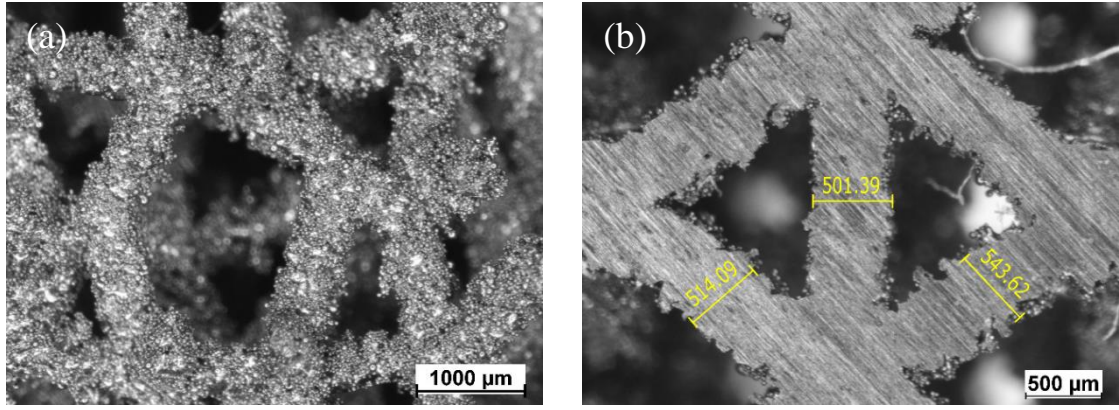


Figure III - 3 Spectro microscopy images for morphological analysis (a) Cubic irregular (b) Star regular indicating the measured strut thickness ( $\mu\text{m}$ )

### 3.2.5. Static tensile and compression test

The static tests were carried out under tensile and compression loading, the machine used, and the test parameters are as described in the section 2.2.5. Even in this study the tests were carried out under two conditions, monotonic and cyclic loading. One specimen was tested under monotonic condition and four specimens were tested under cyclic condition.

The monotonic test is used to obtain the monotonic Young's modulus ( $E_{mT}$  -tensile,  $E_{mC}$  – compression) 0.2% offset yield strength ( $\sigma_{yT}$  - tensile,  $\sigma_{yC}$  – compression), maximum compressive strength ( $\sigma_{mC}$ ), and maximum tensile strength ( $\sigma_{mT}$ ). The cyclic test was carried out by loading the specimen using a triangular shaped wave for five cycles between 20 – 70% of the yield load. The test yielded unloading Young's modulus designated as cyclic Young's modulus ( $E_{cT}$  – tensile ,  $E_{cC}$  – compression).

### 3.2.6. Fatigue test

The fatigue test of the cellular specimens was carried out under compression – compression fatigue loading. A minimum of 12 specimens were tested in each topology at different loads to obtain a S-N curve. The fatigue tests were carried out using RUMUL resonating fatigue test machine with a load capacity of 50kN, shown in Fig. III-4. The test was conducted with an R – ratio of 0.1 in compression and the maximum load applied in fatigue was between 0.1 – 0.8 times the yield load to generate an S-N curve [12, 26]. Before testing, the top and bottom surface of the specimen was polished to make them flat to ensure proper contact during testing. The run-out condition was set for  $10^7$  cycles and the specimens were considered to be failed when a frequency drop of 1 Hz was observed. The number cycles recorded at failure was considered the fatigue life at that particular load. The data points from the test are fitted using the curve fitting from equation. III-1, where  $C_1$ ,  $C_2$ ,  $m$  are the curve fitting parameters, where  $\sigma_{\text{max}}$  is the maximum applied stress,  $N_f$  is the number of cycles to failure. and  $C_1$ ,  $C_2$ ,  $m$  are the curve fitting parameters. The fatigue strength of cellular material was obtained from the S-N curve at  $10^6$  cycles. The scatter of the fatigue data ( $S^2$ ) is computed by equation. III-2, where  $\sigma_{\text{max}-i}$  is the  $i^{\text{th}}$  maximum applied stress,  $\sigma'_{\text{max}-i}$  is the  $i^{\text{th}}$  estimated maximum stress,  $n$  is the number of data points on the curve and  $p$  is the number of parameters in Eq. III-1 i.e., 3. The standard deviation is obtained from the value of  $S$  (square root of  $S^2$ ) from Eq.III-2. Fractography analysis of samples was carried out using JOEL JSM-IT300LV scanning electron microscope.

$$\sigma_{\text{max}} = C_1 + \frac{C_2}{(N_f)^m} \quad \dots\dots\dots \text{Eq. III-1}$$

$$S^2 = \frac{\sum_{i=1}^n (\sigma_{max-i} - \sigma'_{max-i})^2}{n-p} \quad \dots\dots\dots \text{Eq. III-2}$$

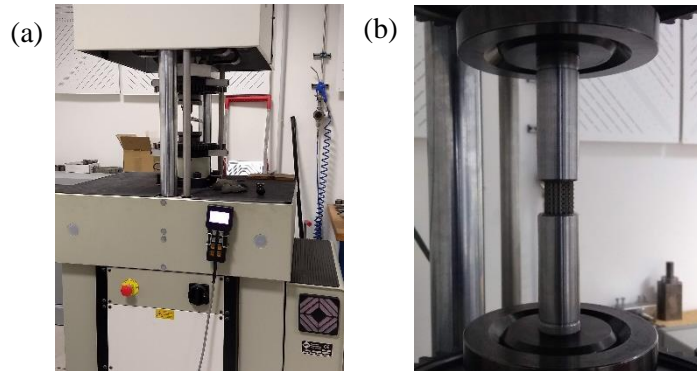


Figure III - 4 (a) RUMUL fatigue testing machine (b) Fatigue test setup with star regular cellular material

One specimen in each configuration (except cubic regular) was subjected to separate fatigue tests to capture their deformation behavior. The tests were carried out using an MTS 809 Axial/Torsional testing machine with load capacity of 100 kN and at a frequency of 5 Hz. A high-speed camera with a capturing frequency of 30 Hz was used to record the complete fatigue test and capture the deformation. Frames from the test are used to explain the deformation mechanism of different cell topologies.

### 3.2.7. Finite element modelling

The finite element modelling in this study was carried out under three different categories based on the loading and the number of topologies considered. However, the main focus of the FE modelling was on the tensile properties of the as-designed configuration.

The FE models were generated from the STL files and the analysis was carried out using the same methodology employed in the section 2.2.6. For as-designed configuration full FE model of the tensile specimen was used since the struts were thin and the number of unit cells were less. The FE models were generated using the *shrink-wrap* option in Hypermesh®. The number of elements in the FE model varied between 800,000 to 1,500,000 depending on the topology.

*Elastic condition:* The main aim of this analysis was to study the effect of transition in the tensile samples on the Young’s modulus. The experimental Young’s modulus from tensile test was slightly higher compared to compression test, it was assumed that this increase is due to the presence of transition in the tensile specimens. Therefore, to confirm this, FE analysis was carried out on models with and without the transition, an example of the same is shown in Fig. III-5. A ratio of the obtained Young’s modulus was used as factor to estimate the tensile Young’s modulus in the absence of transition. The basic code used for this is provided in Appendix I. The code is changed according to the geometry and the required output.

*Elastic - plastic condition:* The main aim of this analysis was to compare the as-designed and the as-built tensile stress-strain curves for all the samples. Further, the plastic strain plots were compared with the fracture plane images of the failed specimens to see the effect of increased strut thickness on the failure location and pattern under tensile loading. The methodology for the elastic-plastic analysis is explained in section 2.2.6.2.

*Tomography model:* The results from the tomography models of cubic regular, cubic irregular and trabecular specimens are compared with the experimental results of the previous chapter and this chapter. The results indicate the effect of porosity as well as the transition in the tensile specimens of this batch.

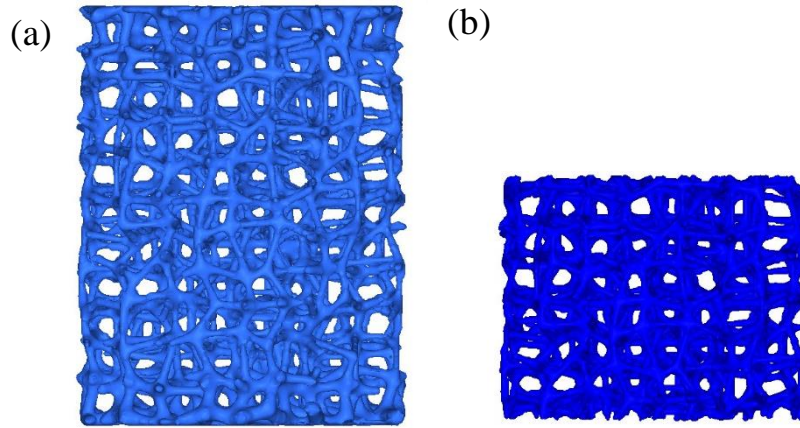


Figure III - 5 FE model of tensile as-designed specimen (a) With transition (b) Without transition

The basic code used for the elastic plastic analysis provided in the Appendix I. The code is changed according to the geometry and the required output. (In this case, the stress and strain).

### 3.3. Results and discussion

#### 3.3.1. Microstructure

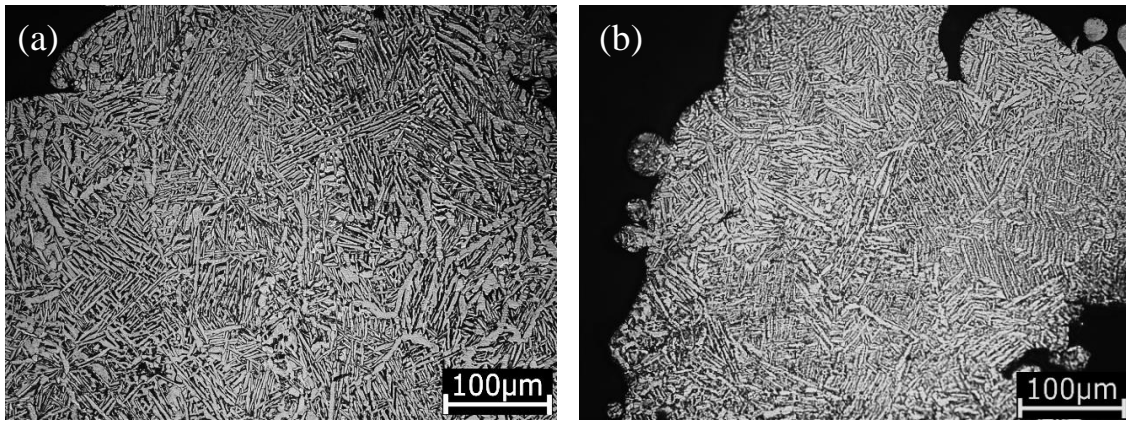


Figure III - 6 Microstructure of Ti6Al4V cellular material (a) XY plane (b) XZ plane

All the manufactured specimens were subjected to heat treatment as mentioned in section 3.2.1. The microstructure analysis was carried to check the transformation of as-built  $\alpha'$  martensitic phase to  $\alpha+\beta$  phase. The microstructure observed in cubic regular specimen is shown in Fig. III-6. The  $\alpha+\beta$  lamellae phase is present in the form of a uniform basket-weave microstructure.

#### 3.3.2. Porosity analysis

The porosity analysis was carried out measure the deviation from the designed porosity of the specimens due to the manufacturing process. The designed porosity measured porosity and porosity from the  $\mu$ CT scans are tabulated in Table III-1. The measured porosity values are lower than the designed values, similar to the results obtained in the previous chapter. Also, a clear difference between the measured porosity of tensile and compression specimens is seen. This difference is due to the presence of transition region in the tensile specimen. However, for trabecular specimens, porosity of tensile and compression specimens is similar since the transition region was absent and was merged inside the solid grip during manufacturing (observed from visual inspection). The porosity of the specimen depends on the cell topology, number of struts and also the strut thickness. Star regular specimens which have 10 struts at a node has higher porosity compared to trabecular specimens which

have 4-6 struts at a node. This is due to variation of strut thickness in different cell topologies. The strut thickness values that affect the porosity values are calculated and explained in the next section.

Table III - 1 Comparison of designed, measured and  $\mu$ CT porosity for all topologies

| Cell topology          | Designed porosity (%) | Measured porosity (%) |               | $\mu$ CT porosity (compression) (%) |
|------------------------|-----------------------|-----------------------|---------------|-------------------------------------|
|                        |                       | Compression           | Tensile       |                                     |
| <b>Cubic regular</b>   | 93                    | 76 $\pm$ 0.15         | 70 $\pm$ 0.34 | 74                                  |
| <b>Cubic irregular</b> | 93                    | 71 $\pm$ 0.21         | 65 $\pm$ 0.20 | 70                                  |
| <b>Star regular</b>    | 89                    | 77 $\pm$ 0.32         | 67 $\pm$ 0.18 | -                                   |
| <b>Star irregular</b>  | 88                    | 77 $\pm$ 0.18         | 68 $\pm$ 0.22 | -                                   |
| <b>Cross regular</b>   | 91                    | 79 $\pm$ 0.18         | 72 $\pm$ 0.15 | -                                   |
| <b>Cross irregular</b> | 91                    | 80 $\pm$ 0.19         | 71 $\pm$ 0.23 | -                                   |
| <b>Trabecular</b>      | 91                    | 71 $\pm$ 0.32         | 70 $\pm$ 0.35 | 73                                  |

### 3.3.3. Strut thickness analysis of all cell topologies

All the struts in the seven topologies are categorized based on their orientation and the cell topology as explained in section 3.2.5. The average strut thickness values are as shown in Fig. III-7(a). The results indicate that the horizontal struts have the lowest thickness values of  $\sim$ 370  $\mu$ m and the random struts from trabecular specimens had the highest strut thickness of  $\sim$ 580  $\mu$ m. The vertical struts and random struts had their thickness closer to 500  $\mu$ m. A normal distribution of the strut thickness is shown in Fig. III-7(b). The thickness of the struts produced from the LPBF process not only depend on the designed values but also on the orientation and the process parameters [27].

Since all the cell topologies in this study were printed under the same process parameters, the strut thickness solely depends on the orientation. In horizontal struts, during the LPBF process the laser melts the powder below the first layer as well since no support structures are present. Due to this and the effect of gravity, the struts are susceptible to waviness and sagging. Therefore, the strut thickness varies of horizontal struts vary between 280 – 450  $\mu$ m showing a larger width in the normal distribution curve. On the contrary, vertical struts have support for the complete area of the strut due to which they are printed uniformly in cubic as well as star regular specimens. Comparing the vertical and oblique struts, the curves overlap and have closer average values, but the width of the curve is higher in oblique struts indicating the effect of orientation. The distribution curve of the irregular struts is similar to the oblique struts but with a shift towards higher thickness values by 20  $\mu$ m. The random struts have the highest thickness values but since the random orientation at a junction leads to an overlap of the struts during the LPBF process.

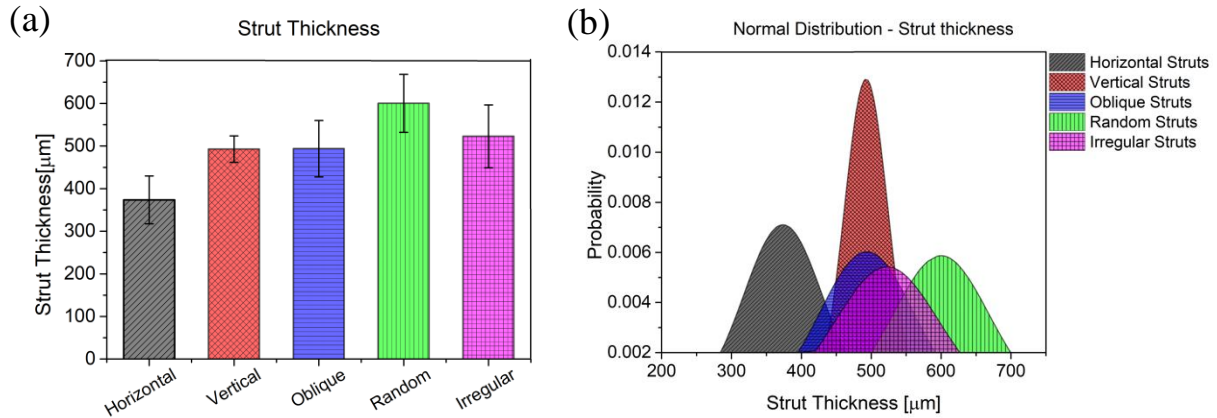


Figure III - 7 (a) Strut thickness of struts oriented in different direction (b) Normal distribution of strut thickness

As mentioned before, the strut thickness and the porosity are inversely related. The lowest porosity was observed for trabecular structures which was composed of random struts with the highest porosity. Cross based and star-based specimens had closer porosity values due to similar thickness values, despite the presence of extra strut in star-based specimens. Even though cubic regular and cubic irregular have comparable configuration, the lower thickness value of horizontal struts in cubic regular specimens increase its porosity compared to cubic irregular specimens by ~ 5%.

### 3.3.4. Compression test

As mentioned before, the stress- strain curve of a cellular material under compression consists of three regions, elastic, plateau, and densification if the specimen is loaded until all the layers fail. The stress – strain curve is highly dependent on the cell topology and the relative density [9]. The tests in this study were carried out until first failure in the specimen was observed. This was done in order to identify a posterior, i.e., the first yielding point which is the weakest location in the cellular material. The tests were conducted under monotonic and cyclic conditions, the stress – strain curves for both the conditions are shown in Fig. III-8. The curves clearly indicate the effect of cell topology to the compression loading.

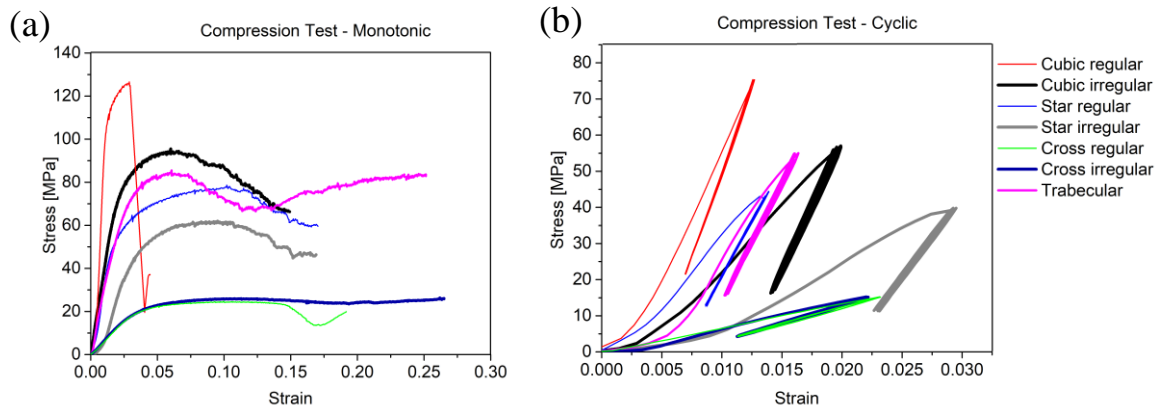


Figure III - 8 Compression test stress-strain curves (a) Monotonic condition (b) Cyclic condition

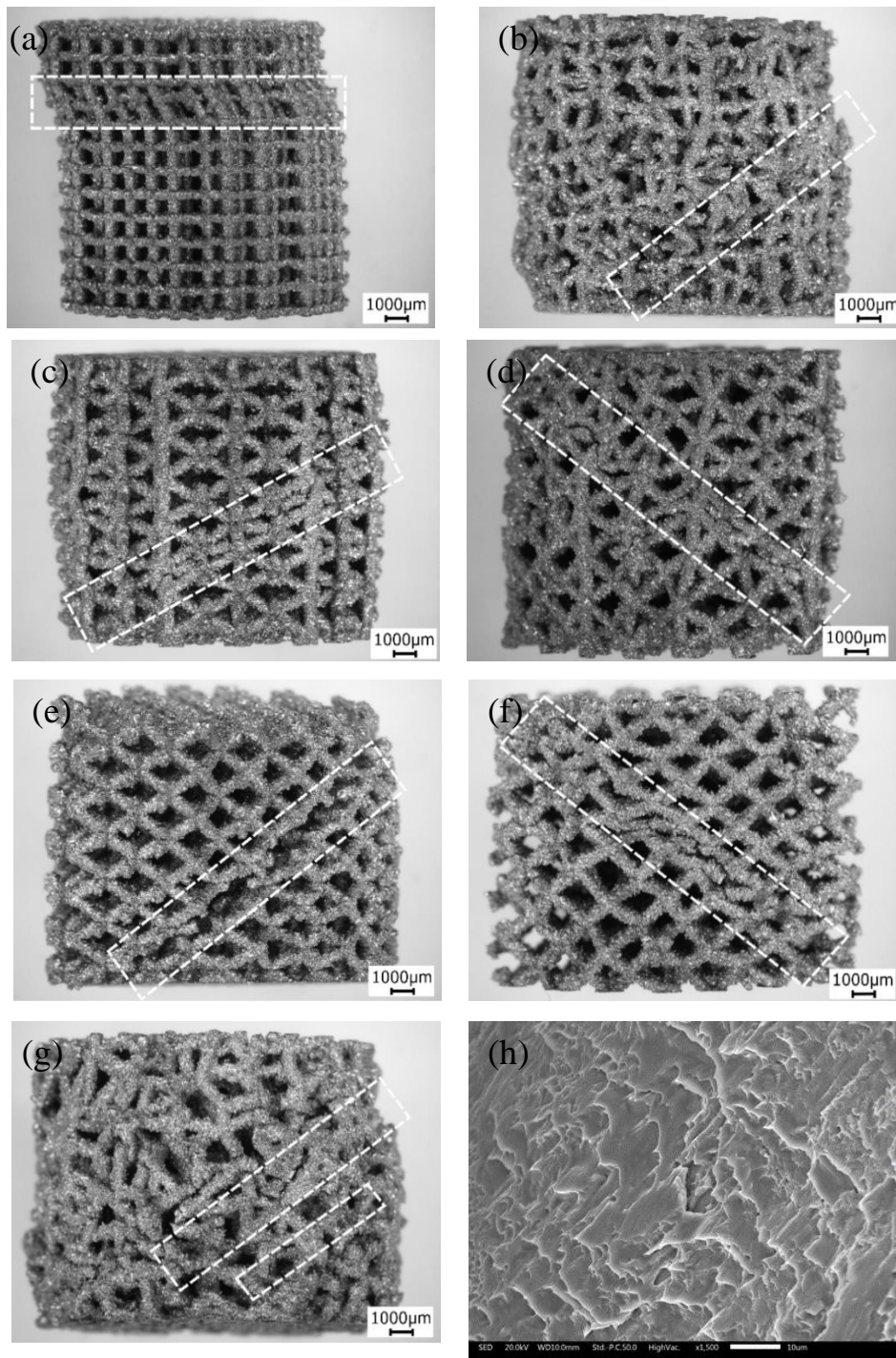


Figure III - 9 Fracture planes under compression loading (a) Cubic regular (b) Cubic irregular (c) Star regular (d) Star irregular (e) Cross regular (f) Cross irregular (g) Trabecular (h) SEM image of fracture surface indicating shear

The curve of the cubic regular specimens shown that the specimens reached the highest strength and stiffness but a sudden and sharp decrease in the stress to  $\sim 20$  MPa was observed at very low strain value. This indicated a catastrophic failure of vertical struts due to buckling under axial load. A layer of struts that failed due to buckling is shown in Fig. III-9(a). The cubic irregular structure had a considerable plateau region compared to cubic regular structures. However, the irregularity due to misalignment of nodes decreases the maximum load the specimen can sustain before failure but helps in achieving higher strain values. The failure plane of cubic irregular shown in shown in Fig. III-9(b) is similar to a shearing band. The star-based topology, both regular and irregular have a plateau region

similar to cubic irregular specimens. Despite the presence of vertical struts in star-based regular specimens, the maximum load sustained is lesser than the cubic regular specimens. The presence of oblique struts induces a certain amount of bending at the junction or nodes. Nevertheless, the oblique struts help in load distribution that leads to a longer plateau region. The presence of irregularity in star-based specimens effects the maximum strength and not the maximum strain values reached. The compression load on star-based specimens leads to failure with a shear band formation at different angles as shown in Fig. III-9(c) and (d). The curves of the cross -based specimens is entirely different from the other topologies. The curve indicates that the elastic region is followed by a smooth and long plateau region but have the lowest stiffness compared to any other configuration considered. This is due to the absence of vertical struts that induce stretching dominated behavior in the specimens. The failure planes shown in Fig. III-9(e) and (f) indicate shearing at 45° at the nodes [28–30]. Also, the irregularity has negligible effect on the cross-based specimens. The last configuration is the trabecular specimens, the curves indicate that the properties of the specimens are between the two extreme curves seen in the Fig. III-8(a). The effect of cell topology is dominant at high porosity values as discussed in chapter II. Trabecular specimens reach strength values similar to cubic irregular but have longer plateau like cross-based specimens. The stress-strain curves give a clear example of ideal stretching dominated behaviour by cubic regular specimens and an ideal bending dominated behaviour by cross-based specimens. For cross-based specimens, SEM image of the fracture surface shown in Fig. III-9(g) indicates a local shearing at failure location during compression loading.

The stress-strain curves under cyclic loading are shown in Fig. III-8(b). The curve overlaps after the first unloading cycle indicating that the stabilisation has reached. During the first loading cycle, the specimens undergo local plasticization which stabilises them after the first unloading cycle. It is seen that despite the difference in the cell topology, all the specimens show complete stabilisation after the first unloading cycle. The overlapped part of the curve is used to calculate the cyclic Young’s modulus in the specimens explained in the next section.

### 3.3.5. Tensile test

The tensile stress-strain curves under monotonic and cyclic loading are shown in Fig. III-10. The tensile curves do not have a plateau region like compression curves, as the specimens do not undergo a layer-by-layer failure. They consist of an elastic region, followed by yielding and plastic region and final failure.

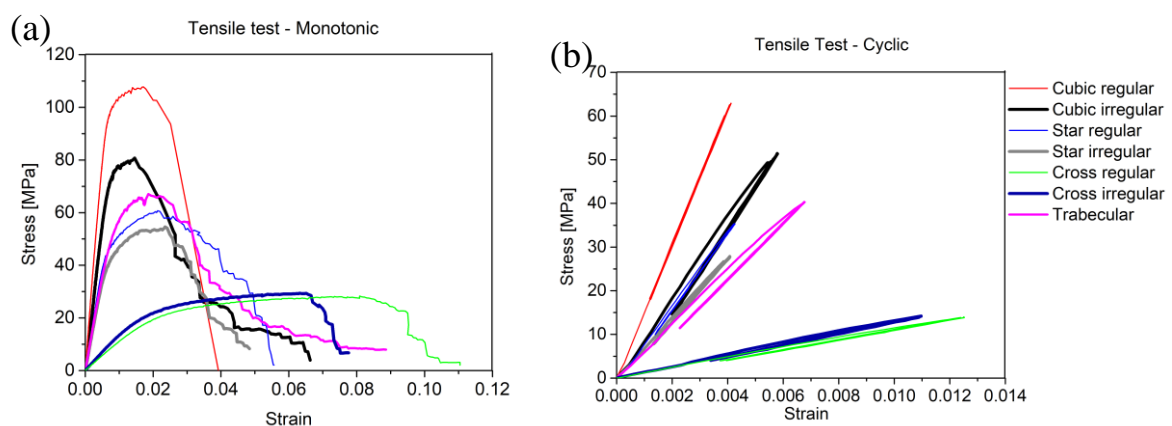


Figure III - 10 Tensile test stress-strain curves (a) Monotonic condition (b) Cyclic condition

Comparing the different cell topologies, cubic regular specimens had the highest strength as observed in compression due to the presence of struts along the loading direction. However, the failure of the specimen took place a low strain value. The cubic irregular specimens can sustain lower loads compared to cubic regular, they also reach the maximum stress at lower strain values, but they undergo

final fracture at a slightly higher strain value. The star-based specimens have lower strength compared to cubic regular due to the presence of oblique struts. The strain value at maximum stress is higher compared to cubic based specimens. The cross-based specimens have lower strength and stiffness compared to all the topologies but reach relatively high strain values before fracture. The absence of any struts along the loading direction increases the ductility of the specimen due to the elongation of the oblique struts at the junctions before failure. The trabecular specimens shown a behaviour in between the stretching dominated cubic regular and bending dominated cross regular specimens. Furthermore, the effect of irregularity is pronounced in cubic specimens, followed by star based. The irregularity has no or negligible effect on the cross-based specimens as seen from the curves.

The cyclic stress-strain curves under tensile loading are shown in Fig. III-10(b). Unlike the compression test curves, an overlap is seen from the first loading cycle for all the specimens except cubic irregular and trabecular. This indicates that under tensile loading, the specimens do not undergo any considerable plasticization or stabilisation. However, the cyclic Young's modulus is calculated from the linear region in the unloading part of the curve.

The failure plane images under tensile loading are provided in the Fig. III-18 for all the cell topologies. The images indicate that the failure in cubic specimen is exactly between the struts along a straight line. In the star-based regular specimens, the failure is at the center of the struts but the failure plane is at an angle similar to shear band. In other specimens, the failure is seen at the junction/nodes as well as between the struts due to the irregularity. An SEM image of the fracture surface in trabecular specimen is shown in Fig. III-11. The Fig. III-11(a) indicates the formation of cup on one side of the failure similar to the typical tensile failure of a ductile specimen. A magnified image shown in Fig. III-11(b) indicates the formation of small dimples on the surface due to tensile loading.

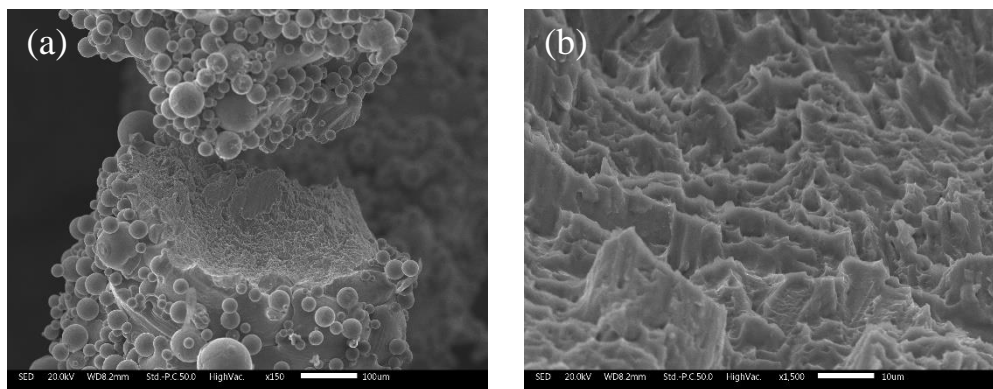


Figure III - 11 SEM images of tensile fracture surface (a) Cup formation in the strut (b) Peaks and valleys indicating ductile failure

Table III - 2 Monotonic and cyclic Young's modulus under tensile and compression loading

| Sample                 | Monotonic Young's Modulus (GPa) |             | Cyclic Young's Modulus (GPa) |                  |
|------------------------|---------------------------------|-------------|------------------------------|------------------|
|                        | Tensile                         | Compression | Tensile                      | Compression      |
|                        | $E_{mT}$                        | $E_{mC}$    | $E_{cT}$                     | $E_{cC}$         |
| <b>Cubic regular</b>   | 16.31                           | 13.43       | $15.42 \pm 0.17$             | $11.29 \pm 1.24$ |
| <b>Cubic irregular</b> | 11.82                           | 3.74        | $9.61 \pm 0.33$              | $6.97 \pm 0.66$  |
| <b>Star regular</b>    | 8.25                            | 4.47        | $8.20 \pm 0.61$              | $6.26 \pm 0.32$  |
| <b>Star irregular</b>  | 7.00                            | 2.33        | $7.01 \pm 0.40$              | $4.50 \pm 0.12$  |
| <b>Cross regular</b>   | 1.12                            | 0.64        | $1.21 \pm 0.14$              | $0.91 \pm 0.01$  |
| <b>Cross irregular</b> | 1.38                            | 0.65        | $1.36 \pm 0.05$              | $0.97 \pm 0.03$  |
| <b>Trabecular</b>      | 7.34                            | 2.82        | $6.61 \pm 0.37$              | $6.39 \pm 0.39$  |

The Young's modulus values from tensile and compression tests are tabulated in Table III-2. Comparing the monotonic and cyclic Young's modulus a slight difference is observed in tensile, but the difference pronounced in compression. The cyclic Young's modulus in compression has increased by atleast 2 GPa compared to monotonic modulus except for cubic regular specimens, indicating the effect of stabilisation. The Young's modulus in compression varied between 13 – 0.6 GPa under monotonic condition and between 11 and 1 GPa for cyclic condition depending on the topology. Comparing the tensile and compression Young's modulus, higher stiffness was observed in tensile for the same topology, this is due to the presence of transition region in the tensile specimen that increases the stiffness. An FE analysis on the effect of transition is carried out in the section 3.3.8.1.

Table III - 3 Yield and maximum strength values under tensile and compression loading

| Sample                 | 0.2% offset yield strength (MPa) |               | Maximum strength (MPa) |               |
|------------------------|----------------------------------|---------------|------------------------|---------------|
|                        | Tensile                          | Compression   | Tensile                | Compression   |
|                        | $\sigma_{yT}$                    | $\sigma_{yC}$ | $\sigma_{mT}$          | $\sigma_{mC}$ |
| <b>Cubic regular</b>   | 100                              | 111           | 108                    | 126           |
| <b>Cubic irregular</b> | 76                               | 71            | 81                     | 95            |
| <b>Star regular</b>    | 48                               | 48            | 61                     | 79            |
| <b>Star irregular</b>  | 44                               | 36            | 55                     | 62            |
| <b>Cross regular</b>   | 18                               | 17.1          | 28                     | 25            |
| <b>Cross irregular</b> | 19                               | 17.8          | 29                     | 26            |
| <b>Trabecular</b>      | 56                               | 55            | 67                     | 85            |

The 0.2% offset yield strength and the maximum strength in the specimens are calculated from the monotonic test and tabulated in Table III-3. Comparing the offset yield strength in the tensile and compression, the values are considerably closer to each other. A maximum difference of 11 MPa is observed for the cubic regular configuration. The values indicate that despite the difference in the loading, the specimens start yielding at similar stress levels. However, when comparing the maximum strength in the specimens, the maximum strength in compression is higher compared to tensile, this is due to the different failure mechanism under compression and tensile loading.

Comparing the strength and stiffness of the specimens by taking the irregularity into consideration, the cubic based specimens are highly influenced. Under both the loading conditions, the irregularity

provides a small increase in the properties, while in all the other topologies the effect is negative. In tensile loading, the irregularity decreases the strength by ~25% and cyclic modulus by ~36%. In star-based specimens, ~10% decrease in strength and ~15% decrease in the cyclic modulus due to the irregularity. Under compression loading, for cubic based specimens, ~38% decrease in cyclic modulus and an average of ~30% decrease in strength is observed. In star-based specimens, the values are ~28% in cyclic loading and ~23% in strength. In trabecular specimens, the strength and stiffness values of trabecular specimens were similar to the cubic irregular and star regular.

### 3.3.6. Fatigue test

The S-N curves for all the topologies obtained from the compression-compression fatigue curves are shown in Fig. III-12. The data points of the S-N plot is fitted using the method described in the section 3.2.6. The scatter in the fatigue data, the fitting parameters, and the standard deviation values for all the cell topologies are provided in the Table. III-4. The effect of cell topology on the fatigue behavior is clearly seen in the S-N curves. The cubic regular specimens showed high fatigue resistance and no failure was observed up to  $10^7$  cycles for any load applied below  $0.8\sigma_{yc}$ . The static tests of cubic regular specimens indicated that the failure is mainly due to buckling of struts under compression loading. The absence of bending component in cubic regular specimen makes them resistant to fatigue loading [12]. Therefore, the S-N curve obtained for cubic regular specimens is a straight line as shown in Fig. III-12(a), to obtain this expected curve, the load applied is slightly higher than  $0.8\sigma_{yc}$ . Similar resistance to failure in cubic cellular specimens was observed by Yavari et al. at all different porosity values [26]. On the contrary, the cubic irregular specimens show significant decrease in the fatigue properties as indicated from the S-N curve in Fig. III-12(a). The effect of node misalignment to induce irregularity is clearly visible. Further, the irregularity has higher effect under fatigue loading compared to loading under static conditions. The cracks starts to grow relatively quickly due to the node misalignment which introduced bending in the specimen. Both cubic regular and star regular have struts along the loading direction but the presence of oblique struts in star based specimens leads to bending at the junction and lower fatigue resistance. The S-N curves comparing the irregularity in star based and cross based specimens are shown in Fig. III-12(b) and (c). The S-N curves of cross based regular and irregular configurations is less compared to cubic and star based. Similar to the static test results, the irregularity has higher impact on the cell topologies with vertical struts. The irregularity decreased the compressive strength under static loading by 21-25%, while as in fatigue loading the this decrease raised upto 80% in the high-cycle region of the S-N curve. The S-N curve of trabecular structure Fig. III-12(d) is between regular star and cubic specimens and irregular star and cubic specimens. The random orientation of struts that quasi-isotropic configuration is clearly noticeable in fatigue test compared to static compression test. The maximum number of cycles that the cross based specimens could sustain for the lowest load values was  $10^6$  cycles. Hence, the fatigue strength for all the cell topologies are calculated at  $10^6$  cycles from the S-N curve and tabulated in Table. III-5. even at the lower range of the applied load. The standard deviation values indicate that the scatter in the data is the lowest for bending-dominated, cross-based specimens and highest for star irregular and cubic irregular after cubic regular specimens. Despite the randomness in trabecular specimens, the scatter in the fatigue data is acceptable as indicated by the standard deviation.

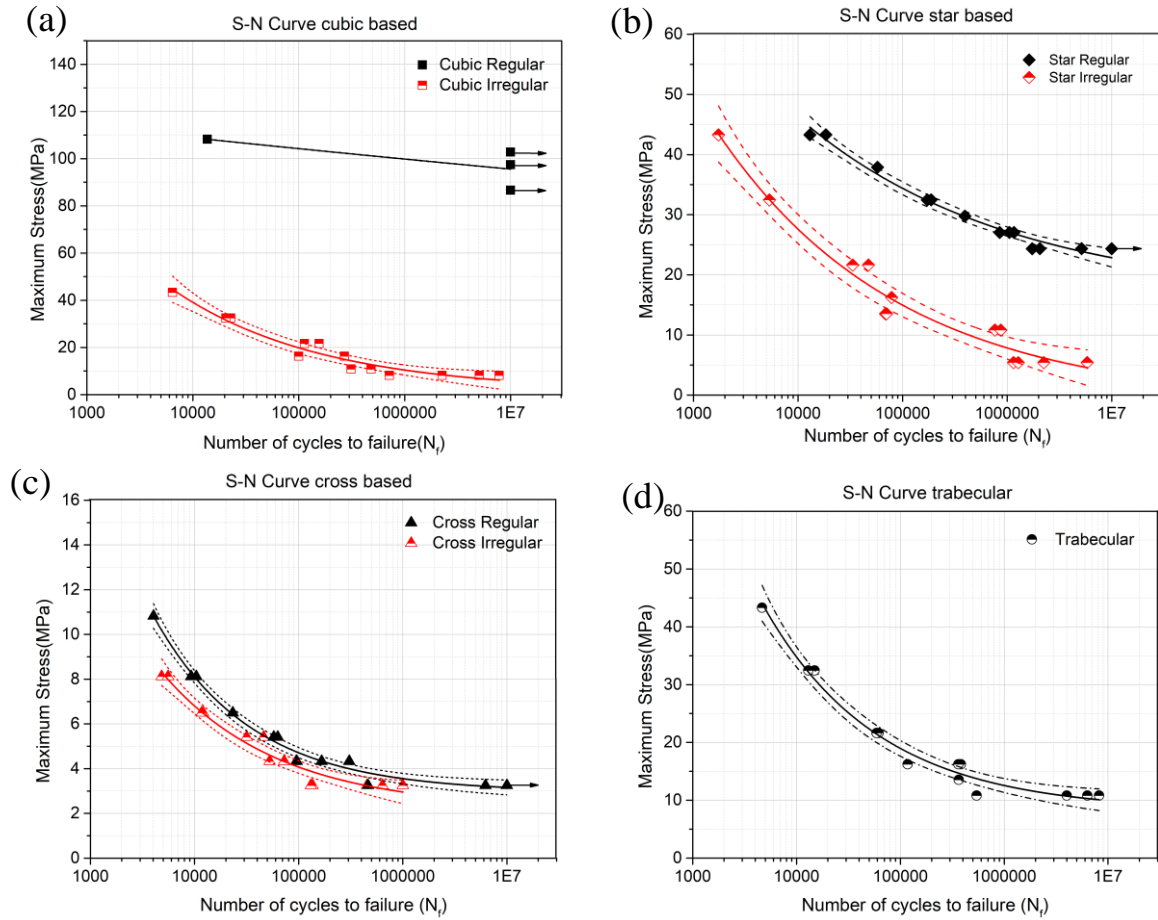


Figure III - 12 S-N curves from fatigue test of cellular material with asymptotic curve fitting and 95% confidence band (a) Cubic based (b) Star based (c) Cross based (d) Trabecular

Table III - 4 S-N curve fitting parameters and fatigue data scatter

| Sample                 | $C_1$ (MPa) | $C_2$  | $m$  | $S^2$  | Std Dev |
|------------------------|-------------|--------|------|--------|---------|
| <b>Cubic regular</b>   | -11.34      | 140    | 0.02 | 136.61 | 11.68   |
| <b>Cubic irregular</b> | 1.49        | 658.52 | 0.31 | 7.71   | 2.78    |
| <b>Star regular</b>    | 16.12       | 221.73 | 0.22 | 1.07   | 1.03    |
| <b>Star irregular</b>  | -1.37       | 286.69 | 0.24 | 9.54   | 3.08    |
| <b>Cross regular</b>   | 2.95        | 380.64 | 0.47 | 0.07   | 0.26    |
| <b>Cross irregular</b> | 2.19        | 166.83 | 0.39 | 0.14   | 0.37    |
| <b>Trabecular</b>      | 8.17        | 979.06 | 0.39 | 2.35   | 1.53    |

Table III - 5 Fatigue strength for different cell topologies

| Sample                 | Cubic Regular | Cubic Irregular | Star Regular | Star Irregular | Cross Regular | Cross Irregular | Trabecular |
|------------------------|---------------|-----------------|--------------|----------------|---------------|-----------------|------------|
| Porosity(%)            | 76 ± 0.15     | 71 ± 0.21       | 77 ± 0.32    | 77 ± 0.18      | 79 ± 0.18     | 80 ± 0.19       | 71 ± 0.32  |
| Fatigue Strength (MPa) | 100±11.7      | 10±2.8          | 27±1.0       | 7.5±3.1        | 3.5±0.3       | 3.1±0.4         | 12.5±1.6   |

For cubic specimens with porosity in the range of 60% and strut thickness of ~600 μm, Zhao et.al. [12] reported a fatigue strength of 75 MPa. In this current study, the fatigue strength of cubic regular structure with porosity of ~76% and strut thickness of ~450 μm had a fatigue strength of 100 MPa. The values obtained in this study are higher when compared to Zhao et al. Despite the lower porosity in our study, a higher strength was seen. However, the microstructure and heat treatment are not the same in both the studies. Comparing the fatigue strength of cross based specimens with the literature, a fatigue strength of 2.5 MPa was reported for BCC (cross based) cell topology using FE analysis by Peng et. al. [31], in our study a fatigue strength of 3.1 MPa was reported for cross based specimens. Irregularity had a major impact on the fatigue strength of cubic based specimens. The irregularity reduces the fatigue strength by almost 10 times in cubic based specimens. The effect of one single vertical strut on the fatigue strength is seen when comparing the star based and cross based specimens. The fatigue strength of the star based specimes is almost 8 times more than the cross based specimens. However, the effect of the presence of vertical struts in irregular configuration is not significant when we compare star irregular and cross irregular. This is because the irregularity in the nodes also inclines the vertical struts in star irregular configuration. The trabecular structures show better fatigue properties compared to cross based, cubic irregular and star irregular specimens despite have lesser number of struts per node. This maybe due to the low porosity but the main reason is the presence in all the directions forming a topology closer to isotropy. The effect of struts in all the directions is explained using the frequency variation curve shown in Fig. III-13.

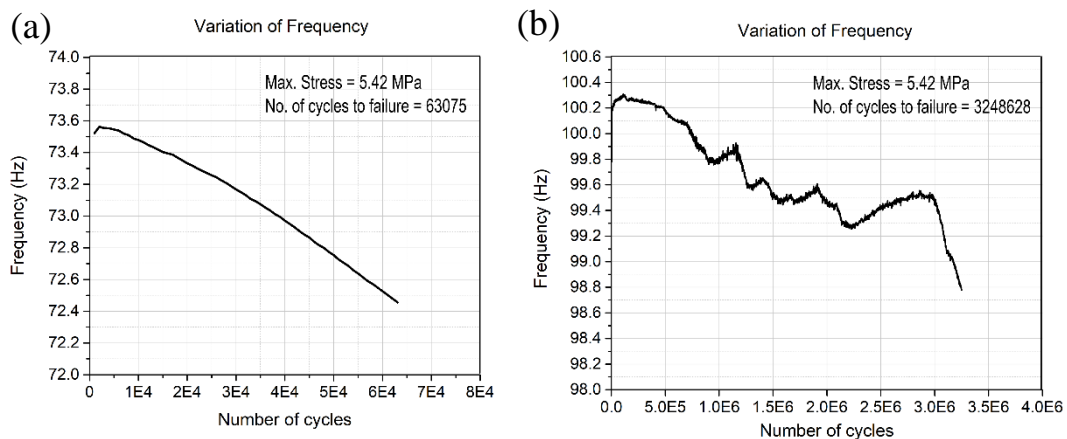


Figure III - 13 Frequency variation during the fatigue test (a) steady decrease in cross regular specimen (b) formation of peaks and valleys in trabecular specimen

Fig. III-13 represent the frequency versus number of cycles curve for cross regular and trabecular specimen subjected to the same maximum load. In the case of cross regular specimen, a steady linear decrease in the frequency is observed as shown in Fig. III-13(a). Similar behavior was observed for all regular configuration specimens. On the contrary, for some of the irregular configuration specimens and especially for trabecular configurations a distinctive behavior shown in Fig. III-13(b) was observed. The curve representing the decrease in the frequency was not steady and consisted of peaks and valleys

before a decrease of 1 Hz in the frequency was observed, indicating that the specimens sustain higher number of cycles before failure. The random distribution of struts, leads to local failure at various location due to stress redistribution and decelerates the crack growth across the entire section of the specimen. This is indicated in the fracture plane of trabecular specimens shown in Fig. III-15(g).

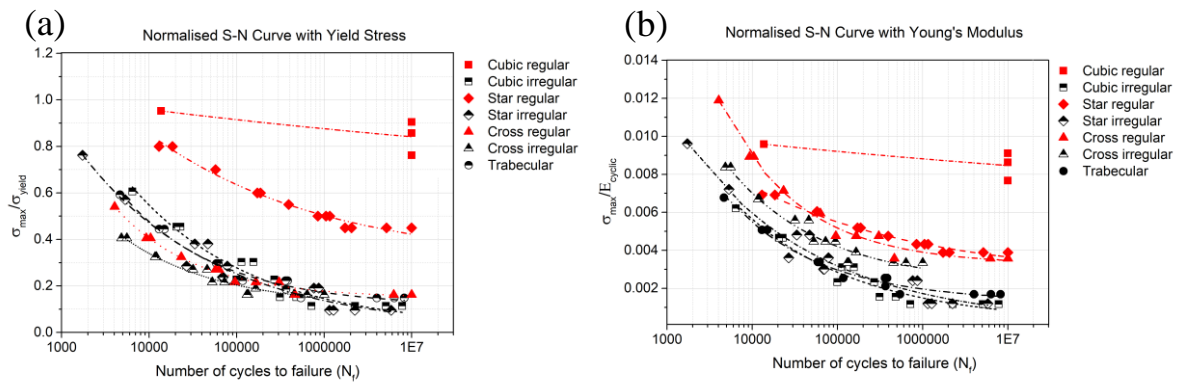


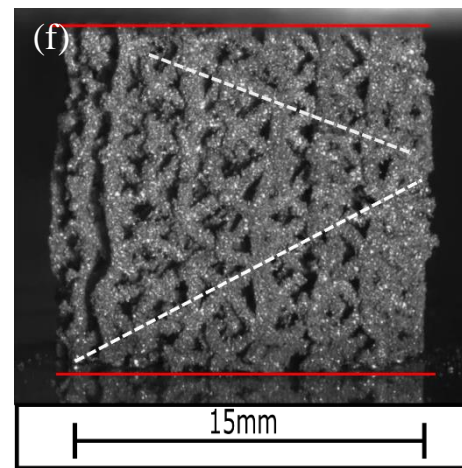
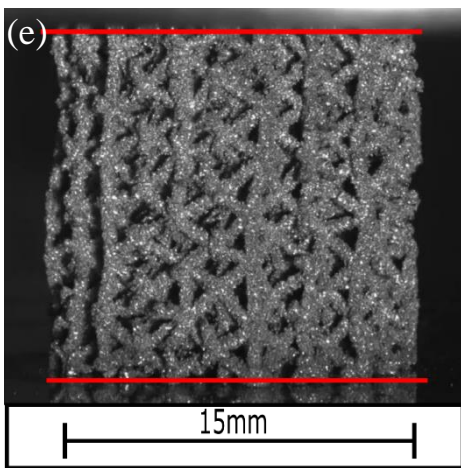
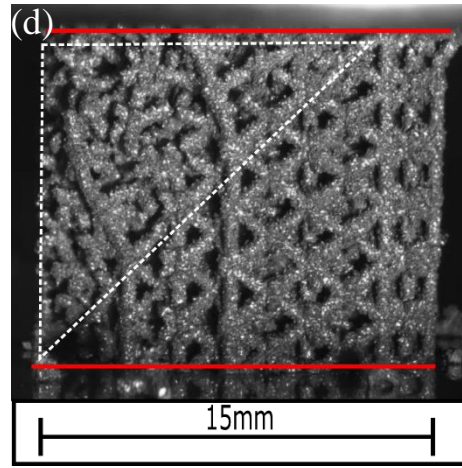
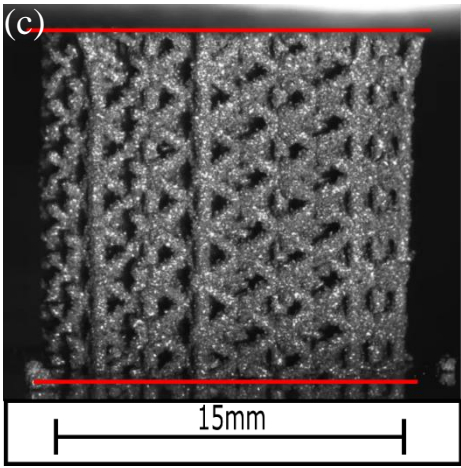
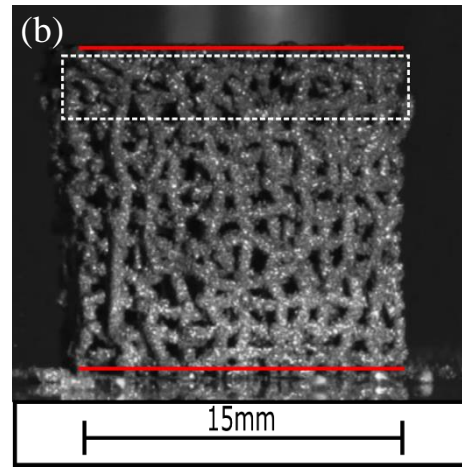
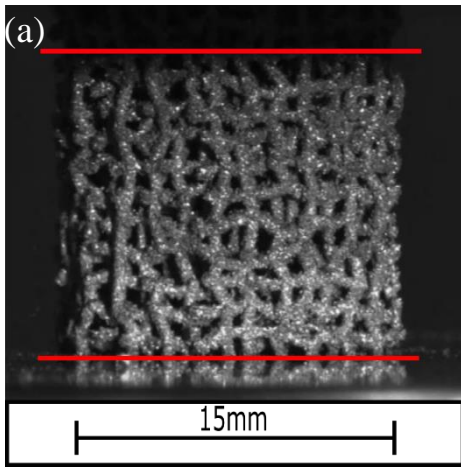
Figure III - 14 (a) S-N curve normalized with yield stress (b) S-N curve normalized with cyclic Young's modulus

Studies involving cellular materials with varying topology have shown that normalized S-N curve for one particular cell topology overlap and follow a single curve fitting or power law. Ahmadi et al.[14] indicated the effect of material on the fatigue properties using normalised S-N curve. In this present study, the normalized S-N curves were obtained by normalizing the fatigue data using offset yield strength and the cyclic Young's modulus as shown in Fig. III-14(a) and (b) respectively. The normalized curves of Fig. III-14(a) suggest that the irregular specimens, trabecular specimens and bending dominated cross based specimens overlap with each other indicating the effect of bending due to irregularity. The curve of star regular specimens is exactly between the bending dominated cross based specimens and the stretching dominated cubic regular specimens. The normalized S-N curves of SC (simple cubic), BCC, SC-BCC and FCC are compared by Peng et al.[31] which yield similar results. The difference between the regular and irregular specimens is shown in the normalized curve from Fig. III-14(b). The curves of irregular specimens overlap in one region except irregular cross and the star regular and cross regular curves overlap with each other. This indicates the decrease in the fatigue strength due to irregularity.

### 3.3.7. Fracture plane and Fracture surface

The fracture plane images under fatigue loading were obtained from the video captured during the compression-compression test carried out specifically carried out to observe the failure mechanism. The failure plane is marked in the images as shown in Fig. III-15. The different cell topologies have a significant impact on the failure mechanism under fatigue loading. The analysis was carried out for all the topologies except cubic regular since no failure was observed as discussed in the previous section.

The fatigue failure in cubic irregular specimens was in the top layers of the cellular part. The images indicate that failure was mostly due to a combination of buckling from vertical struts and bending from junction misalignment. However, in the other topologies, an inclined fracture plane similar to shear bands was observed. In star regular and cross-based specimens, a single failure plane was observed. But in star irregular specimens, two shear bands in different directions (+30° and -30°) were observed. In cross regular specimens which are completely bending dominated, a failure plane was observed exactly at +45°. This was followed by a complete densification of the specimen forming a barrel shape. In trabecular specimens, the random orientation of struts led to multiple failure locations. This kind of failure helps in retarding crack growth along the entire section of the specimen. It is indicated in the frequency plots explained in the previous section.



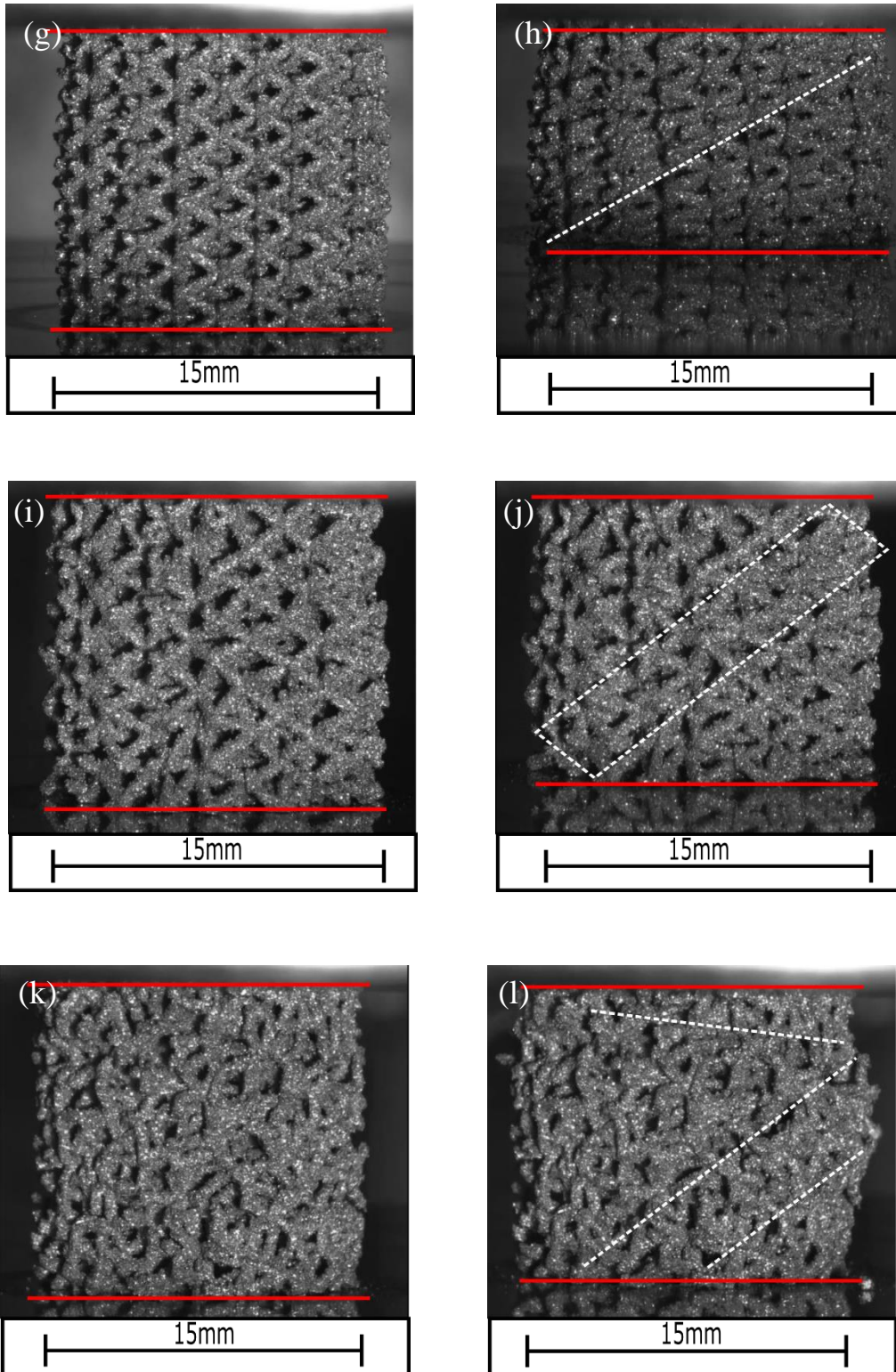


Figure III - 15 Undeformed and deformed cellular specimens under fatigue loading (a-b) Cubic irregular (c-d) Star regular (e-f) Star irregular (g-h) Cross regular (i-j) Cross irregular (k-l) Trabecular

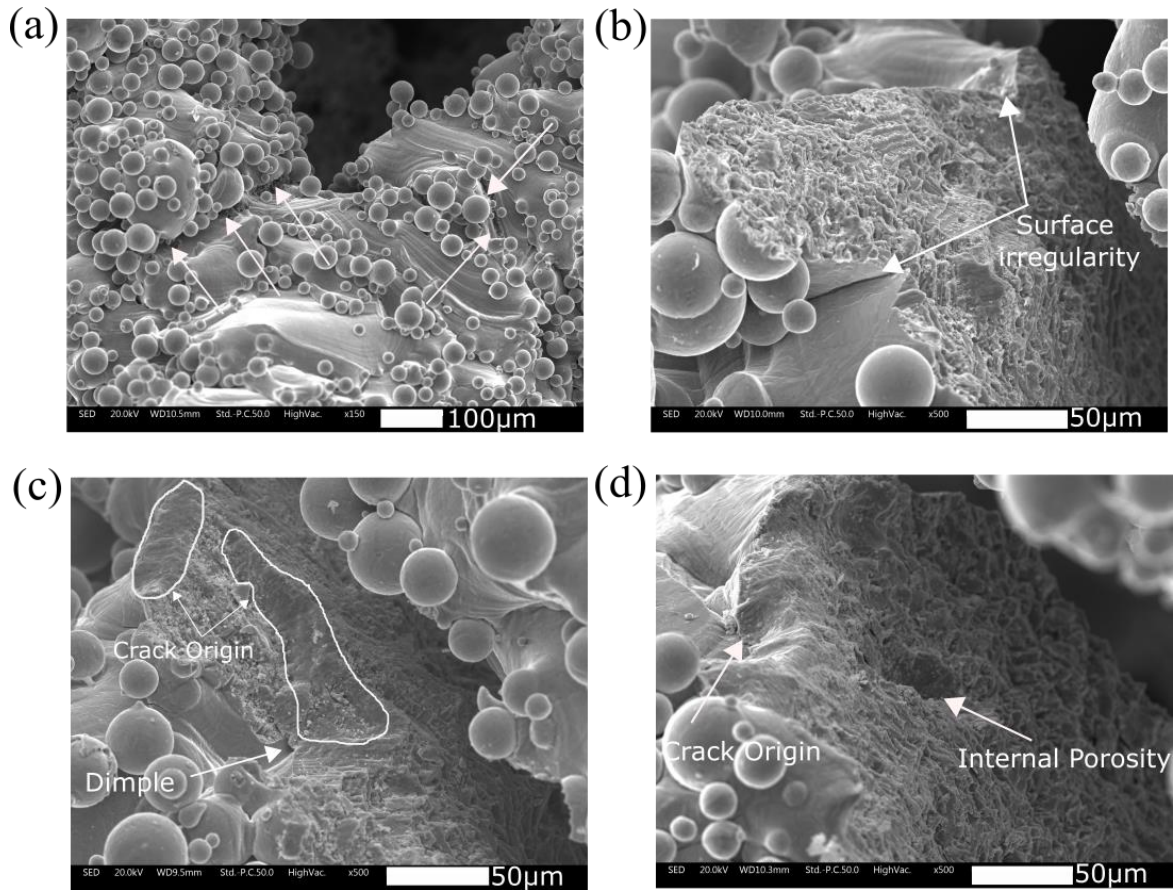


Figure III - 16 SEM images of fatigue fracture surface (a) Crack propagation at junctions (b) Irregular surface near crack (c) Crack initiation at surface dimple (d) Internal porosity at the crack surface.

The fracture surface analysis and the fatigue crack locations are obtained from the fatigue specimens from the resonating testing machine. Some of the fracture surface images from the study are as shown in Fig. III-16. In cellular specimens subjected to fatigue loading, the crack initiated at the irregular features on the strut surfaces or at the stress concentrated regions such as junctions. The same is seen in this study, where the cracks initiate at the junctions as shown in Fig. III-16(a). The crack propagation in the specimens is along the surface textures that are formed due to the LPBF process, similar crack path was shown by Hrabec et al. [32] indicating that the surface textures act as critical locations and can reduce the fatigue strength depending on the depth of the textures. Other surface defect and irregularities such as satellite powder attached to the struts, dimples and voids shown in Fig. III-16(a), (b) and (c) also acts as crack initiation sites. The study conducted on fatigue of cellular materials by Zhao et al. [12] also concluded that dimples and attached powder particles on struts act as crack initiation sites. The dependency of the surface irregularities on the build angle was studied by Razavi et al. [33]. The samples built with  $+45^\circ$  orientation with the building direction has higher surface roughness, melted powder and deeper defects acts as crack initiation sites. Studies on fatigue behaviour of AM components have shown that internal defects such as porosity and unmelted powders also influence the fatigue properties [34]. An internal pore on the fatigue crack surface is shown in Fig. III-16(d). Nevertheless, studies have concluded that the surface defects have a higher impact on the fatigue properties compared to internal defects [35]. However, some of the post manufacturing processes such as heat treatment, chemical etching and HIP have shown to improve the fatigue properties by changing the material and surface properties [20, 35].

### 3.3.8. FE Analysis

#### 3.3.8.1. As-designed elastic

In this study the FE analysis in the elastic region was carried out to study the effect of transition on the stiffness of the cellular material. Since the novelty of this work is tensile testing of cellular materials and the transition was seen only in the tensile specimens, the FE analysis is also carried out for tensile loading. Two FE models were considered for each cell topology as shown in section 3.2.7 and the Young's modulus is obtained. The values of the Young's modulus in for with and without transition are presented in Table III-5. Depending on the cell topology, 10 – 20% increase in the Young's modulus is observed for specimens with transition due to thicker struts and higher porosity. A ratio is obtained between the two values (with and without transition) to be used as a reduction factor to predict the Young's modulus in as-built cellular materials.

Table III - 6 As-designed Young's modulus with and without transition

| Sample                 | As-designed Young's modulus (GPa)<br>[FEM] |                 |  |
|------------------------|--|-----------------|--|
|                        | Without Transition                         | With Transition | With Transition/<br>Without Transition |
| <b>Cubic regular</b>   | 4.29                                       | 5.05            | 1.18                                   |
| <b>Cubic irregular</b> | 2.50                                       | 3.09            | 1.24                                   |
| <b>Star regular</b>    | 2.51                                       | 2.83            | 1.13                                   |
| <b>Star irregular</b>  | 2.21                                       | 2.52            | 1.14                                   |
| <b>Cross regular</b>   | 0.25                                       | 0.32            | 1.28                                   |
| <b>Cross irregular</b> | 0.33                                       | 0.37            | 1.14                                   |
| <b>Trabecular</b>      | 2.83                                       | 3.09            | 1.09                                   |

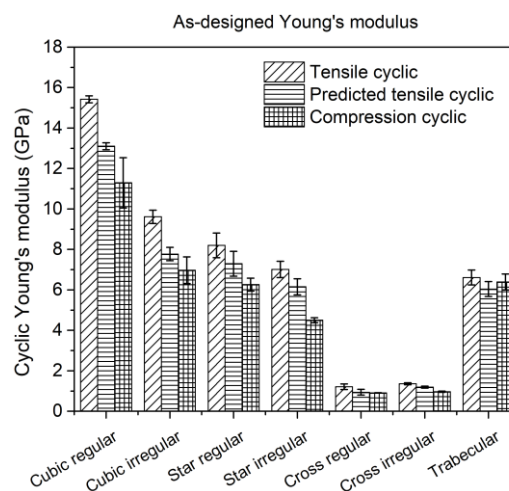


Figure III - 17 Effect of transition of the experimental tensile cyclic modulus using the ratio from FE analysis.

The ratio from Table III-5 is used to predict the as-built cyclic Young's modulus of the tensile specimens in the absence of transition. This reduced modulus should be closer to the Young's modulus obtained from the compression specimens since they did not have any transition. Therefore, the tensile test values and the predicted values are compared with the compression test results in Fig. III-17 and tabulated in Table. III-A1 of Appendix-3.6.2. Depending on the cell topology, the percentage error

between the tensile modulus and compression is reduced by half if the predicted value is taken into consideration. The reduced values are closer to the compression test results in all the cases. However, in some cases such as cubic irregular, star regular, cross regular and trabecular the predicted values and the compression test values are within the standard deviation. Therefore, the method employed provided satisfactory results in predicting the Young's modulus from the as-built results.

### 3.3.8.2. As-designed vs As-built elastic plastic

The elastic plastic analysis was carried out on the as-designed cellular materials as discussed in the section 3.2.7. The stress in the model was calculated using the nominal area of the FE model. The strain was calculated from the applied displacement. The difference between the as-designed and as-built properties are tabulated in Table III-7 and Table III-8. The porosity of the as-built specimens is approximately 15% lower than the porosity of the as-designed FE models. This difference in the porosity has a greater impact on the mechanical properties. Depending on the difference in the porosity and the cell topology, the properties of the as-built specimens are approximately 3 to 4 times more than the designed values. The stress-strain curves of as-designed and as-built specimens are compared in Fig. III-A1 of Appendix 3.6.3.

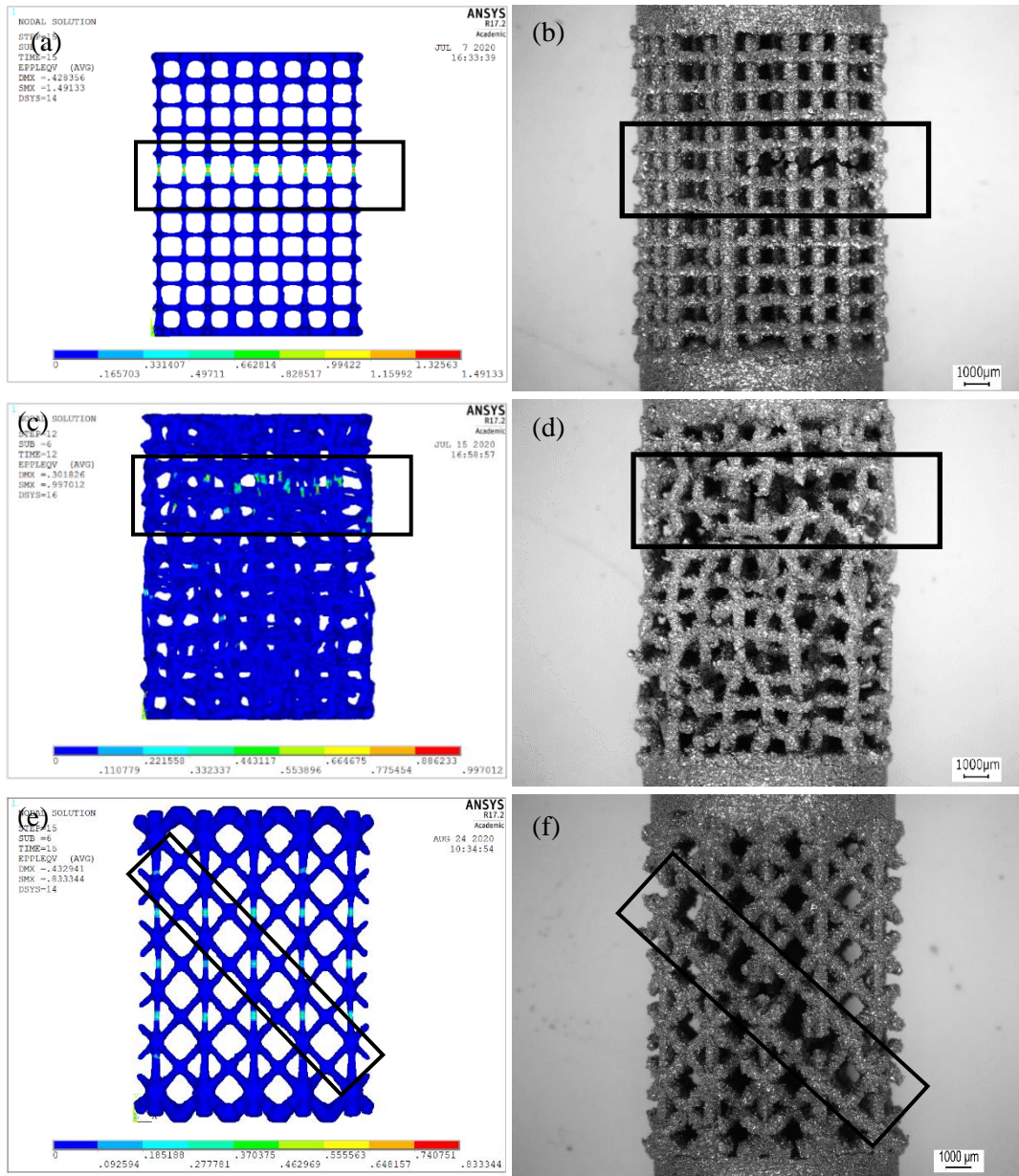
Table III - 7 Comparison of porosity and Young's modulus between as-designed and as-built configuration

| Specimen               | Porosity    |          | Young's modulus |          |
|------------------------|-------------|----------|-----------------|----------|
|                        | As-designed | As-built | As-designed     | As-built |
| <b>Cubic regular</b>   | 86.44       | 69.69    | 5.19            | 16.31    |
| <b>Cubic irregular</b> | 84.10       | 65.25    | 3.49            | 11.82    |
| <b>Star regular</b>    | 84.36       | 67.21    | 2.96            | 8.25     |
| <b>Star irregular</b>  | 83.70       | 67.61    | 2.72            | 7.00     |
| <b>Cross regular</b>   | 85.80       | 71.72    | 0.35            | 1.12     |
| <b>Cross Irregular</b> | 85.30       | 71.46    | 0.41            | 1.38     |
| <b>Trabecular</b>      | 80.90       | 69.53    | 3.20            | 7.34     |

Table III - 8 Comparison of yield strength and maximum strength between as-designed and as-built configuration

| Specimen               | Yield strength |          | Maximum strength |          |
|------------------------|----------------|----------|------------------|----------|
|                        | As-designed    | As-built | As-designed      | As-built |
| <b>Cubic regular</b>   | 22.12          | 100      | 23.87            | 107.76   |
| <b>Cubic irregular</b> | 16.11          | 71.00    | 21.95            | 80.69    |
| <b>Star regular</b>    | 13.20          | 47.60    | 18.75            | 60.75    |
| <b>Star irregular</b>  | 12.52          | 44.00    | 17.75            | 54.57    |
| <b>Cross regular</b>   | 5.90           | 18.10    | 9.64             | 28.32    |
| <b>Cross Irregular</b> | 6.00           | 19.10    | 9.94             | 29.4     |
| <b>Trabecular</b>      | 25.2           | 56.00    | 31.60            | 67.05    |

The maximum strain in the FE models is plotted using the plastic strain from the analysis. The damage locations in the FE models are compared with the experimentally failed locations in the Fig. III-18. The damage locations in the cubic regular, cubic irregular, star regular and star irregular materials is generally at the struts. While in cross based cellular materials, the damage is at the junctions/nodes. Trabecular specimens have a combination of failure at struts as well as at the junctions. Despite the difference in the porosity between as-designed and as-built specimens, the failure is exactly at the same location for FE model and experimental specimens.



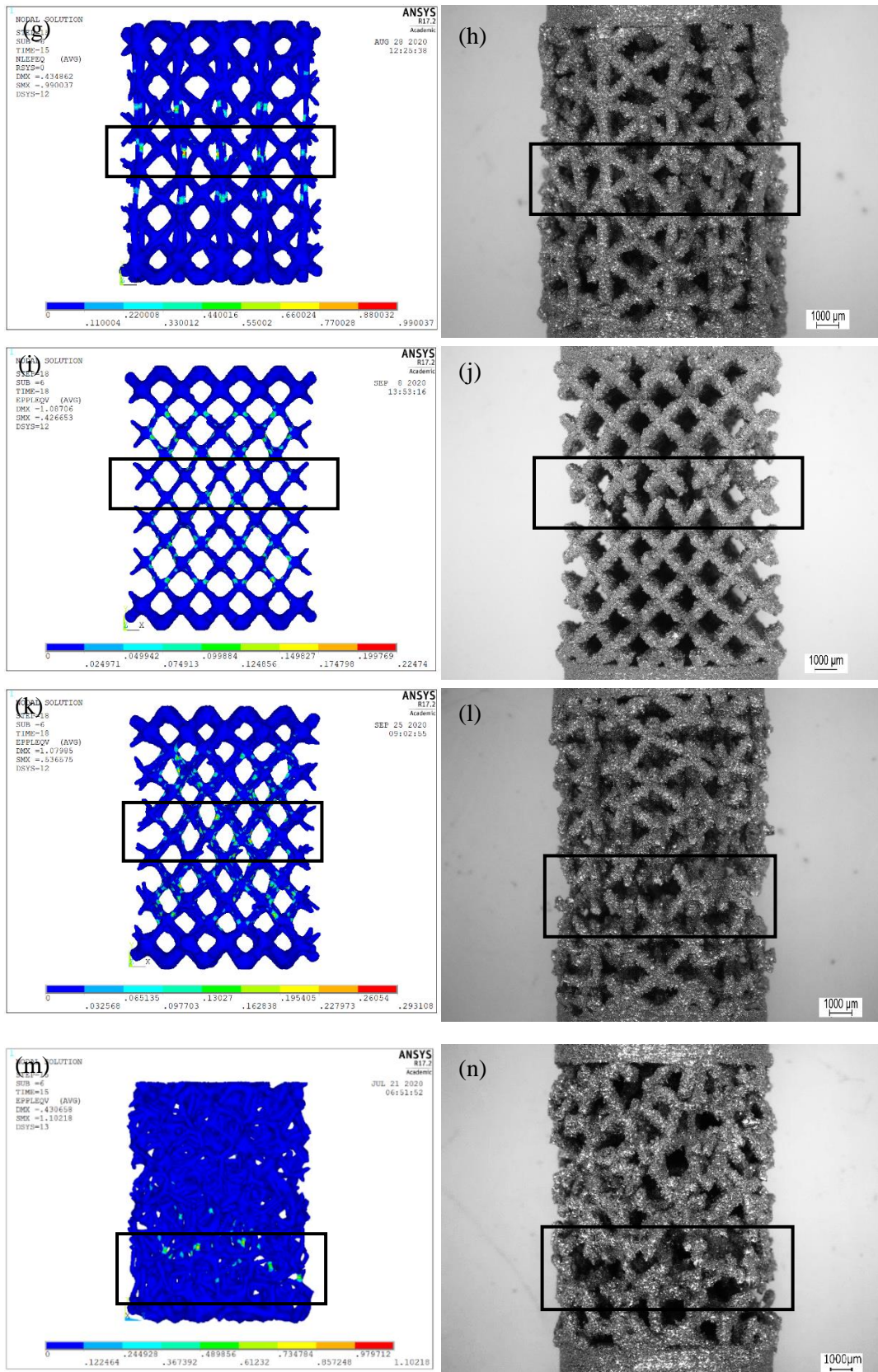


Figure III - 18 Comparison of failure locations in as-designed FE model and experimental specimens (a-b) Cubic regular (c-d) Cubic irregular (e-f) Star regular (g-h) Star irregular (i-j) Cross regular (k-l) Cross irregular (m-n) Trabecular

### 3.3.8.3. Comparison of experimental and FE of tomography model

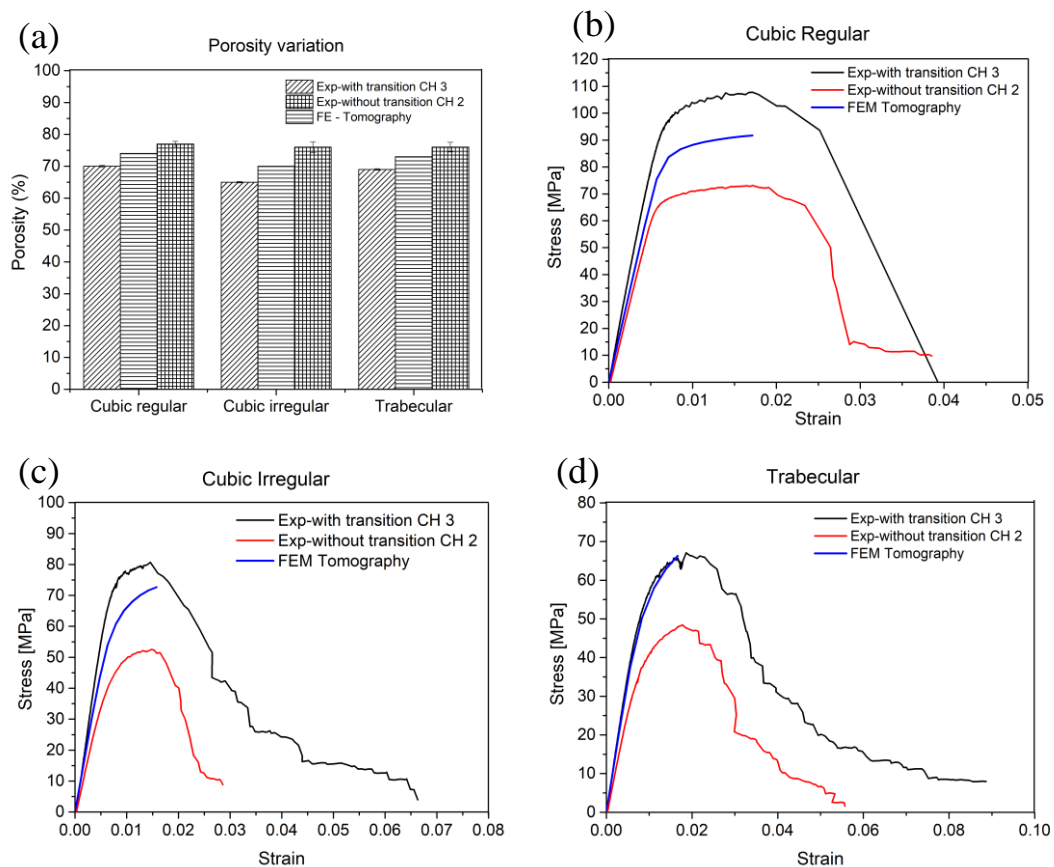


Figure III - 19 (a) Porosity difference between specimens from two chapters and tomography FE model (b) Stress-strain curves cubic regular (c) Stress-strain curves cubic irregular (d) Stress-strain curves cubic trabecular

The tensile monotonic stress-strain curves of cubic regular, cubic irregular and trabecular are compared with the experimental and tomography results from chapter II. The porosity variation is shown in Fig. III-19(a) and stress-strain curves are shown in Fig. III-19(b), (c) and (d). The porosity percentage of the tomography models is between the porosity percentage of the specimens of chapter II and this current study. The effect of this is seen in the stress-strain curves. The curve of tomography model is below the experimental curves of this study due to the difference in the porosity. On the contrary, the tomography curve of trabecular overlap with the experimental curve of this study. The other reason for this behaviour is the random distribution of struts and also depend on the RVE model considered from the full tomography specimen. Also, the material properties used for the FE analysis is the bulk material data from the previous chapter, which might have a slight contribution to this behaviour. However, the main contributor is the porosity as mentioned before. The effect of transition is visible when we compare the stress-strain curves of chapter 2 with the curves of this study.

### 3.4. Section summary

This chapter deals with the tensile, compression and fatigue properties of Ti6Al4V cellular materials manufactured using LPBF process. Seven different topologies were considered in this study to understand the effect of irregularity and compared the results with the behaviour of trabecular based specimens.

- The Young's modulus of all the considered specimens falls between 0.3 – 20 GPa, which make them suitable for biomedical applications. When comparing the values under cyclic and

monotonic loading, a stabilization is observed in compression loading. While under tensile loading, cyclic condition has not considerable effect.

- Under static loading, out of the seven topologies considered, cubic regular and cross regular specimens had the highest and lowest mechanical properties, respectively. The irregularity due to the misalignment in the nodes decreases the strength and stiffness but increases the strain values sustained by the cellular materials. The properties of trabecular specimens were between the highly stiff cubic regular and the highly compliant cross based specimens.
- Under fatigue loading, the cubic regular specimens did not undergo failure for loads below  $0.8\sigma_{yC}$  due to the presence of struts along the loading directions and from the absence of bending component during the compression loading.
- Similar to the static test, the irregularity decreased the fatigue strength of the specimen. The effect of irregularity decreases with the increase in the bending dominated behaviour. Cubic based specimens were highly effected due to irregularity while cross based specimens had negligible influence from the irregularity. Furthermore, effect of irregularity was higher for fatigue loading compared to static loading.
- The irregular and trabecular specimens demonstrate similar bending dominated behaviour which is indicated from the normalized S-N curves.
- The presence of struts in random directions in trabecular specimens leads to quasi-isotropic behaviour exhibiting better static and fatigue properties. Under fatigue loading, the randomly oriented struts decelerate the crack propagation across the complete section of the specimen at once.
- The presence of satellite particles, steps/textures from the LPBF process influence the fatigue behavior. A detailed analysis of these surface properties has not been considered in this study. However, fracture surface analysis of fatigue specimens indicated that the cracks initiated at surface defects such as dimples, voids, and textures from the LPBF process or at the stress concentrated sections such as junction/node.
- The FE analysis of the as-designed specimens indicates the effect of transition in the tensile specimens and also the effect of increased strut thickness on the mechanical properties. Despite the increase in porosity from the LPBF process, the failure locations in the experimental specimens are same as that observed the as-designed FE models.

### 3.5. References

1. Cheng XY, Li SJ, Murr LE, et al (2012) Compression deformation behavior of Ti-6Al-4V alloy with cellular structures fabricated by electron beam melting. *J Mech Behav Biomed Mater* 16:153–162. <https://doi.org/10.1016/j.jmbbm.2012.10.005>
2. Amerinatanzi A, Shayesteh Moghaddam N, Ibrahim H, Elahinia M (2016) The Effect of Porosity Type on the Mechanical Performance of Porous NiTi Bone Implants. V002T06A018. <https://doi.org/10.1115/smasis2016-9293>
3. Xiao L, Song W, Wang C, et al (2017) Mechanical properties of open-cell rhombic dodecahedron titanium alloy lattice structure manufactured using electron beam melting under dynamic loading. *Int J Impact Eng* 100:75–89. <https://doi.org/10.1016/j.ijimpeng.2016.10.006>
4. Ying S, Sun C, Fai K, Wei J (2017) Materials & Design Compressive properties of functionally graded lattice structures manufactured by selective laser melting. *Mater Des* 131:112–120. <https://doi.org/10.1016/j.matdes.2017.06.006>

5. Wei K, Yang Q, Ling B, et al (2018) Mechanical responses of titanium 3D kagome lattice structure manufactured by selective laser melting. *Extrem Mech Lett* 23:41–48. <https://doi.org/10.1016/j.eml.2018.07.001>
6. Yáñez A, Cuadrado A, Martel O, et al (2018) Gyroid porous titanium structures: A versatile solution to be used as scaffolds in bone defect reconstruction. *Mater Des* 140:21–29. <https://doi.org/10.1016/j.matdes.2017.11.050>
7. Zaharin HA, Rani AMA, Azam FI, et al (2018) Effect of unit cell type and pore size on porosity and mechanical behavior of additively manufactured Ti6Al4V scaffolds. *Materials (Basel)* 11:. <https://doi.org/10.3390/ma11122402>
8. Ahmadi SM, Yavari SA, Wauthle R, et al (2015) Additively manufactured open-cell porous biomaterials made from six different space-filling unit cells: The mechanical and morphological properties. *Materials (Basel)* 8:1871–1896. <https://doi.org/10.3390/ma8041871>
9. Kadkhodapour J, Montazerian H, Darabi AC, et al (2015) Failure mechanisms of additively manufactured porous biomaterials: Effects of porosity and type of unit cell. *J Mech Behav Biomed Mater* 50:180–191. <https://doi.org/10.1016/j.jmbbm.2015.06.012>
10. Gibson LJ, Ashby MF (1997) *Cellular Solids*, Second. Cambridge University Press
11. Amin Yavari S, Wauthle R, Van Der Stok J, et al (2013) Fatigue behavior of porous biomaterials manufactured using selective laser melting. *Mater Sci Eng C* 33:4849–4858. <https://doi.org/10.1016/j.msec.2013.08.006>
12. Zhao S, Li SJ, Hou WT, et al (2016) The influence of cell morphology on the compressive fatigue behavior of Ti-6Al-4V meshes fabricated by electron beam melting. *J Mech Behav Biomed Mater* 59:251–264. <https://doi.org/10.1016/j.jmbbm.2016.01.034>
13. Van Hooreweder B, Apers Y, Lietaert K, Kruth JP (2017) Improving the fatigue performance of porous metallic biomaterials produced by Selective Laser Melting. *Acta Biomater* 47:193–202. <https://doi.org/10.1016/j.actbio.2016.10.005>
14. Ahmadi SM, Hedayati R, Li Y, et al (2018) Fatigue performance of additively manufactured meta-biomaterials: The effects of topology and material type. *Acta Biomater* 65:292–304. <https://doi.org/10.1016/j.actbio.2017.11.014>
15. Ghouse S, Babu S, Nai K, et al (2018) The influence of laser parameters, scanning strategies and material on the fatigue strength of a stochastic porous structure. *Addit Manuf* 22:290–301. <https://doi.org/10.1016/j.addma.2018.05.024>
16. du Plessis A (2019) Effects of process parameters on porosity in laser powder bed fusion revealed by X-ray tomography. *Addit Manuf* 30:100871. <https://doi.org/10.1016/j.addma.2019.100871>
17. du Plessis A, Razavi SMJ, Berto F (2020) The effects of microporosity in struts of gyroid lattice structures produced by laser powder bed fusion. *Mater Des* 194:108899. <https://doi.org/10.1016/j.matdes.2020.108899>
18. Kelly CN, Francovich J, Julmi S, et al (2019) Fatigue behavior of As-built selective laser melted titanium scaffolds with sheet-based gyroid microarchitecture for bone tissue engineering. *Acta Biomater* 94:610–626. <https://doi.org/10.1016/j.actbio.2019.05.046>
19. Wu MW, Chen JK, Lin BH, et al (2020) Compressive fatigue properties of additive-manufactured Ti-6Al-4V cellular material with different porosities. *Mater Sci Eng A* 790:139695. <https://doi.org/10.1016/j.msea.2020.139695>
20. Ren D, Li S, Wang H, et al (2019) Fatigue behavior of Ti-6Al-4V cellular structures fabricated by additive manufacturing technique. *J Mater Sci Technol* 35:285–294. <https://doi.org/10.1016/j.jmst.2018.09.066>
21. Liu YJ, Wang HL, Li SJ, et al (2017) Compressive and fatigue behavior of beta-type titanium porous structures fabricated by electron beam melting. *Acta Mater* 126:58–66. <https://doi.org/10.1016/j.actamat.2016.12.052>

22. Yuan W, Hou W, Li S, et al (2018) Heat treatment enhancing the compressive fatigue properties of open-cellular Ti-6Al-4V alloy prototypes fabricated by electron beam melting. *J Mater Sci Technol* 34:1127–1131. <https://doi.org/10.1016/j.jmst.2017.12.003>
23. Pazzaglia UE, Ghisellini F, Barbieri D, Ceciliani L (1988) Failure of the stem in total hip replacement - A study of aetiology and mechanism of failure in 13 cases. *Arch Orthop Trauma Surg* 107:195–202. <https://doi.org/10.1007/BF00449667>
24. Andriacchi TP, Galante JO, Belytschko T, Hampton SJ (1976) A stress analysis of the femoral stem in total hip prostheses. *J Bone Joint Surg Am* 58 5:618–624
25. ASTM International (2014) Standard Specification for Additive Manufacturing Titanium-6 Aluminum-4 Vanadium with Powder Bed Fusion. *ASTM Int F2924*:1–9. <https://doi.org/10.1520/F2924-14.2>
26. Amin Yavari S, Ahmadi SMM, Wauthle R, et al (2015) Relationship between unit cell type and porosity and the fatigue behavior of selective laser melted meta-biomaterials. *J Mech Behav Biomed Mater* 43:91–100. <https://doi.org/10.1016/j.jmbbm.2014.12.015>
27. Delroisse P, Jacques PJ, Maire E, et al (2017) Effect of strut orientation on the microstructure heterogeneities in AlSi10Mg lattices processed by selective laser melting. *Scr Mater* 141:32–35. <https://doi.org/10.1016/j.scriptamat.2017.07.020>
28. Gümruk R, Mines RAW (2013) Compressive behaviour of stainless steel micro-lattice structures. *Int J Mech Sci* 68:125–139. <https://doi.org/10.1016/j.ijmecsci.2013.01.006>
29. Mazur M, Leary M, Sun S, et al (2016) Deformation and failure behaviour of Ti-6Al-4V lattice structures manufactured by selective laser melting (SLM). *Int J Adv Manuf Technol* 84:1391–1411. <https://doi.org/10.1007/s00170-015-7655-4>
30. Liu X, Sekizawa K, Suzuki A, et al (2020) Compressive properties of Al-Si alloy lattice structures with three different unit cells fabricated via laser powder bed fusion. *Materials (Basel)* 13:1–16. <https://doi.org/10.3390/ma13132902>
31. Peng C, Tran P, Nguyen-Xuan H, Ferreira AJM (2020) Mechanical performance and fatigue life prediction of lattice structures: Parametric computational approach. *Compos Struct* 235:111821. <https://doi.org/10.1016/j.compstruct.2019.111821>
32. Hrabe NW, Heintz P, Flinn B, et al (2011) Compression-compression fatigue of selective electron beam melted cellular titanium (Ti-6Al-4V). *J Biomed Mater Res - Part B Appl Biomater* 99 B:313–320. <https://doi.org/10.1002/jbm.b.31901>
33. Razavi SMJ, Van Hooreweder B, Berto F (2020) Effect of build thickness and geometry on quasi-static and fatigue behavior of Ti-6Al-4V produced by Electron Beam Melting. *Addit Manuf* 36:101426. <https://doi.org/10.1016/j.addma.2020.101426>
34. Benedetti M, Torresani E, Leoni M, et al (2017) The effect of post-sintering treatments on the fatigue and biological behavior of Ti-6Al-4V ELI parts made by selective laser melting. *J Mech Behav Biomed Mater* 71:295–306. <https://doi.org/10.1016/j.jmbbm.2017.03.024>
35. Dallago M, Fontanari V, Torresani E, et al (2018) Fatigue and biological properties of Ti-6Al-4V ELI cellular structures with variously arranged cubic cells made by selective laser melting. *J Mech Behav Biomed Mater* 78:381–394. <https://doi.org/10.1016/j.jmbbm.2017.11.044>

### 3.6.Appendix 3

#### 3.6.1. STL files of the cellular part of tensile specimens with transition

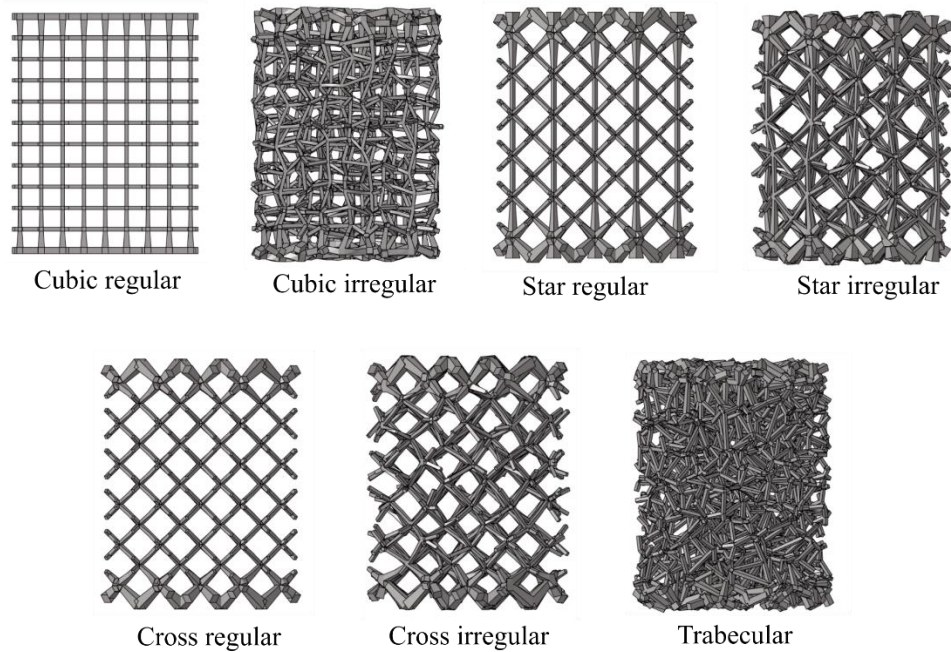


Figure III - A 1 STL files for manufacturing tensile specimens indicating the transition at the top and bottom

#### 3.6.2. Comparison of as-built Young's modulus in the absence of transition

Table III - A 1 Effect of transition on as-built Young's modulus

| Sample          | As – Built Young's Modulus (GPa)<br>[Cyclic Test] |  |              |
|-----------------|---|--|--------------|
|                 | Tensile   | Prediction of<br>Tensile without<br>Transition | Compression  |
| Cubic regular   | 15.42 ± 0.17                                      | 13.10  | 11.29 ± 1.24 |
| Cubic irregular | 9.61 ± 0.33                                       | 7.77   | 6.97 ± 0.66  |
| Star regular    | 8.20 ± 0.61                                       | 7.29   | 6.26 ± 0.32  |
| Star irregular  | 7.01 ± 0.40                                       | 6.15   | 4.50 ± 0.12  |
| Cross regular   | 1.21 ± 0.14                                       | 0.94   | 0.91 ± 0.01  |
| Cross irregular | 1.36 ± 0.05                                       | 1.19   | 0.97 ± 0.03  |
| Trabecular      | 6.61 ± 0.37                                       | 6.04   | 6.39 ± 0.39  |

### 3.6.3. As-designed and as-built stress-strain curves under tensile loading

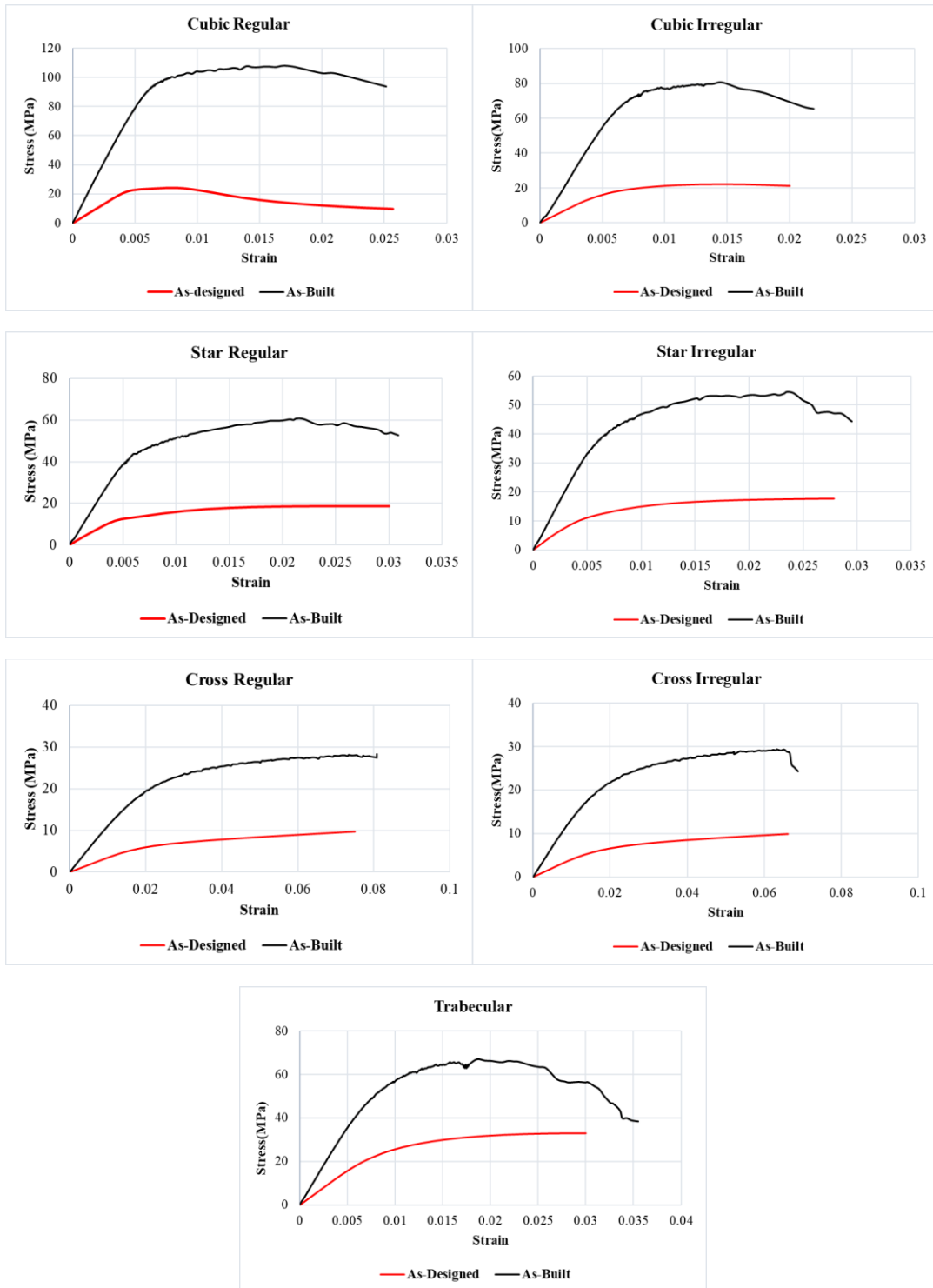


Figure III - A 2 Comparison of as-designed (FEM) and as-built (experimental) stress - strain curves for tensile loading

---

## Chapter 4

### Effect of building orientation, strut thickness, and fillet radius on morphology and fatigue of Ti6Al4V cubic cellular structure

---

The previous chapters based on different types on unit cell showed a clear deviation between the as-designed and as-built parameters of the specimen due to the LPBF process. This morphological deviation also impacted the overall mechanical properties of the cellular specimens. Therefore, in this chapter, an in-depth morphological analysis was carried out on a new set of specimens to better understand the effect of the LPBF process. The investigation was carried out on cubic regular cellular specimens with larger dimensions compared to the specimens mentioned in the previous chapter. Nine different specimens were manufactured by varying their strut thickness and fillet radius and printed at three different orientations. The aim was to derive a relationship between the as-designed and the as-built geometrical parameters to generate a compensation method for the input CAD models. Also, internal porosity analysis was carried out to study the effect of thickness and orientation on the internal defects. The effectiveness of the compensation technique was verified by manufacturing a new batch of specimen using the compensated geometry as input for the LPBF process.

The second part of the study focused on the effect of fillets, compensation technique and the printing direction on the mechanical properties of cubic regular unit cells. Six different specimens were subjected to compression loading and fully reversed fatigue loading, along with their morphological analysis.

This study was conducted jointly along with another doctoral student at the University.

A part of this chapter has been published in:

Dallago M, Raghavendra S, Luchin V, Zappini G, Pasini D, Benedetti M. *Geometric assessment of lattice materials built via Selective Laser Melting*. In: *Materials Today: Proceedings*. Vol 7. Elsevier Ltd; 2019:353–361.

Dallago M, Raghavendra S, Luchin V, Zappini G, Pasini D, Benedetti M. *The role of node fillet, unit-cell size, and strut orientation on the fatigue strength of Ti-6Al-4V lattice materials additively manufactured via laser powder bed fusion*. *Int J Fatigue*. 2021;142: 105946.

## 4.1. Introduction

The cellular materials manufactured using the LPBF have shown defects from the manufacturing process. These defects from the LPBF process influence their mechanical properties as seen in the literature review and mentioned in the introduction. The effect of manufacturing process on the as-designed porosity and mechanical properties has been discussed in chapter 2 and 3. Further, the work carried out by Dallago et al. [1] compare the as-designed geometry with the  $\mu$ CT scan of the as-built specimens for cubic based specimens which showed that the as-built fillets have irregular shape. This phenomenon motivated to study the geometrical deviation and the effect of building orientation on the geometrical properties of cubic cellular material. Compensated models were generated to reduce the mismatch between the designed and the manufactured specimens. Furthermore, the fatigue performance of cubic cellular materials by replacing sharp junctions with filleted junctions to reduce stress concentration.

The geometrical mismatch between the designed (as-designed) and manufactured (as-built) structures is influenced by the LPBF process parameters such as scanning speed, laser power and layer thickness [2–4]. The above-mentioned parameters primarily influence the size of the melt pool that determine the build quality of the structure. Other factors such as material shrinkage during the LPBF process influences the outcome of the process and depends on the base material. Apart for the process parameters, the orientation of the specimens or struts in the case of cellular materials with the printing plane impact the build quality especially in thin structures. Studies have shown that horizontal struts parallel to the printing plane have irregular surfaces due to the absence of support when melting the first few layers of powder, due to which the heat is dissipated to the below layer, which melts and attaches to the first layer, also gravity induces sagging of molten metal. On the contrary, vertical struts are manufactured with less deviation due to the presence of support and proper heat dissipation. However, in inclined struts, the heat from the laser is conducted to the surrounding powder at certain regions, which partially or completely attaches powder particles causing geometrical irregularity [5–7]. The difference between the as-designed and as-built geometry directly deviates the mechanical properties from the predicted values. But the difference between the designed and the obtained geometrical values of cellular materials can be co-related. One such relation between the as-designed and the as-built pore size of LPBF manufactured Ti6Al4V was carried out by van Bael et al. [8], the results from comparing one batch of specimen were used to modify the input CAD model, thereby reducing the geometrical error in the second batch of specimens. Bagheri et al. proposed a linear correlation between the as-built and as-designed strut thickness, which involved using a compensation factor for the designed values in order to obtain the required geometry. Post-manufacturing treatment such as chemical etching was used by Pyka et al. [7] to reduce the offset in the as-built strut thickness compared to the as-designed values. However, all the methodologies discussed above depend on the initial CAD design, cell topology, inclination of the struts with the building plane, and the process parameters.

The geometrical deviations not only influence the static properties but also influence the fatigue performance. The geometrical defects such as irregular surface of the struts and junctions act as stress concentration locations [9, 10]. In general, these imperfections act as crack initiation locations under fatigue loads compared to the internal defects from the LPBF process [11, 12]. Furthermore, the effect of these defects is pronounced in Ti6Al4V specimens due to their high notch sensitivity [13, 14].

This chapter deals with the metrological analysis and fatigue properties of cubic regular specimens manufactured using LPBF process. The dimensions of the cubic cellular specimens are larger than the cubic regular specimens discussed in the previous chapters. Three sizes of unit cell, 8 mm, 6 mm, and 4 mm were considered. The junctions of the cubic unit cells were designed with a constant fillet radius. Unit cell size, strut thickness and fillet radius values were combined to form nine different combinations of specimens. These nine specimens were printed at three different orientations with the printing plane

to obtain a total of 27 different configurations. The first set of specimens were used to compare the geometrical deviation between the as-designed and the as-built specimens. From the measurements, a mathematical relationship was formulated between the as-designed and as-built strut thickness and fillet radius. This correlation helped in developing compensated CAD models for manufacturing the second batch of specimens. The percentage of geometrical deviation in the first and second batch of specimens is used as an indication for the effectiveness of the compensated CAD models. The strut thickness and the fillet radius measurements were carried out using the specimen images captured using the optical microscope and processing them using a MATLAB code. Internal porosity analysis was also carried out for the specimens to study the effect of strut thickness and specimen orientation. This method is not as accurate as the  $\mu$ CT analysis but yields considerable results at lower cost, this method works well since the cellular specimens are larger in size.

A last part of the work also focuses on the effect of printing direction, fillet radius and unit cell size on the fully reversed fatigue properties of cubic regular specimens. Fatigue tests are carried out on six specimens printed with  $0^\circ$  inclination,  $90^\circ$  inclination, and inclined along the diagonal of the cube. Specimens with different strut thickness, unit cell size and with and without fillets have been considered. Electron microscopy images were used to analyse the fatigue fracture surfaces.

## 4.2. Materials and methods

### 4.2.1. Specimen design

Cubic regular specimens were used to carry out the geometrical analysis, the cubic unit cell struts had a circular cross – section, and strut thickness/diameter  $t_0$ , fillet radius  $R$  and unit cell size  $L$  as shown in Fig. IV-1(a). A 3D representation of the unit cell with fillet radius is seen in Fig. IV-1(b). Nine different specimens were obtained by varying the geometric parameters as tabulated in Table.IV-1.

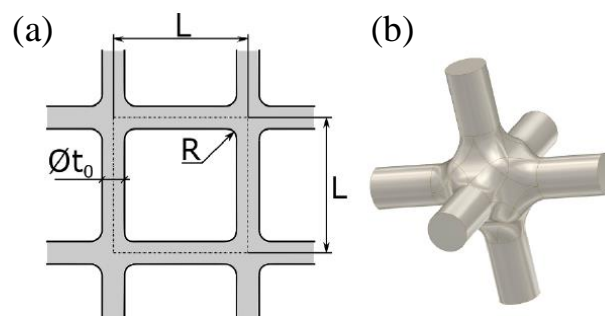


Figure IV - 1 (a) Representation of unit cell parameters (b) Unit cell with fillet radius at junctions

Based on the previous study by Dallago et al. [1], the geometrical parameters of the specimen were chosen to obtain a designed Young's modulus of 3 GPa. The  $R/L$  ratios was set to 0.05, 0.1 and 0.15 to obtain a range of fillet radius and the  $t_0/L$  ratios were calculated from the semi-analytical model developed by Dallago et al. [1]. FE analysis was carried out in the elastic region on the designed unit cell to check the designed Young's modulus using ANSYS®. The obtained Young's modulus values are closer to 3 GPa for all the specimens and tabulated in Table IV-1.

Table IV - 1 Specimen details with combination of geometric parameters

| Specimen No. | L (mm) | t <sub>0</sub> (mm) | R (mm) | t <sub>0</sub> /L | R/L  | E FEM 3D (MPa) |
|--------------|--------|---------------------|--------|-------------------|------|----------------|
| 1            | 4      | 0.70                | 0.2    | 0.176             | 0.05 | 2944.3         |
| 2            | 4      | 0.68                | 0.4    | 0.171             | 0.1  | 2952.6         |
| 3            | 4      | 0.67                | 0.6    | 0.167             | 0.15 | 3097.3         |
| 4            | 6      | 1.06                | 0.3    | 0.176             | 0.05 | 3004.1         |
| 5            | 6      | 1.03                | 0.6    | 0.171             | 0.1  | 3017.6         |
| 6            | 6      | 1.00                | 0.9    | 0.167             | 0.15 | 3066.1         |
| 7            | 8      | 1.41                | 0.4    | 0.176             | 0.05 | 2989.4         |
| 8            | 8      | 1.37                | 0.8    | 0.171             | 0.1  | 3002.5         |
| 9            | 8      | 1.34                | 1.2    | 0.1675            | 0.15 | 3097.1         |

As mentioned before, the nine specimens were printed with three different orientations with respect to the building plane to investigate the effect of struts inclination on their as-built geometrical values. The specimens shown in Fig. IV-2(a) and 2(d) have two series of struts are parallel to the printing plane (X and Y) and Z-directions struts are perpendicular to the printing plane. In the second set, the complete specimen is inclined with respect to one plane as shown in Fig. IV-2(b), one set of specimens (X) are parallel to the printing plane and other two struts (Y and Z) are inclined at 45° to the printing plane. The last set was obtained by inclining the specimen with respect to two planes as shown in Fig. IV-2(c). Hence all the struts are inclined at 35.26° with respect to the printing plane. The specimens are designated as 0°, 45° and 45°-35.26°, respectively. The printed specimens are shown in Fig. IV-2(d), (e) and (f), the inclined struts are printed with support structures. A total of 27 specimen were printed with nine specimens for each orientation. The specimens were manufactured using LPBF process using a biomedical grade Ti4Al4V powder with particle size between 15 – 45 μm. A layer thickness of 60 μm was used and the specimens were subjected to heat treatment after manufacturing.

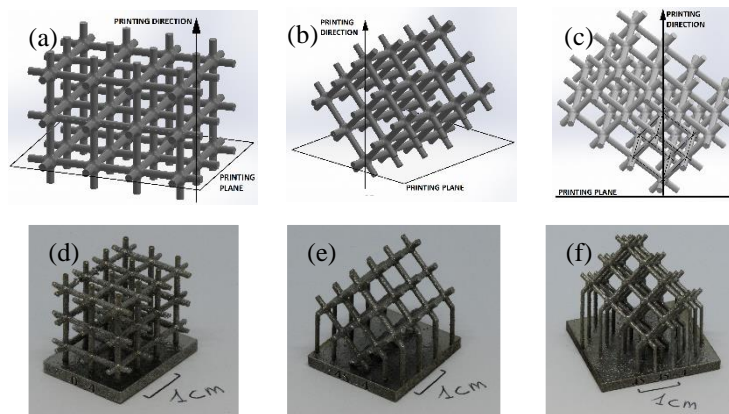


Figure IV - 2 (a-c) STL files of as-designed cubic cellular structure along with orientation (d-f) Manufactured specimens with three different orientation

#### 4.2.2. Geometrical analysis

For the geometrical analysis of the specimens, images of the specimen were captured along all the three directions indicated by XYZ axes using a Nikon SMZ25 stereo optical microscope. Total of 6 images were captured for each specimen. Images of two-unit cells were captured along each plane (XY, XZ, YZ) to obtain the images of struts along all the directions as indicated in Fig. IV-3.

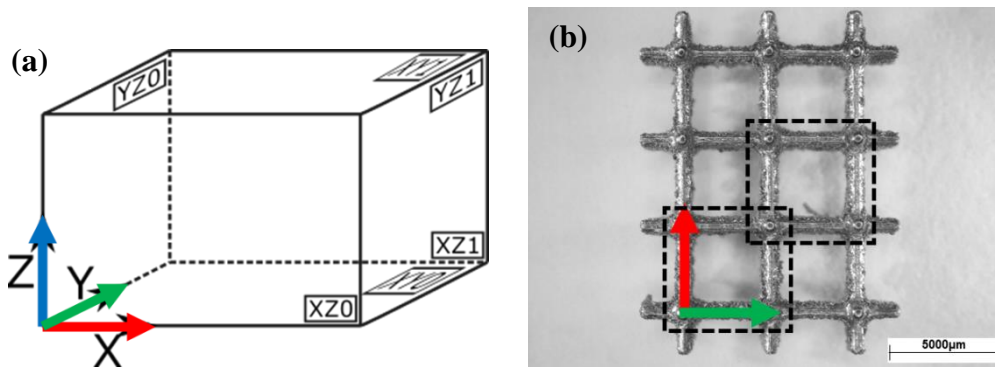


Figure IV - 3 (a) Representation of different planes of 0° specimen, printed along Z-direction (b) Optical microscope image of 0° specimen in XY plane

The microscopy images of the unit cell were processed using an in-house MATLAB® code to recognize its boundaries using the images segmentation function in MATLAB®. The properties or the units of the images was converted from pixels to microns with the help of the scale from microscopy images. The images of the complete face of the specimen were not captured due to the segmentation issue that arises from the misalignment of struts below the top face or the shadow from the struts. These disturbances tend to alter the boundary of the unit cell after image segmentation. The parameters obtained from the MATLAB® processing are listed below and indicated in the Fig. IV- 4 :

- Boundary of the unit cell.
- Average strut thickness.
- Junction center.
- Average fillet radius.
- Comparison of as-designed geometry with as-built by overlaying.

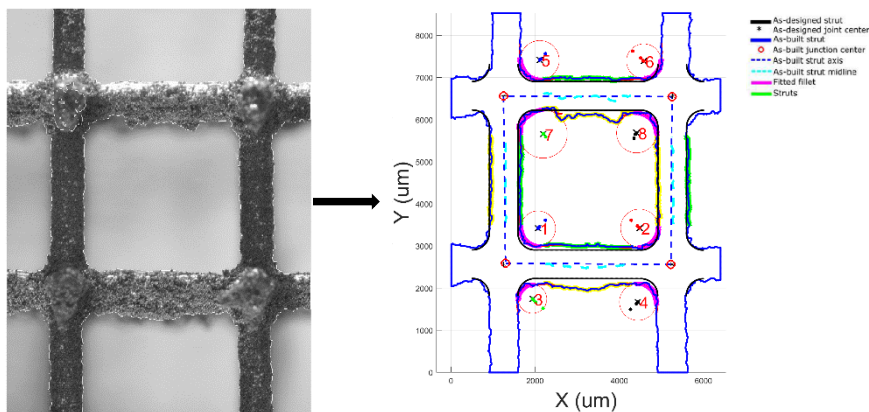


Figure IV - 4 Unit cell image segmentation and analysis to measure different geometrical parameters

The center of the junction is the most crucial part of the analysis since the act as the reference point for all the other calculations. Once the junction center is set the code is independent to recognize the features from the image to calculate the required measurements. This method helps in processing a greater number of images with minimum human intervention and very less manual calculation. Since the unit cells are irregular and distorted due to the LPBF process, the calculation of the junction center is obtained through an iterative process used to estimate the centroid of the junction as shown in Fig. IV-5(a). The first step in the junction center calculation starts from the estimating the center from as-designed geometry ( $X_0, Y_0$ ) in the global system XY. The next step is the selecting the smallest possible square to fit the complete junction as shown in Fig. IV-5(b). Four areas (A1, A2, A3 and A4) are calculated by taking the corners of the square and the fillet boundary as shown in Fig. IV-5(b). If the mentioned area values are unbalanced, it can be assumed that the center of the square and the center of

the junction are not coincident. The difference between the areas is calculated and the maximum allowable deviation between the minimum and maximum area values is set to 5%. Two vectors ( $V_x'$ ,  $V_y'$ ) are defined in the  $x'$ ,  $y'$  reference system by taking the difference between the extension of the areas in the diagonally opposite corners as shown in Fig. IV-5(b). These vectors are transformed into global systems for the ease of implementation as  $V_x$  and  $V_y$  vectors.  $V_x$  and  $V_y$  vectors are used in the iterative algorithm/process to change the position of the square until balanced areas (tolerance < 5%) is obtained between the areas. At this stage, the center of the junction and the center of the fitted square are in coincident.

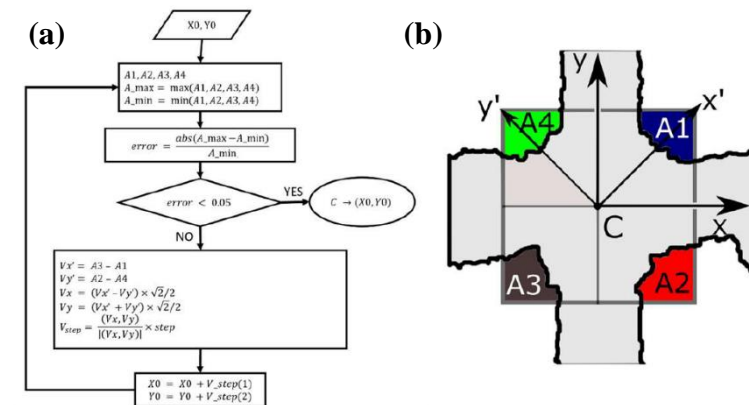


Figure IV - 5 Junction center estimation (a) MATLAB® algorithm used for the analysis (b) Parameters used for the junction center estimation

The above-mentioned approach cannot be applied for all the junction since the method assumes that the fillets at the junction have a similar shape despite the distortion due to the LPBF process. However, due to the inclination of the junction with the printing planes, there are chances of material accumulation at one of the fillets as marked in Fig. IV-6. Therefore, calculation of junction center at such locations is not suitable anymore. Since the aim is to utilize the junction center is to overlay the as-designed geometry and the as-built unit cell, it can be assumed that overlaying the struts can help in understanding the physics behind this material accumulation (parasitic mass) at the fillets. For such instances, the methodology mentioned in the previous paragraph is tweaked when considering the areas. The areas A1, A2, A3 and A4 are considered at two fillets where no materials accumulation is observed as shown in Fig. IV-6. The new areas are used in the algorithm shown in Fig. IV-5(b) for the iteration process. This approach was developed in order to ensure that the autonomous calculation process can be employed with very little change. The results obtained and discussed in the future section show that the results were satisfactory and reliable.

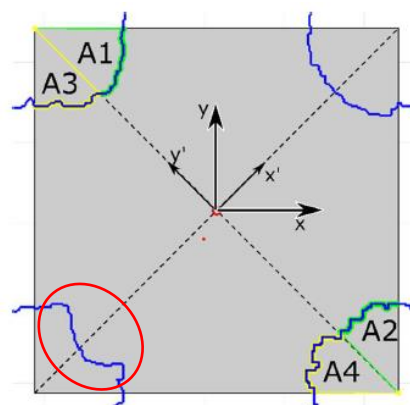


Figure IV - 6 Modified parameters for the junction center estimation due to material accumulation at the fillets due to LPBF process (highlighted by red circle)

As mentioned, the as-built and the as-designed geometry are overlapped using the junction centers using the procedure shown in Fig. IV-7(a). Three different co-ordinate systems are defined as follows:

- First one is a global co-ordinate system (O x y) based on the rows and columns of the image of the unit cell.
- Second co-ordinate system (O' x' y') is an integral part of the as-built unit cell.
- Third co-ordinate system (O'' x'' y'') is for the as-designed unit cell.

An optimal overlap between the as-designed and the as-built geometry is dependent on the position of O'' and  $\theta$ , it is obtained by reducing the sum of the squares of the distance between the corresponding junction centers of as-built ( $P_{pr}$ ) and as-designed geometry ( $P_{CAD}$ ) shown in Fig. IV-7(a):

$$P_{CAD,i} = OO'' + P_{CAD,i}O'' = (x_{o''} \ y_{o''}) + (x''_{P_{CAD,i}} \ y''_{P_{CAD,i}}) \begin{bmatrix} +\cos\theta & +\sin\theta \\ -\sin\theta & +\cos\theta \end{bmatrix} \text{ .Eq. IV-1(a)}$$

$$P_{pr,i} = OO' + P_{pr,i}O' = (x_{o'} \ y_{o'}) + (x'_{P_{pr,i}} \ y'_{P_{pr,i}}) \text{ ..... Eq. IV-1(b)}$$

$$d_i^2 = |P_{CAD,i}O' - P_{pr,i}O'|^2 \text{ ..... Eq. IV-1(c)}$$

$$\min \sum_{i=1}^4 d_i^2 \rightarrow (x_{o''}, y_{o''}, \theta) \text{ ..... Eq. IV-1(d)}$$

The average strut thickness value is calculated from the 100 thickness values calculated along the strut and measured normal to the axis. The thickness values are measured far away from the junction to obtain just the strut thickness and to avoid the effect of fillet as shown in Fig. IV-7(b). An accurate overlay is useful to measure the difference between the as-designed and the as-built geometry. Fig. IV-7(b) gives a clear comparison for one of the struts. The back lines indicate the as-designed geometry and the blue line indicates the as-built geometry, some of the locations on the strut have excess material while in some places, there is a lack of material and hence the strut thickness is lesser than the as-designed value. The excess material is designated as positive while lack of material is designated as negative. The distance between the two edges is calculated for further analysis.

The fillet radius of the as-built profile is measured by fitting a circle on the profile. However, fitting a circle to the fillet is a difficult task given the irregularity, overlap between the fillet and the strut region and the different fillet radii at different junctions. Therefore, an iterative procedure shown in Fig. IV-8 was adopted to obtain a best fitting circle is obtained. An initial position center  $C_i$  is selected, and a circle is drawn based on the points on the as-built profile. Then a new center  $C_{i+1}$  is selected, and circle is drawn by considering new set of data points. This is continued until the difference between the two consecutive centers is less than 5%. The fit is considered to be good when the normalized root mean square deviation of the residual is less than 5%. Furthermore, to obtain a better fitting circle on the as-built geometry and to improve the iterative process, the fillet region is smoothed as shown in Fig. IV-8(b).

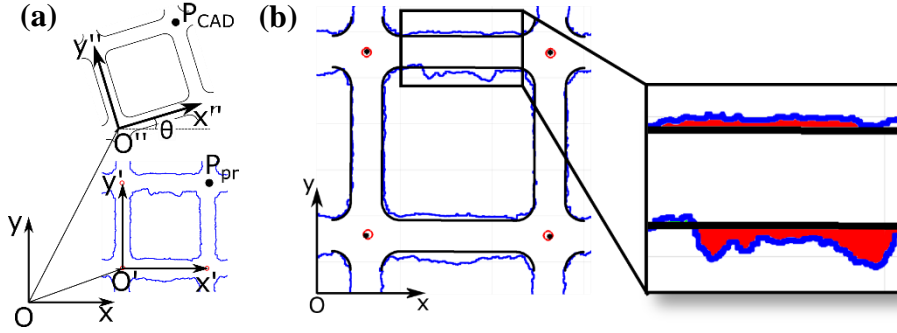


Figure IV - 7 (a) Procedure used to overlap the as-designed and as-built geometry (b) Indication of excess material in the strut obtained through overlapping

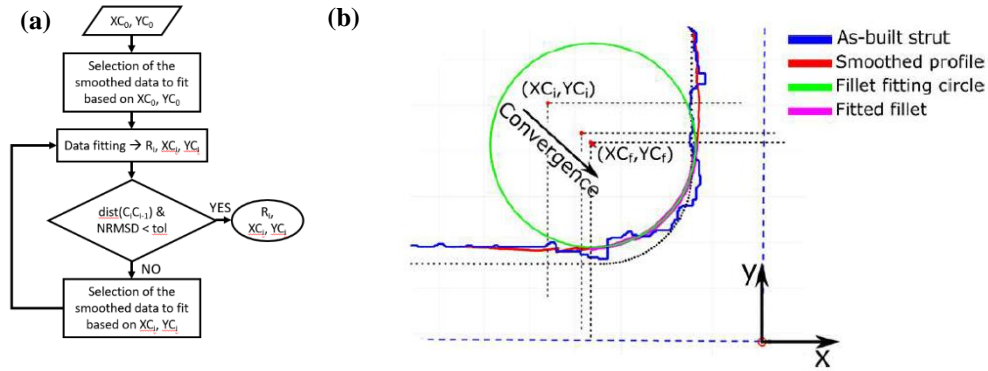


Figure IV - 8 (a) Algorithm used in MATLAB to calculate fillet radius (b) Convergence method used to fit the fillet radius

The deviation of the as-built unit cell with respect to the as-designed geometry is obtained by calculating the error on the length of the side and the diagonals of the square obtained by joining the centers of the junctions. The error % is calculated using the Eq. IV-2. The statistical analysis of the measured values is discussed in the subsequent section.

$$Error (\%) = \frac{As\_built - As\_designed}{As\_designed} \times 100 \quad \dots \text{Eq. IV-2}$$

### 4.2.3. Internal Porosity analysis

This analysis was carried out to see the effect of strut thickness and orientation on the internal porosity in the specimens. The specimens were moulded in hard resin and polished using SiC abrasive papers with different grit size. The strut thickness was measured during the polishing process and specimens were polished until the mid-section of the struts were reached. The specimens were then polished on cloth with diamond paste. Images of the polished surface was captured using stereo optical microscope (Nikon SMZ25) and the images were processed using an in-house MATLAB code to measure the pore size and distribution. The analysis was carried out on specimens #1, #2, #3, #6, and #9 for 0° and 45° - 35.26° configuration. The measured porosity values were divided into specimen porosity at junctions, porosity in horizontal and vertical struts in the case of 0° specimens. In the case of 45° - 35.26° specimens, we had inclined struts and inclined junctions.

### 4.2.4. Mechanical test

The second part of the study focused on the effect of node fillet, building orientation and unit cell size on the fatigue properties of cubic regular cellular structures. The specimen design and the geometric parameters are different from the specimens mentioned before but are designed based on the results of the geometrical analysis.

#### 4.2.4.1. Specimen details

The specimens were made up of cubic regular unit cells with strut thickness  $t_0$ , unit-cell size  $L$  and fillet radius  $R$ . The specimens were manufactured using LPBF process in a Renishaw machine with laser power of 200W and a layer thickness of 60  $\mu\text{m}$ . Biomedical grade Ti6Al4V powder particles with particle size between 15 – 45  $\mu\text{m}$  was used for manufacturing. The specimens were subjected to heat treatment process at temperature above 800°C in vacuum to relieve stresses and to obtain a stable  $\alpha+\beta$  phase microstructure.

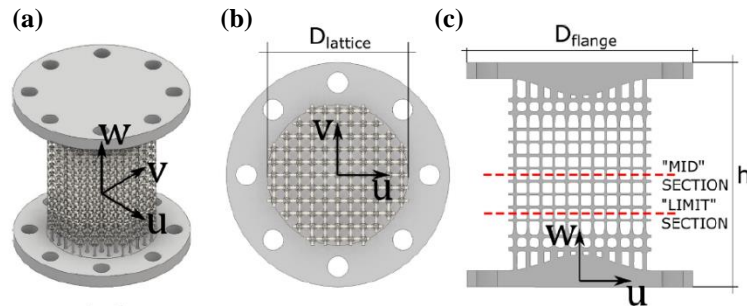


Figure IV - 9 Cellular specimen for mechanical test (a) Isometric view of full specimen (b) Cross-section indicating the cellular part diameter (c) Cross-section indicating strut transition and bell-shaped center of the flange

The fatigue and the compression test specimens are as shown in Fig. IV-9. The specimens were designed according to ISO 14333, the cellular section of the specimen is cylindrical and has 12-unit cells along the height and 11-unit cells along the diameter. Solid flanges are provided at the end of the specimen since they are subjected to tensile loading during the fatigue test. If an XYZ reference system is considered to indicate the printing process, the printing plane is XY and the printing direction is Z.

As mentioned in the previous sections, the deviation of the as-built geometry from the as-designed values is a common phenomenon in the case of LPBF process. Therefore, based on the results from the geometrical analysis discussed, the CAD parameters of the as-designed CAD are adjusted. A graphical representation of the nominal and compensated as-designed geometry is shown in Fig. IV-10. A total of four different specimens were developed for analysis (Fig. IV-11) and are listed below.

- Specimen A: The specimens were developed with compensated thickness, the vertical load bearing struts were parallel to the printing direction.
- Specimen B: Compensated thickness like specimen A, but the vertical load bearing struts were perpendicular to the printing direction.
- Specimen C: Similar to specimen B, but without compensation.
- Specimen D: The printing was similar to the specimen A. The strut thickness was compensated but there were no fillets at the junctions.
- Specimen E: The printing was similar to specimen A, but the geometrical parameters were adjusted for a unit cell size of 3000  $\mu\text{m}$ .
- Specimen F: The printing direction is inclined along the diagonal of the cube. The struts are inclined to the printing plane as well as the loading direction. The struts thickness has been increased accordingly to obtain a nominal elastic modulus of 3 GPa.

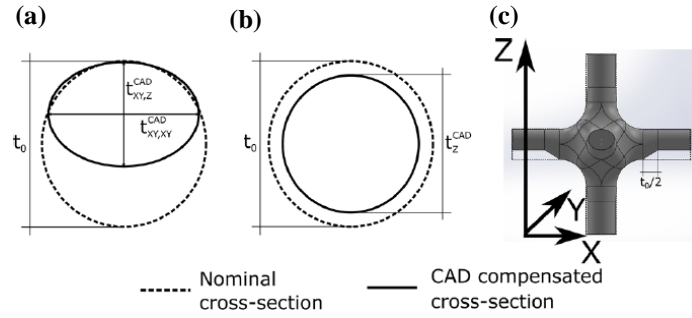


Figure IV - 10 (a) Compensated horizontal strut cross-section (b) Compensated vertical strut cross-section (c) Compensated unit cell CAD model with printing along Z-direction

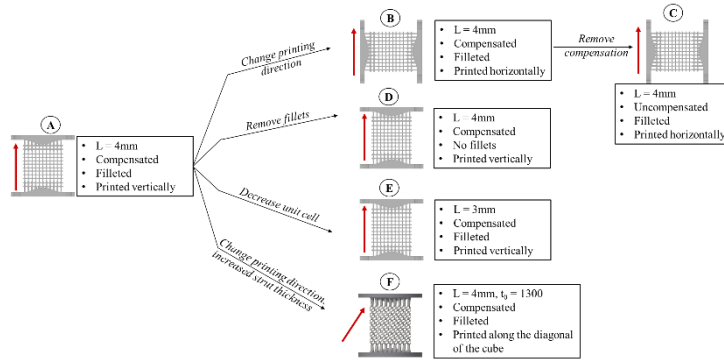


Figure IV - 11 Different configurations of cellular specimens used for mechanical testing

The as-designed nominal values of the specimens are tabulated in Table. IV-2. The compensated values depend on the nominal thickness values of the specimen. The strut thickness and the unit cell size of specimen A, B, C and D is same, but the geometrical values of specimen E and F are different. The specimen dimension for all the specimens is provided in Table IV-3.

Table IV - 2 Nominal as- designed geometrical parameters

| Specimen | Nominal geometry       |                            |                        |
|----------|------------------------|----------------------------|------------------------|
|          | R<br>( $\mu\text{m}$ ) | $t_0$<br>( $\mu\text{m}$ ) | L<br>( $\mu\text{m}$ ) |
| A        | 600                    | 670                        | 4000                   |
| B        | 600                    | 670                        | 4000                   |
| C        | 600                    | 670                        | 4000                   |
| D        | 0                      | 670                        | 4000                   |
| E        | 450                    | 500                        | 3000                   |
| F        | 600                    | 1300                       | 4000                   |

Table IV - 3 Specimen dimensions

| Specimen      | h<br>(mm) | $D_{\text{flange}}$<br>(mm) | $D_{\text{lattice}}$<br>( $\mu\text{m}$ ) |
|---------------|-----------|-----------------------------|---|
| A, C, B, D, F | 69        | 70                          | 44  |
| E             | 58        | 59                          | 33  |

To ensure that the failure due to fatigue loading occurs at the cellular region of the specimen and not at the interface near the flange, the vertical strut thickness, and the fillet radius of the unit cells closer to the top and bottom flange are increased. Since a flat flange increases the tensile load experience by the outer struts, the flange is thickened in the center in the form of a bell as shown in Fig. IV- 9(c).

#### 4.2.4.2. Metrological analysis

Metrological analysis was carried out using the images of randomly selected 8 – 12 unit cells from the specimen. The images were captured along the planes parallel and perpendicular to the printing direction. The obtained images were used to compare the as-built specimen geometry with the nominal as-designed geometry.

#### 4.2.4.3. Compression test

The compression test was carried out using an Instron 8516 universal testing machine equipped with 100kN load cell. The test was carried out at a crosshead speed of 1mm/min and the displacement was measured using an extensometer (25 mm and 12.5 mm) depending on the specimen size. The Young's modulus was calculated using the unloading cycles according to ISO 13314. Modulus is calculated using the unloading cycle since stabilization occurs in the specimen after the first loading cycle due to plasticization as mentioned in chapter 2 and 3. Monotonic test was carried out to obtain the 0.2% offset yield stress and the maximum stress under compression loading. One specimen in each batch was test under compression loading.

#### 4.2.4.4. Fatigue test

Fully reversed fatigue tests ( $R = -1$ ) were carried out on seven specimens in each configuration to obtain the S-N curve. The tests were conducted on a RUMUL Testronic resonating fatigue machine with a maximum load capacity of 50 kN under load control and at 120 Hz. Specimen is considered to be failed when the resonant frequency decreases by 1 Hz. This decrease in frequency corresponds to the failure of 4 – 5 struts. Later, the failed specimens were subjected to monotonic tensile load to clearly identify the fatigue crack locations. The run-out condition for these specimens was set to 107 cycles. Specimen that sustained  $10^7$  cycles were used again by increasing the load by 1.5 times. The S-N curve fitting and the scatter of fatigue data was calculated using the equation III-1 and III-2 mentioned in chapter 3 respectively. To differentiate the fatigue failure surfaces from the failure due to tensile loading after fatigue test, fracture surfaces were analyzed using JOEL JSM-IT300LV scanning electron microscope.

### 4.3. Results and discussion: Geometrical analysis

#### 4.3.1. Geometrical analysis

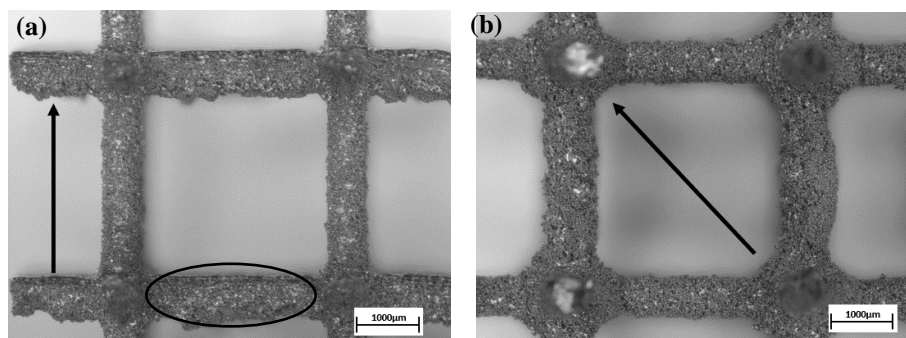


Figure IV - 12 Unit cell images indicating the accumulation of powder particles on struts (a) 0° specimen (b) 45° specimens ; arrow indicates the printing direction

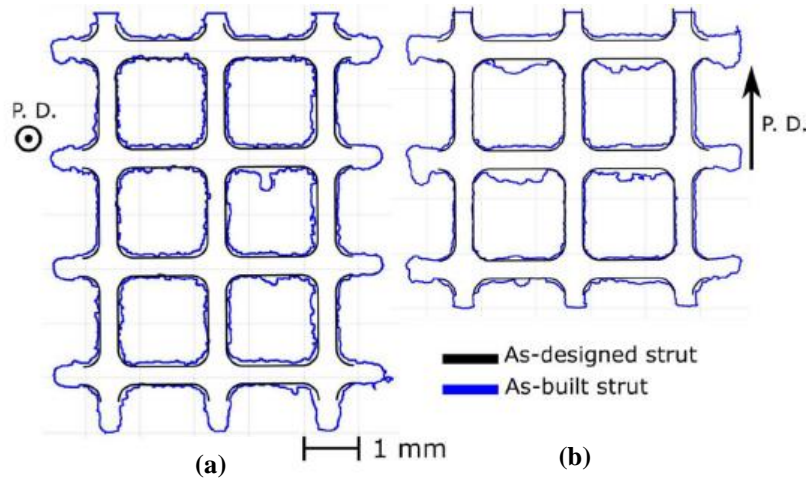


Figure IV - 13 Overlapping of as-designed and as-built geometry of specimen #3 printed at  $0^\circ$  (a) Unit cells perpendicular to printing direction (b) Unit cells parallel to printing direction

Some images of the unit cell are as shown in Fig. IV-12. Even though the structures are large, we see a considerable amount of particle attached to the struts. The amount of particle attached is higher at the bottom than at the top. Also, the irregularity in the geometry due to these particles is pronounced at the bottom of the struts due to the excess material accumulation (parasitic mass) as highlighted in Fig. IV-12(a). From the visual inspection, the larger specimens with thicker struts appear to be least affected by excess material accumulation. However, thickness analysis revealed that increase in the strut thickness is relatively same as that of the specimens with thinner struts. The other parameter that effects the build quality is the strut inclination with the building plane. Horizontal struts had the maximum irregularity while vertical struts had a considerably uniform thickness. For the fillet radii, considering the scale of the specimen and the LPBF process limitations, they are reproduced well. The effect of printing direction is not evident to the naked eye. However, a certain amount of excess material accumulation is observed on the bottom fillets of the inclined specimens.

A representation of the as-designed geometry overlaid on the as-built profile in two planes is shown in Fig. IV-13 (specimen #3,  $0^\circ$ ) for better comparison. Due to the difference in the size between the specimen, it was not possible to capture the entire face of the specimen in bigger geometries such as specimen #4 and #9. The section parallel to the printing plane shown in Fig. IV-13(a) is printed accurately without any severe accumulation of excess material. On the contrary, in the section perpendicular to the printing plane, the horizontal struts have a large amount of excess material attached at the center. Due this excess material the horizontal struts have an elliptical cross section. The excess material at the bottom of horizontal struts is due to the lack of support during the printing process, and the excess material on top of the struts is possibly due to the slicing process of the input STL file.

Another issue that must be considered is the evaluation of 3D thickness values of the struts using 2D images. This issue has least effect on the  $0^\circ$  specimens since the thickness can be evaluated using the images along three planes. However, for the  $45^\circ$  inclined specimens, the thickness of the horizontal struts should be similar to the horizontal struts of the  $0^\circ$  specimens but when the images are captures their true value is not obtained since we see the “skewed” struts or in other words due to the parallax error from the viewing angle as shown in Fig. IV-14. The same effect is seen for the struts of  $45^\circ$ - $35.26^\circ$  specimens. On the contrary, based on the same concept, the struts inclined at  $45^\circ$  can be accurately measured.

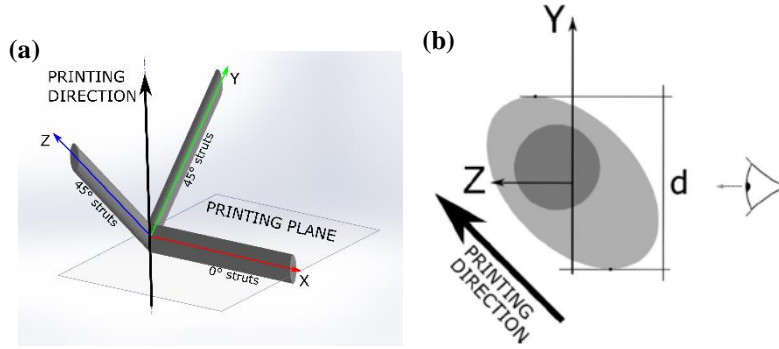


Figure IV - 14 (a) Orientation of struts in the 45° specimens with respect to the printing plane (b) Skewed view of the horizontal strut when capturing images along XY and XZ planes

#### 4.3.1.1. Strut thickness

*0° specimens:* The struts in the 0° specimens are grouped as parallel to the printing direction (vertical struts, Z-direction) and perpendicular to the printing direction (horizontal struts, X and Y direction). The variation in the strut thickness is divided according to the orientation. The vertical struts are reproduced without any asymmetry in the thickness since they are perpendicular to the printing plane and are supported from the first layer. The thickness of the horizontal struts can be divided into measurements for the same strut (0° horizontal and 0° vertical). The strut thickness values are not influenced by the fillet radius since the thickness measurements are obtained far from the fillet. Also, the strut length has negligible effect as the strut length considered in this sample is larger than ones used in chapter 2 and chapter 3. The comparison of as-designed and the measured as-built thickness is plotted in Fig. IV-15 along with the graphical representation of as-designed and as-built strut thickness. As mentioned before, the horizontal struts have a considerable amount of excess material or parasitic mass in the lower region of the struts making them elliptical. The data points for all the three categories are linear and hence the curve fitting shown by the dashed line give a relation between the as-designed and the as-built thickness as mentioned in the Eq. IV-3.

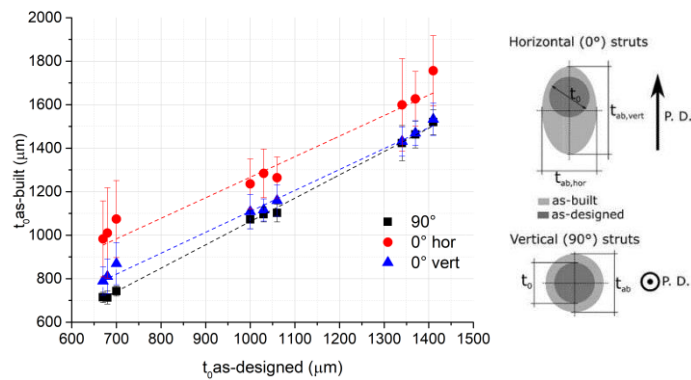


Figure IV - 15 Comparison of as-designed and as-built thickness in for different strut orientation in 0° specimens. The dashed lines represent linear fitting.

$$t_{90^\circ} = 1.08t_{0,as-d} - 17.29 \quad \dots\dots\dots \text{Eq. IV - 3(a)}$$

$$t_{0^\circ, vert} = 0.93t_{0,as-d} - 358.58 \quad \dots\dots\dots \text{Eq. IV - 3(b)}$$

$$t_{0^\circ, hor} = 0.95t_{0,as-d} - 163.31 \quad \dots\dots\dots \text{Eq. IV - 3(c)}$$

The slope of the fitting is close to 1 in all the three cases, indicating that the offset in the thickness due to the LPBF is nearly constant. The thickness values are also tabulated in the Table. IV- 4.

Table IV - 4 As-designed and as-built thickness values for all the specimens printed at 0° orientation (values in μm)

| Specimen No. | As-designed |                | As-built                   |                           |
|--------------|-------------|----------------|----------------------------|---------------------------|
|              | $t_0$       | $t_{90^\circ}$ | $t_{0^\circ, \text{vert}}$ | $t_{0^\circ, \text{hor}}$ |
| 1            | 700         | 743±23         | 1074±177                   | 869±97                    |
| 2            | 680         | 713±30         | 1010±208                   | 810±80                    |
| 3            | 670         | 714±24         | 983±175                    | 789±65                    |
| 4            | 1060        | 1102±41        | 1264±96                    | 1159±72                   |
| 5            | 1030        | 1096±35        | 1284±112                   | 1116±51                   |
| 6            | 1000        | 1072±42        | 1236±115                   | 1108±79                   |
| 7            | 1410        | 1520±57        | 1756±162                   | 1533±74                   |
| 8            | 1370        | 1463±62        | 1627±126                   | 1469±57                   |
| 9            | 1340        | 1423±81        | 1599±213                   | 1431±68                   |

45° Specimens: The struts in these specimens are divided into two categories, inclined (Y and Z) and horizontal (X struts). The inclined struts displayed a similar cross-section as that of the horizontal struts of the 0° specimen. The cross-section was elongated along one direction and hence elliptical in shape. The horizontal struts i.e., the X struts are perpendicular to the printing direction and are similar to horizontal struts of the 0° specimen. However, the optical microscope images of these struts do not represent the true cross-section and thickness as explained at the beginning of this section. The measured as-built thickness values are compared with the as-designed thickness for three categories (0°, 45° vertical and 45° horizontal) as shown in Fig. IV-16. The data points are fit using a linear function providing the relation between as-built and the as-designed strut thickness values as indicated in the Eq. IV-4.

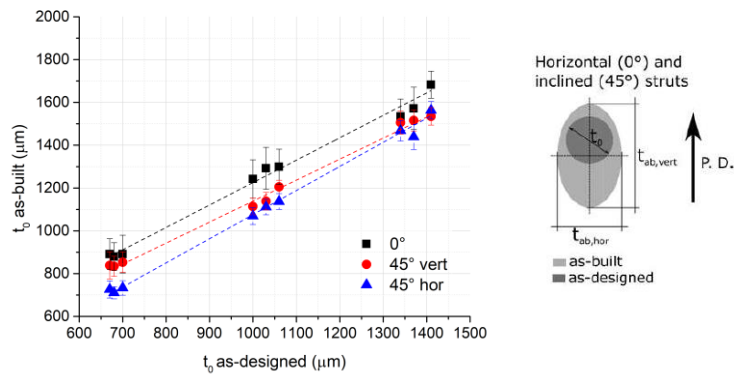


Figure IV - 16 Comparison of as-designed and as-built thickness in for different strut orientation in 0° specimens. The dashed lines represent linear fitting.

$$t_{0^\circ} = 1.03 t_{0, \text{as-d}} - 192.98 \quad \dots\dots\dots \text{Eq. IV - 4(a)}$$

$$t_{45^\circ, \text{vert}} = 0.98 t_{0, \text{as-d}} - 162.81 \quad \dots\dots\dots \text{Eq. IV - 4(b)}$$

$$t_{45^\circ, \text{hor}} = 1.14 t_{0, \text{as-d}} - 58.32 \quad \dots\dots\dots \text{Eq. IV - 4(c)}$$

The slope of the fitting lines is closer to 1 indicating that the thickness offset due to the LPBF process is closer to a constant value. The measured thickness values are tabulated in Table IV-5.

Table IV - 5 As-designed and as-built thickness values for all the specimens printed at 45° orientation (values in  $\mu\text{m}$ )

| Specimen No. | As-designed |               | As-built                    |                            |
|--------------|-------------|---------------|-----------------------------|----------------------------|
|              | $t_0$       | $t_{0^\circ}$ | $t_{45^\circ, \text{vert}}$ | $t_{45^\circ, \text{hor}}$ |
| 1            | 700         | 891±88        | 853±48                      | 733±34                     |
| 2            | 680         | 879±65        | 834±47                      | 710±28                     |
| 3            | 670         | 891±72        | 838±64                      | 726±40                     |
| 4            | 1060        | 1299±83       | 1205±31                     | 1137±37                    |
| 5            | 1030        | 1292±98       | 1138±41                     | 1111±36                    |
| 6            | 1000        | 1242±90       | 1114±39                     | 1069±40                    |
| 7            | 1410        | 1683±63       | 1535±41                     | 1563±41                    |
| 8            | 1370        | 1572±99       | 1516±49                     | 1439±59                    |
| 9            | 1340        | 1534±82       | 1506±54                     | 1468±48                    |

45° - 35.26° Specimens: All the struts in these specimens are inclined at the same angle of 35.26° with respect to the printing plane. Therefore, the measured values of all the struts along X, Y and Z direction should represent similar values. Due to the inclination, the struts cross-section is expected to be elliptical. Therefore, the measured values do not represent the major axis, or the minor axis dimension of the ellipse as mentioned at the beginning of the section. This is due to the change in the viewpoint while capturing the images. Hence, the measured values are represented in terms of the diameter ( $d_{\text{as-built}}$ ) as indicated in the Fig. IV-17. The comparison between the as-designed thickness and the measured diameter is provided in Fig. IV-17. The thickness and the diameter values are tabulated in Table IV-6.

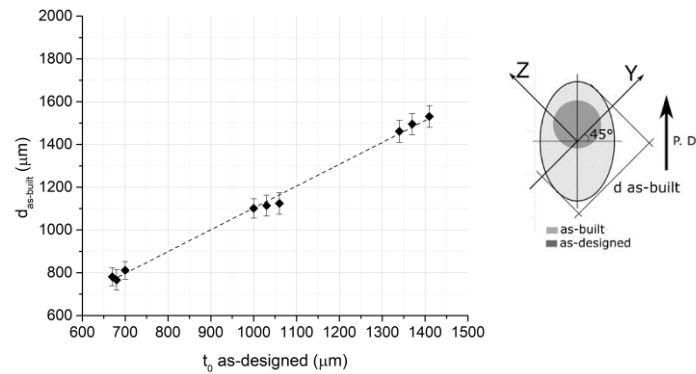


Figure IV - 17 Comparison of as-designed thickness and as-built diameter for struts oriented at 45° - 35.26°. The dashed lines represent linear fitting.

Table IV - 6 As-designed thickness and as-built diameters values for all the specimens printed at 45° - 35.26° orientation (values in  $\mu\text{m}$ )

| Specimen No. | $t_0$ | $d_{\text{as-built}}$ |
|--------------|-------|-----------------------|
| 1            | 700   | 811 $\pm$ 41          |
| 2            | 680   | 766 $\pm$ 48          |
| 3            | 670   | 781 $\pm$ 42          |
| 4            | 1060  | 1124 $\pm$ 50         |
| 5            | 1030  | 1114 $\pm$ 49         |
| 6            | 1000  | 1101 $\pm$ 45         |
| 7            | 1410  | 1531 $\pm$ 51         |
| 8            | 1370  | 1495 $\pm$ 50         |
| 9            | 1340  | 1461 $\pm$ 51         |

To outline the results obtained, the as-designed thickness values are dependent on the orientation of the individual struts with respect to the printing direction. The results also indicate that the strut length does not affect the as-built thickness values. Further the linear relationship between the designed and the measured values indicated that amount of excess material in the struts is constant. However, the amount of material added is dependent on the inclination of the struts. Also, the as-built thickness values are always higher than the as-designed thickness. Apart from the vertical struts, all the other struts tend to have an elliptical cross-section. Also, the amount of extra material is higher on the major axis of the ellipse representing the horizontal struts of 0° specimens. Hence, it can be concluded that it is not advisable to print cellular materials with struts parallel to the printing plane, but it is recommended to incline the specimen to avoid having struts parallel to the printing plane.

#### 4.3.1.2. Excess material

The above analysis indicates just the increase in the strut thickness compared to the as-designed thickness values. However, the analysis does not indicate how much excess material has been added and where it is added. This section deals with the measurement of the excess material added on the struts. The results of the measurement of the excess material are presented in this section. The excess material in the struts is dependent on the orientation of the struts similar to the strut thickness offset. The excess material measurement is carried out for all the three types of specimens and the struts are categorized as seen in the section 4.3.1.1. The excess material is measured on the upper part of the strut, lower part of the strut and laterally as shown in Fig. IV-18, maximum material accumulation is observed on the lower part of the strut. However, it was observed that the excess material accumulation follows symmetry with respect to the strut axis. For vertical struts, the excess material is uniformly distributed throughout the circumference of the struts. The relation between the excess material and designed thickness is plotted in Fig. IV-18. The data points were fitted with a linear equation, thereby providing the Eqs.IV-5.

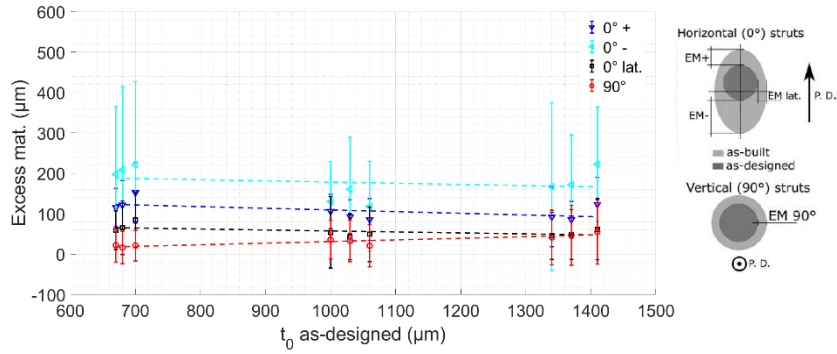


Figure IV - 18 Excess material on struts in 0° specimens, categorized based on struts orientation and excess material location. Dashed lines represent linear curve fitting.

$$EM_{0^{\circ}}^{-} = -0.029t_0^{*} + 207.70 \quad \dots\dots\dots \text{Eq. IV - 5(a)}$$

$$EM_{0^{\circ}}^{+} = -0.041t_0^{*} + 150.87 \quad \dots\dots\dots \text{Eq. IV - 5(b)}$$

$$EM_{0^{\circ}}^{lat} = -0.024t_0^{*} + 81.63 \quad \dots\dots\dots \text{Eq. IV - 5(c)}$$

$$EM_{90^{\circ}} = +0.040t_0^{*} - 8.64 \quad \dots\dots\dots \text{Eq. IV - 5(d)}$$

In the case of 45° specimens, the horizontal as well as the inclined struts have elliptical cross-section as discussed before. Even in the inclined specimens, the amount of excess material is higher on the lower part of the strut. For the horizontal struts, since they have the similar configuration of the horizontal struts of 0° specimen, it can be assumed that the amount of excess material on the lower part of the strut is more than that seen in the inclined struts. However, as mentioned before, the images of the horizontal struts of 45° specimens do not represent the major or minor axis of the cross-section. Hence, the excess material measured is not categorized with respect to minor or major axes of elliptical cross-section. Fig. IV-19 provides the variation of excess material at different locations, with respect to the as-designed thickness. The relation between the excess material and the as-designed thickness is given by the Eqs.IV-6 mentioned below:

$$EM_{45^{\circ}}^{-} = +0.017t_0^{*} + 48.66 \quad \dots\dots\dots \text{Eq. IV - 6(a)}$$

$$EM_{45^{\circ}}^{+} = -0.037t_0^{*} + 114.13 \quad \dots\dots\dots \text{Eq. IV - 6(b)}$$

$$EM_{45^{\circ}}^{lat} = +0.040t_0^{*} - 29.17 \quad \dots\dots\dots \text{Eq. IV - 6(c)}$$

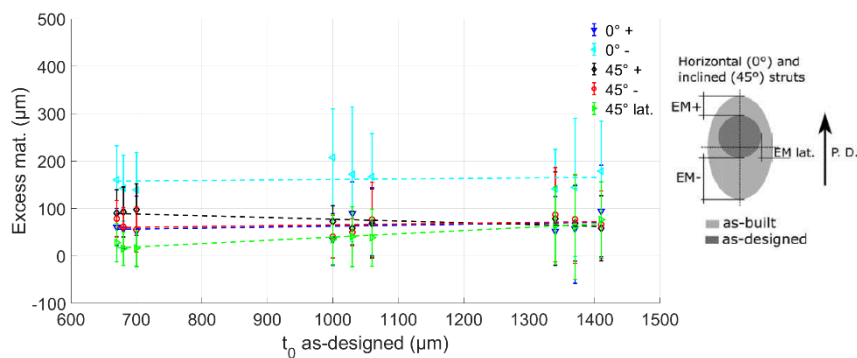


Figure IV - 19 Excess material on struts in 45° specimens, categorized based on struts orientation and excess material location. Dashed lines represent linear curve fitting.

For the  $45^\circ$ - $35.26^\circ$  specimens, the measured thickness value does not provide the dimensions of the elliptical cross-section as mentioned before. The same is observed here, the excess material observed in the specimens is not parallel to the printing direction but is inclined at  $45^\circ$  with the printing plane. Therefore, exact estimation of the excess material is not obtained. Fig. IV-20 compares the variation of the excess material measured with respect to the as-designed thickness.

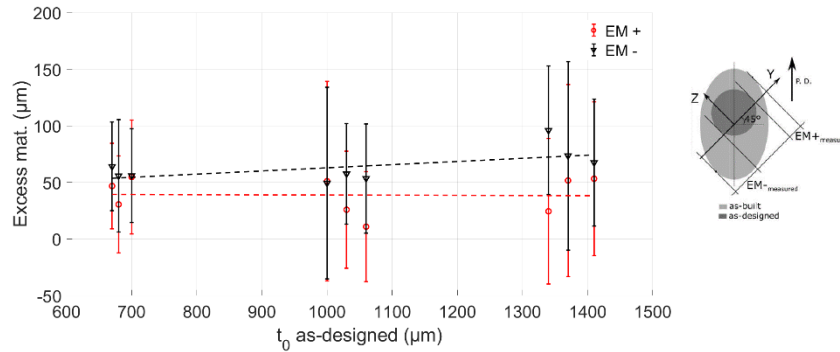


Figure IV - 20 Excess material on struts in  $45^\circ$  -  $35.26^\circ$  specimens, categorized based on the excess material location. Dashed lines represent linear curve fitting.

To conclude, the amount of excess material is mainly dependent in the inclination of the struts with the printing direction and the influence of as-designed thickness is negligible. The closer to constant value of excess material indicates that the amount of material added is dependent on the LPBF process parameters and the thermal properties of the powder. The horizontal struts had the highest deviation from the as-designed thickness values when compared to inclined struts. Both horizontal and inclined struts are built without any support on a loose bed of powder particles. Since powder particles have low thermal conductivity, the powder particles around the melt pool or melt layer are also melted and attached to the geometry, thereby increasing the excess material on the lower part of the strut. The vertical struts are built uniformly with excess material distributed around the circumference. The presence of support in vertical struts helps in maintaining the circular cross-section.

#### 4.3.1.3. Fillet radius

The evaluation of the fillet radius is a complex process as its value depends on as-designed fillet radius as well as the as-designed thickness. Similar to the strut thickness, the fillet radius is also influenced by the specimen orientation with the printing direction. For the ease of measurement, the fillet radii at different locations of the specimen are classified as shown in Fig. IV-21.

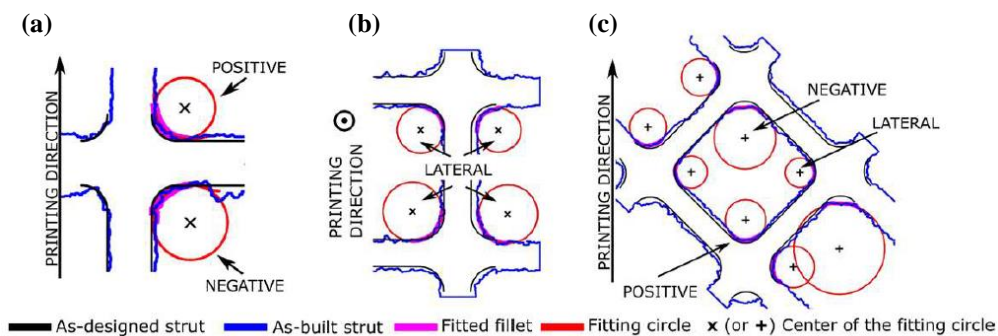


Figure IV - 21 Classification of different fillets in the specimen (a) Parallel to printing direction (b) Perpendicular to printing direction (c) Inclined

In  $0^\circ$  specimens, the fillets above the junction or struts are considered positive fillets (printing direction is the reference direction) and the fillets below the junction or struts is considered negative. Similar classification is applied for  $45^\circ$  specimens along the inclined planes (Fig. IV-21(a)). In the plane

parallel to the printing plane, the fillets are referred as lateral fillets as shown in Fig. IV-21(b). The remaining fillets of the 45° specimens and the 45° - 35.26° specimens are classified into positive, negative, and lateral fillets if they are below, above or along the sides of junction respectively as shown in Fig. IV-21(c). The fillet radii measurement and the fitting models are discussed in the subsequent sections.

### Fillet radii measurement

0° specimens: The fillet radius variation in these specimens is represented in Fig. IV-22. The image analysis and the calculation indicated that the negative fillets observed in the vertical planes have the smallest values compared to positive and lateral fillet radius. The presence of excess material in some of the negative fillet region leads to fillet radius values lesser than the as-designed value. The fillet radius of the positive fillets has intermediate size while the lateral fillets had the highest fillet radius values. The high scatter in the fillet radii values seen in the Fig. IV-22, indicate that the values are not uniform and there is a high possibility of having sharp as well as wide fillets across the specimen. The fillet radius values for 0° specimens are tabulated in Table. IV-7.

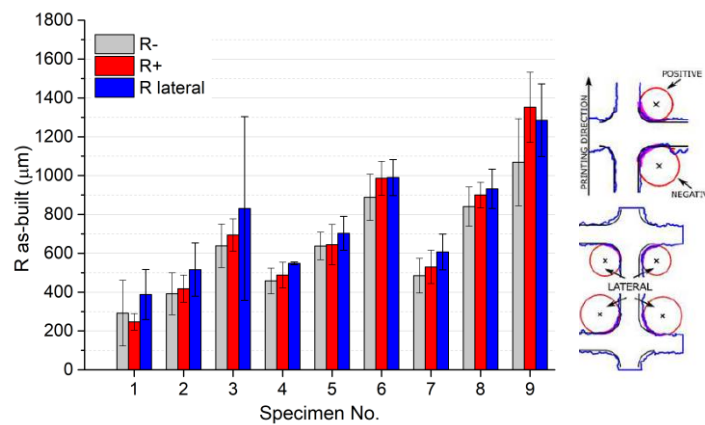


Figure IV - 22 As-built fillet radii values for different fillets in 0° specimens.

Table IV - 7 As-built fillet radii for 0° specimens with standard deviation (values in μm)

| Specimen No. | As-designed |                | As-built |          |           |
|--------------|-------------|----------------|----------|----------|-----------|
|              | R           | t <sub>0</sub> | R-       | R+       | R lateral |
| 1            | 200         | 700            | 292±169  | 247±43   | 388±129   |
| 2            | 400         | 680            | 392±108  | 418±70   | 516±137   |
| 3            | 600         | 670            | 639±112  | 694±83   | 831±473   |
| 4            | 300         | 1060           | 458±66   | 488±66   | 548±7     |
| 5            | 600         | 1030           | 638±71   | 645±104  | 703±87    |
| 6            | 900         | 1000           | 888±119  | 986±88   | 990±93    |
| 7            | 400         | 1410           | 485±89   | 530±86   | 607±92    |
| 8            | 800         | 1370           | 841±101  | 900±66   | 932±101   |
| 9            | 1200        | 1340           | 1069±224 | 1352±181 | 1285±187  |

45° specimens: In these specimens, the negative and positive fillets on the inclined plane have similar trend like the fillets in the vertical plane of 0° specimens. The negative fillets radii were smaller than

the positive fillet radii as expected, due to excess material accumulation. In case of fillets associated with the inclined struts (vertical planes), the negative fillets have a larger radius compared to the positive and lateral fillets. The fillet radii values for all the specimens and the scatter are shown in Fig. IV-23. The parasitic mass or the extra material in the fillets flattens the curvature of the fillet. The average fillet radii for different tables are tabulated in Table. IV-8.

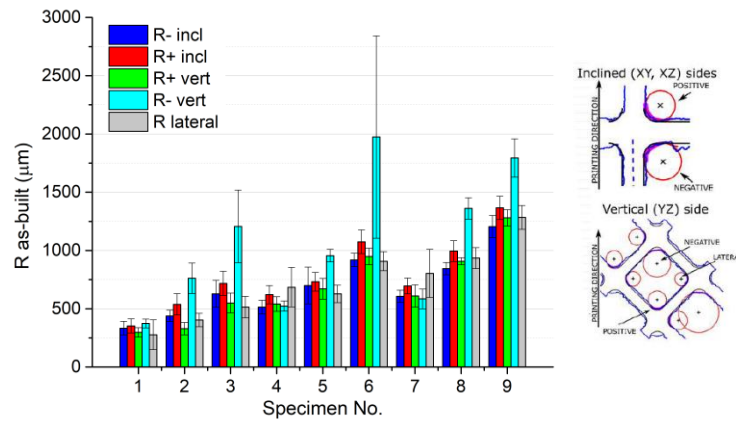


Figure IV - 23 As-built fillet radii values for different fillets in 45° specimens.

Table IV - 8 As-built fillet radii for 45° specimens with standard deviation (values in µm)

| Specimen No. | As-designed |                | As-built |          |          |          |            |
|--------------|-------------|----------------|----------|----------|----------|----------|------------|
|              | R           | t <sub>0</sub> | R- incl  | R+ incl  | R + vert | R- vert  | R lat vert |
| 1            | 200         | 700            | 333±59   | 353±61   | 297±40   | 374±38   | 277±128    |
| 2            | 400         | 680            | 439±48   | 538±91   | 329±53   | 762±130  | 403±58     |
| 3            | 600         | 670            | 628±115  | 718±103  | 549±85   | 1207±312 | 514±92     |
| 4            | 300         | 1060           | 514±59   | 621±78   | 541±63   | 523±44   | 685±169    |
| 5            | 600         | 1030           | 700±158  | 732±80   | 671±89   | 956±54   | 628±75     |
| 6            | 900         | 1000           | 919±58   | 1075±101 | 949±71   | 1974±868 | 908±82     |
| 7            | 400         | 1410           | 607±53   | 696±68   | 610±95   | 585±85   | 803±206    |
| 8            | 800         | 1370           | 845±53   | 995±89   | 908±30   | 1361±92  | 935±90     |
| 9            | 1200        | 1340           | 1205±95  | 1366±100 | 1280±70  | 1794±164 | 1284±102   |

45° - 35.26° specimens: These specimens are inclined with respect to all the directions, due to which all the fillets in the specimen are inclined with respect to the printing plane. The fillet radii variation in these specimens should be like the fillets in the vertical plane of 45° specimens due to the inclination. Only three types of fillets are observed in these specimens, positive, negative, and lateral, their distribution is shown in Fig. IV-24. The measured values indicate that the negative fillet radius was larger compared to positive and lateral fillets. The measured radii values and the standard deviation are tabulated in Table IV-9.

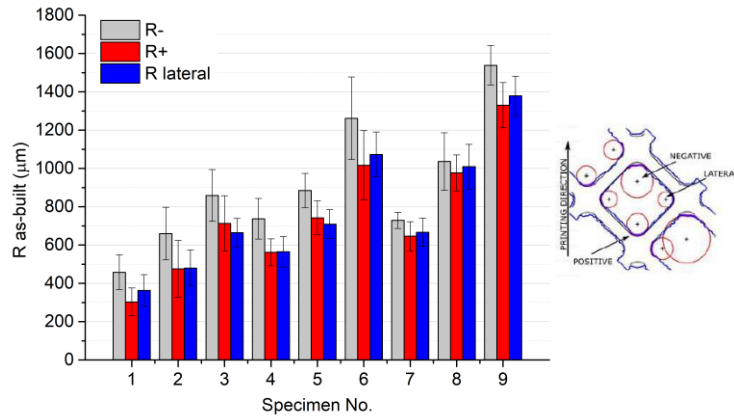


Figure IV - 24 As-built fillet radii values for different fillets in 45° - 35.26° specimens.

Table IV - 9 As-built fillet radii for 45° - 35.26° specimens with standard deviation (values in µm)

| Specimen No. | As-designed |                | As-built |          |           |
|--------------|-------------|----------------|----------|----------|-----------|
|              | R           | t <sub>0</sub> | R-       | R+       | R lateral |
| 1            | 200         | 700            | 458±91   | 303±73   | 363±82    |
| 2            | 400         | 680            | 660±137  | 476±148  | 480±94    |
| 3            | 600         | 670            | 859±135  | 713±145  | 665±74    |
| 4            | 300         | 1060           | 737±106  | 562±70   | 565±79    |
| 5            | 600         | 1030           | 885±89   | 742±88   | 709±76    |
| 6            | 900         | 1000           | 1262±216 | 1016±181 | 1073±117  |
| 7            | 400         | 1410           | 729±42   | 646±76   | 667±74    |
| 8            | 800         | 1370           | 1036±150 | 977±94   | 1009±117  |
| 9            | 1200        | 1340           | 1538±103 | 1330±118 | 1379±103  |

To summarize the results obtained for all the three inclinations, the LPBF process was able to reproduce the fillets in these specimens with acceptable shape. The as-built fillet radius values are higher than the as-designed values. From the average values it was seen that a considerable regular trend is seen in the distribution. Therefore, the experimental data relating the as-designed fillet radius, as-designed strut thickness and the as-built fillet radius can be fitted to obtain a relation. The higher scatter of the radii values indicate that the specimen can have wider fillets or have sharp junctions without due to the material accumulation from the LPBF process.

#### Fillet radius fitting

As mentioned in the previous section, the as-built fillet radius is dependent on the as-designed fillet radius as well as the as-designed strut thickness. Even though the effect of strut thickness is considerably less compared to the as-designed fillet radius, eliminating the thickness parameter can lead to increase in the error. As explained in the section 4.3.1.1, the relation between the as-built and as-designed strut thickness is linear. Similar to that, the relation between the as-built fillet radius and the as-designed radius and thickness values is fit using a linear function. The 3-dimensional contour plots are used in to represent the relationship.

*0° specimens:* The three as-built fillet radii values measured are plotted against the designed values as shown in Fig. IV-25. The plots indicate that the as-designed radius had higher influenced on the

obtained fillet radii values compared to the as-designed thickness. The fitting error for this specimen is ~10%. The curve fitting expression relating the parameters given by Eqs. IV-7:

$$R_+ = -16.58 + 0.99R_{as-d} + 0.12t_{0,as-d} \quad \dots\dots\dots \text{Eq. IV - 7(a)}$$

$$R_- = +97.86 + 0.75R_{as-d} + 0.08t_{0,as-d} \quad \dots\dots\dots \text{Eq. IV - 7(b)}$$

$$R_{lat} = +210.19 + 0.85R_{as-d} + 0.03t_{0,as-d} \quad \dots\dots\dots \text{Eq. IV - 7(c)}$$

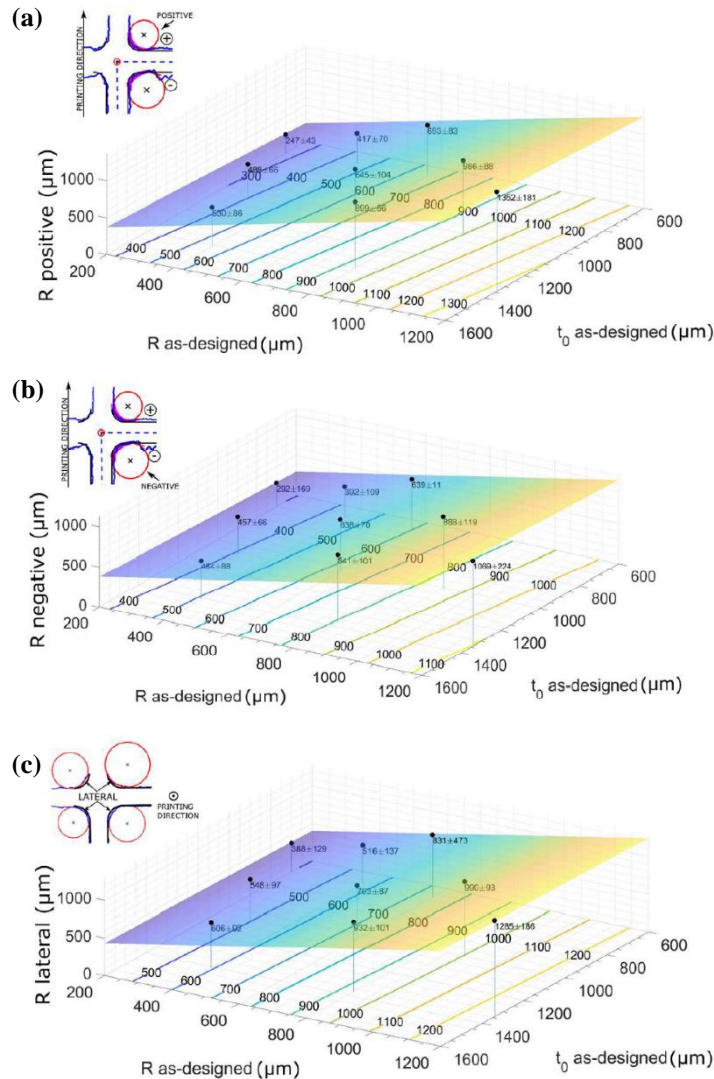


Figure IV - 25 Variation of as-built fillet radii with as-designed radii and thickness for 0° specimens (a) Positive fillets (b) Negative fillets (c) Lateral fillets

45° specimens: The contour plots relating the fillet radii on the vertical plane of the specimen (XZ plane) with the designed values are shown in Fig. IV-26. The plots indicate that the as-designed fillet radius has a pronounced influence on the as-built fillet radius of negative fillets, followed by positive fillets. On the other hand, the lateral radii values are equally sensitive to the as-designed fillet radius as well as the as-designed strut thickness. The fitting errors in this case is ~ 15%, the fitting equation relating the parameters in the vertical plane are given by Eqs.IV-8.

$$R_{+,vert} = -129.20 + 0.79R_{as-d} + 0.33t_{0,as-d} \quad \dots\dots\dots \text{Eq. IV- 8(a)}$$

$$R_{-,vert} = +360.08 + 1.84R_{as-d} - 0.39 t_{0,as-d} \quad \dots\dots\dots \text{Eq. IV- 8(b)}$$

$$R_{lat,vert} = -180.62 + 0.58R_{as-d} + 0.53t_{0,as-d} \quad \dots\dots\dots\text{Eq. IV- 8(c)}$$

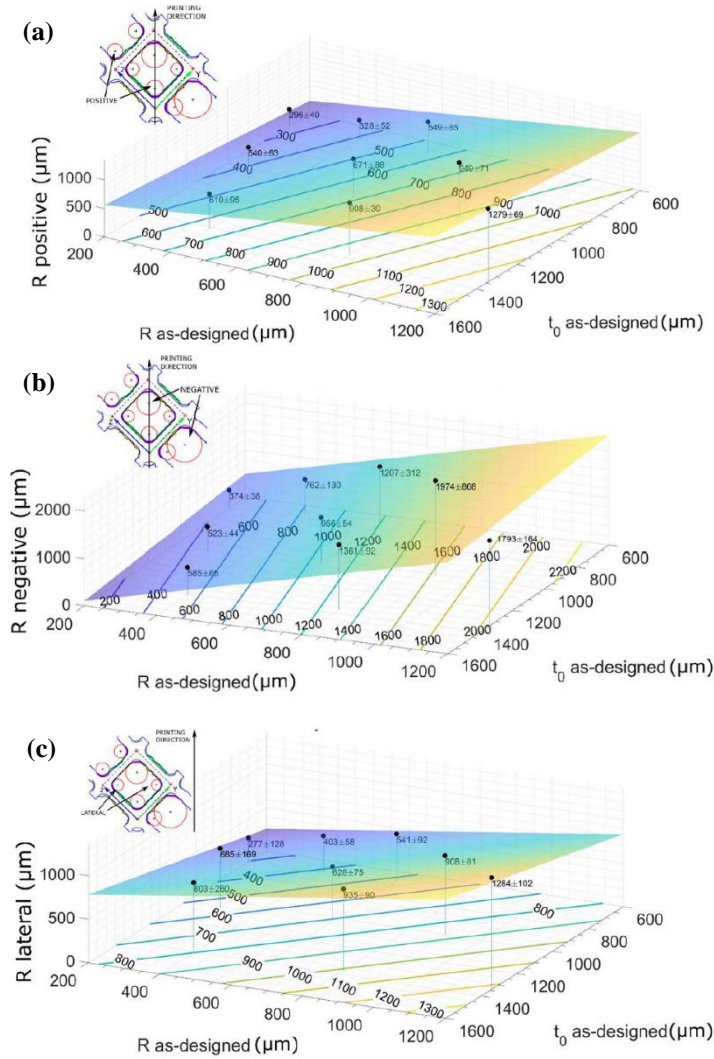


Figure IV - 26 Variation of as-built fillet radii with as-designed radii and thickness for fillets in the vertical plane of 45° specimens (a) Positive fillets (b) Negative fillets (c) Lateral fillets.

The positive and the negative fillets on the inclined plane are fitted as shown in Fig. IV-27. The fitting error is approximately 10% for these values. The as-built radius is affected by the as-designed radius more compared to the as-designed thickness as seen in the 0° specimens. The fitting equation for both the fillet radii are as given by Eqs.IV-9:

$$R_{+,vert} = +64.70 + 0.84R_{as-d} + 0.21t_{0,as-d} \quad \dots\dots\dots\text{Eq. IV- 9(a)}$$

$$R_{-,vert} = +59.81 + 0.74R_{as-d} + 0.18t_{0,as-d} \quad \dots\dots\dots\text{Eq. IV- 9(b)}$$

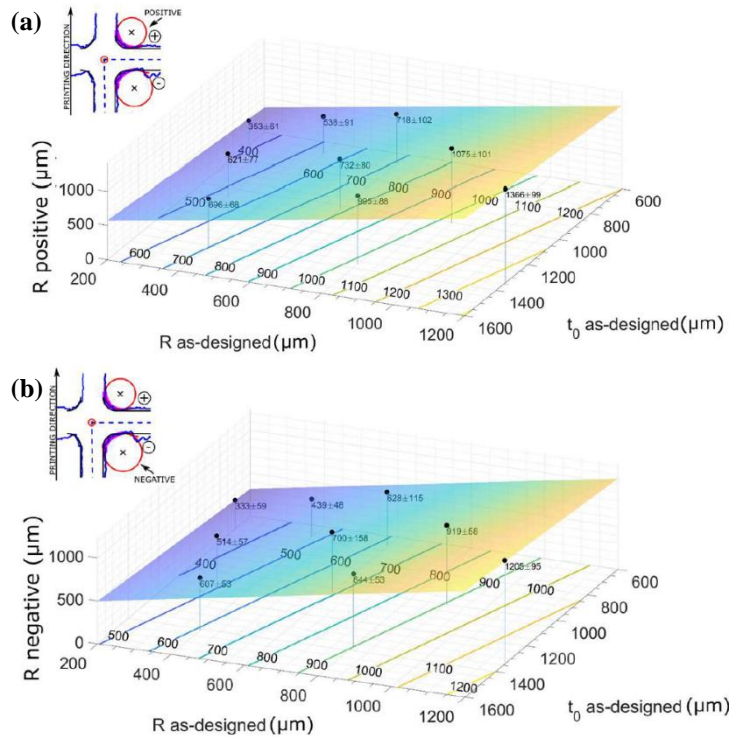


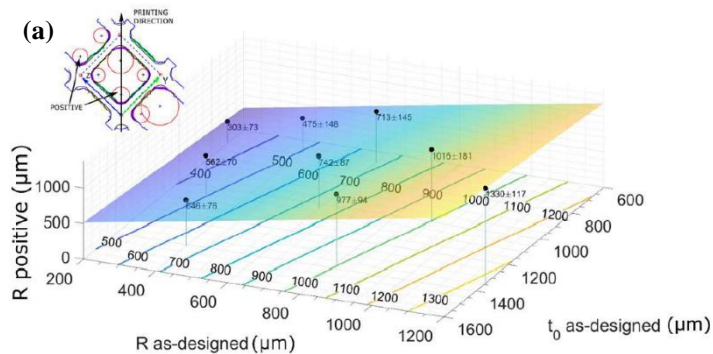
Figure IV - 27 Variation of as-built fillet radii with as-designed radii and thickness for fillets in the inclined plane of 45° specimens (a) Positive fillets (b) Negative fillets.

45°-35.26° specimen: The fitting between the as-built fillet radii and the as-designed parameter is similar to what was seen in the other two specimens (0° and 45°). The effect of as-designed fillet radius is prominent compared to the as-designed strut thickness as shown in Fig. IV-28. The fitting errors in this case is closer to 10%, the fitting equations are given by Eqs.IV-10 :

$$R_+ = +21.45 + 0.87R_{as-d} + 0.20t_{0,as-d} \quad \dots\dots\dots\text{Eq. IV- 10(a)}$$

$$R_- = +243.65 + 0.97R_{as-d} + 0.077t_{0,as-d} \quad \dots\dots\dots\text{Eq. IV- 10(b)}$$

$$R_{lat} = - 3.59 + 0.88R_{as-d} + 0.24t_{0,as-d} \quad \dots\dots\dots\text{Eq. IV- 10(c)}$$



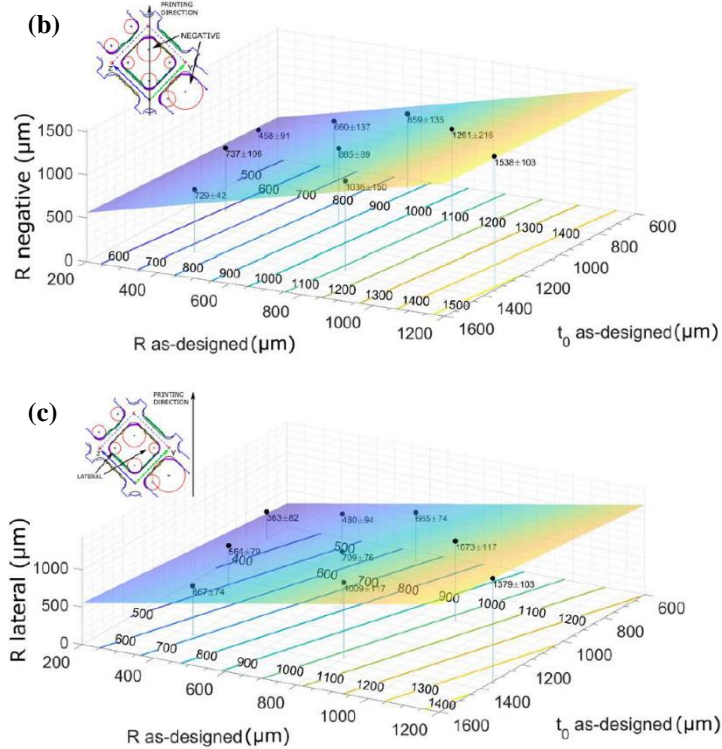
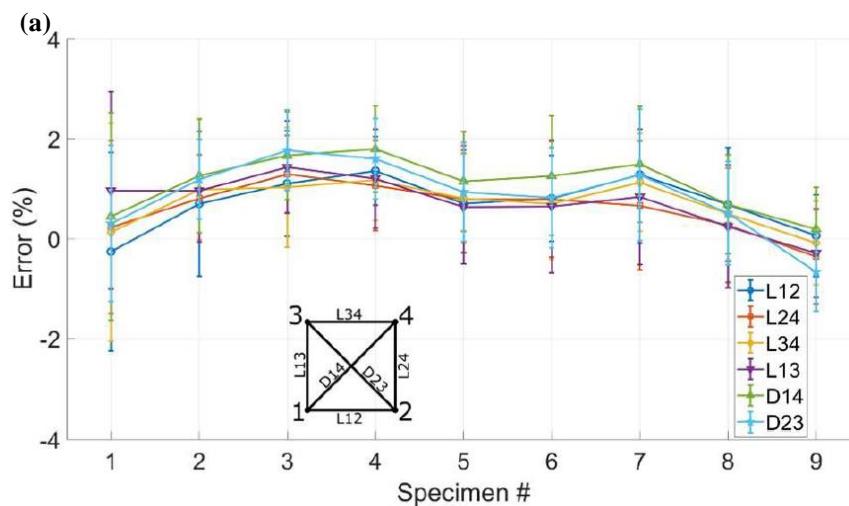


Figure IV - 28 Variation of as-built fillet radii with as-designed radii and thickness for 45° - 35.26° specimens (a) Positive fillets (b) Negative fillets (c) Lateral fillets.

#### 4.3.1.4. Distortion

The LPBF process has shown to increase the as-designed strut thickness and fillet radius values. But the effect of the process on the overall shape of the unit cell is not prominent. The percentage error in the unit cell dimension shown in Fig. IV-29 for all the three inclinations is between -0.5 % to +2%. The variation of this error is not dependent on the as-designed values since no trend is seen in the % error.



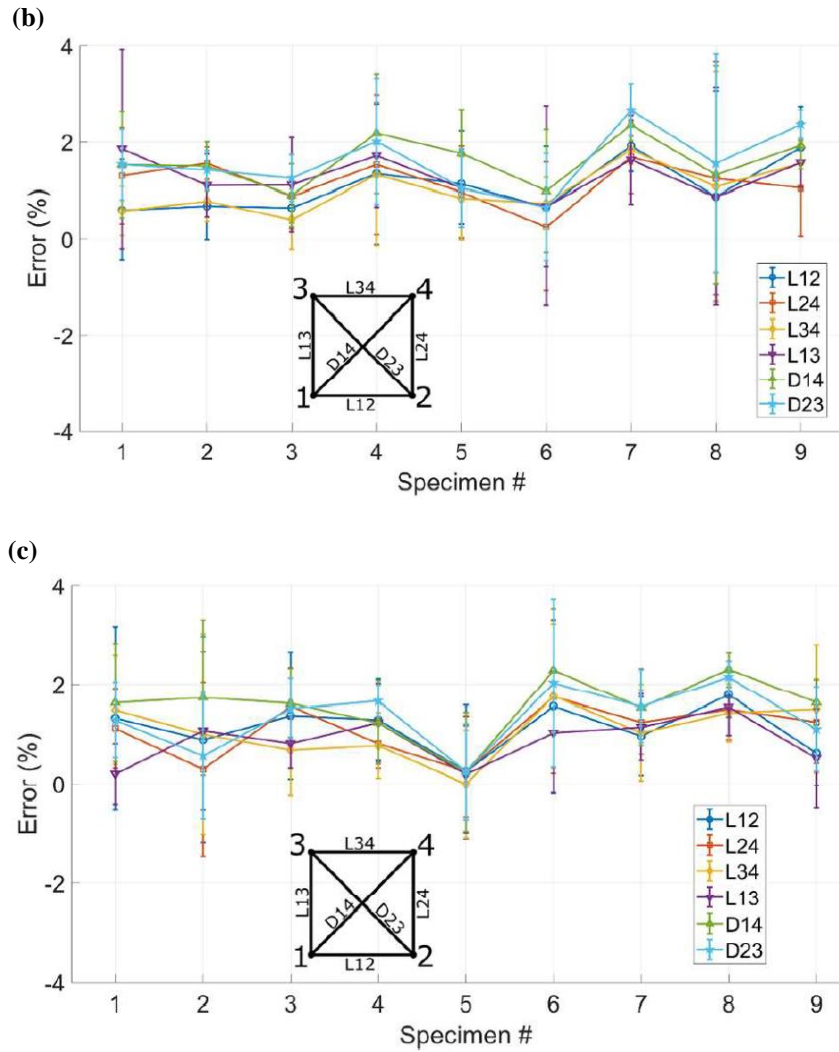


Figure IV - 29 Distortion of lattice in all the specimens (a) 0° Specimens (b) 45° specimens (c) 45 - 35.26° specimens.

#### 4.3.1.5. Compensation of geometrical parameters

The above sections discussed and provided the relationship between the as-designed and as-built parameters of strut thickness and fillet radii. The experimental measurement displayed that the strut thickness and fillet radii are larger than the designed values due to the LPBF process. We were able to deduce mathematical equations relating the designed CAD values and the measured values. Consequently, these equations can be altered or reversed to modify the geometrical values of input CAD to obtain the desired output. This process of changing the input CAD is known as compensation. To generate the compensated CAD models, one should first generate a relation between the as-designed and the as-built parameters by manufacturing and conducting measurements as shown in the previous sections. The mathematical functions from the first batch of specimens are used to generate the compensated CAD geometry for manufacturing next set of specimens. An example of the compensated CAD geometry and the expected is shown in Fig. IV-30.

The previous sections focused on the as-built strut thickness, excess material on the struts and the as-built fillet radius. Therefore, compensation formula can be obtained for all the three parameters from their respective equations.

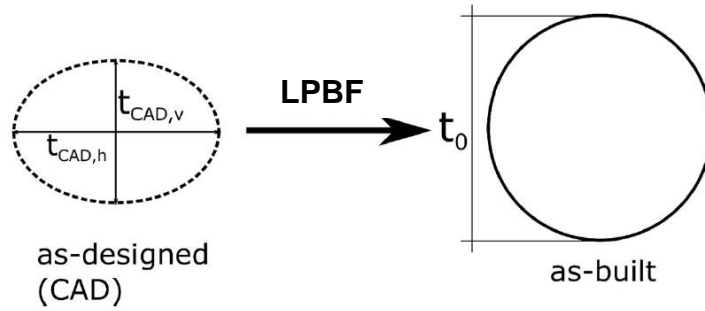


Figure IV - 30 Representation of compensated CAD model to obtain the nominal or desired geometry from LPBF process.

*Strut thickness:* The struts in all the specimens can be divided into 0°, 45°, and 90° based on the inclination. As shown previously, the struts parallel to the printing plane and inclined at 45° to the printing plane have an elliptical cross-section. Hence, the thickness must be compensated in using two parameters, along the major (vertical) and the minor axis (horizontal) of the ellipse. The struts perpendicular to the printing plane (90°) have a uniform circular cross-section. Therefore, one equation is sufficient to compensate the vertical strut thickness. Equations of the compensated thickness is obtained by reversing the equations Eqs.IV-11. The equations for the compensated thickness are as indicated below, where  $t_0$  is the desired thickness or the nominal thickness.

$$\text{Compensated thickness } t_{90^\circ} = \frac{t_0 + 17.29}{1.08} \quad \dots\dots\dots \text{Eq. IV- 11(a)}$$

$$\text{Compensated thickness } t_{45^\circ, v} = \frac{t_0 + 162.81}{0.98} \quad \dots\dots\dots \text{Eq. IV- 11(b)}$$

$$\text{Compensated thickness } t_{45^\circ, h} = \frac{t_0 + 58.32}{1.14} \quad \dots\dots\dots \text{Eq. IV- 11(c)}$$

$$\text{Compensated thickness } t_{0^\circ, v} = \frac{t_0 + 358.58}{0.93} \quad \dots\dots\dots \text{Eq. IV- 11(d)}$$

$$\text{Compensated thickness } t_{0^\circ, h} = \frac{t_0 + 163.31}{0.95} \quad \dots\dots\dots \text{Eq. IV- 11(e)}$$

The above compensated thickness values help in evaluating the extent to which the thickness of the CAD has to be altered. However, the position of this compensated cross-section with the strut axis is determined from the excess material analysis carried out previously. Fig. IV-31 represents the effect of excess material on a strut cross-section.

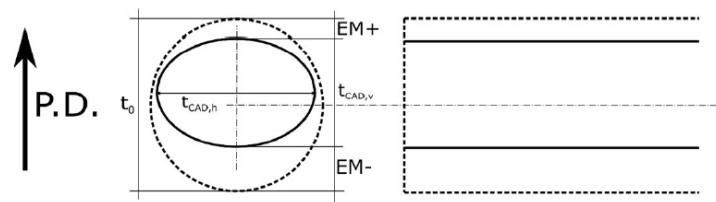


Figure IV - 31 Illustration of compensation principle in a strut with excess material.

In vertical struts, the excess material is distributed uniformly throughout the cross-section, therefore, the center of the compensated and the required geometry coincide. However, for inclined and horizontal struts, the excess material is present above and below (positive and negative). However, assuming symmetry between the axis, excess material in one direction is sufficient. Compensation using negative excess material is provided in the subsequent equation. The thickness of the excess material to be compensated is obtained by Eqs.IV-5(a), 5(d) and 6(a), same as mentioned in the below Eqs.IV-12:

$$EM_{90^\circ} = +0.040t_0^* - 8.64 \quad \dots\dots\dots\text{Eq. IV- 12(a)}$$

$$EM_{0^\circ} = -0.029t_0^* + 207.70 \quad \dots\dots\dots\text{Eq. IV- 12(b)}$$

$$EM_{45^\circ} = +0.017t_0^* + 48.66 \quad \dots\dots\dots\text{Eq. IV- 12(c)}$$

The  $t_0^*$  is the CAD thickness value to which the excess material will be attached due to the LPBF process. Once the compensated thickness value is determined, this compensated thickness is substituted in the place of  $t_0^*$ .

The as-built fillet radius and the as-designed geometrical parameters are fitted using a linear function as mentioned in the section 4.3.1.3. The function is in the form,  $R_{as-built} = aR_{as-d} + bt_{0,as-d} + c$ . The compensated fillet radius value can be obtained by altering the above equation to obtained Eq. IV-13:

$$R_{CAD} = \frac{R_{as-built} - bt_{0,CAD} - c}{a} \quad \dots\dots\dots\text{Eq. IV- 13}$$

Where  $R_{CAD}$  is the compensated fillet radius,  $R_{as-built}$  is the nominal or desired radius after manufacturing and  $t_{0,CAD}$  is the compensated strut thickness.

**4.3.1.6. Evaluation of compensation model**

The evaluate the compensation model, a new set of specimens were manufactured by maintaining the same process parameters used for the first batch of specimens. However, the number of specimens studied was reduced. Specimen #3, #6 and #9 were printed at  $0^\circ$  and  $45-35.26^\circ$  inclinations. The compensated CAD models used for LPBF process were generated by using compensated thickness and excess material, and by excluding the fillet radius compensation. The fillet radius compensation will be considered as a part of the future work.

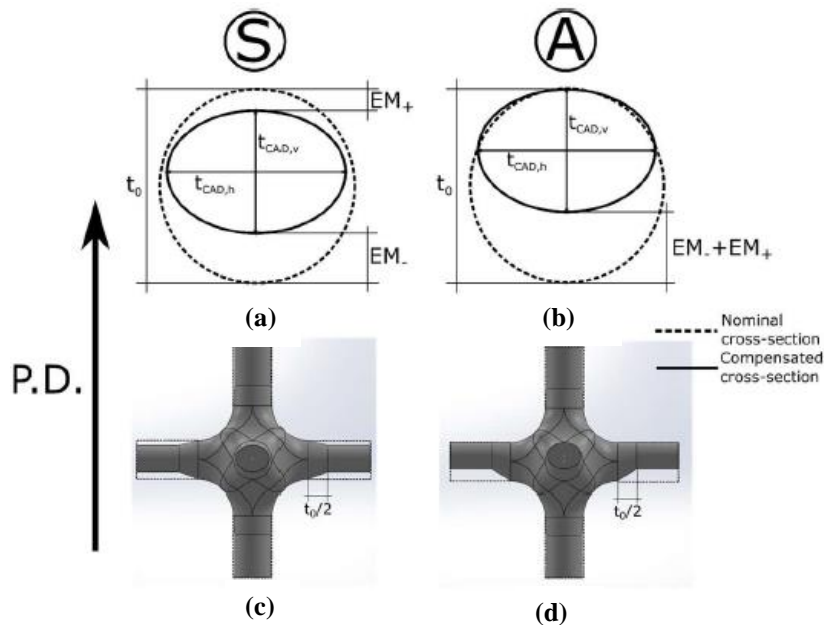


Figure IV - 32 Illustration of two compensation techniques on horizontal strut (a) Standard method with compensated and desired cross-section (b) Alternative method with compensated and desired cross-section (c) CAD model with standard compensation (d) CAD model with alternative compensation.

Two types of compensation modelling were employed, depending on the position of the excess material. Standard (S) and Alternative (A) as shown in Fig. IV-32. The standard compensation model considers excess material above and below the strut thickness. But the alternative compensation model

is simplified with excess material being considered only on the lower part of the strut. The difference between the compensation models is indicated in Fig. IV-32(a) and (b). The CAD models generated from standard and alternative methods are as shown in Fig. IV-32(c) and (d) respectively. The objective of this study is to understand the effect of positive excess material on the outcome from the LPBF process.

The nominal (desired geometry) and the compensated geometrical parameters are tabulated in Table IV-10 and Table IV-11 for 0° and 45° - 35.26° specimens respectively.

Table IV - 10 Nominal and compensated parameters for 0° specimens

| Specimen No | Nominal CAD values |                     |        | Compensated CAD parameters |                        |                        |                      |                      |
|-------------|--------------------|---------------------|--------|----------------------------|------------------------|------------------------|----------------------|----------------------|
|             | R (μm)             | t <sub>0</sub> (μm) | L (μm) | t <sub>90°</sub> (μm)      | t <sub>0°,v</sub> (μm) | t <sub>0°,h</sub> (μm) | EM <sub>0°</sub> (S) | EM <sub>0°</sub> (A) |
| 3           | 600                | 670                 | 4000   | 636                        | 335                    | 532                    | 198                  | 335                  |
| 6           | 900                | 1000                | 6000   | 942                        | 690                    | 879                    | 188                  | 310                  |
| 9           | 1200               | 1340                | 8000   | 1257                       | 1056                   | 1236                   | 177                  | 284                  |

Table IV - 11 Nominal and compensated parameters for 45° - 35.26° specimens

| Specimen No | Nominal CAD values |                     |        | Compensated CAD parameters |                         |                       |                       |
|-------------|--------------------|---------------------|--------|----------------------------|-------------------------|-----------------------|-----------------------|
|             | R (μm)             | t <sub>0</sub> (μm) | L (μm) | t <sub>45°,v</sub> (μm)    | t <sub>45°,h</sub> (μm) | EM <sub>45°</sub> (S) | EM <sub>45°</sub> (A) |
| 3           | 600                | 670                 | 4000   | 518                        | 640                     | 57                    | 152                   |
| 6           | 900                | 1000                | 6000   | 854                        | 930                     | 63                    | 146                   |
| 9           | 1200               | 1340                | 8000   | 1201                       | 1229                    | 69                    | 130                   |

The produced specimens were subjected to metrological analysis similar to the one carried out for the first batch. Images of the unit cell were captured and compared with the nominal CAD/desired CAD outline. Fig. IV-33 shows the overlap between the nominal CAD and the as-built unit cell for specimen #6 (0° orientation). Comparison indicates that satisfactory results were obtained from the compensation modelling. From Fig. IV-33(a) of the standard modelling, a small step was observed on the struts at the transition location between fillet and the strut, this effect was more pronounced in the case of thinner struts.

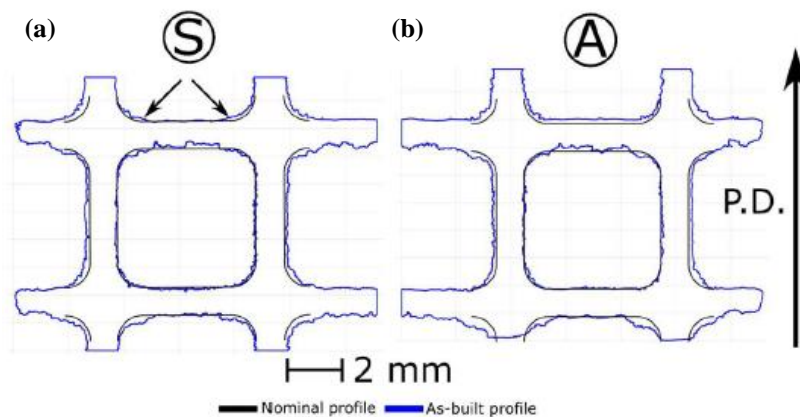
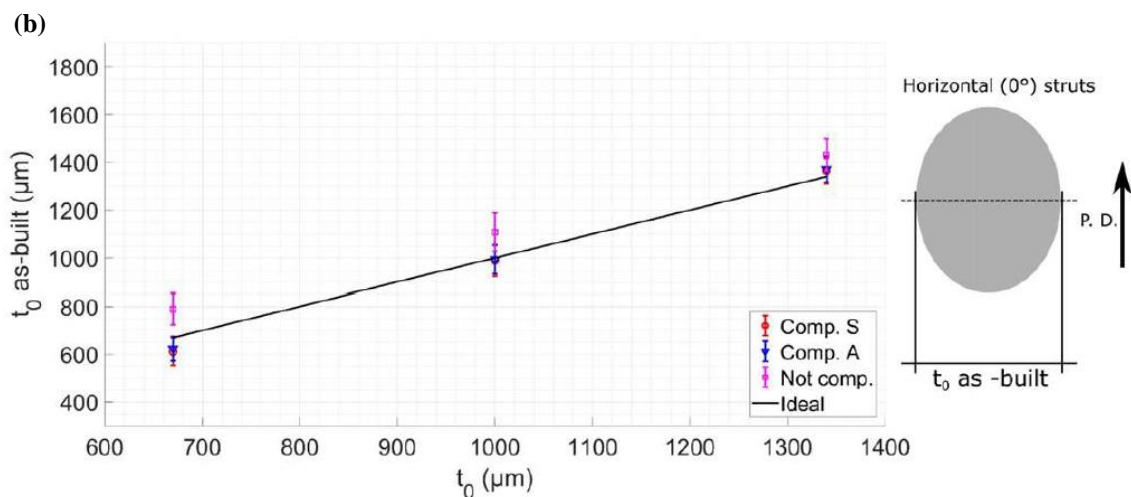
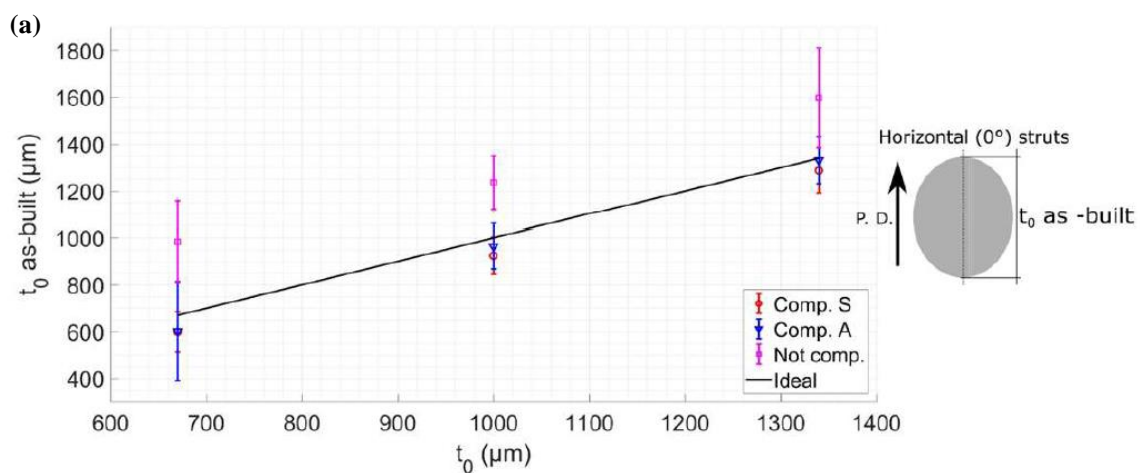


Figure IV - 33 Overlapping of desired unit cell and as-built geometry obtained from compensation model (a) Standard compensation (b) Alternative compensation.

The effect of the compensation models on the horizontal, vertical and inclined struts was obtained from comparing the as-built thickness values of compensated and non-compensated specimen with the as-designed values.

$0^\circ$  specimens: The comparison as-built and as-designed thickness for horizontal and vertical struts are provided in Fig. IV-34(a), (b) and Fig. IV-34(c) respectively. The results indicate that the compensation models showed beneficial effect on the horizontal struts printed parallel to the printing plane. Also, a circular cross-section was obtained with the compensated specimens when compared to the elliptical cross-section obtained from the non-compensated specimens. On the contrary, the compensation did not have any considerable effect on the thickness of the vertical struts. The amount of excess material was close to  $40\ \mu\text{m}$ , which is closer to the average particle size used in the LPBF process. However, the compensation procedure provides similar horizontal and vertical struts with uniform cross-section.



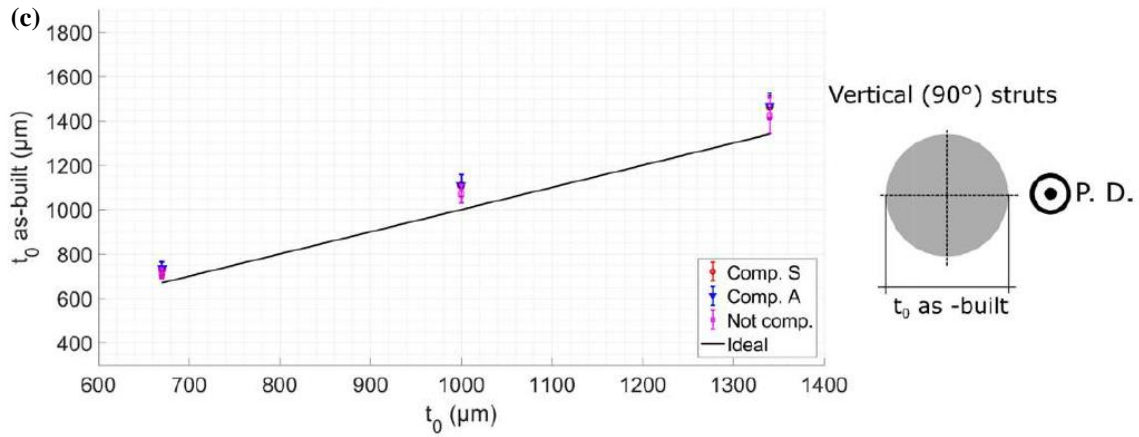


Figure IV - 34 As-built strut thickness of struts obtained from using compensated and uncompensated CAD models (a) Vertical axis of strut parallel to printing plane (b) Horizontal axis of strut parallel to printing plane (c) Strut perpendicular to printing plane. The solid line indicates perfect as-built thickness.

The positive effect of the compensation technique is evaluated by calculating the error % between the desired or nominal strut thickness and the as-built strut thickness by using the Eq. IV-14. Since both standard and alternative compensation methods worked effectively, the % error from the two methods has been averaged. The % error for uncompensated and compensated 0° specimens is given in Table IV-12. The compensation modelling drastically reduces the % error by almost 30% in some cases and the % error in all the directions is closer to or less than 10%.

$$error (\%) = \frac{|t_{0,as-built} - t_0|}{t_0} \times 100 \quad \dots\dots\dots Eq. IV- 14$$

Table IV - 12 Comparison of average error from uncompensated and compensated 0° specimens

| Specimen No | t <sub>0</sub> (μm) | Error             |                   |                   | Error            |                   |                   |
|-------------|---------------------|-------------------|-------------------|-------------------|------------------|-------------------|-------------------|
|             |                     | Uncompensated (%) |                   |                   | Compensated (%)  |                   |                   |
|             |                     | t <sub>90°</sub>  | t <sub>0°,v</sub> | t <sub>0°,h</sub> | t <sub>90°</sub> | t <sub>0°,v</sub> | t <sub>0°,h</sub> |
| 3           | 670                 | 6.59              | 46.78             | 17.74             | 9.85             | 10.16             | 6.95              |
| 6           | 1000                | 7.16              | 23.62             | 10.79             | 10.89            | 3.62              | 0.63              |
| 9           | 1340                | 6.21              | 19.32             | 6.81              | 9.45             | 0.66              | 2.28              |

45° - 35.26° specimen: In these specimens, since the complete or true thickness could not be obtained due to the inclination, the effective thickness value that can be measured is used for the evaluation. The variation of as-built thickness measured from the uncompensated and compensated specimens with the as-designed thickness as shown in Fig. IV-35. Also, the cross-section was closer to circular shape due to compensation. The % error considerably decreased for compensated specimens compared to uncompensated specimens as given in Table IV-13.

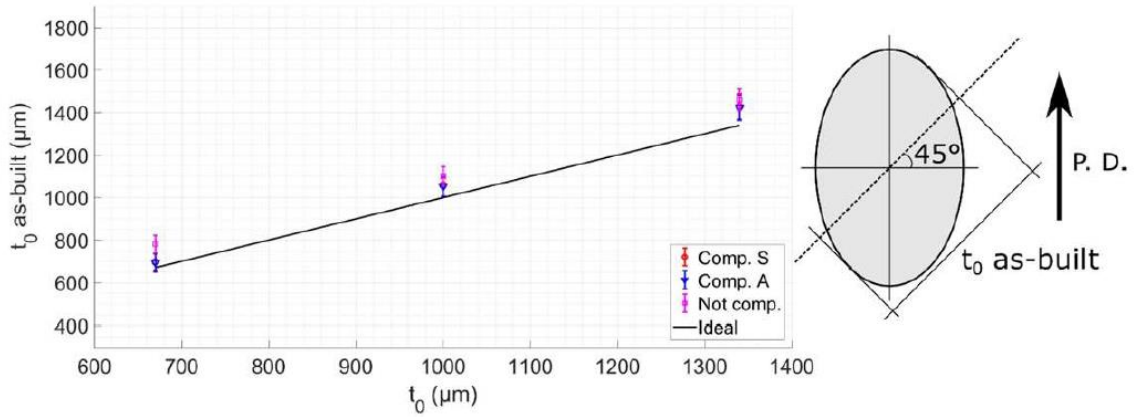


Figure IV - 35 As-built strut thickness of inclined struts obtained from using compensated and uncompensated CAD models.

Table IV - 13 Comparison of average error from uncompensated and compensated 45° -35.26° specimens

| Specimen No | $t_0$ ( $\mu\text{m}$ ) | Error (%)     |             |
|-------------|-------------------------|---------------|-------------|
|             |                         | Uncompensated | Compensated |
| 3           | 670                     | 16.56         | 3.73        |
| 6           | 1000                    | 10.05         | 5.51        |
| 9           | 1340                    | 9.00          | 6.36        |

### 4.3.2. Internal porosity analysis

The internal porosity analysis was carried out on the uncompensated specimens. Specimen #1, #2, #3, #6 and #6 were considered in 0° and 45° - 35.26° specimens. The specimens were polished along two vertical faces of 0° and two inclined faces of 45° - 35.26°. A polished face to reveal the porosity is shown in Fig. IV-36(a) and the output of the MATLAB code differentiating the porosity in different sections of the unit cell is shown in Fig. IV-36(b).

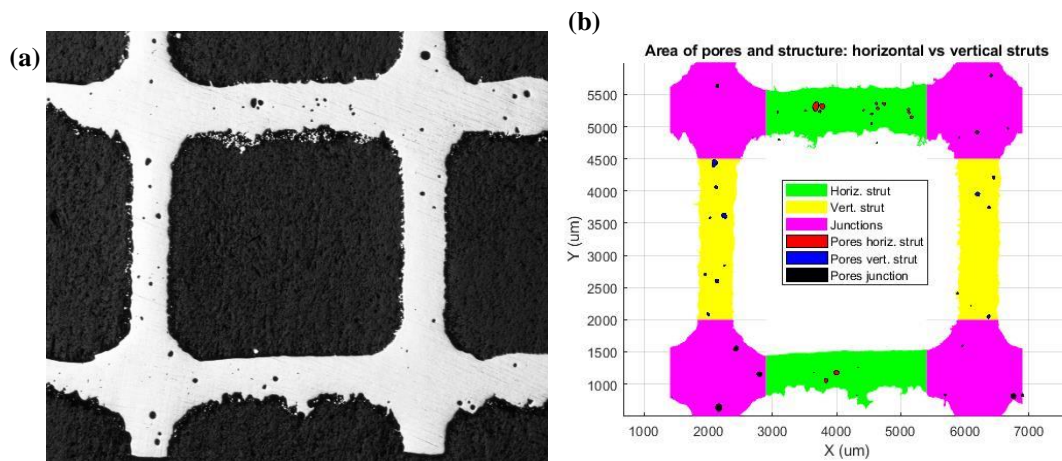


Figure IV - 36 Polished unit cell to reveal the internal porosity in the struts (b) classification of pores in the unit cell into junctions and struts using MATLAB code.

Table IV - 14 As-designed thickness of specimens used for internal porosity analysis

| Specimen No                         | 1   | 2   | 3   | 6    | 9    |
|-------------------------------------|-----|-----|-----|------|------|
| As-designed $t_0$ ( $\mu\text{m}$ ) | 700 | 680 | 670 | 1000 | 1340 |

The struts considered were grouped into horizontal and vertical for  $0^\circ$  specimens and inclined for  $45^\circ - 35.26^\circ$  specimens. Similarly, the junctions were grouped into  $0^\circ$  junctions and  $45^\circ - 35.26^\circ$  inclined junctions. The variation of porosity is plotted with respect to the specimen number for clear representation, since the thickness values of specimen #1, #2, #3 are very close. The as-designed strut thickness  $t_0$  is indicated in Table IV-14. The average porosity (Fig. IV-37(a)) of specimen#1, #2 and #3 overlap if the scatter is considered. The porosity tends to decrease with increase in the strut thickness (#6 and #9). The orientation has no considerable effect on the porosity for bigger specimens. The strut porosity and the junction porosity also show a similar behavior where, the porosity decreases with a considerable increase in strut thickness as shown in Fig. IV-37(b) and (c). The % of porosity is lower at the junctions when compared to the struts. The porosity in all the locations varied between a minimum value of 0.125% to 2.75% considering the scatter in the data.

The average pore diameter is obtained by assuming the pores to be circular in shape. The variation of pore diameter is shown in Fig. IV-37(d). No trend was seen in the pore diameter variation with the strut thickness. The average pore diameter in the considered specimens was between 25 – 80  $\mu\text{m}$ .

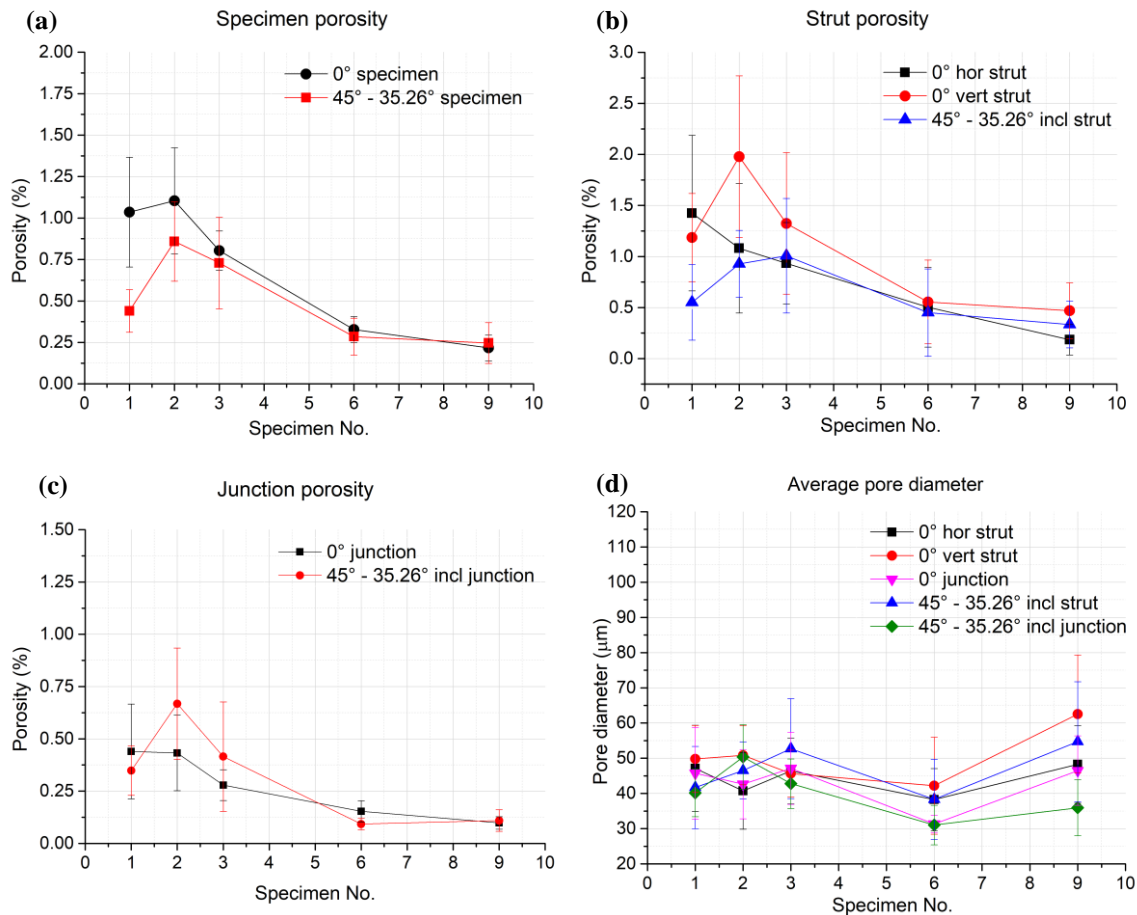


Figure IV - 37 Variation of (a) Porosity in specimen (b) Porosity in different struts (c) Porosity in junctions (d) Average pore diameter at different locations.

## 4.4.Mechanical test

The mechanical test of the specimens was carried out to understand the effect of compensation and the orientation with the printing plane on the fatigue properties. The specimens were different from the specimens used for geometrical analysis. The results from the metrological analysis, compression test and fatigue tests are discussed in the subsequent sections.

### 4.4.1. Metrological analysis

At present the metrological analysis has been carried out for the specimens, A, B, C, D and E. The results indicated that despite the compensation, horizontal struts had certain amount of irregularity compared to the vertical struts. The as-built strut thickness for different struts is illustrated in Fig. IV-38. The scatter in the 0° (horizontal struts) indicated the irregularity in the horizontal struts. The comparison between the as-built and the as-designed values indicate that the vertical struts were closer to the designed values in all the specimens. The average vertical thickness of 0° specimen was higher than the as-designed thickness, while the horizontal thickness is lower than the designed value. For specimen E, which was compensated and had the lowest strut thickness was reproduced well. Overall, the compensation strategy and increasing the size of the specimens compared leads to well produced specimen in terms of morphology.

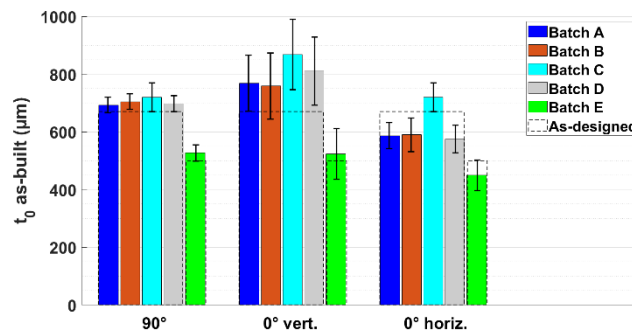


Figure IV - 38 As-built thickness values for specimens A-E compared with the as-designed thickness value.

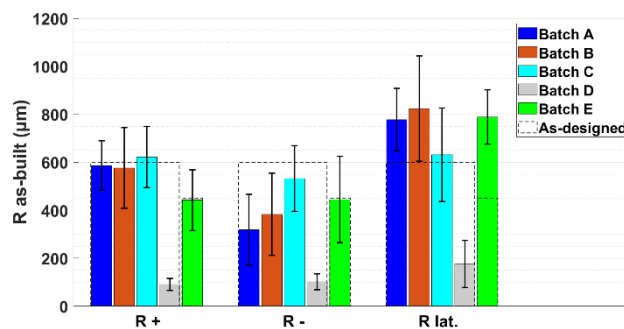


Figure IV - 39 As-built fillet radius for specimens A-E compared with the as-designed radius values

The fillets in the specimens are classified into positive, negative, and lateral as mentioned before. The variation in the as-built fillet radii for all the specimens is shown in Fig. IV-39. The positive fillets which are above the horizontal struts are closer to the as-designed values, while the negative fillets are sharper have a smaller radius compared to the designed values. Therefore, the negative fillets act as location for fatigue failure. As anticipated, the as-built fillet of specimen D is the sharpest with the lowest fillet value of  $\sim 100 \mu\text{m}$ .

The specimens B and C which were printed horizontally had slight overall curvature in the cellular region due to the unsupported printing process. This makes the specimens less stiff by introducing bending actions in the specimen when subjected to compression loads.

#### 4.4.2. Compression test

The specimens were designed to obtain a designed or nominal Young's modulus of 3 GPa. From the six specimens considered, the Young's modulus of specimen A and E are closer to the nominal value followed by specimen F as shown in Table. IV-15. On the contrary, the horizontally printed specimens B and C have the lowest modulus, this might be due to the curvature observed in the specimens due to the printing process which decreases the overall stiffness of the specimens. The specimen D printed with sharp fillets also have low modulus values.

The 0.2% offset and peak stress are obtained from the monotonic stress-strain curves (Fig.IV-40). The values were higher for specimen A and E which were printed vertically compared to specimen B which was printed horizontally and specimen D without fillets. The sharp fillets act as stress-concentration locations there by leading to early failure. However, specimen C, which was printed horizontally sustained higher loads similar to the specimens printed vertically. This maybe due to their high as-built strut thickness as shown in Fig. IV-38.

The exceptional behavior of specimen F is shown in Fig.VI-40. This is due to the higher strut thickness and the inclination in the printing direction with respect to the printing plane, which increases the peak stress, but the modulus is closer to the nominal elastic modulus value of 3GPa. However, the unit cell size did not have any considerable effect on the compression properties.

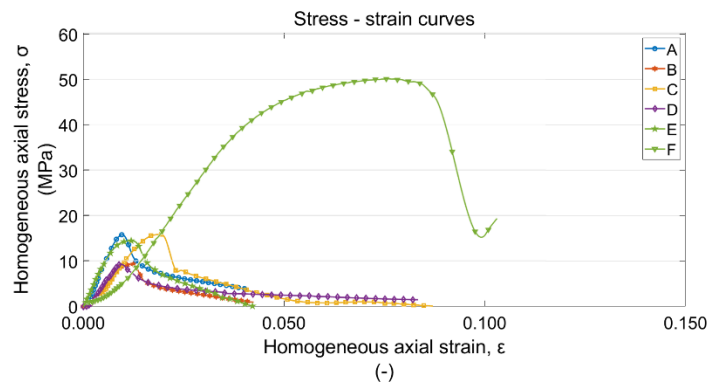


Figure IV - 40 Monotonic compressive stress-strain curves for all specimens

Table IV - 15 Mechanical properties from compression test (Young's modulus measured from loading - unloading curve)

|                                 | <b>A</b> | <b>B</b> | <b>C</b> | <b>D</b> | <b>E</b> | <b>F</b> |
|---------------------------------|----------|----------|----------|----------|----------|----------|
| <b>Young's modulus (MPa)</b>    | 3021     | 1749     | 1828     | 1844     | 2984     | 2552     |
| <b>0.2% offset stress (MPa)</b> | 16       | 9        | 14       | 9        | 14       | 42       |
| <b>Peak stress (MPa)</b>        | 16       | 9        | 16       | 9        | 15       | 50       |

#### 4.4.3. Fatigue test

The effect of fillet radius and printing direction on the fatigue properties is discussed in this section using absolute and normalized S-N curves provided in Fig.IV-41.

The effect of fillets is obtained from comparing the fatigue test results of specimen A (filleted junction) and specimen D (sharp junction). The S-N curves (Fig.IV-41(a)) indicate that the fatigue

strength of the specimen A is two times higher than the specimen D. The specimens A, D, and E had similar nominal properties except the unit cell and printed vertically. The horizontally printed specimens B and C had the significantly lower fatigue resistance compared to all the other specimens. This is because the struts that are subjected to loading are printed horizontally. Despite having filleted junctions, their performance is lower than the specimen D. Comparing, specimen B and C, better performance was seen for specimen C due to higher struts thickness compared to batch B as mentioned before. The highest fatigue strength was observed for specimen F due to their thickness struts (nominal thickness of 1300  $\mu\text{m}$ ) and inclined printing direction which yields better vertical struts than horizontal printing direction.

The S-N curves normalized with 0.2% offset stress shown in Fig.IV-41(b) clearly differentiate the effect of printing direction on the fatigue properties. A near overlap of the curves of specimens printed vertically (A, D and E) is at the top of the curve indicating a higher normalized fatigue strength, followed by specimen F with inclined printing, and at the bottom a clear overlap is seen for specimen B and C which were printed horizontally.

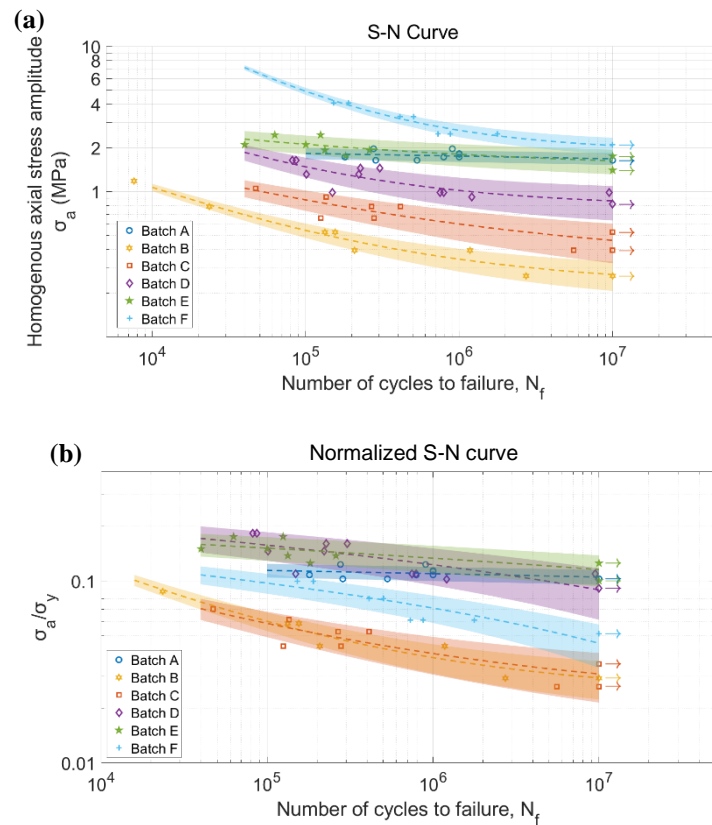


Figure IV - 41(a) Absolute S-N curve (b) Normalized S-N curve with 10% and 90% failure probability for all the specimens

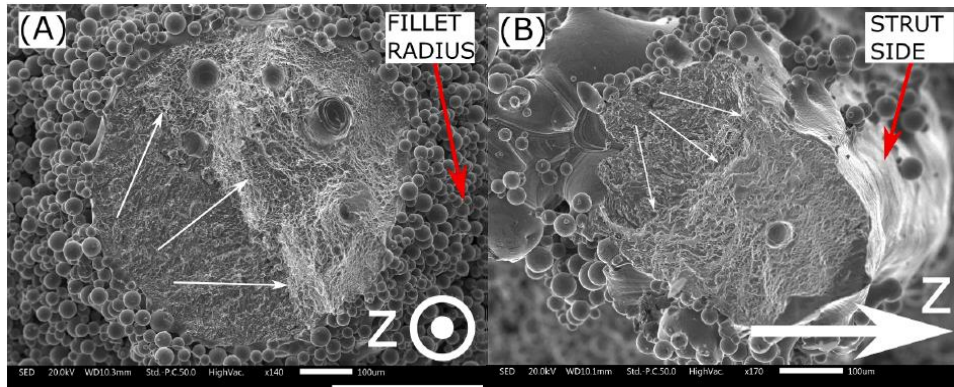


Figure IV - 42 Fatigue fracture surfaces of (a) Specimen A indicating failure closer to the junctions (b) Specimen B with failure at the middle of the struts

The failure in all the vertically printed specimens were closer to the junctions as shown in Fig.IV-42(a). Furthermore, it was observed that the junctions that experienced failure was always below the horizontal struts i.e., near the negative fillets. As mentioned before, the negative fillets had smaller diameter leads to sharper struts and stress concentrated locations. Also, the irregularity in the negative fillets was higher compared to positive fillets. Failure in similar locations was also observed for specimen F as well. However, in specimens printed horizontally, the fatigue failure occurs away from the junctions and closer to the center of the strut as shown in Fig.IV-42(b). This is because the loaded struts are printed horizontally and are irregular compared to the loaded struts of the vertically printed specimens.

#### 4.5. Section summary

This chapter dealt mainly with the geometrical deviation in regular cubic cellular specimens manufactured from LPBF process. Specimens with different struts thickness and fillet radius were considered for this study to obtain a relation between the as-designed and the as-built geometrical parameters. In the second part of the study, the effect of building direction and fillets on the fatigue properties is analyzed. Six different specimens were considered by varying the building direction, fillets and the compensation of strut thickness. The conclusion from the study is divided into two parts:

##### *Geometrical deviation:*

- The as-built strut thickness values are dependent on the as-designed thickness as well as the orientation of the strut with the printing plane. A linear relation between the as-designed and the as-built thickness is obtained.
- Vertical struts have a uniform circular cross-section, while elliptical cross-section is obtained for inclined and horizontal struts. The elliptical cross-section is due to uneven distribution of the excess material at the lower part of the strut.
- The LPBF successfully prints the fillet radius in the junctions. However, a deviation from the designed values is observed. The as-built fillet radius is dependent on both the as-designed radius and thickness. However, the former has more influence on the as-built radius. A linear relation is obtained between as-built radius, as-designed radius, and as-designed thickness. The location of the fillet also influences the fillet radius. Also, the high scatter in the data is due to excess material accumulation at some of the fillets.
- The designed geometrical parameters show minimum influence on the distortion of the unit cell, which randomly varied between -0.5% to +2%.

- The compensated CAD models obtained from the first batch which considers increased thickness, fillet radius and excess material was used as input for the second batch. This yielded specimens with better geometrical accuracy with the as-designed parameters. The % of error between as-built and as-designed geometry was less than 10% for compensated specimens and was between 20 – 40% for uncompensated specimen.

*Mechanical test:*

- The building direction of the specimens highly influences the mechanical performance under static as well as fatigue loading. Specimens with load bearing struts printed vertically had good compression and fatigue resistance. Also, the strut was weakest closer to the junctions, hence fatigue crack propagated closer to the junctions.
- The specimens printed horizontally had the lowest mechanical properties due to the irregular load bearing struts. Also, the struts were the weakest location in the specimen, where the fatigue failure was observed.
- Specimen F, with all the struts inclined to the printed direction and the loading direction had the highest peak stress and fatigue strength compared to specimens printed vertically. This is due to the higher designed strut thickness, reduced strut irregularity due to the inclined printing process, and inclination of struts with the loading direction.
- The S-N curve indicates that the fillet radius improves the fatigue strength of the specimen by reducing the stress concentration at the junctions.
- The normalized S-N curves shows the extent to which the printing direction influences the fatigue properties. Vertically printed struts had best fatigue performance followed by specimens printed with an inclination and the least fatigue resistance was seen in specimens printed horizontally.
- The normalized S-N curve of the specimen F indicated that printing the struts with an inclination to the building plane and the loading directions has a positive effect on the fatigue performance.

## 4.6. References

1. Dallago M, Winiarski B, Zanini F, et al (2019) On the effect of geometrical imperfections and defects on the fatigue strength of cellular lattice structures additively manufactured via Selective Laser Melting. *Int J Fatigue* 124:348–360. <https://doi.org/10.1016/j.ijfatigue.2019.03.019>
2. Mullen L, Stamp RC, Fox P, et al (2010) Selective laser melting: A unit cell approach for the manufacture of porous, titanium, bone in-growth constructs, suitable for orthopedic applications. II. Randomized structures. *J Biomed Mater Res Part B Appl Biomater* 92B:178–188. <https://doi.org/10.1002/jbm.b.31504>
3. Sing SL, Wiria FE, Yeong WY (2018) Selective laser melting of lattice structures: A statistical approach to manufacturability and mechanical behavior. *Robot Comput Integr Manuf* 49:170–180. <https://doi.org/10.1016/j.rcim.2017.06.006>
4. Qiu C, Yue S, Adkins NJE, et al (2015) Influence of processing conditions on strut structure and compressive properties of cellular lattice structures fabricated by selective laser melting. *Mater Sci Eng A* 628:188–197. <https://doi.org/10.1016/j.msea.2015.01.031>
5. Kessler J, Balc N, Gebhardt A, Abbas K (2017) Basic design rules of unit cells for additive manufactured lattice structures. *MATEC Web Conf* 137:. <https://doi.org/10.1051/mateconf/201713702005>
6. Yan C, Hao L, Hussein A, et al (2014) Advanced lightweight 316L stainless steel cellular lattice structures fabricated via selective laser melting. *Mater Des* 55:533–541.

<https://doi.org/10.1016/j.matdes.2013.10.027>

7. Pyka G, Kerckhofs G, Papantoniou I, et al (2013) Surface Roughness and Morphology Customization of Additive Manufactured Open Porous Ti6Al4V Structures. *Materials (Basel)* 6:4737–4757. <https://doi.org/10.3390/ma6104737>
8. Van Bael S, Kerckhofs G, Moesen M, et al (2011) Micro-CT-based improvement of geometrical and mechanical controllability of selective laser melted Ti6Al4V porous structures. *Mater Sci Eng A* 528:7423–7431. <https://doi.org/10.1016/j.msea.2011.06.045>
9. du Plessis A, Razavi SMJ, Berto F (2020) The effects of microporosity in struts of gyroid lattice structures produced by laser powder bed fusion. *Mater Des* 194:108899. <https://doi.org/10.1016/j.matdes.2020.108899>
10. Lohmuller P, Favre J, Piotrowski B, et al (2018) Stress Concentration and Mechanical Strength of Cubic Lattice Architectures. *Materials (Basel)* 11:1146. <https://doi.org/10.3390/ma11071146>
11. Boniotti L, Beretta S, Patriarca L, et al (2019) Experimental and numerical investigation on compressive fatigue strength of lattice structures of AlSi7Mg manufactured by SLM. *Int J Fatigue* 128:105181. <https://doi.org/10.1016/j.ijfatigue.2019.06.041>
12. Benedetti M, Fontanari V, Bandini M, et al (2018) Low- and high-cycle fatigue resistance of Ti-6Al-4V ELI additively manufactured via selective laser melting: Mean stress and defect sensitivity. *Int J Fatigue* 107:96–109. <https://doi.org/10.1016/j.ijfatigue.2017.10.021>
13. Niinomi M, Boehlert CJ (2015) Titanium alloys for biomedical applications. *Springer Ser Biomater Sci Eng* 3:179–213. [https://doi.org/10.1007/978-3-662-46836-4\\_8](https://doi.org/10.1007/978-3-662-46836-4_8)
14. Benedetti M, Santus C (2019) Notch fatigue and crack growth resistance of Ti-6Al-4V ELI additively manufactured via selective laser melting: A critical distance approach to defect sensitivity. *Int J Fatigue* 121:281–292. <https://doi.org/10.1016/j.ijfatigue.2018.12.020>

---

## Conclusion and future scope

---

### Conclusion

This work focused on investigating the mechanical properties and geometrical accuracy of Ti6Al4V cellular materials, manufactured using the LPBF process. The first part of the study focused on the mechanical characterization of different types of cell topologies for biomedical applications such as porous implants and or porous coatings. The aim was to examine if the properties of these cellular materials were closer to the properties of the human bone with stiffness between 0.3 – 20 GPa. The lesser explored tensile testing of cellular material had been performed on these specimens, to see if they qualify as a reliable testing procedure. The deviation of the mechanical properties of cellular materials from the designed values due to the LPBF process has been studied. The second part of the work involved the development of the mathematical relationship between the as-designed and the as-built parameters to reduce the geometrical deviation in the specimens manufactured subsequently. The effect of printing direction, fillets at the junction, and strut thickness on the geometrical and mechanical response have been explored. Taking all the things into consideration, some of the conclusion that can be drawn from the study are mentioned below:

- The porosity of the specimens tends to decrease and deviate from the designed values due to the LPBF process, thereby increasing the strength and stiffness of the specimen. The porosity of the specimen has a great influence on the mechanical properties of the cellular specimens. Also, the effect of cell topology on the mechanical properties is predominant in the case of high porosity specimens when compared to the low porosity specimens.
- The tensile testing of cellular materials yields satisfactory results and can be used in the place of a compression test. The stiffness measured in the loading cycles and the unloading cycle is closer to each other. While the stiffness of the specimen measured in the unloading cycle of compression tests is considerably higher than the values from the first loading cycle or from the slope of the monotonic stress-strain curve. The inclination in the compression test specimens led to a decreased stiffness as compared to the tensile test results.
- The analysis of the as-designed configuration indicated that the irregularity in the specimens introduces bending-dominated behavior in cubic irregular and trabecular specimens compared to cubic regular specimens. This is further confirmed by the Gibson-Ashby parameters from the curve fitting. The FE analysis also displayed the influence of strut defects and strut cross-section on the mechanical properties. The comparison of the as-designed and the as-built Young's modulus yielded a considerable linear relationship between the values, based on the pore size and the cell topology considered.
- The comparison of the mechanical properties of the cubic, star, and cross-based specimens in regular and irregular configurations showed that the irregularity has a stronger influence on the stretching-dominated specimens but has a negligible effect on the bending-dominated specimens. Also, the presence of oblique struts in the cell topology reduces the stretching-dominated behavior despite the presence of struts along the loading direction. The effect of irregularity on the fatigue behavior is clearly obtained from the normalized S-N curves that form a band at the lower part of the curve. Star-based specimens displayed properties exactly in between the stretching-dominated cubic regular and bending-dominated cross-based specimens.
- The trabecular specimens considered in the study display excellent static and fatigue properties. The random distribution of the struts leads to a quasi-isotropic behavior, which good load-bearing capacity with good compliance to compression loading. The random distribution of

struts also retards crack growth under fatigue loading thereby making them suitable for application in implants.

- If the development of a porous spinal cage is considered, the outer lining of the spinal cage can be composed of star-regular cellular materials with vertical struts and the inner layer can be composed of bending dominated irregular structures. The top and the bottom surface can be coated with trabecular cellular material to induce quick and effective osseointegration due to their bone like morphology. Similarly, for total disc arthroplasty, the surfaces that can encounter the bone tissue can be coated with trabecular specimen while the edges and the load bearing part can be a graded combination of regular star and cross based cellular material.
- The in-depth geometrical analysis of cubic regular cells helped in establishing a mathematical model to obtain desired geometry by altering the input CAD. The as-built strut thickness is dependent on the as-designed thickness values, but the as-fillet radius is influenced by the as-designed thickness and fillet radius. Furthermore, the geometrical values are dependent on the inclination of the struts and fillets with the printing direction.
- The main parameters that must be considered while developing the compensation models are designed strut thickness and the inclination of struts with the building direction. The developed mathematical models have been effectively used to generate compensated models which reduce the % error between the as-designed and as-built geometry to less than 10%, by maintaining the same process parameters. However, the manufacturing parameters also has an influence on the manufactured specimen.
- The introduction of defined smooth fillets in cellular specimens positively influences the fatigue performance of cellular materials by reducing the stress concentration at the junctions or nodes. Also, printing the load-bearing struts along the printing direction or with an inclination to the printing direction yield better results compared to printing them perpendicular to the printing direction.

## Future scope

With the current availability of additive manufacturing techniques such as the LPBF process and the requirements of the biomedical industry, there is scope for carrying out more research based on the outcome of this study. The points mentioned below indicate give a broad idea about the same:

- Development of empirical relationship between the as-designed and the as-built mechanical properties for different types of irregular and regular cellular materials to create a database. This study can be further enhanced by taking into consideration a combination of process parameters.
- A better understanding of failure initiation at the nodes of cellular material by considering the recent advancements in the notch mechanics and the effect of multi-axial loading on the local failure at the nodes.
- Explore the lesser-studied shear behavior of cellular materials by creating a standard and optimized specimen design. Testing under shear should be given importance since implants experience shear loading based on the location of the implant.
- Successfully design and analyze a completely porous spinal cages and vertebral implant to reduce stress shielding and promote bone ingrowth. One or more types of cellular materials discussed in the work can be used to develop these implants.
- Comparison of the morphological analysis model with the morphological analysis using  $\mu$ CT technique can be used to establish and improve the accuracy of the method employed in this study. Furthermore, optimization of process parameters combined with the CAD compensation strategy can be used to improve the outcome of the LPBF process, especially for high porosity cellular materials with different topologies.

---

## Scientific publications

---

### Journal publications

Raghavendra S, Molinari A, Fontanari V, Dallago M, Luchin V, Zappini G, Benedetti M. Effect of strut cross section and strut defect on tensile properties of cubic cellular structure. *Mater Des Process Commun.* 2020;2: 1–6.

Raghavendra S, Molinari A, Fontanari V, Dallago M, Luchin V, Zappini G, Benedetti M. Tension-compression asymmetric mechanical behaviour of lattice cellular structures produced by selective laser melting. *Proc Inst Mech Eng Part C J Mech Eng Sci.* 2020;234: 3241–3256.

Raghavendra S, Molinari A, Dallago M, Zappini G, Zanini F, Carmignato S, Benedetti M. Uniaxial static mechanical properties of regular, irregular and random additively manufactured cellular materials: Nominal vs. real geometry. *Forces Mech.* 2021;2: 100007.

Raghavendra S, Molinari A, Cao A, Gao C, Berto F, Zappini G, Benedetti M. Quasi – Static Compression and Compression – Compression Fatigue Behavior of Regular and Irregular Cellular Biomaterials. *Fatigue Fract Eng Mater Struct.* (under publication)

Dallago M, Raghavendra S, Luchin V, Zappini G, Pasini D, Benedetti M. The role of node fillet, unit-cell size and strut orientation on the fatigue strength of Ti-6Al-4V lattice materials additively manufactured via laser powder bed fusion. *Int J Fatigue.* 2021;142: 105946.

Dallago M, Raghavendra S, Fontanari V, Benedetti M. Stress concentration factors for planar square cell lattices with filleted junctions. *Mater Des Process Commun.* 2019: 1–8.

Benedetti M, Berto F, Marini M, Raghavendra S, Fontanari V. Incorporating residual stresses into a Strain-Energy-Density based fatigue criterion and its application to the assessment of the medium-to-very-high-cycle fatigue strength of shot-peened parts. *Int J Fatigue.* 2020;139: 105728.

### Peer-reviewed conference publications

Raghavendra S, Molinari A, Fontanari V, Luchin V, Zappini G, Benedetti M, Johansson F, Klarin J. Tensile and compression properties of variously arranged porous Ti-6Al-4V additively manufactured structures via SLM. *Procedia Struct Integr.* 2018;13: 149–154.

Raghavendra S, Molinari A, Fontanari V, Luchin V, Zappini G, Benedetti M. Effect of Porosity and Cell Topology on Elastic-Plastic Behavior of Cellular Structures. *Procedia Struct Integr.* 2019;18: 93–100.

Raghavendra S, Molinari A, Fontanari V, Zappini G, Benedetti M. Evaluation of Static and Fatigue Properties of Regular Lattice and Trabecular Cellular Structures. *Procedia Struct Integr.* 2020;28: 517–524.

Dallago M, Raghavendra S, Luchin V, Zappini G, Pasini D, Benedetti M. Geometric assessment of lattice materials built via Selective Laser Melting. In: *Materials Today: Proceedings.* Vol 7. Elsevier Ltd; 2019:353–361.

---

## Conferences, summer schools and workshops attended

---

### Conferences

22<sup>nd</sup> European Conference on Fracture, Belgrade, Serbia. August 26 – 31, 2018.

Oral presentation: “ Tensile and compression properties of variously arranged porous Ti-6Al-4V additively manufactured structures via SLM”

25<sup>th</sup> International Conference on Fracture and Structural Integrity, Catania, Italy . June 12 – 14, 2019.

Oral presentation: “Effect of porosity and cell topology on elastic-plastic behavior of cellular structures”

1<sup>st</sup> Virtual European Conference on Fracture – 2020.

Oral presentation: “Evaluation of static and fatigue properties of regular lattice and trabecular cellular structures”

### Summer schools

TOPSTARS Summer School, EIT Raw material, Trento, Italy.

Fracture Mechanics Summer School, Catania, Italy. June 9 – 11, 2019.

### Workshops

Additive Manufacturing Workshop at ProM facility , Rovereto, Italy

ECOPADS Workshop, Riva del Garda, Italy



```

!!!!!!!!!!!!!!!!!!!!!!!!!!!!!!!!!!!!!!!!!!!!!!!!!!!!!!!!!!!!!!
FINISH
!!!!!!!!!!!!!!!!!!!!!!!!!!!! RESULTS !!!!!!!!!!!!!!!!!!!!!!!!!!!!!
/POST1
SET, 1, 1

/DIRECTORY, file_exist, EL_MODULUS_RESULTS, txt
*get,numfiles3,parm,file_exist,dim,3
*IF, numfiles3, EQ, 0, THEN
    *CFOPEN,EL_MODULUS_RESULTS,TXT,.,APPEND
    *VWRITE,
        FILE NAME      Number of element   E22 [MPa]
    *CFCLOS
*ENDIF
! Evaluation of properties

CSYS,12
DSYS,12
RSYS,12

! calculation of reaction
NSEL, S, LOC, Y, - eps, + eps
force,static
fsum,,all
*get,react_Y,fsum,0,item,fy
ALLSEL,ALL

NSEL, S, LOC, X, - eps, + eps
force,static
fsum,,all
*get,react_X_sx,fsum,0,item,fx
ALLSEL,ALL

NSEL, S, LOC, Z, - eps, + eps
force,static
fsum,,all
*get,react_Z_d,fsum,0,item,fz
ALLSEL,ALL

NSEL, S, LOC, X, + lato_X - eps, + lato_X + eps
*GET,n_mx_dx,node,,num,max
*DIM,nmask_dx,array,n_mx_dx
*VGET,nmask_dx(1),node,1,nsel
*DIM,disp_dx_v,array,n_mx_dx
*VMASK,nmask_dx(1)
*VGET, disp_dx_v, NODE, 1, U, X, , , 0
ALLSEL, ALL
*VMASK,nmask_dx(1)
*VSCFUN, disp_X, MEAN, disp_dx_v(1)

NSEL, S, LOC, Z, + lato_Z - eps, + lato_Z + eps
*GET,n_mx_av,node,,num,max
*DIM,nmask_av,array,n_mx_av
*VGET,nmask_av(1),node,1,nsel
*DIM,disp_av_v,array,n_mx_av
*VMASK,nmask_av(1)

```

```

*VGET, disp_av_v, NODE, 1, U, Z, , , 0
ALLSEL, ALL
*VMASK,nmask_av(1)
*VSCFUN, disp_Z, MEAN, disp_av_v(1)

eps_1 = disp_X/lato_X
eps_2 = def/lato_Y
eps_3 = disp_Z/lato_Z
sig_1 = react_X_sx/(lato_Y*lato_Z)
sig_2 = react_Y/(lato_X*lato_Z)
sig_3 = react_Z_d/(lato_X*lato_Y)

! Components of the compliance matrix
C12 = eps_1/sig_2
C22 = eps_2/sig_2
C32 = eps_3/sig_2

*CFOPEN,COMP_MAT_cella_%struttura%,TXT,,APPEND
*VWRITE,
(15x,'C12',15x,'C22',15x,'C32')
*VWRITE, C12, C22, C32
(3F18.8)
*CFCLOSE
*CFOPEN,COMP_RIEPILOGO_cella_%struttura%,TXT,,APPEND
*VWRITE,
('Carico lungo direzione 2 (Y)')
*VWRITE,
(15x,'eps_X',15x,'eps_Y',15x,'eps_Z')
*VWRITE, eps_1, eps_2, eps_3
(3F18.8)
*VWRITE,
(15x,'sig_X',15x,'sig_Y',15x,'sig_Z')
*VWRITE, sig_1, sig_2, sig_3
(3F18.8)
*VWRITE, 1/C22
(/,'E22 = ',F18.8,' MPa')
*CFCLOSE
*CFOPEN,EL_MODULUS_RESULTS,TXT,,APPEND
*VWRITE, struttura,num_el, 1/C22
%30c %18.8F %18.8F
*CFCLOSE

```

## Ansys code for elastic plastic analysis

```

!INPUT:
!* material property
!* geometry parameters (length = lato)
!* make sure the local coordinate systems specified are correct
FINISH
/CLEAR,START
!!!!!!!!!!!!!!!!!!!! PARAMETRI DA IMPOSTARE !!!!!!!!!!!!!!!!!!!!!
M_Y = 110e3          ! Elastic modulus
M_P = 0.34          ! Poisson ratio
struttura = 'File name'

```

```

file_name = 'FE file name'
file_ext = 'dat'
dir      = 'file location'
lato_X = 11
lato_Y = 14.37
lato_Z = 11
pi      = 3.14159

!pos_X_0 = 0
!pos_Y_0 = 0
!pos_Z_0 = 0
lato     = lato_Y
def_max = 0.075*lato_Y  ! Global displacement (delta/solid length)
! parametri prova di trazione
LOAD_STEPS = 20
eps = 5E-8             ! depends on the top and bottom surface of the FE model
!!!!!!!!!!!!!!!!!!!! MODEL GENERATION !!!!!!!!!!!!!!!!!!!!!
/PREP7
/INPUT, file_name,file_ext, dir, , 0
/PREP7
MP, EX, 1, M_Y
MP, NUXY, 1, M_P
!Material data file to be imported
/INQUIRE, data_pts, LINES, Materialdata_dec2018_final2_shifted, txt
data_pts = data_pts - 1
*DIM, data_tab, ARRAY, data_pts, 2
*DIM, TABLE1, TABLE, data_pts, 2, 1
*TREAD, TABLE1(0, 0), Materialdata_dec2018_final2_shifted, txt
*MFUN, data_tab(1,1), COPY, TABLE1(1, 1)

TB, PLASTIC, 1, , , MISO
TBTEMP, 0
*DO, ii, 1, data_pts, 1
  TBPT, DEFI, data_tab(ii, 1), data_tab(ii, 2)
*ENDDO
*GET, num_el, ELEM, 0, COUNT

!Local co-ordinate system, Here Number 12 is assigned to local co-ordinate
CSYS, 12
! Loading conditions
NSEL, S, LOC, Y, - eps, + eps
D, ALL, ALL, 0
ALLSEL, ALL
NSEL, S, LOC, Y, + lato_Y - eps, + lato_Y + eps
D, ALL, UX, 0
D, ALL, UZ, 0
ALLSEL, ALL

!Deformation in steps

*DIM, def, ARRAY, LOAD_STEPS, 1
*VLEN, LOAD_STEPS
*VFILL, def, RAMP, 0, def_max/(LOAD_STEPS - 1)

*DO, NN, 1, LOAD_STEPS, 1
  NSEL, S, LOC, Y, + lato_Y - eps, + lato_Y + eps

```

```

D, ALL, UY, def(NN)
ALLSEL, ALL
ANTYPE,0           ! Static analysis
NLGEOM,ON         ! Nonlinear geometry on
NSUBST,20,1000,1  ! 20 load steps
OUTRES,ALL,ALL    ! Output data for all load steps
AUTOTS,ON         ! Auto time-search on
LNSRCH,ON         ! Line search on
NEQIT,1000        ! 1000 iteration maximum
CNVTOL, F, , , , E-11

```

```

EQSLV,PCG
PCGOPT,4, , YES,

```

```

TIME, NN
LSWRITE, NN
*ENDDO

```

```

!!!!!!!!!!!!!!!!!!!!!!!!!!!!!!!!!!!!!!!!!!!!!!!!!!!!!!!!!!!!!!
FINISH
!!!!!!!!!!!!!!!!!!!!!!!!!!!!SOLUZIONE!!!!!!!!!!!!!!!!!!!!!!!!!!!!

```

```

/SOLU
ALLSEL,ALL
LSSOLVE, 1, LOAD_STEPS, 1
!!!!!!!!!!!!!!!!!!!!!!!!!!!!!!!!!!!!!!!!!!!!!!!!!!!!!!!!!!!!!!
FINISH
!!!!!!!!!!!!!!!!!!!!!!!!!!!! RESULTS !!!!!!!!!!!!!!!!!!!!!!!!!!!!!

```

```

SAVE, struttura, DB, , ALL
/POST1
! Evaluation of properties
CSYS,12
DSYS,12
RSYS,12
*DIM, force_Y, ARRAY, LOAD_STEPS, 1

```

```

*DIM, stress_1, ARRAY, LOAD_STEPS, 1
*DIM, stress_2, ARRAY, LOAD_STEPS, 1
*DIM, stress_3, ARRAY, LOAD_STEPS, 1
*DIM, strain_1, ARRAY, LOAD_STEPS, 1
*DIM, strain_2, ARRAY, LOAD_STEPS, 1
*DIM, strain_3, ARRAY, LOAD_STEPS, 1
*DIM, VM_stress_max, ARRAY, LOAD_STEPS, 1
*DIM, VM_stress_mid, ARRAY, LOAD_STEPS, 1
*DIM, VM_tot_strain_max, ARRAY, LOAD_STEPS, 1
*DIM, VM_tot_strain_mid, ARRAY, LOAD_STEPS, 1
*DIM, VM_el_strain_max, ARRAY, LOAD_STEPS, 1
*DIM, VM_el_strain_mid, ARRAY, LOAD_STEPS, 1
*DIM, VM_pl_strain_max, ARRAY, LOAD_STEPS, 1
*DIM, VM_pl_strain_mid, ARRAY, LOAD_STEPS, 1

```

```

! Create status bar
*ABSET, 'Extracting data from model', BOTH
*IF, _ABORT,GT,0,EXIT
new_title = 'Progress: LS 0/%LOAD_STEPS% completed'
progress = 0
*ABCHECK, progress, new_title

```





```

('Mod. el. materiale      = ',F18.8, ' MPa')
*VWRITE, M_P
('Coeff. Poisson materiale = ',F18.8)
*VWRITE, lato
('Lato cella              = ',E18.8, ' m')
*VWRITE, raggio/lato
('Raggio/lato             = ',E18.8)
*VWRITE, S0/2/lato
('Spessore/2*lato        = ',E18.8,/)
*VWRITE, num_el
('Numero di elementi     = ',E18.8,/)
*CFCLOS

*CFOPEN, TENSILE_TEST_repeat_cella_%struttura%, txt
*VWRITE,
('      DISP -- TOT. STRAIN  -- STRESS -- VM_stre_mid -- VM_stre_max--VM_el_str_mid--
VM_el_str_max--VM_pl_str_mid--VM_pl_str_max--VM_tot_str_mid--VM_tot_str_max')
*VWRITE, def(1), strain_2(1), stress_2(1), VM_stress_mid(1), VM_stress_max(1), VM_el_strain_mid(1),
VM_el_strain_max(1), VM_pl_strain_mid(1), VM_pl_strain_max(1), VM_tot_strain_mid(1),
VM_tot_strain_max(1)
(11F15.6)
*CFCLOS

```

---

## Acknowledgement

---

The journey of a successful PhD is composed of many people who contribute in different ways. I would like to take this opportunity to express my gratitude towards them.

Firstly, I would like to thank my supervisors, Prof. Matteo Benedetti and Prof. Alberto Molinari for believing in my ideas throughout my PhD. It was their continuous guidance, support and enthusiasm that motivated me to be a confident and innovative researcher. The knowledge I have gained through our interactions have influenced my professional as well as personal growth.

The experimental part of the work was completed from the specimens provided by Lincotek Medical, Trento, Italy. This collaboration with Lincotek Medical provided me with an opportunity to interact with Mr. Gianluca Zappini and Mr. Valerio Luchin who enlightened me on the current developments and the industrial aspects of the additive manufacturing process. Thank you, for your inputs, clarifications and for sharing your knowledge, in our interactions.

Prof. Vigilio Fontanari, I thank you for advice, patience and help in improving the quality of my articles. I would like to thank Lorena Maines and Gloria Ishchia for helping me capture nice SEM images, which were an integral part of my work. Lorena Emanuelli, thank you for having the kindness and patience to teach me different material characterization equipment.

I will ever be grateful to my parents Raghavendra KS and Manjula for their never-ending support and love in every aspect of my life. Thank you, for believing in me, standing by my side and encouraging me to always follow my dreams. I would not have achieved this without your blessings and support. I would like to thank my sister Rajalakshmi, brother-in-law Manjunatha N and my nephew Ruthvik for being there for me throughout my journey. I would like to express my humble gratitude towards my in-laws Balaji GN and Shreedevi Iyengar for their blessings and support during my PhD.

From the day I started my PhD, I was lucky enough to meet some wonderful people at the University without whom PhD would not have been fun. Thank you, Michelangelo, Mara, Matteo, Marco, Giulia, Balanand, Daniele, Ana, Stefano, Ankur, and Alberto Zanellini for making these years memorable. I would like to thank my dear friend Mohammedhusen Manekiya for all the fun conversations that would bring relief on a busy day. A special thanks to my friend, teammate and colleague Michele Dallago for all his help, suggestions and your patience. Your contribution towards my work has been crucial to complete my work successfully. I would also like to thank everyone else who have contributed directly or indirectly to make my life easy at the University.

To the most important person, my wife, and my best friend, Priya!!! Seeing you work towards your PhD has been a form of motivation for mine. I cannot imagine going through this journey without your unconditional love and support during my ups and downs. Thank you for believing in me and encouraging me to do more. This fabulous journey of doing PhD together will be a cherishable part of our wonderful life ahead!!!

Finally, thank you God, for giving me the strength and stability to enjoy this journey.

*Sunil*